Advanced methods for analyzing non-linear dynamical systems

Tomas Gotthans

UNIVERSITÉ PARIS-EST

BRNO UNIVERSITY OF TECHNOLOGY
FACULTY OF ELECTRICAL ENGINEERING AND COMMUNICATION

Thèse de doctorat en cotutelle

Université Paris-Est, ESIEE Paris, Laboratoire ESYCOM, École Doctorale Maths STIC, Spécialité: Electronique, Optronique et Systèmes

Et

Brno University of Technology, Faculty of Electrical Engineering and Communication, Department of Radio Electronics

présentée et soutenue publiquement par

Tomas GOTTHANS

le 15 janvier 2014

Advanced methods for analyzing nonlinear dynamical systems

Méthodes avancées pour l'analyse des systèmes dynamiques non-linéaires

---

Directeurs de thèse

Prof. Geneviève Baudoin (UPE, ESYCOM, ESIEE Paris, France)
Assoc. Prof. Ing. Jiří Petržela (BUT Brno, DREL, République Tchèque)

Jury

Yves Louët	Professeur	SUPELEC - Rennes, France	Président
Claude Duvanaud	Maitre de conférence	Université de Poitiers, France	Rapporteur
Milan Štork	Professeur	UWB Plzeň, République Tchèque	Rapporteur
Roman Maršálek	Professeur associé	BUT Brno, République Tchèque	Examinateur

ACKNOWLEDGEMENTS

First of all, I would like to express my deepest gratitude to my two supervisors: Mrs. Geneviève Baudoin and Mr. Jiří Petržela. They have inspired me by the high standards and by their deep devotion to their work. Your professional and patient attitude helped me to better understand countless research problems. Thank you also for encouraging, exciting and thoughtful discussions and for your friendly attitude that greatly contributed to my professional development.

Many thanks belong definitely to Mr. Roman Maršálek, who introduced me to the research team at ESIEE Paris. Without his support and expert advices, this work could not have started.

I am grateful to all committee members and particularly to Mr. Claude Duvanaud and Mr. Milan Štork who have accepted to become official reviewers of this thesis.

I would like also to thank to the administrative staff for their kindness and support during the research as well to the government authorities for their financial support. My thanks belong to my colleagues and friends in the ESYCOM laboratory in France and in the Department of Radio Electronics in the Czech Republic.

Last, but truly not least, I would also like to express my deepest gratitude to my parents and to my family. I also wish to especially thank to my girlfriend Eliška and to her family. Thank you for your love, encouragement and support. Thank you for your patience during the time I was far away from home.

PREFACE

This thesis represents a culmination of work and learning that has taken place over a period of three years (2010 - 2013). It started as a small group of people(leaded by Assoc. Prof. Jiří Petržela) with backgrounds primarily in electronics, physics and maths, with idea that an explanation and analysis of nonlinear systems, mainly focused on the deterministic chaotic theory, can be done using electronic circuit theories.

In 2011 I joined a research group at ESIEE Paris led by Prof. Geneviève Baudoin where I started my work at project AMBRUN (with participants from: ESIEE Paris, SUPELEC, TeamCast and Thales Communications & security). The project is mainly focused at linearization of high power amplifiers and description of non-linear devices. With background in electronics and non-linear devices I have joined the laboratory ESYCOM. We have decided to do a Ph.D. under double supervision (cotutelle) by Université Paris Est and Brno University of Technology.

Therefore the thesis is divided in two parts that are practically connected only by the non-linear phenomenas. The first part deals with linearization of power amplifiers. The second part describes phenomena and analyzing techniques related with chaotic systems.

I have also been involved in other collaborative work; in particular with Univ.Prof. Christoph Mecklenbräuker (TU Wien) and Prof. Aleš Prokeš (BUT) trying to assembly test-bench for UWB measurements in the optical domain (1550nm) for in-car communication. The obtained measurements will be used for modeling the channel in cars.

I have been a member of Wireless communication teams (WICOMT) since 2011 focused on the investigation of microwave components of communication systems and on research of wireless communication systems. The WICOMT project was followed by the regional research centre of Sensor, Information and Communication Systems (SIX) where I have been a member since 2012.

Original contributions of the thesis

This thesis is primarily focused on the modeling and analyzing of non-linear dynamical systems.

The main contributions can be summarized to several categories:

PART I:

- First the generalities on radio frequency power amplifiers have been introduced.
- Several known techniques for linearizing and modeling the non-linear systems (especially PA) have been presented (RF models, baseband modes - static and quasi-static, multistage, dynamical and neural network models).
- Identification of models (and DPDs) have been presented. Brief complexity have been discussed.
- Test signals for measuring PAs have been created.
- Modeling and linearization of five measured amplifiers from several manufacturers (TeamCast, Thales) has been presented. Subsequently the comparison is presented.
- The fractional least mean square algorithm for modeling and linearizing is presented.
- The optimal order estimation of DPDs and models using integer genetic algorithm is presented.
- Influence of time delay mismatch (integer and fractional time) on the DPD performance is presented. Consequently in order to compensate an integer advance time mismatch, the PMM model is introduced.
- Modeling and linearization of PA with spectral artifacts (an asymmetrical spectrum and spikes in adjacent channels) are discussed. Consequently the filtered LS solution is presented.
- Multiple solutions in adaptive indirect learning architectures for predistortion have been shown with proposed solution.
- A testbench has been assembled in order to measure and validate wideband RF power amplifiers.

PART II:

- Methods for analyzing the mathematical models and time series (with reconstruction) have been introduced.
- Fractional order series is briefly discussed and it is shown, that there can exists autonomous chaotic dynamical system with order lower than 3. Research of fractional behavior is leading to interesting properties, such as memory effects, that natural description can not provide.
- New dynamical system with chaotic solution having periodical discrete jumps is presented. Consequently new method for analysis called spherical quantification have to be used.
- Generalization of piecewise-linear approximation of vector field is used for several examples. As the result of the linearization, possible analytical solutions of chaotic systems arises.
- In the next section as a consequence of discretization of vector fields system with so-called sampled dynamics is presented and verified by practical circuit.
- New quantifier for systems with large state attractor dynamics is generalized into the n-spherical quantifier.
- The area of generating dynamical chaotic jerk-functions is investigated from the sampled dynamic point of view. Therefore synthesis of circuit having discrete vector field step function is presented.
- Parallelization of calculation of Lyapunov exponents is presented.
- Parallel particle swarm optimization is presented and is used in order to find chaotic solutions of generic set of differential equations with piecewise-linear vector fields.

CONTENTS

LIST OF FIGURES

LIST OF TABLES

List of Acronyms

RF	Radio Frequency
PA	Power Amplifier
VHF	Very High Frequency
DPD	Digital Predistortion
GMP	Generalized Memory Polynomials
OMPS	Orthogonal Memory Polynomial Series
OPS	Orthogonal Polynomial Series
PMS	Polynomial Memory Series
DDR	Dynamic Deviation Reduction
DDR2	Dynamic Deviation Reduction Second Order
LMS	Least Mean Squares
RLS	Recursive Least Squares
DNA	Damped Newton Algorithm
FLMS	Fractional Least Mean Squares
NN	Neural Network
PMM	Polynomial Memory Modified Series
LS	Least Squares
NMSE	Normalized Mean Square Error
PAPR	Peak to Average Power Ratio
ACPR	Adjacent Channel Power Ratio
IP3	Third-order Intercept Point
RMS	Root Mean Square
OFDM	Orthogonal Frequency Division Multiplexing
PAE	Power Added Efficiency

MEE	Memory Effects
IMD	Intermodulation Distortion
EVM	Error Vector Magnitude
IF	Intermediate Frequency
DAC	Digital to Analog Converter
ADC	Analog to Digital Converter
TWT	Traveling Wave Tube
FET	Field Effect Transistor
SSPA	Solid State Power Amplifier
ANN	Artificial Neural Network
RVTDNN	Real Valued Time Delayed Neural Network
EKF	Extended Kálmán Filtering
UKF	Unscented Kálmán Filter
DAB	Digital Audio Broadcasting
MUX	Multiplex
DVB-T	Digital Video Broadcast - Terrestrial
GA	Genetic Algorithm
LDMOS	Laterally Diffused Metal Oxide Semiconductor
FPGA	Field Programmable Gate Array
FIR	Finite Impulse Response
IIR	Infinite Impulse Response
VSG	Vector Signal Generator
RTSA	Real-time Spectrum Analyzer
LAN	Large Area Network
VISA	Virtual Instrument Software Architecture

DUT	Device Under Test
DSO	Digital Signal Oscilloscope
ALC	Automatic Level Control
LO	Local Oscillator
CPU	Central Processing Unit
PSO	Particle Swarm Optimization
PPSO	Parallel Particle Swarm Optimization
JM	Jacobi Matrix
LE	Lyapunov Exponent
GP system	Gotthans-Petrzela system
RC network	Resistor-Capacitor network
SP	Surface Pieces
PWL	Piecewise-Linear
DFT	Discrete Fourier Transform
GL	Grunwald-Letnikov
DSP	Digital Signal Processor
ASIC	Application Specific Integrated Circuit
AM	Amplitude modulation
FM	Frequency modulation
LLE	Largest Lyapunov exponent
ESIEE	École Supérieure d'Ingénieurs en Électronique et Électrotechnique

Part I

Modeling and linearization of non-linear systems

1 MOTIVATION

It is common situation that nonlinear devices are simulated using computers. There can be complex models modeling physical phenomenas of each electronic part. Models on physical level are usually very complex and difficult to handle even with modern computers. Another approach can be modeling systems in fact as a black-box device.

Another aspect of non-linear systems is the reduction and modeling of inconvenient effects connected with a real characteristic of many real-world parts [3, 123, 140], especially the modeling aspects connected with non-linear power amplifiers (PA) used in wireless communications and broadcasting.

Power amplifiers are critical elements of mobile communication and broadcasting systems because their efficiency conditions the autonomy and the weight of mobile handset batteries and their linearity influences on performance of the communication. In practice, PAs are not perfectly linear and present memory effects, i.e. the output signal is a function of the current and of previous input signal values. And a compromise must be achieved between the efficiency and the linearity of the PA [4].

The aim of this work is to bring new innovative solutions to improve the performance of RF power transmitters.

The work conducted in this thesis is a part of work for the project AMBRUN (FUI project with partners: Thales, TeamCast, Supélec and ESIEE Paris). The project aims to improve the radio performance of the amplification of multiplexed signals using adaptive algorithms for dual applications: tactical communication and broadcasting VHF band. The originality and ambition of the project lie in the bandwidths of processed signals (above 40 MHz) the involved powers (up to 100W) and the non-stationarity of tactical multiplex signals.

In Fig.1.1 one can see increasing demands on communications system with every generation of devices. One may observe, that in 1985 for AMPS systems the required bandwidth of signal was 30kHz. Comparing for example with the latest LTE Advanced, that can require 100MHz of bandwidth. The LTE Advanced requires approximatively 3400 times larger bandwidth than AMPS systems. That is also challenging in terms of signal processing.

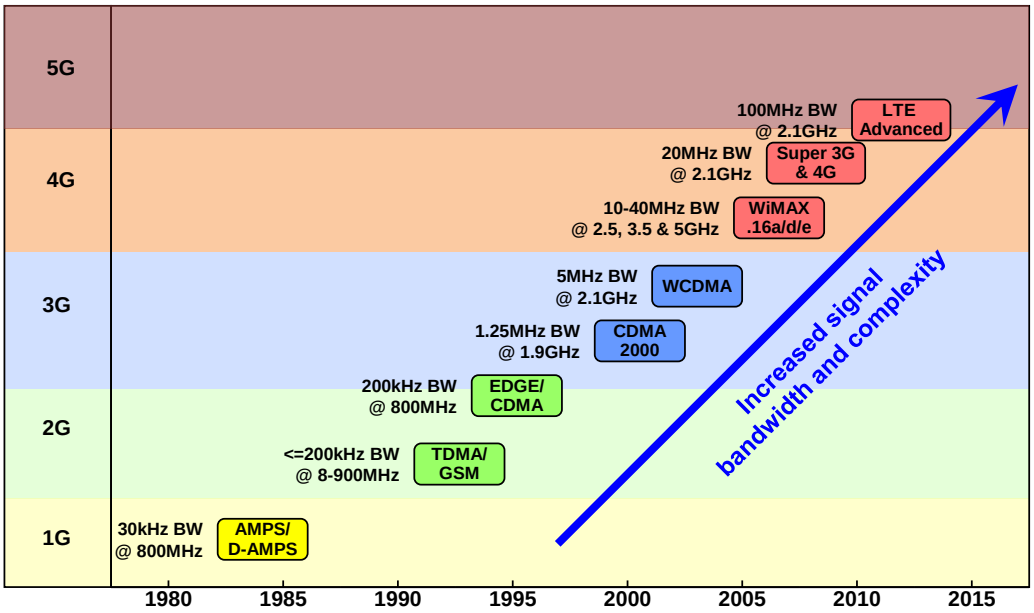

Fig. 1.1: Time schedule for the complexity and signal bandwidth.

2 GENERALITIES ON RADIO FREQUENCY POWER AMPLIFIERS

In this chapter we would like to introduce some generalities related with power amplifiers. This first, general chapter consists of three sections. The first section is dedicated to description of ideal power amplifier. The second section brings overview of performance evaluation methods. Finally the last section introduces generalities on linearization of power amplifiers.

2.1 Ideal and Real Power Amplifier

The main task of power amplifier is to increase strength of signal. The ideal power amplifier doesn't introduce any distortion. Therefore the output V_{out} of ideal power amplifier is directly proportional to its input signal V_{in} with gain G:

$$V_{out} = G\ V_{in}. \tag{2.1}$$

The layout is presented in Fig.2.1. For small input signal powers, this is often

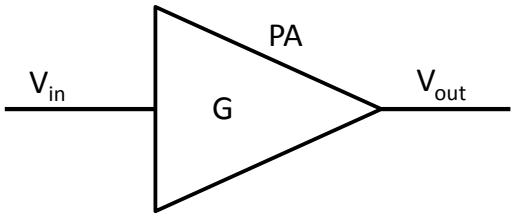

Fig. 2.1: Schematic representation of power amplifier.

a sufficient description of the functionality. The ideal characteristic is not limited by any value so called saturation effects and does not produce any memory effects. However, if the input signal power is increased, at some point the PA begins to saturate. The ideal saturation could be modeled by a limiter. As a consequence of saturation, the gain decreases with increased input power. Gain compression occurs because eventually the output signal (voltage, current, power) saturates, due to the supply voltage or bias current limitation.

2.1.1 1dB Compression Point

A real power amplifier typically maintains a constant gain for low-level input signals. However, at higher input levels, the amplifier usually goes into saturation and its

gain naturally decreases. The 1 dB compression point (P1dB) is a typical value used for characterization and indicates the power level that causes the gain to drop by 1 dB from its small signal value. The 1 dB compression point is derived from the gain relationship between output power and input power. It is measured by slowly increasing source amplitude while monitoring the output power drop.

2.1.2 AM/AM and AM/PM Conversion

Using the AM/AM and AM/PM conversion characteristics is based on the idea of separable effects of the non-linearities. AM-to-AM conversion characteristics describe output power depending on the input power.

Similarly an AM-to-PM conversion measures the amount of undesired phase deviation (PM) that is caused by input power variations (AM) of the system. Usually the conversion characteristics are measured with one tone signals.

The example of such conversion characteristics can be seen in the Fig.2.2.

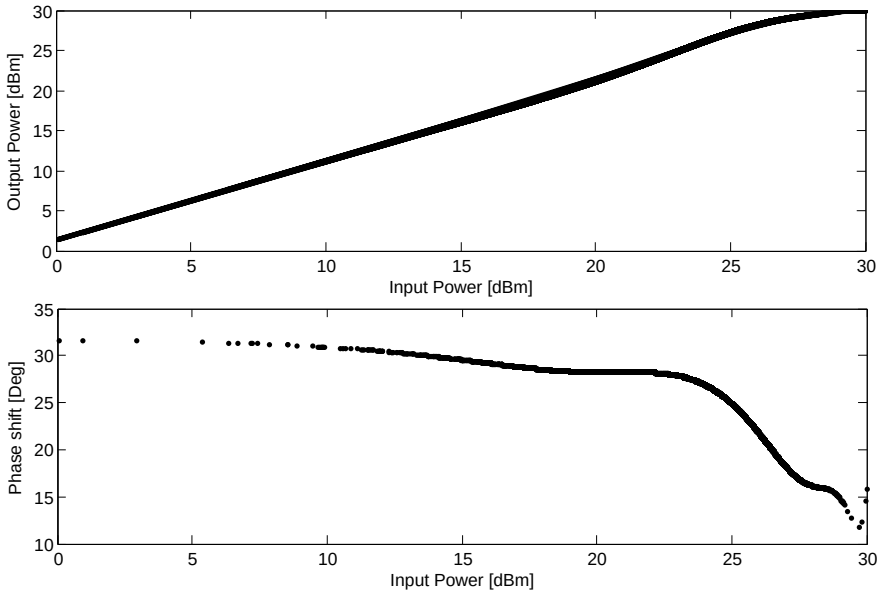

Fig. 2.2: AM/AM conversion characteristics (top) and AM/PM conversion characteristics (bottom).

2.1.3 Two Tone Test and Intermodulation Distortions

A widely used method for evaluating an amplifier's linearity is the two-tone test. The two tone test signal is constructed by summing two closely-spaced unmodulated RF carriers with amplitude A, and frequencies $f_{1,2}$. Modulating the signal with ideal RF modulator we get:

$$V_{inRF}(t) = A\ cos(2\pi f_1 t) + A\ cos(2\pi f_2 t) = 2\ A\ cos(2\pi f_m t)\ cos(2\pi f_c t), \tag{2.2}$$

where $f_m = \frac{f_2 - f_1}{2}$ and $f_c = \frac{f_1 + f_2}{2}$.

Now applying the signal to an amplifier considering only amplitude distortions of the signal we may describe the amplifier characteristics by general polynomial series as:

$$V_{out}(t) = a_1 V_{in}(t) + a_2 V_{in}(t)^2 + ... + a_k V_{in}(t)^k + ... + k_N V_{in}(t)^N. \tag{2.3}$$

When the two-tone signal is applied to input of this amplifier, each order of nonlinearity will generate additional frequency components or intermodulation products:

$$f_{IM} = mf_1 + nf_2, \tag{2.4}$$

where m and n are positive or negative integers and $|m| + |n| = k$ where k is the order of intermodulation. The even order terms generate intermodulation (IMD) products that are located away from the input frequencies.Therefore they can be easily filtered. Unfortunately, the odd-order IMD products are close to the useful band (Fig.2.3).

Over the decades, the two-tone test has proven to be a powerful PA linearity test

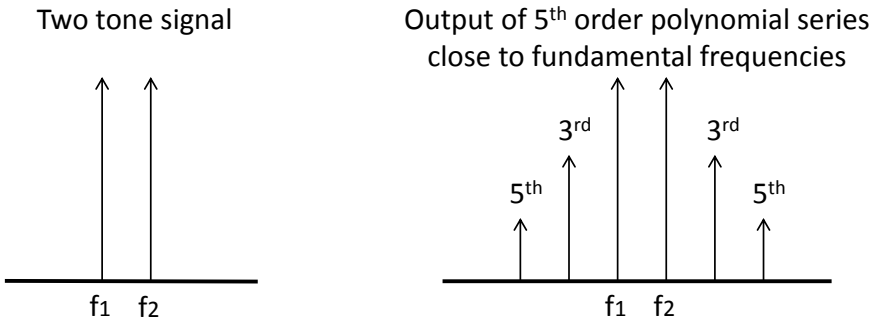

Fig. 2.3: In-band IMD products for an amplifier with up to fifth orders of nonlinearity.

procedure that can be performed with a relatively simple experimental setup. However, nowadays modulated signals are far more complex and the simple two-tone test may be insufficient.

2.1.4 Nth Order Intercept Point

The interception point is defined at the extrapolated intersection of two lines in AM/AM plot - extrapolated fundamental component line and the line that gives power of the Nth order intermodulation product as a function of the input power. For example the third-order intercept point (IP3) relates nonlinear products caused by the third-order nonlinear term to the linearly amplified signal. The intercept point is a purely mathematical concept, and does not usually correspond to physical power level. In many cases, it lies far beyond the damage threshold of the device.

The typical approach measuring an Nth-order intercept point uses two-tone signals. It begins by applying two sinusoids to the circuit input at frequencies f_1 and f_2. We increase their power while plotting the power at the output in a fundamental and in an Nth-order intermodulation product (for example for the IP3 we chose either $2f_1 - f_2$ or $2f_2 - f_1$).

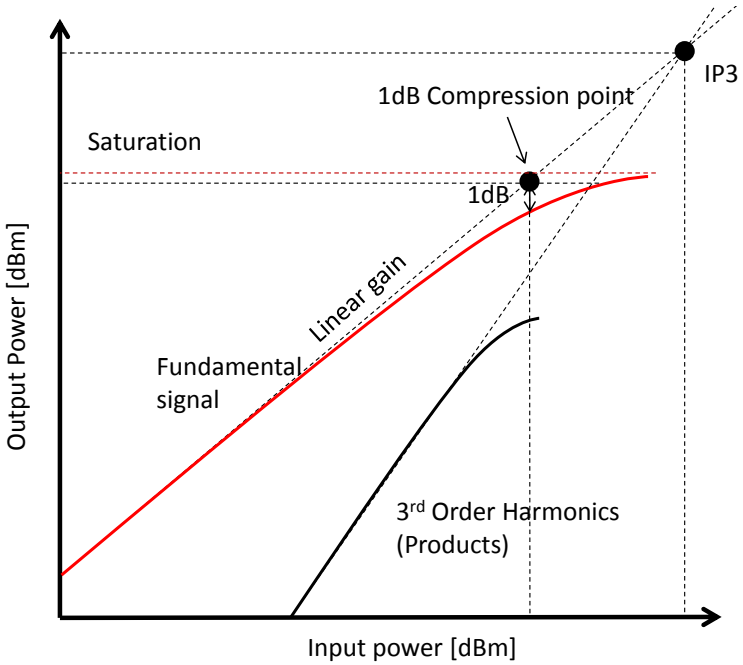

Fig. 2.4: Graphical representation of Saturation point, IP3 and 1dB Compression point.

The graphical representation of each definition is visualized in Fig.2.4.

Parameters like 1dB compression point and IP3 are parameters usually given by PA manufactures (Fig.2.4). However such points are not sufficient, because the measurements are performed only for tone signals. Thus PA characterization is not

sufficient for wideband signals.

2.1.5 Efficiency of Power Amplifier

A very important figure of merit for a power amplifier is its efficiency which denotes how much of the supplied power is transfered to the output and how much of the power is transformed to other forms of energy(usually heat). The efficiency is related with power consumption. The worst the efficiency, the worst the battery life is. Different definitions of efficiency can be given, one of the most useful is the Power Added Efficiency (PAE). PAE is calculated as follows:

$$PAE = \frac{P_{out} - P_{in}}{P_{DC}}\ 100\%, \tag{2.5}$$

where P_{DC} is the power consumption.

2.1.6 Signal Crest Factor - PAPR

The crest factor of a signal is defined as the ratio between peak amplitude input and its root mean square (RMS) value:

$$C = \frac{|x|_{peak}}{x_{rms}}. \tag{2.6}$$

A derived measure from Crest factor is the peak-to-average power ratio (PAPR). The PAPR is usually used in signal processing applications. It is defined as power ratio:

$$PAPR = \frac{|x|^2_{peak}}{x^2_{rms}} = C^2. \tag{2.7}$$

Usually the PAPR is expressed in decibels (dB). The knowledge of PAPR is important, because it is a measure of the envelope dynamics.

The PAPR can be measured on radio-frequency (RF) or baseband complex envelope signals. There is a 3dB difference between the two definitions.

Widely used Orthogonal Frequency-Division Multiplexing (OFDM) signals have quite high PAPR (approx. 12dB in RF) unlike sine wave which has $3.01dB$. The PAPR is an important signal parameter for a PA, because it leads to using large back-off to preserve linearity whilst the efficiency is degraded.

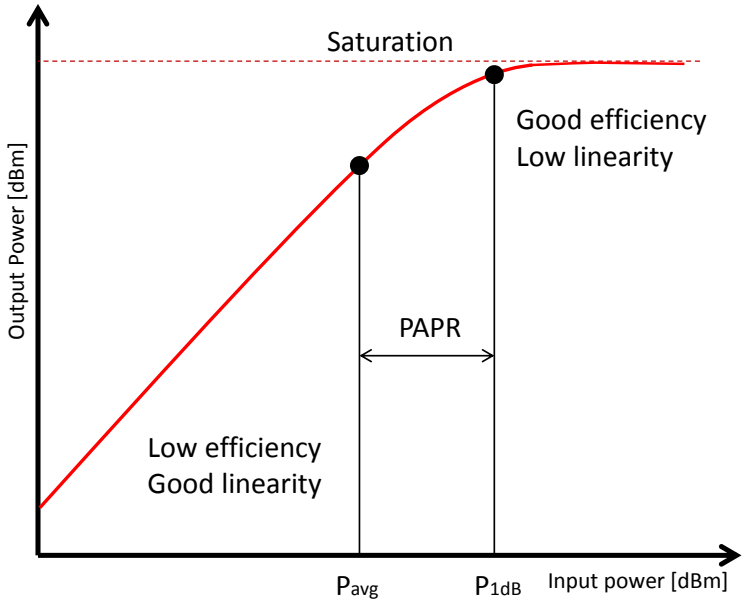

Fig. 2.5: Graphical representation of PAPR, AM/AM characteristics of PA with average power P_{AVG} and saturation power P_{1dB}.

In order to have good efficiency, the operating point of PA needs to be set close to saturation area, but the higher the operating point is, the worst the linearity. Usually we need to set a certain compromise between linearity and efficiency. Therefore a back-off is used. The value of the back-off is of the same order as the PAPR ($Back - off \approx PAPR$).

2.1.7 Memory Effects

Memory effects (MEs) have been receiving a great deal of attention as they are known to impair most common (memoryless) PA linearization schemes. When using narrowband signals, memory effects does not play an important role, however in wideband and high-power systems, the memory should be taken into account.

In fact, since traditional PA linearizers are designed as memoryless devices, they simply breakdown in presence of some sort of dynamic IMD behavior. This is so important that microwave PA industry has been asking for some form of MEs metric [5], capable of evaluating the PA linearizability. The memory effects could be expressed basically as frequency-domain fluctuations in the transfer function or in time domain.

MEs can be subdivided into two different groups of phenomena basically according to the time constants involved.

Short-term MEs are characterized by time constants comparable with the carrier period. They are usually caused by the reactive components of the active device and matching networks at the RF band. Such PAs are usually modeled with small memory order.

On the contrary, long-term MEs are low-frequency phenomena involving time constants that are comparable to period of useful signal envelope. They can be caused by thermal effects, active device charge carrier traps, or by biasing networks.

In general these memory effects results in AM/AM and AM/PM characteristic depending on the input signal.

2.2 System performance evaluation: ACPR, EVM, NMSE

There are several parameters used to evaluate the influence of PA non-linearity on system performance in the case of modulated signals, in particular ACPR and EVM.

2.2.1 Adjacent Channel Power Ration - ACPR

The imperfections and non-linearities usually results in some adjacent channel spectral regrowth. This phenomenon can be quantified with the parameter ACPR that is defined as a bandwidth limited ratio between the power in the main channel and the power in one adjacent channel (Fig.2.6). Therefore we can define this property for left and right adjacent channel. The right and left channel ACPRs are defined by:

$$\begin{aligned} ACPR_R[dB] &= 10\log\left(\frac{\int_{-B/2}^{B/2} P_y(f)df}{\int_{B/2}^{3B/2} P_y(f)df}\right) \\ ACPR_L[dB] &= 10\log\left(\frac{\int_{-B/2}^{B/2} P_y(f)df}{\int_{-3B/2}^{-B/2} P_y(f)df}\right), \end{aligned} \tag{2.8}$$

where B represents the bandwidth of the signal and $P_y(f)$ is power spectral density.

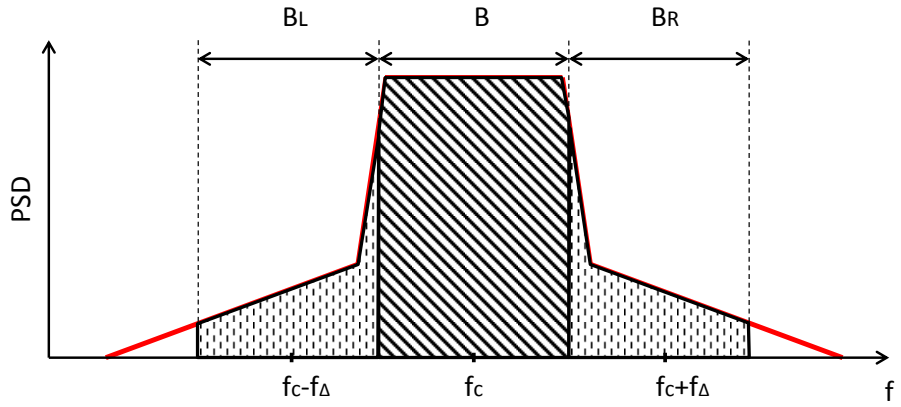

Fig. 2.6: Graphical representation of ACPR for left and right sides.

2.2.2 Normalized Mean Square Error - NMSE

For the quantification of performance we can also use Normalized Mean Square Error (NMSE)[6]. It is an estimator of the overall deviations between predicted and measured values. For two complex vectors $\mathbf{x}$ and $\mathbf{y}$ of N samples the NMSE is defined as:

$$NMSE(\mathbf{x},\mathbf{y})[dB] = 10\log\left(\frac{(\mathbf{x}-\mathbf{y})^H(\mathbf{x}-\mathbf{y})}{\mathbf{x}^H\mathbf{x}}\right). \tag{2.9}$$

Where $(.)^H$ stands for transposed complex conjugation of vector also so-called Hermitian transpose.

The NMSE is a global measure of quality. But it does not distinguish between linear and non-linear distortion.

For example bad NMSE could be due to time shift between signals and/or bad gain alignment.

2.2.3 Error Vector Magnitude - EVM

Error vector magnitude (EVM) is a measurement of performance in the presence of impairments. The measured symbol location obtained after decimating the recovered waveform at the demodulator output are compared with the ideal symbol locations of constellation points. EVM is defined as normalized average value of the vector error. It is usually estimated on a window of N samples. As shown in Fig.2.7, the measured symbol location is given by w. However, the ideal symbol location (using the symbol map) is given by v. Therefore, the resulting error vector is the difference between the actual measured and ideal symbol vectors defined as $e = w - v$.

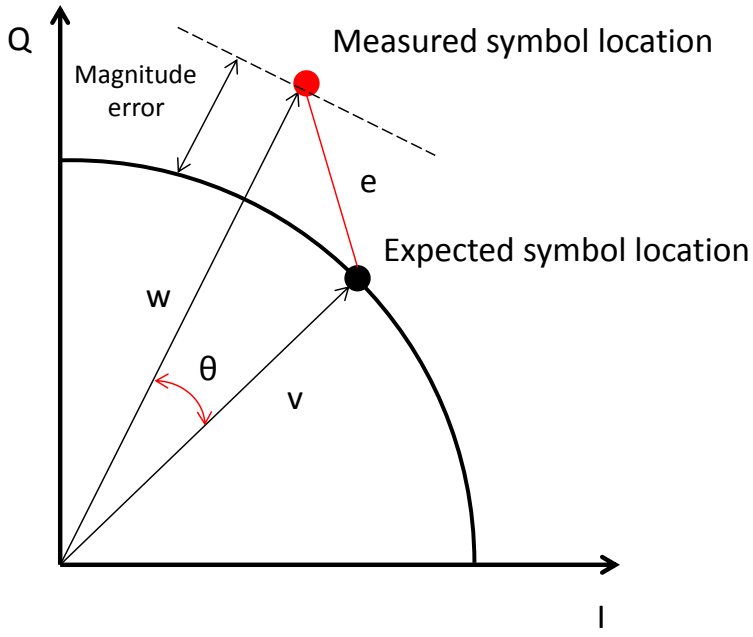

Fig. 2.7: Graphical representation of error vector magnitude (EVM).

The EVM is calculated after compensation of simple constellation determination: offset and complex gain. Analytically, RMS EVM is defined as:

$$EVM = \frac{E(|v - c_1 w - c_0|^2)}{E(|v|^2)}, \tag{2.10}$$

where E(.) represents the average value, c_0 and c_1 are the optimal values of gain and offset. Using ergodic properties, it is estimated on N symbols by (in the case where $c_0 = 0$ and $c_1 = 1$):

$$EVM = \frac{\sum_{j=1}^{N} \left[(I_j - I_j^{meas})^2 + (Q_j - Q_j^{meas})^2\right]}{\sum_{j=1}^{N} |I_j^2 + Q_j^2|} \; 100\%. \tag{2.11}$$

2.3 Linearization of Power amplifier

In order to use very efficient power amplifiers, usage of signal processing methods to compensate or reduce the distortion caused by the PA would be beneficial. Unfortunately, PAs are most efficient when operated near saturation.

The PA linearization techniques are well known approaches widely used for several decades in analogue techniques. Due to rise of computational power, bandwidth and advanced modulation techniques, the interest in digital predistortion techniques

increased. The digital predistortion overcomes the analogue solution in its simplicity, stability and adaptivity.

2.3.1 RF Feedforward Linearization

The principle itself is old and was invented in Bell Laboratories [7]. The principle is to calculate the distortion signal at the output of PA and then subtract it from the output signal. Therefore an input signal splits into two paths as we can see in the Fig.2.8. The first path consists of the main PA and time delay with some coupling elements. The second one amplifies the difference between output of the first PA and time delayed input. At the output we subtract by a coupler the amplified error signal from the time delayed distorted output of the PA. Thus we reduce distortions at PA output.

Such principle is simple but with some disadvantages. One of the greatest is the high number of components and therefore also high sensitivity to perfect circuit matching. The main advantage is the unconditioned stability and wide bandwidth of such systems.

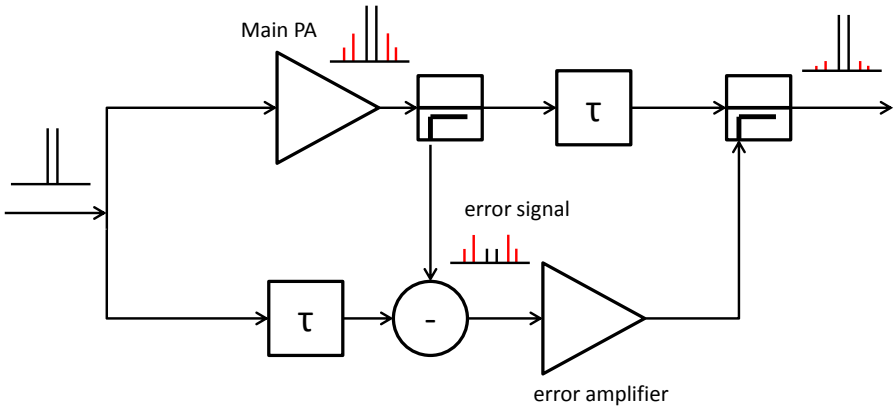

Fig. 2.8: Fundamental layout of RF feedforward linearization.

Note that distortion from memory effects can also be compensated using the feedforward technique, since these effects are included in the error signal. Such scheme can be modified to be adaptive by adding feedback control loop.

2.3.2 RF Feedback Linearization

The use of feedback is well known across all the fields of electronics (oscillators, amplifiers, optical systems, etc).

In principle the output from feed-backed amplifier is subtracted from the input signal with a certain attenuation. Therefore the PA is driven by the error signal. The advantage is the relative simplicity of additional circuitry needed to provide feedback. On the contrary, the main disadvantage of feedback is caused by problems of stability. We may classified feed-back linearization in two main groups: RF feed-back and cartesian feed-back (or more generally transmitter feedback).

The fundamental layout of RF feed-back linearization can be seen in the Fig.2.9. Only nonlinear components are fed-back. The performance depends on the quality of the cancellation process linked to the gain loop. The method can improve only modestly the linearity in the case of wideband signal due to the limitation of the loop-bandwidth product for static systems.

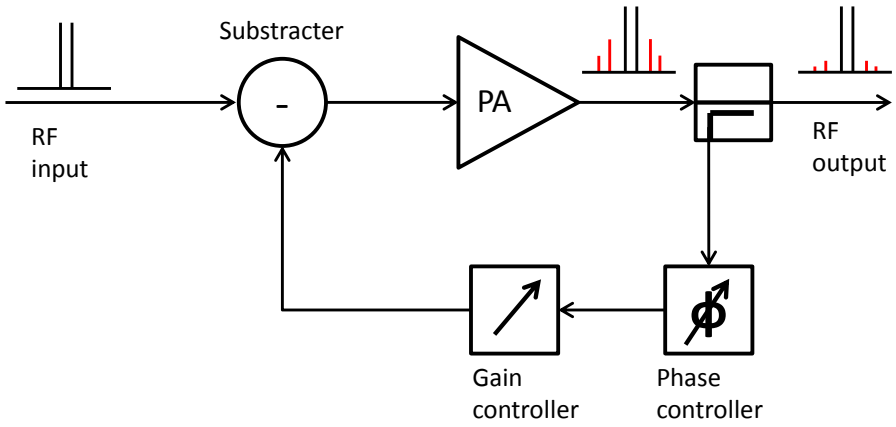

Fig. 2.9: Fundamental layout of RF feedback linearization.

Another possible solution of feedback linearization is the utilization of Cartesian feedback transmitter presented in the Fig.2.10. It is based on negative feedback applied to the Cartesian coordinates of the baseband signals, I(t) and Q(t). The error signal is created by subtraction of the down-converted output of PA from the generated baseband I and Q signals. This approach is interesting since it can linearize transmitters but it is limited to narrow-band signals because of long delays in the loop that increases stability constraints.

There exists other methods like Envelope feed-back, Polar-Loop Transmitter and others. All of the other mentioned methods are derived from feedback theory.

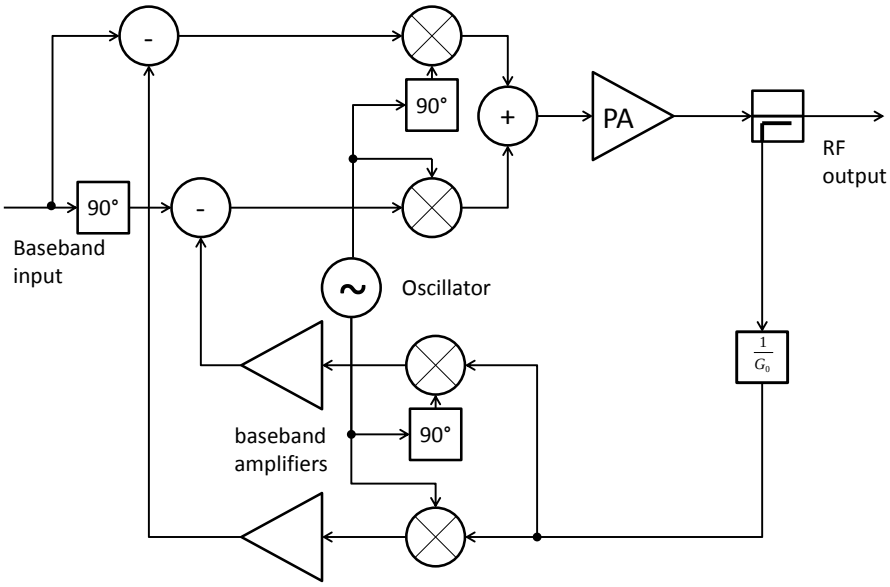

Fig. 2.10: Fundamental layout of Cartesian-loop feedback transmitter linearization.

2.3.3 Analog and Digital Predistortion

First let us begin with a brief description of the principle of predistortion before presenting the main structures or behavioral models usable for predistortion.

The principle of predistortion is to transform the signal before entering the amplifier to compensate for the distortions which are introduced by the amplifier. The predistortion system should ideally have the inverse characteristics of the distortion generated by the amplifier as shown in Fig.2.11.

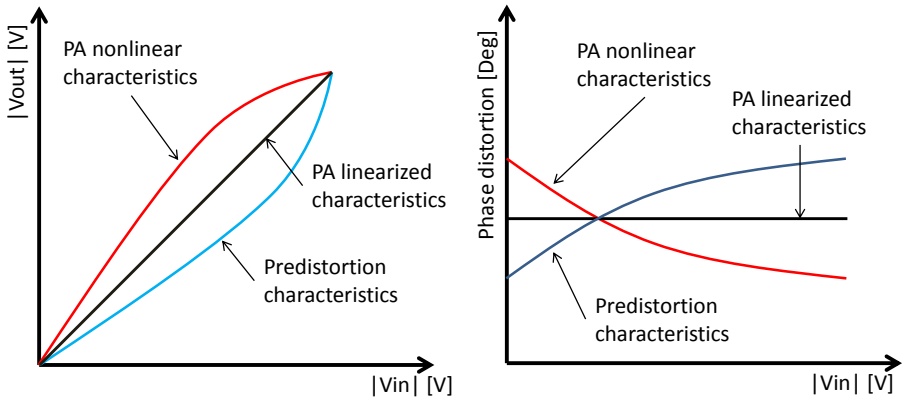

Fig. 2.11: Principle of linearization of filtered baseband complex signals using digital predistortion.

The predistortion circuit may be inserted at different levels of the amplification system: baseband, intermediate frequency (IF) or radio frequency (RF). Example of analog predistortion can be found in [8].

There are two main issues for a system of predistortion. The first question is how to implement such systems, or more precisely what structure use for the predistortion. The second question is how to calculate the parameters of the predistorter.

In this thesis we limit ourselves to the digital baseband predistortion, because it has the best performance and can be adaptive. As the amplification function, the predistortion can be implemented with or without memory function.

The predistortion can be made adaptive to avoid the need to characterize the amplifiers before implementation, or in order to compensate the variations of the amplifier according to the temperature, aging, etc.

Basically the first digital predistortion systems were proposed by Nagata [9] in 1989, Cavers [10, 11] in 1990.

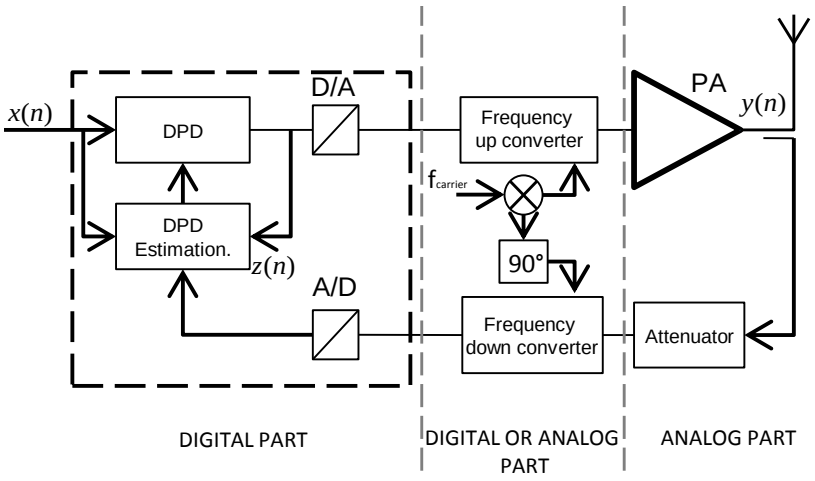

Fig. 2.12: Fundamental layout of real DPD system.

Fig.2.12 shows the basic layout of baseband digital predistortion where an adaptive control could be implemented (return path is realized by taking a part of the output signal by a coupler). For the adaptive case, the predistortion function is continually adjusted according to a certain criterion. In this figure the frequency conversion is performed by an analog IQ modulator, which has the drawback of

potential imbalances between the I and Q channels. Of course we can imagine different variants of this scheme involving an intermediate frequency, or do fully digital frequency up-conversion (and/or down-conversion).

The return signal is used to control the predistortion. It is important to provide very good quality of feedback circuitry, because it serves as a reference signal for the correction. The usage of converters DAC and ADC is not negligible (especially for broadband signals). The resolution, and dynamic range, of converters are important factors. Wrong setup could degrade the performance of predistortion. Also important is the choice of sampling frequency. It should be chosen high enough to take into account spectral regrowth.

As we can see in the Fig.2.13 using digital predistortion can increase the efficiency of the power amplifier by operating the PA closes to the saturation point (noted as P_{sat}). The average output power without predistortion in order to have good linearity is denoted as P_{out}. We may see that the linearity is increased when using predistortion, therefore the average output power P_{pd} can be slightly increased too. Also the power efficiency is better for output power of PA close to saturation.

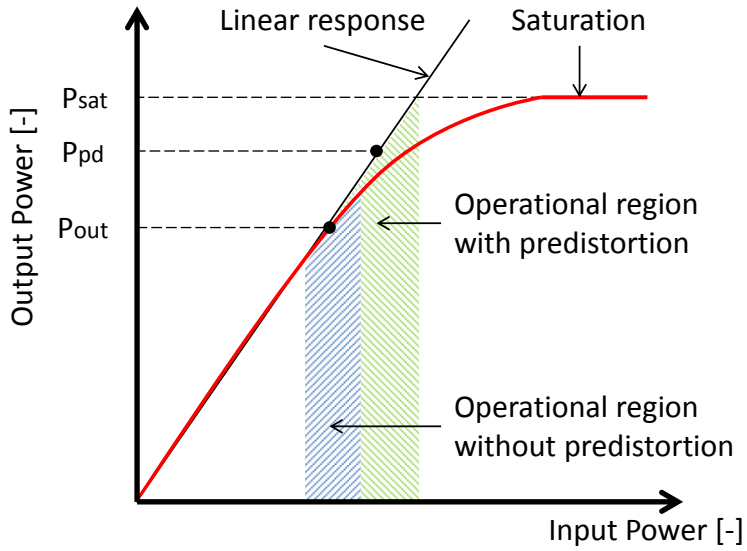

Fig. 2.13: Power amplifier operating regions with and without digital predistortion.

In predistortion we can distinguish between direct and indirect learning approach denoted in Fig.2.14 and Fig.2.15.

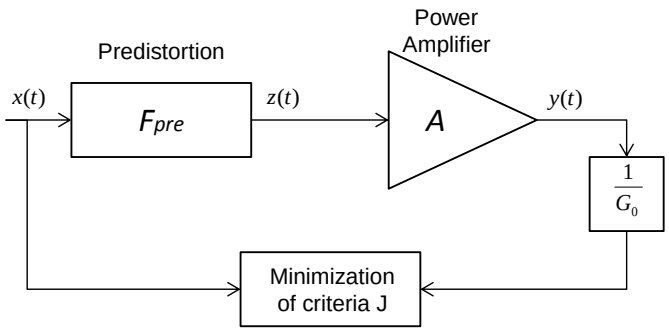

Fig. 2.14: Direct approach to predistortion of PA.

In the direct learnind approach, the operator of predistortion F_{pre} is determined in order to minimize a criterion J between the attenuated output of the amplifier and the original input signal. In the case of memoryless relations, the ideal predistortion operator can be defined by:

$$A[F_{pre}(x)] = G_0 x \quad or \quad F_{pre}(x) = A^{-1}(G_0 x), \tag{2.12}$$

where G_0 is the chosen reference gain.

Since A is a non-linear function, the identification of function F_{pre} is a non-linear problem.

The instantaneous error is:

$$e(t) = \frac{y(t)}{G_0} - x(t) = \frac{A\left\{F_{pre}\left[x(t)\right]\right\}}{G_0} - x(t) \tag{2.13}$$

and the operator F_{pre} is "hidden" by the nonlinear operator A.

In the indirect learning approach, which uses a fictional postdistortion F_{post}, the operator is determined to minimize a criterion between the output of the postdistorted system (attenuated output of the amplifier) and the signal at the input of the amplifier. In the case of memoryless relation, the ideal operator for postdistortion can be defined by:

$$x(t) = F_{post}\left(\frac{y(t)}{G_0}\right). \tag{2.14}$$

The instantaneous error $e(t)$ is:

$$e(t) = x(t) - F_{post}\left(\frac{A(x(t))}{G_0}\right) \tag{2.15}$$

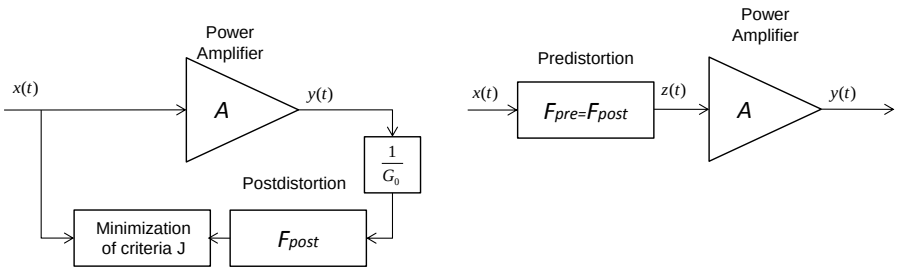

Fig. 2.15: Indirect learning approach to predistortion of PA.

and the operator is "hidden" by A.

Setting:

$$y(t) = \frac{A\left(x(t)\right)}{G_0}, \tag{2.16}$$

we obtain:

$$F_{post}(y) = A^{-1}\left(G_0 y\right). \tag{2.17}$$

We note that the optimal expressions for F_{post} and F_{pre} are identical but this time F_{post} can be explicitly written from the available signals and x and y, where function A^{-1} is the inverse function of the power amplifier. The postdistortion function is then used as predistortion function.

The hypothesis of memoryless relations in not necessary. It can be shown that more generally, the post-inverse of order k is also a post-inverse of order k for Volterra series.

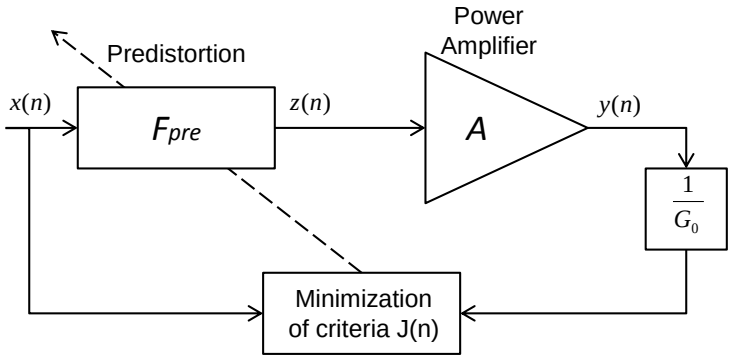

Fig. 2.16: Direct adaptive predistortion approach of PA.

Furthermore, the identification of predistortion coefficients can be estimated adaptively either sample by sample or by blocks. Fig.2.16 and Fig.2.17 illustrate

the approach in which the adaptive predistortion coefficients are calculated at time n and are then applied as predistortion coefficients to time $n + 1$.

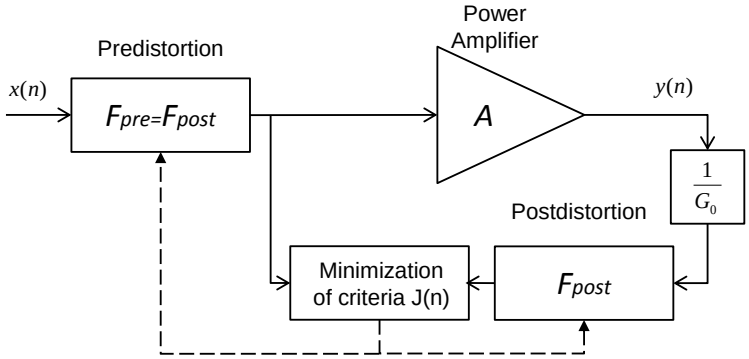

Fig. 2.17: Indirect adaptive predistortion approach of PA.

2.3.4 Digital Postdistortion

Digital postdistortion is a technique equivalent directly to digital predistortion. The main difference is in the position of the nonlinear correcting block as we may see in Fig.2.18. The postdistorter is placed after the PA, therefore it has to disadvantageously work with high output powers. The postdistorter can be used on the other hand in receivers. There, it do not have to deal necessarily with high powers and can correct channel distortions. The digital postdistorters can be also used in baseband.

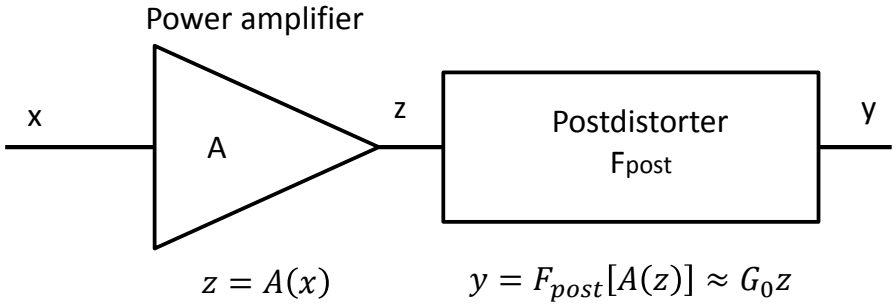

Fig. 2.18: Principle of linearization of PA with baseband digital postdistortion.

2.4 Conclusion

The second chapter has introduced the concept of ideal power amplifiers. The parameters for the evaluation the communication systems performance have been presented in the second subsection. It also gave a basic survey through the general linearization techniques.

More detailed overview of the algorithms for modeling the power amplifiers and digital predistorters will be given in the third chapter.

3 TECHNIQUES FOR ANALYZING AND MODELING NON-LINEAR SYSTEMS

3.1 Introduction

This chapter presents the principals models that can be used for modeling PA or for digital predistortion (DPD). It is composed of two main parts: first the description of the models, then the methods for identification of the models. It focuses on models that can be used in the case of PA linearization.

There are several models used in modeling the PA (or used for DPD) from the simplest models modeling just the amplitude distortions to the most general form known as Volterra series and its derivatives.

We may distinguish the models to three basic categories: memoryless or static, quasi-static and dynamic (or memory) models. For memoryless models, the output at time t only depends on input at time t and it can be shown that the system introduces only amplitude distortions. These amplitude distortions only depends on the magnitude of the input signal. Quasi-static models can also model phase distortions depending on the signal magnitude.

The third category is called dynamic, because these models are able to model memory effects.

3.2 RF Models and Baseband Models of PA

In this section we would like to briefly describe the relationships between RF models and filtered baseband equivalent models. The notation of signals and corresponding spectrum can be seen in Fig.3.1.

We note $x_{RF}(t)$ and $y_{RF}(t)$ the input and output signals of the RF model, $x(t)$ and $y(t)$ are the input and output signals of baseband filtered model: $x(t)$ is the complex envelope of $x_{RF}(t)$ and $y(t)$ is the complex envelope of $y_{RF1}(t)$, where $y_{RF1}(t)$ is obtained by filtering $y_{RF}(t)$ by a passband filter centered on the fundamental RF frequency.

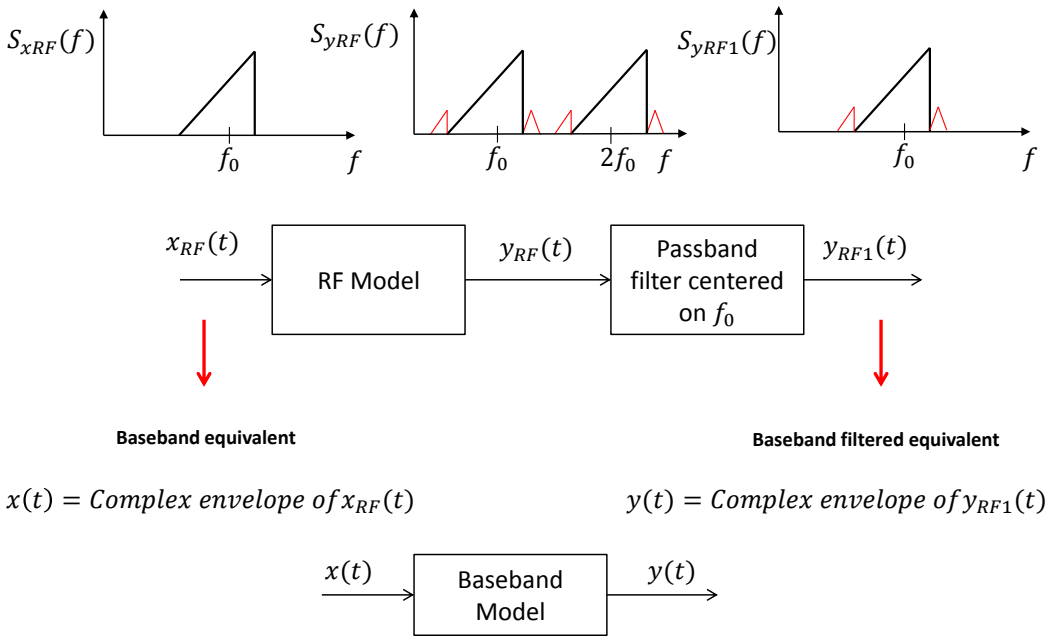

Fig. 3.1: Relationships and notations for RF an Baseband filtered models of PA.

The baseband equivalent signals of RF signals can be expressed using Hilbert transform as:

$$\begin{aligned} x(t) &= \left\{ x_{RF}(t) + j\left[x_{RF}(t) * \frac{1}{\pi t} \right] \right\} e^{-j\omega_0 t} \\ y(t) &= \left\{ y_{RF1}(t) + j\left[y_{RF1}(t) * \frac{1}{\pi t} \right] \right\} e^{-j\omega_0 t}. \end{aligned} \tag{3.1}$$

Similarly the RF signals can be expressed by baseband equivalent signals as:

$$\begin{aligned} x_{RF}(t) &= Re\left(x(t)e^{j\omega_0 t} \right) = \frac{1}{2}\left(x(t)e^{j\omega_0 t} + x^*(t)e^{-j\omega_0 t} \right) \\ y_{RF1}(t) &= Re\left(y(t)e^{j\omega_0 t} \right) = \frac{1}{2}\left(y(t)e^{j\omega_0 t} + y^*(t)e^{-j\omega_0 t} \right). \end{aligned} \tag{3.2}$$

3.3 Static and Quasi-static models

3.3.1 Memoryless RF Polynomial Series

One of the most straightforward models are the polynomial series. We can define the RF model for power amplifier as:

$$y_{RF}(t) = \sum_{n=1}^{N} a_n x_{RF}^n(t). \tag{3.3}$$

The coefficients of models can be obtained from simple measurements such as P_{L1dB}, IP3; etc. Let us establish the baseband equivalent model of the RF polynomial series.

Let us investigate the behavior in the presence of n-th order nonlinearity [12]:

$$\begin{aligned} x_{RF}^n(t) &= \frac{1}{2^n}\left[x(t)e^{j\omega_0 t} + x^*(t)e^{-j\omega_0 t}\right]^n \\ &= \frac{1}{2^n}\sum_{k=0}^{n}\binom{n}{k}x(t)^k x^*(t)^{(n-k)}e^{j\omega_0(2k-n)t}. \end{aligned} \tag{3.4}$$

We are interested by $y_{RF1}(t)$ that is the component at frequency $\pm f_0$. So we look for component for which:

$$(2k-n) = \pm 1. \tag{3.5}$$

For n even, $(2k-n)$ never equals 1, therefore $\omega_0(2k-n)$ is always out of band. For n odd the frequencies can be in-band. Hence (for $-\omega_0$) we may write:

$$\begin{aligned} k &= \frac{n-1}{2}, \\ (n-k) &= \frac{n-1}{2}+1. \end{aligned} \tag{3.6}$$

Then using (3.7) we may define:

$$\begin{aligned} x(t)^k x^*(t)^{n-k} &= x(t)^{\frac{n-1}{2}} x^*(t)^{\frac{n-1}{2}+1} \\ &= |x(t)|^{n-1}x(t)^*. \end{aligned} \tag{3.7}$$

Similarly for frequency $+f_0$ for $(2k-n)=1$ we obtain:

$$x(t)^k x^*(t)^{n-k} = |x(t)|^{n-1}x(t). \tag{3.8}$$

Using these results the baseband output is defined as:

$$y(t) = \sum_{\substack{n=1 \\ n\ odd}}^{N} \frac{a_n}{2^{n-1}}\binom{n}{(n-1)/2}|x(t)|^{n-1}x(t), \tag{3.9}$$

setting

$$b_n = \frac{a_n}{2^{n-1}}\binom{n}{(n-1)/2}. \tag{3.10}$$

This explains why the baseband models are often defined with odd coefficients only. They can be defined as:

$$y(t) = \sum_{\substack{n=1 \\ n\ odd}}^{N} b_n x(t) \left|x(t)\right|^{n-1} = \sum_{k=0}^{\frac{N-1}{2}} b_{2k+1} x(t) \left|x(t)\right|^{2k}, \tag{3.11}$$

where x is the input baseband signal of the power amplifier, y is the output baseband signal of PA and b_n are the polynomial coefficients.

Another explanation why equivalent baseband models contain only odd terms can be done using Shimbo formula [13, 14]. For the rest of the thesis we will refer only to baseband models of PA (the PA is followed by bandpass filter).

In practice including even order terms in baseband models can improve performance.

Several models corresponding to modeling the AM/AM and AM/PM characteristic have been given, for example: Saleh, Rapp, quasi-static models. Their general expression is given by:

$$y(t) = A(|x(t)|)e^{j\phi(|x(t)|)}x(t). \tag{3.12}$$

We precise some of them in the following sections.

3.3.2 Saleh model

Saleh model [15, 14, 16] is commonly used amplifier model, which was designed primarily for traveling wave tube (TWT) amplifiers. This model is defined by gain distortion G and phase distortion ϕ as:

$$G(|x|) = \frac{a_A|x|}{1 + b_A|x|^2}, \phi(|x|) = \frac{a_\phi|x|^2}{1 + b_\phi|x|^2}, \tag{3.13}$$

where a_A, b_A, a_ϕ and b_ϕ are coefficients of the PA which are calculated by fitting to measured data.

Often-used values for the coefficients are $a_A = 2.1587$, $b_A = 1.1517$, $a_\phi = 4.033$ and $b_\phi = 9.104$ presented in [14]. The AM/AM characteristics for different values are presented in Fig.3.2 and the AM/PM characteristics in Fig.3.3.

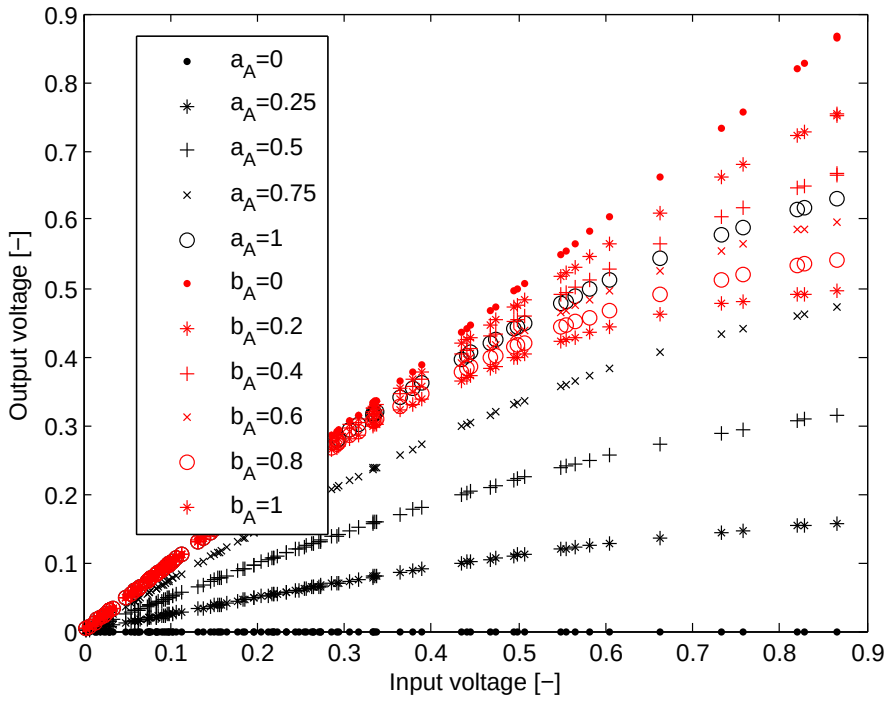

Fig. 3.2: Saleh amplitude distortion. When plotting a_A the b_A is set to 1 and vice versa.

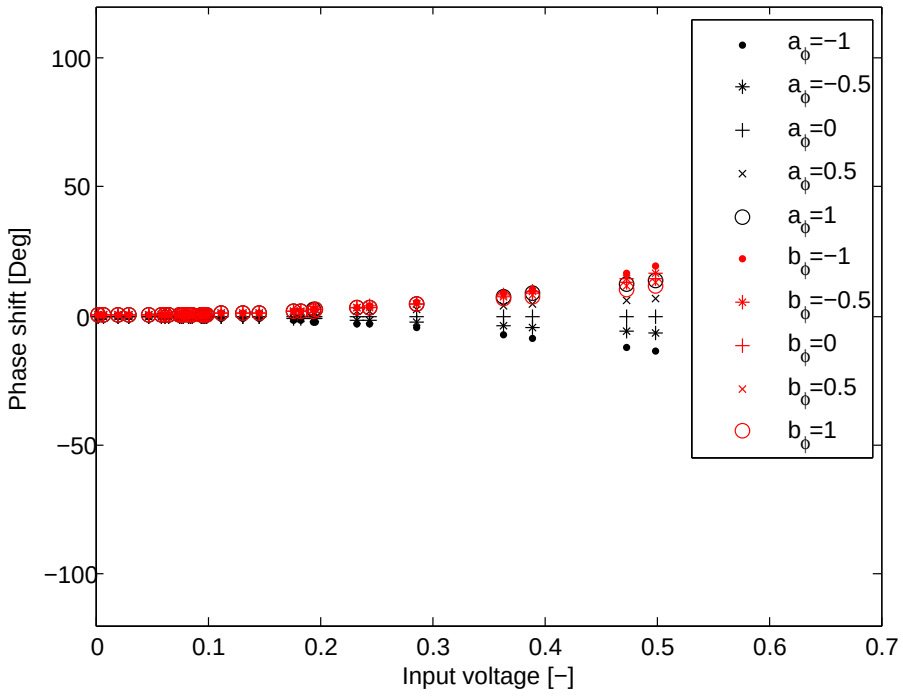

Fig. 3.3: Phase shifts for Saleh model. When plotting a_ϕ the b_ϕ is set to 1 and vice versa.

As it was mentioned before, such models were designed for TWT amplifiers, therefore they do not describe well solid state amplifiers.

Saleh model can be enhanced to a dynamical model by adding dependency of the coefficients on the frequency.

3.3.3 Rapp model

Rapp model was developed for solid-state power amplifiers. It is a baseband memoryless model. It produces a smooth transition for the envelope characteristic as the input amplitude approaches saturation.

$$y(t) = \frac{x(t)}{\left[1 + \left(\frac{|x(t)|}{V_{sat}}\right)^{2P}\right]^{\frac{1}{2P}}}, \tag{3.14}$$

where V_{sat} is the saturation voltage of the power amplifier and P is the smoothness factor.

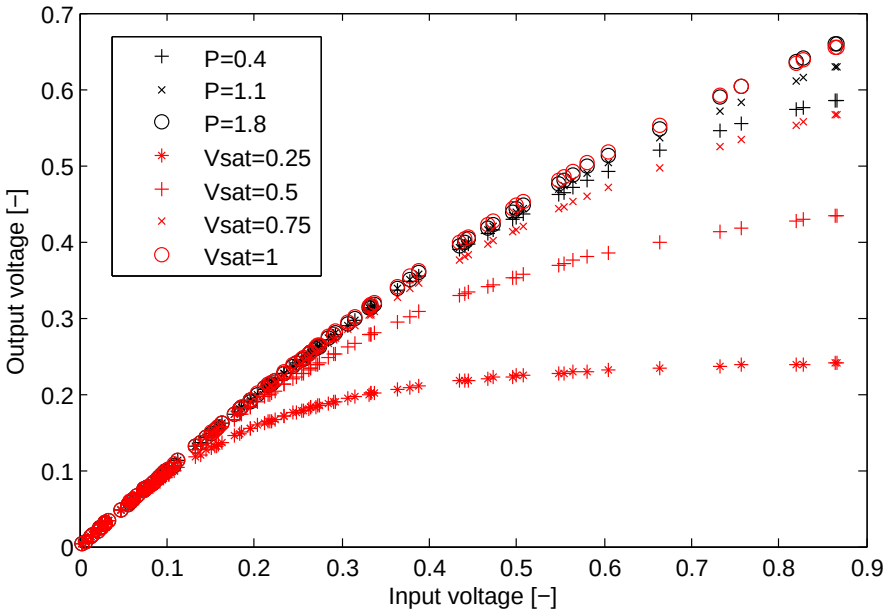

Fig. 3.4: Rapp models for different P and V_{sat}. When plotting P the V_{sat} is set to 1 and vice versa.

The AM/AM characteristics for different values of P and V_{sat} can be seen in the Fig.3.4. As we see the equation(3.4) describes only amplitude distortions. The Rapp model does not provide any phase modeling.

3.3.4 Modified Rapp model

Honkanen and Haggman [17] altered the low-level portion of the AM/AM characteristic in order to better mirror the exponential relationships of bipolar junction devices. Their model also represents AM/PM distortions. It matches better actual class AB mobile phone amplifiers.

$$A(|x(t)|) = \frac{K_1|x(t)|}{\left[1 + \left(\frac{K_1|x(t)|}{V_{sat}}\right)^{2P}\right]^{\frac{1}{2P}}}, \tag{3.15}$$

where V_{sat} is the saturating amplitude, K_1 is the small signal gain, $|x(t)|$ is the complex envelope of the input signal and P is a parameter which controls the smoothness of the transition from the linear region to the saturation region. In [18] they propose values: $K_1 = 17$ and $A_0 = 160.5$ and $P = 3.8$.

For the phase-shift distortion $\phi(|x(t)|)$, the behavior is quite closely modeled with the mathematical expression:

$$\phi(|x(t)|) = \frac{\epsilon\,|x(t)|^{q_1}}{1 + \left(\frac{|x(t)|}{\gamma}\right)^{q_2}}, \tag{3.16}$$

where as defined in [18] can be $\epsilon = 0.0747$, $\gamma = 0.1281$, $q_1 = -0.03462$ and $q_2 = -1.758$.

3.3.5 Ghorbani-model

The Ghorbani model [19] is a baseband PA model designed for solid-state PAs. The gain and phase functions for this model are:

$$G_{PA}(|x|) = \frac{a_A|x|^{c_A}}{1 + b_A|x|^{c_A}} + d_A|x|, \phi_{PA}(|x|) = \frac{a_\phi|x|^{c_\phi}}{1 + b_\phi|x|^{c_\phi}} + d_\phi|x|, \tag{3.17}$$

a_A, b_A, c_A, d_A, a_ϕ, b_ϕ, c_ϕ and d_ϕ are the nonlinearity parameters. The Ghorbani model is simple and suitable for modeling FET amplifiers.

3.3.6 White model

The White model was presented in [20]. This baseband model was proposed for modeling the Ka-band (26-40 GHz) solid-state PAs (SSPAs). It uses 4 parameters for amplitude a saturation level, b linear region gain and c, d a nonlinear region matching and uses 3 parameters for phase f magnification g steepness of the curve

and h shift along x-axis. The model is defined:

$$G_{PA}(|x|) = a(1 - e^{-b\ |x|}) + c\ |x|\ e^{-d\ |x|^2},$$
$$\phi_{PA}(|x|) = \begin{cases} f(1 - e^{-g(|x|-h)}) & \text{if } |x| \geq \text{h} \\ 0 & \text{if } |x| < \text{h} \end{cases} \tag{3.18}$$

3.4 Two-Stage and Multi-Stage Models

Two stage and more generally multi-stage models decompose the input-output relationship into two or more interconnected elements.

3.4.1 Wiener, Hammerstein Models

Wiener, Hammerstein structures are employed as simplifying approximations to reduce the complexity of memory models. All of this models are based on separation of static and dynamic non-linearity from the model and dividing the system into several stages made by linear filters and static nonlinearity models. For the static non-linearity the polynomial series can be used. The representation of Wiener and Hammerstein layout can be seen in Fig.3.5.

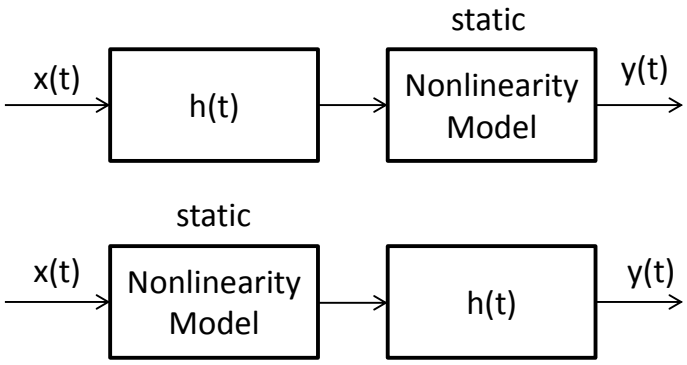

Fig. 3.5: Wiener(Top) and Hammerstein (Bottom) models.

Using memoryless polynomial series for the non-linearity model, the Hammerstein model can be defined as:

$$y(n) = \sum_{m=0}^{M} h(m) \sum_{k=1}^{K} b_k x(n-m)\,|x(n-m)|^{k-1}\,. \tag{3.19}$$

Analogue of Hammerstein model, we can define the Wiener model as:

$$x_2(n) = \sum_{m=0}^{M} h(m)\ x(n-m), \tag{3.20}$$

$$y(n) = \sum_{k=1}^{K} b_k x_2(n) \left| x_2(n) \right|^{k-1} . \tag{3.21}$$

Improvement of such systems can be obtained by connection of both structures into Wiener-Hammerstein or Hammerstein-Wiener models drawn in Fig.3.6. Hammerstein-Wiener model applications span several areas. These models are popular because they have a convenient block representation, transparent relationship to linear systems, and are easier to implement than complex nonlinear models (such as neural networks and Volterra models).

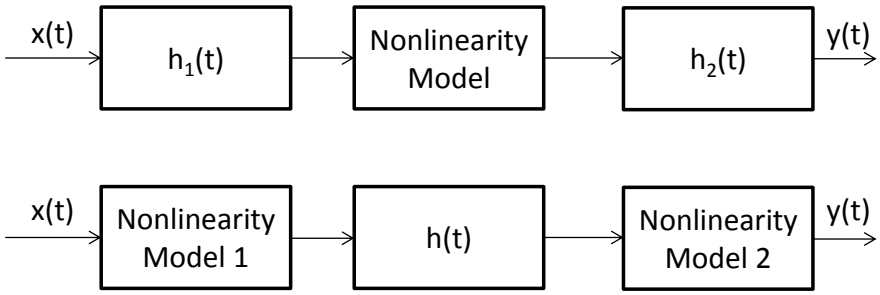

Fig. 3.6: Wiener-Hammerstein(Top) and Hammerstein-Wiener (Bottom) models.

The presented models have good performance in terms of error, but the identification of coefficients is difficult. Basically the estimation of the system parameters is an iterative process. For example for the Wiener model, the estimation of the linear system uses the estimation of the static nonlinearities of the previous iteration, while the estimation of the parameters of the static nonlinearities depends on the parameters of the linear system identified in the same iteration.

3.4.2 Multi-stage Models

One possible solution in order to increase capabilities of nonlinear models is to use multi-stage models. The idea is very simple. One can use for each stage different elementary models with different properties. These models can be connected in parallel [21, 22], shown in Fig.3.7 for parallel Hammerstein structure and Fig.3.8 for parallel Wiener structure, or in cascade.

One possible cascaded solution for PA modeling is presented in Fig.3.9.

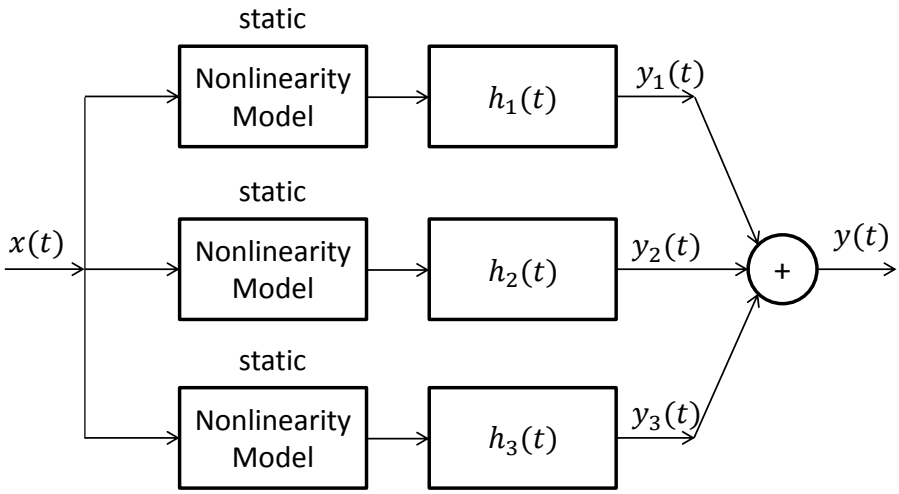

Fig. 3.7: Parallel Hammerstein structure of nonlinear models.

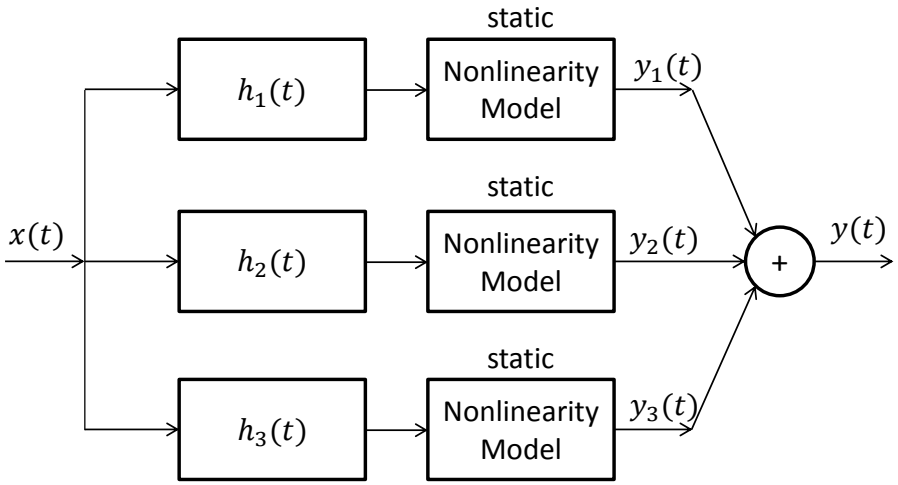

Fig. 3.8: Parallel Wiener structure of nonlinear models.

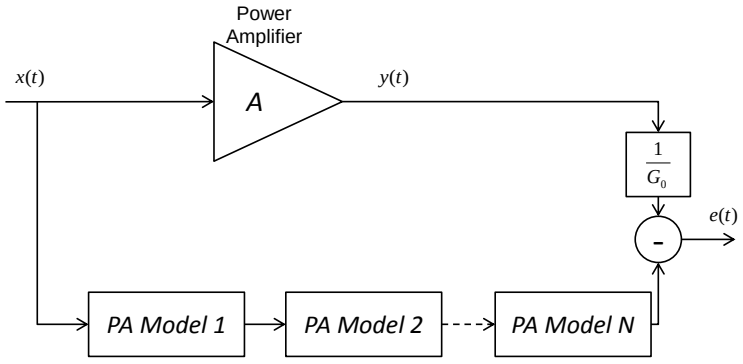

Fig. 3.9: Principle of PA modeling using N stage cascaded models.

This idea was presented for example in [23, 24, 25]. Despite the simplicity of idea, one will have issues related with parameters identification of solution.

3.5 Dynamical Models Derived From Volterra Series

3.5.1 Volterra Series

The Volterra series is a model for non-linear behavior similar to the Taylor series. It differs from the Taylor series in its ability to capture memory effects. The Volterra series can be used to approximate the response of a non-linear system to a given input. The RF model can be defined as:

$$\begin{aligned} y_{RF}(t) &= k_0 + \sum_{n=1}^{\infty} \int_{-\infty}^{\infty} \cdots \int_{-\infty}^{\infty} h_n(t_1, t_2, \ddots, t_n) x_{RF}(t - t_2) \cdots x_{RF}(t - t_n) dt_1 d_{t2} \cdots dt_n \\ &= \sum_k \int \cdots \int h_k(\Psi_k) \prod_{i=1}^{k} x_{RF}(t - \tau_i) d\Psi_k, \end{aligned} \tag{3.22}$$

where h_n is called the Volterra series kernel and can be regarded as a higher-order impulse response of the system, $x_{RF}(t)$ is a real passband input and $y_{RF}(t)$ is a real passband output respectively, $\Psi_k = [\tau_1, ..., \tau_k]^T$.

Transiting to baseband signal [26], let us denote by $x(t)$ the complex input of a nonlinear system and by $y(t)$ the corresponding filtered complex output. The definition can be found in [12]:

$$\begin{aligned} y(t) &= \sum_k \int \cdots \int h_{2k+1}(\Psi_{2k+1}) \\ &\quad \times \prod_{i=1}^{k+1} x(t - \tau_i) \prod_{i=k+2}^{2k+1} x^*(t - \tau_i) d\Psi_{2k+1}, \end{aligned} \tag{3.23}$$

where the baseband Volterra kernel can be expressed as:

$$\begin{aligned} h_{2k+1}(\Psi_{2k+1}) &= \frac{1}{2^{2k}} \binom{2k+1}{k} \times \tilde{h}_{2k+1}(\Psi_{2k+1}) \\ &\quad \times e^{-j2\pi f_0 \left(\sum_{i=1}^{k+1} \tau_i - \sum_{i=k+2}^{2k+1} \tau_i \right)}, \end{aligned} \tag{3.24}$$

where $\tilde{h}$ is a passband Volterra kernel.

These models are not directly suitable to be used in practical modeling and predistortion because of their complexity (very large number of kernels) and difficulties related with identifying the kernels.

The most general form of nonlinearity is described by the Volterra series [27], which consists of a sum of multidimensional convolutions. Therefore simplified forms have been presented and usually were derived by simplifying (pruning) the Volterra series. The simplest model with memory derived from Volterra series is obtained by keeping only the diagonal terms of the series and is called polynomial series with memory. In the following we will present only baseband versions of the models.

3.5.2 Polynomial series with memory

Polynomial memory series (PMS) were first presented in [28] and are widely used for modeling the non-linearities [29, 12, 30]. They can be interpreted as a special case of a generalized Hammerstein model. The presented series can model the memory effects. In this model, all off-diagonal terms of the Volterra series are set to zero. The series is defined as:

$$\begin{aligned} y(t) &= \sum_{k=1}^{K}\sum_{q=0}^{Q} b_{kq}\; x(t-q)|x(t-q)|^{k-1} \\ &= \sum_{k=1}^{K}\sum_{q=0}^{Q} b_{k,q}\Phi_{k,q}(x(t)) = \mathbf{\Phi}(t)\mathbf{b}, \end{aligned} \tag{3.25}$$

where

$$\Phi_{k,q}(x(t)) = |x(t-q)|^{k-1}x(t-q), \tag{3.26}$$

$$\mathbf{b} = [b_{1,0}, b_{2,0}, ..., b_{1,1}, ..., b_{1,Q}, ..., b_{K,Q}]^T \tag{3.27}$$

$$\mathbf{\Phi}(t) = [\Phi_{1,0}(x(t)), ..., \Phi_{K,Q}(x(t))]. \tag{3.28}$$

Their structure is determined by 2 parameters: K the non-linearity order and Q the memory length. The number of coefficients is $K(Q+1)$.

These models have good performance for applications with narrow or medium bandwidths. But they are often insufficient when large bandwidth applications are needed because of their limitation in modeling memory effects. For large bandwidth applications more complicated models are necessary.

3.5.3 Selective Polynomial series with memory

In order to include long-term memory effects, long memory depth has to be used. That can lead to numerical problems for the identification of model coefficients and to real time implementation problems. The main question is if it is really necessary to use all memory terms. Omitting the redundant terms we may define the series as:

$$y(t) = \sum_{k=1}^{K} \sum_{q=R(1)}^{\sup\{R\}} b_{kq}\ x(t-q)|x(t-q)|^{k-1}, \tag{3.29}$$

where sup{.} is supremum (called Least Upper Bound) that is the smallest integer number that is equal to largest number in set R and R is set of integers for example $R = \{0, 5, 50, ...\}$. Equivalently the same approach can be used with order of nonlinearity K. One of the questions to be solved is the determination of the sets R.

3.5.4 Orthogonal polynomial series with memory

When dealing with identification of the coefficients of the polynomials, one can encounter several problems related with matrix inversion (see section on model identification). In fact the matrix can be almost singular, and the computation of its inverse is prone to large numerical errors. For the matrix inversion, the numerical condition of is of special interest. In order to improve numerical conditions, orthogonal polynomials can be used.

Each of the well-known polynomials, such as Hermite, Chebyshev, Laguerre, and Legendre, are orthogonal with respect to a certain probability density function [31]. These classical polynomials are not easy to apply to the baseband model for two reasons. First, their orthogonality is usually defined with respect to a real-valued variable. And secondly, the probability density function which they are based on, does not necessarily comply with probability density function of communication signals.

Raich et al. [32] proposed families of orthogonal memory polynomial models suited to different probability distributions of signal suitable, in particular for uniform or Gaussian cases.

If $|x(t)|$ is uniformly distributed in the range from 0 to 1 then the memoryless model, called orthogonal polynomial series (OPS), can be for example expressed as:

$$\begin{aligned} z(t) &= \sum_{k=1}^{K} b_k \sum_{l=1}^{k} (-1)^{l+k} \cdot \\ &\cdot \quad \frac{(k+l)!}{(l-1)!(l+1)!(k-l)!} |x(t)|^{k-l} x(t), \\ &= \mathbf{\Phi}(t)\mathbf{b} \end{aligned} \tag{3.30}$$

where K is polynomial order and where:

$$\Phi_{k,q}(x(t)) = \frac{(k+l)!}{(l-1)!(l+1)!(k-l)!} |x(t)|^{k-1} x(t), \tag{3.31}$$

$$\mathbf{\Phi}(t) = [\Phi_{1,0}(x(t)), ..., \Phi_{K,Q}(x(t))]. \tag{3.32}$$

The precision of the identification of model coefficients will depend on the condition number of the matrix $\mathbf{U}$:

$$\mathbf{U} = \begin{pmatrix} \mathbf{\Phi}(0) \\ \mathbf{\Phi}(t) \\ \vdots \\ \mathbf{\Phi}(N-1) \end{pmatrix}. \tag{3.33}$$

Then the condition number of rectangular matrix is defined as:

$$cond(\mathbf{U}) = \|\mathbf{U}\|_2 \, \|\mathbf{U}^{-1}\|_2, \tag{3.34}$$

where $||.||_2$ represents spectral norm (2-norm), which is the square root of the maximum eigenvalue of $\mathbf{U}\mathbf{U}^H$, defined as:

$$\|\mathbf{U}\|_2 = \sqrt{\text{maximum eigenvalue of } \mathbf{U}\mathbf{U}^H}. \tag{3.35}$$

Condition number tells how accurate we can expect the vector $\mathbf{b}$ when solving a linear system.

Investigation of the condition number depending on the nonlinear order K for OFDM signal with 64-QAM modulated symbols (Gaussian probability distribution) can be seen in the Fig.3.10. Extending the OPS to memory problem we can get the orthogonal memory polynomials (OMPS) defined as:

$$\begin{aligned} z(t) &= \sum_{k=1}^{K} \sum_{q=0}^{Q} b_{k,q} \sum_{l=1}^{k} (-1)^{l+k} \cdot \\ &\cdot \quad \frac{(k+l)!}{(l-1)!(l+1)!(k-l)!} |x(t-q)|^{k-l} x(t-q) \end{aligned} \tag{3.36}$$

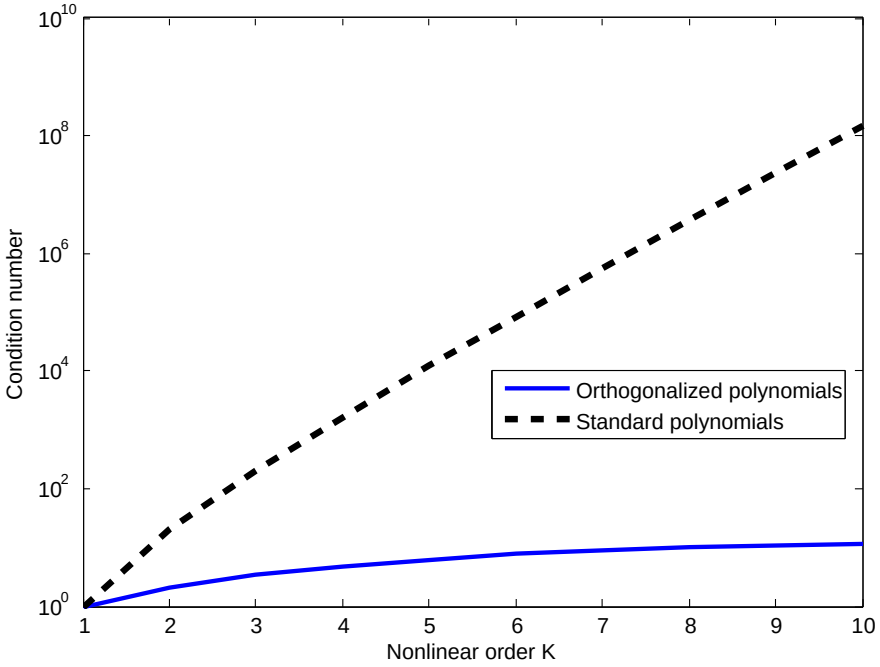

Fig. 3.10: Dependency of the condition number on the nonlinear order K for Q=0. The input signal is made of 15000 samples.

where Q is the depth of memory. The number of coefficients is $K(Q+1)$.The extension is not anymore perfectly orthogonal, because the matrix is made by linearly dependent lines, but as we can see in Fig.3.11, the matrix seems to be still well conditioned.

The PMS and OPMS are not sufficient for modeling the long term memory effects, that is why some more complex models like dynamic deviation reduction series or generalized memory polynomial series were proposed.

3.5.5 Dynamic Deviation Reduction Models

To overcome the complexity of the general Volterra series, an effective model pruning method, called dynamic deviation reduction (DDR) [33, 34, 35] was proposed. It is based on the fact that the effects of dynamics tend to fade with increasing nonlinearity order in many real PAs, so that the high-order dynamics can be removed in the model, leading to a significant simplification in model complexity.

Note that this dynamic-order truncation does not affect the nonlinearity or memory truncation in the same way as in the classical series. In other words, it only removes higher order dynamics, preserving the static nonlinearities and low-order

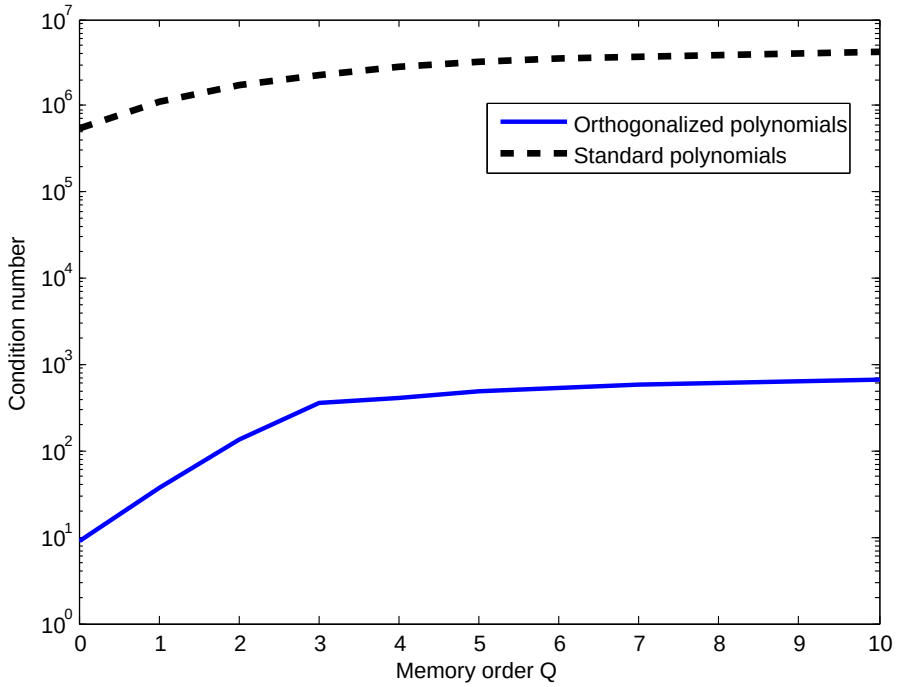

Fig. 3.11: Dependency of the condition number on the memory depth Q for K=7. The input signal is made of 15000 samples.

dynamics[33].

The 1st-order dynamic truncation of the DDR-based baseband Volterra model in the discrete time can be written as:

$$\begin{aligned} y(t) = & \sum_{k=0}^{\frac{K-1}{2}} \sum_{i=1}^{Q} g_{2k+1,1}(i)\ |x(t)|^{2k} x(t-i) \\ & + \sum_{k=1}^{\frac{K-1}{2}} \sum_{i=1}^{Q} g_{2k+1,2}(i)\ |x(t)|^{2(k-1)} x^2(t) x^*(t-i). \end{aligned} \tag{3.37}$$

where $x(n)$ and $y(n)$ are the complex envelopes of the input and output of the PA, respectively, and $g_{2k+1,j}$ is the complex Volterra kernel of the system.

The 2nd-order DDR model can be written as:

$$\begin{aligned} y(t) = & \sum_{k=0}^{\frac{K-1}{2}} \sum_{i=1}^{Q} g_{2k+1,1}(i)\ |x(t)|^{2k} x(t-i) \\ + & \sum_{k=1}^{\frac{K-1}{2}} \sum_{i=1}^{Q} g_{2k+1,2}(i)\ |x(t)|^{2(k-1)} x^2(t) x^*(t-i) \\ + & \sum_{k=1}^{\frac{K-1}{2}} \sum_{i_1=1}^{Q} \sum_{i_2=1}^{Q} g_{2k+1,3}(i_1,i_2) |x(t)|^{2(k-1)}\ x^*(t) x(t-i_1) x(t-i_2) \\ + & \sum_{k=1}^{\frac{K-1}{2}} \sum_{i_1=1}^{Q} \sum_{i_2=1}^{Q} g_{2k+1,4}(i_1,i_2) |x(t)|^{2(k-1)}\ x(t) x^*(t-i_1) x(t-i_2) \\ + & \sum_{k=1}^{\frac{K-1}{2}} \sum_{i_1=1}^{Q} \sum_{i_2=1}^{Q} g_{2k+1,5}(i_1,i_2) |x(t)|^{2(k-2)}\ x^3(t) x^*(t-i_1) x^*(t-i_2). \end{aligned} \tag{3.38}$$

A simplified version of the model is defined by:

$$\begin{aligned} y(t) = & \sum_{k=0}^{\frac{K-1}{2}} \sum_{i=0}^{Q} g_{2k+1,1}(i)\ |x(t)|^{2k} x(t-i) \\ + & \sum_{k=1}^{\frac{K-1}{2}} \sum_{i=1}^{Q} g_{2k+1,2}(i)\ |x(t)|^{2(k-1)} x^2(t) x^*(t-i) \\ + & \sum_{k=1}^{\frac{K-1}{2}} \sum_{i=1}^{Q} g_{2k+1,3}(i) |x(t)|^{2(k-1)}\ x(t) |x(t-i)|^2 \\ + & \sum_{k=1}^{\frac{K-1}{2}} \sum_{i=1}^{Q} g_{2k+1,4}(i) |x(t)|^{2(k-1)}\ x^*(t) x^2(t-i). \end{aligned} \tag{3.39}$$

3.5.6 Generalized Memory Polynomials

Another model including cross terms is the generalized memory polynomials (GMP)[36]. Inserting a delay of samples between the signal and its exponentiated envelope using positive and negative cross-term time shifts we get:

$$\begin{aligned} y(n) = & \sum_{k=0}^{K_a-1} \sum_{l=0}^{L_a-1} a_{k,l} x(n-l) |x(n-l)|^k \\ + & \sum_{k=1}^{K_b} \sum_{l=0}^{L_b-1} \sum_{m=1}^{M_b} b_{k,l,m} x(n-l) |x(n-l-m)|^k \\ + & \sum_{k=1}^{K_c} \sum_{l=0}^{L_c-1} \sum_{m=1}^{M_c} c_{k,l,m} x(n-l) |x(n-l+m)|^k, \end{aligned} \tag{3.40}$$

where the structure of GMP models is determined by 8 parameters: K_a, K_b , K_c non-linearity orders, L_a, L_b, L_c memory lengths and M_b, M_c distances from the

diagonal of Volterra series, and $a_{k,l}$, $b_{k,l,m}$ and $c_{k,l,m}$ are the linear coefficients of the equation.

In order to reduce the complexity, it is not necessary in many cases to use all of the coefficients. For example, odd-order nonlinearities usually dominate so that we may only want to consider odd-order terms. Also additionally, depending on the signal bandwidth and sampling rate, it may not be necessary to implement all cross-term time shifts.

3.5.7 Remark On Models With A Linear Dependency With Respect To The Coefficients

For all these models (PMS, OMPS, DDR and GMP) can be noticed that they have a linear dependency with respect to their coefficients, hence the optimal solution of LS (Least Square) criterion is obtained by solving set of linear equations (as will be discussed in Section 3.6). It is possible to write these models as:

$$y(t) = \mathbf{\Phi}(t)\mathbf{b}, \tag{3.41}$$

where $\mathbf{b}$ is the coefficient vector of size $N_c \times 1$ (N_c represents the number of coefficients) and $\mathbf{\Phi}(n)$ is a line vector $1 \times N_c$ build from samples of $x(t)$. The content of $\mathbf{\Phi}(n)$ also depends on the model. For example for the case of PMS:

$$\mathbf{\Phi}(t) = [\Phi_{1,0}(x(t)), ..., \Phi_{K,Q}(x(t))] \tag{3.42}$$

with:

$$\Phi_{k,q}(x(t)) = |x(t-q)|^{k-1}x(t-q) \tag{3.43}$$

$$\tag{3.44}$$

and in general $\Phi_{k,q}(x(t))$ is a line vector of dimension $1 \times N_c$ depending on $\mathbf{x}$. If we consider a set of N samples , we can define vectors:

$$\mathbf{y} = [y(0), \ldots, y(N-1)]^T \tag{3.45}$$

$$\mathbf{x} = [x(0), \ldots, x(N-1)]^T \tag{3.46}$$

and

$$\mathbf{y} = \mathbf{U}\mathbf{b}, \tag{3.47}$$

with:

$$\mathbf{U} = \begin{pmatrix} \mathbf{\Phi}(0) \\ \mathbf{\Phi}(t) \\ \vdots \\ \mathbf{\Phi}(N-1) \end{pmatrix}. \tag{3.48}$$

3.5.8 Neural Network models

Artificial Neural Networks (ANN) represents imitation of biological central nervous systems. The idea is to connect nodes (neurons) between each other with weighted connections. Neural networks are also similar to biological neural networks in performing functions collectively and in parallel by the units.

There exists several types of Artificial Neural Networks. ANN may differ in the topology of the network connections between neurons, in the nonlinear activation functions of neurons (input-output relation between each neuron: sigmoid function, etc.) and in learning techniques used for the network estimation (back-propagation gradient technique, simulated annealing optimization, etc.).

The idea of using neural networks for power amplifier modelization or linearization was presented for example in [37, 38, 39, 40, 41].

With a single layer network we can solve a problem as long as it is linearly separable. Therefore for predistortion multilayer neural networks has to be used. Multi-layer perceptrons are basically more attractive for their generality. In the mathematical theory of neural networks, George Cybenko [42] proposed the universal approximation theorem. It states that a feed-forward network with a single hidden layer, the simplest form of multilayer perceptron, containing a finite number of hidden neurons, is a universal approximator among continuous functions (he proved the theorem with sigmoid activation functions). Another benefit is the existence of effective learning algorithms.

In order to demonstrate the idea of neural network , the simplest networks with a single layer (left) and hidden layers (right) can be seen in Fig.3.12.

The output y_k can be expressed as:

$$y_k(\mathbf{x}) = \sum_{i=0}^{d} w_{ki} x_i + b_{ki}, \tag{3.49}$$

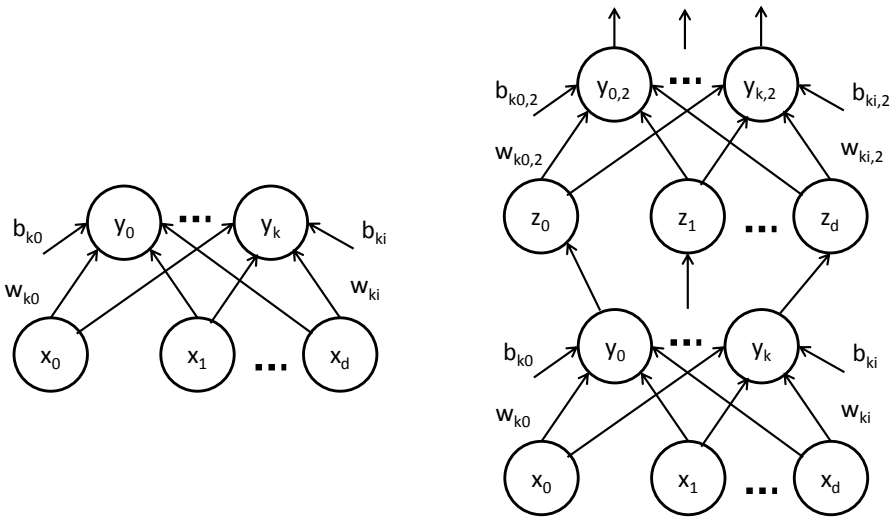

Fig. 3.12: Description of neural networks. Left is single layer ANN and right is double layer ANN (ANN with hidden layer).

where w represents the weight.

Similar to biological neurons which are activated when a certain threshold is reached, we use a sigmoid transfer function to provide a nonlinear activation of neural network:

$$f_s(x) = \frac{1}{1 + e^{-\kappa(x-\Theta)}}, \tag{3.50}$$

where κ represents slope and Θ is the threshold of sigmoid. Then the single layer ANN can be written as:

$$y_k(\mathbf{x}) = f_s\left(\sum_{i=0}^{d} w_{ki}x_i + b_{ki}\right). \tag{3.51}$$

Despite their simplicity, neural network are not implicitly designed to work with complex signals, so for the baseband modeling of PA different approaches have been proposed to deal with complex signals [43]. For example the real and imaginary parts can be separated.

The usage of real signals simplifies the calculation. Among the networks with real values, it was proposed to use two independent networks to model the AM-AM and AM-PM curves [43]. But the results are not sufficient. More effective is to use a single network with inputs (and outputs) I and Q.

To improve the consideration of memory effects and extend the models to a class of dynamic models [44], dynamic neural networks have been proposed [45]: real-

valued time-delay neural network (RVTDNN).

There exists several neural networks suitable for modeling the PAs [46]. But all af the networks require estimation algorithm. Such algorithm is quite hard to implement adaptively.

3.5.9 Limitation of Peaks in The Models (Clipping)

One of the most important property of power amplifier models is capability to limit unwanted peaks that can be generated by the PA models and DPD. It is a very important property, because it generally imitates the physical behavior of saturation. Typically clipping is added to an output af PA model (or DPD).

Basically when using the simplest clipping, the signal is limited to a certain amplitude and is distorted in keeping under that level. It is also called hard clipping. One have to know that clipping creates extra harmonics that are not present in the original signal. Also the clipping reduces signal power. Therefore it is considered as a nonlinear operation. The clipping can be defined as:

$$y_{clipped}(t) = \begin{cases} A(t)\ cos\left[\omega\ t\ + \Phi(t)\right] & \text{if } |x(t)| < V_{sat} \\ V_{sat} & \text{if } |x(t)| \geq V_{sat}, \end{cases} \tag{3.52}$$

where $A(t)$ represents input amplitude of clipper and V_{sat} represents saturation voltage of an amplifier.

In the Fig.3.13 we can see real signal clipped in time to value $V_{Sat} = 0.6$ with signal without applied clipping. In the Fig.3.14 we can see the AM/AM characteristics difference between clipped output signal and signal without clipping. Also in the Fig.3.14 we can see the spectral regrowth in adjacent channels for clipped signal.

3.6 Identification of Models

In this section we will focus on models with linear dependency with respect to their coefficients. The interest of these models is that we will obtain a convex minimization problem for the least-squares (LS) criteria for PA modeling and DPD with indirect learning architecture.

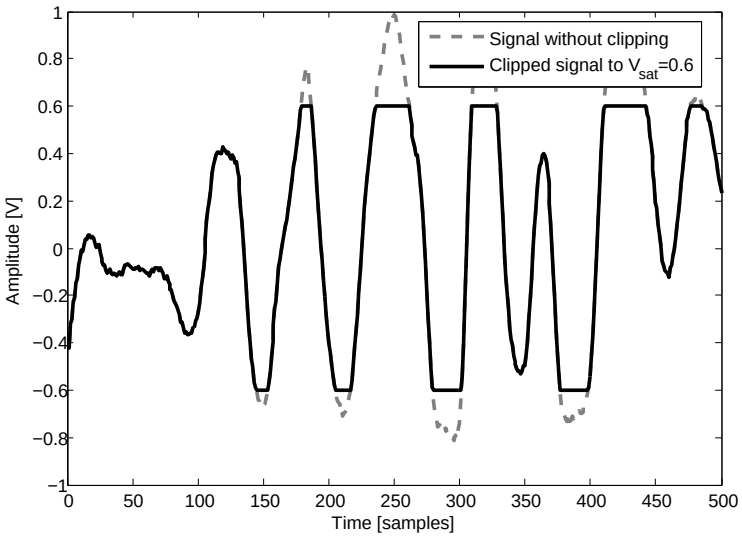

Fig. 3.13: Power amplifier AMAM characteristics measured and clipped to value $V_{sat} = 0.6$.

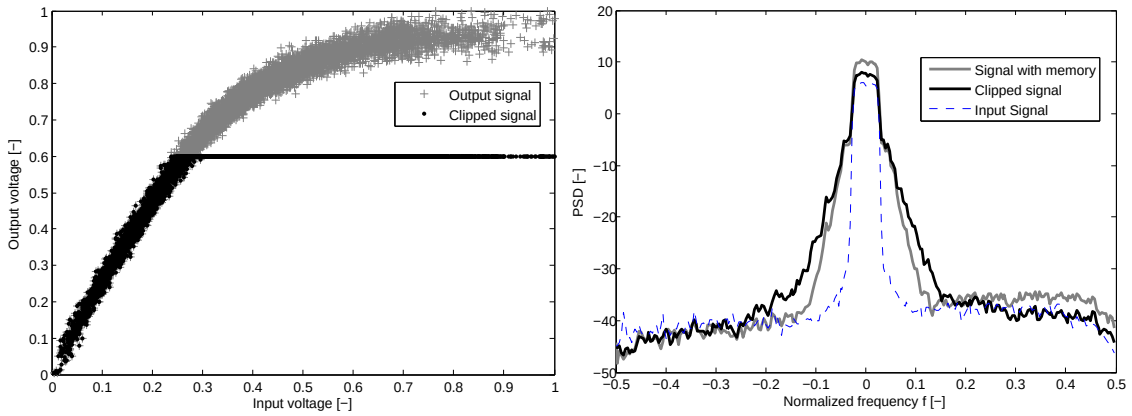

Fig. 3.14: Left: Power amplifier AMAM characteristics measured and clipped to value $V_{sat} = 0.6$. Right: Power amplifier power spectrum density measured and clipped to value $V_{sat} = 0.6$.

In order to identify the coefficients of PA model or DPD coefficients, we use LS optimization criterion:

$$\mathbf{e} = \min_{b} ||\mathbf{y} - \mathbf{z}||^2 . \tag{3.53}$$

We apply notations defined in Fig.3.15, where for PA modeling $y(t)$ is measured signal (for DPD $x(t)$ is measured signal) and $z(t)$ is the output of the model. We consider here only indirect learning approach for the DPD.

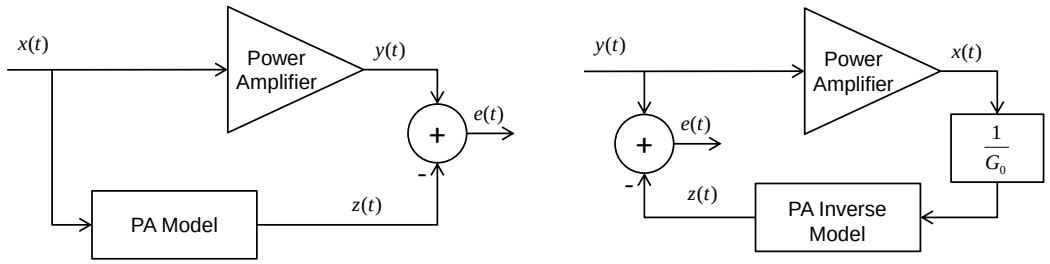

Fig. 3.15: Schematic of minimizing problem between measured and modeled signals. The left schematic represents calculation of PA model. The right schematic represents calculation of PA inverse model (note that the input $x(t)$ and output $y(t)$ notation is swapped in order to meet error defined in (3.53).

The $||.||^2$ represent the quadratic norm of vector and $\mathbf{z}$ is expressed as:

$$\mathbf{z} = \mathbf{U}\mathbf{b}, \tag{3.54}$$

and where a $\mathbf{z}$ is a in vector with dimensions $N \times 1$:

$$\mathbf{z} = [z(0), ..., z(N-1)]^T. \tag{3.55}$$

$$\mathbf{y} = [y(0), ..., y(N-1)]^T. \tag{3.56}$$

$$\mathbf{e} = [e(0), ..., e(N-1)]^T. \tag{3.57}$$

As seen in equation (3.48) $\mathbf{U}$ is a matrix of size $N \times N_c$ (where N_c represents number of coefficients and for example for PMS $N_c = K(Q+1)$):

$$\mathbf{U} = \begin{pmatrix} \mathbf{\Phi}(0) \\ \mathbf{\Phi}(t) \\ \vdots \\ \mathbf{\Phi}(N-1) \end{pmatrix}. \tag{3.58}$$

$\mathbf{b}$ a vector of size $N_c \times 1$

$$\mathbf{b} = [b_0, ..., b_{N_c-1}]^T. \tag{3.59}$$

The optimization problem can be written:

$$\min_{\mathbf{b}}(\mathbf{e}^H\mathbf{e}). \tag{3.60}$$

3.6.1 Least Squares one-shot solution

The LS solution minimizing distance between each data point and the space of best fit passing through the data points for (3.54). The criteria $\mathbf{J}$ can be expressed as:

$$\begin{aligned} \mathbf{J(b)} &= ||\mathbf{z}-\mathbf{y}||^2 = \mathbf{e}^H\mathbf{e} = (\mathbf{y}-\mathbf{Ub})^H(\mathbf{y}-\mathbf{Ub}) \\ &= \mathbf{b}^H\mathbf{U}^H\mathbf{Ub} - \mathbf{y}^H\mathbf{Ub} - \mathbf{b}^H\mathbf{U}^H\mathbf{y} + \mathbf{y}^H\mathbf{y} \end{aligned} \tag{3.61}$$

The solution of (3.62) can be obtained by calculating the gradient and setting it to 0. The gradient is equal to:

$$\frac{\partial \mathbf{J}((\mathbf{b}))}{\partial \mathbf{b}} = 2\ \mathbf{U}^H\mathbf{Ub} - 2\ \mathbf{U}^H\mathbf{y}, \tag{3.62}$$

The least square solution yields to:

$$\mathbf{U}^H\mathbf{Ub} - \mathbf{U}^H\mathbf{y} = 0. \tag{3.63}$$

$$\mathbf{b} = (\mathbf{U}^H\mathbf{U})^{-1}\mathbf{U}^H\mathbf{y} = \mathbf{U}^+\mathbf{y}, \tag{3.64}$$

where $\mathbf{U}^+$ denotes Moore - Penrose pseudo-inverse. The LS algorithm is in fact one-shot solution for block of data.

LS one-shot solution is quite good in terms of performance. Nevertheless an interest in adaptive algorithms grows (adaptive filtering, adaptive equalization, etc.). The problem with LS one-shot solution is, that it is not able to track PA variations. Therefore adaptive algorithms have been proposed for the case of DPD identification either.

3.6.2 Damped Newton Algorithm

In many applications, adaptive estimation is performed on a block by block basis. There exists method called Damped Newton Algorithm (DNA) that upgrades the LS solution by adding possibility to control the speed of convergence depending on the preceding error. The DNA works block by block and it adapts preceding vector of coefficients to take into account the new block of data with a damping factor. In this section we will describe DNA used for predistortion of PA. The approach for predistortion using DNA was defined in [36].

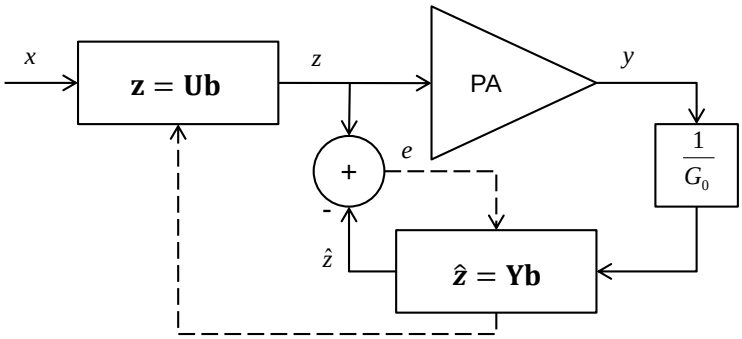

Fig. 3.16: Schematic of DNA system.

The initialization vector $\mathbf{b}_0$ is usually chosen to use predistorter as a transparent block as:

$$\mathbf{b}_0 = [1, 0, \cdots, 0]^T . \tag{3.65}$$

According to notation in Fig.3.16 we can describe the algorithm for $n \in 1, 2, 3, ...$, where n represents the block number, with the following equation for block n (each block has N samples):

$$\mathbf{z} = \mathbf{U}\ \mathbf{b}_{n-1}. \tag{3.66}$$

Equivalently as in (3.55-3.58) we define the output matrix $\mathbf{Y}$ from the signal $\frac{y}{G_0}$ as:

$$\hat{\mathbf{z}} = \mathbf{Y}\ \mathbf{b}_{n-1}. \tag{3.67}$$

Then we define the error vector $\mathbf{e}$

$$\mathbf{e} = \mathbf{z} - \hat{\mathbf{z}}. \tag{3.68}$$

The coefficients $\mathbf{b}$ can be updated as:

$$\mathbf{b}_n = \mathbf{b}_{n-1} + \mu \left(\mathbf{Y}^H \mathbf{Y}\right)^{-1} \mathbf{Y}^H\ \mathbf{e}, \tag{3.69}$$

where μ is a relaxation variable. When setting the relaxation variable $\mu = 1$ the damping is removed and the solution becomes the standard LS solution.

3.6.3 LMS algorithm

The Least Mean Square (LMS) algorithm is often used in adaptive systems due its simplicity and relative precision. The algorithm works sample by sample. The algorithm computes instantaneous error and then corrects the actual value of coefficients.

Using any of models defined before with linear relation with respect to their coefficients (for example PMS, OMPS, DDR) we note:

$$\mathbf{\Phi}(n) = n^{th}\ row\ of\ matrix\ \mathbf{U}. \tag{3.70}$$

Then the criterion function can be defined as:

$$\begin{aligned} \min\ J(n) &= min\,|e(n)|^2 \\ &= min\,|y(n) - \mathbf{\Phi}(n)\mathbf{b}(n)|^2\,. \end{aligned} \tag{3.71}$$

The estimated gradient vector becomes:

$$\nabla J(n) = \frac{\partial |e(n)|^2}{\partial \mathbf{b}(n)} \tag{3.72}$$

Because

$$e(n) = z(n) - \mathbf{\Phi}(n)\mathbf{b}(n), \tag{3.73}$$

applying equation (3.73) to equation (3.72) we get:

$$\nabla J(n) = -e(n)\mathbf{\Phi}^H(n). \tag{3.74}$$

Then using the steepest descent weight update equation we obtain iterative solution:

$$\mathbf{b}(n+1) = \mathbf{b}(n) + \mu e(n)\mathbf{\Phi}^H, \tag{3.75}$$

where parameter μ adjusts the compromise between convergence speed and the error value after convergence.

Due to sensitivity to value μ that can lead to instability, the algorithm was modified by using a normalization that improves stability of the algorithm. This algorithm is so-called Normalized Least Mean Square (NLMS) defined as:

$$\mathbf{b}(n+1) = \mathbf{b}(n) + \mu\ e(n)\ \frac{\mathbf{\Phi}^H}{\mathbf{\Phi}\ \mathbf{\Phi}^H} \tag{3.76}$$

Both LMS and NLMS suffers from low convergence speed and limited precision.

3.6.4 RLS algorithm

For solving the LS criterion optimization problem recursive least squares (RLS) algorithm can also be used. In its adaptive form it converges faster than LMS. Theoretically where the forgetting factor is equal to 1, it achieves the optimal solution

(Wiener solution) but it is more complex than LMS. Now defining the input of the system:

$$\mathbf{x}(n) = [x(n), x(n-1), \ldots, x(0)]^T, \tag{3.77}$$

and vector of desired output:

$$\mathbf{y}(n) = [y(n), y(n-1), \ldots, y(0)]^T. \tag{3.78}$$

Then we define line vector $\mathbf{\Phi}(n)$ as before of size $1 \times N_c$ and matrix $\mathbf{\Theta}$ of size $(n+1) \times N_c$ as:

$$\mathbf{\Theta}(n) = \begin{pmatrix} \mathbf{\Phi}(0) \\ \vdots \\ \mathbf{\Phi}(n) \end{pmatrix}. \tag{3.79}$$

Then the output of the system will be:

$$\mathbf{z}(n) = \mathbf{\Theta}(n)\mathbf{b}(n). \tag{3.80}$$

The instantaneous error at time n is:

$$e(n) = y(n) - \mathbf{\Phi}(n)\mathbf{b}(n). \tag{3.81}$$

Now defining the criterion function with a forgetting factor denoted as λ:

$$\begin{aligned} \min_{\mathbf{b}} J(n) &= \sum_{k=0}^{n} \lambda^{n-k} |e(k)|^2 \\ &= \sum_{k=0}^{n} \lambda^{n-k} |y(k) - \mathbf{\Phi}(k)\mathbf{b}(n)|^2 \\ &= \mathbf{e}^H \mathbf{\Lambda} \mathbf{e}(n) \end{aligned} \tag{3.82}$$

where:

$$\mathbf{\Lambda} = \operatorname{diag}\left[1, \lambda, \lambda^2, \ldots, \lambda^n\right] \tag{3.83}$$

To use recursive implementation we need to define the correlation matrix $\mathbf{R}(n)$ by a recurrence equation:

$$\begin{aligned} \mathbf{R}(n) &= \mathbf{\Theta}^H(n)\mathbf{\Lambda}\mathbf{\Theta}(n) \\ &= \sum_{k=0}^{n} \lambda^{n-k} \mathbf{\Phi}^H(k)\mathbf{\Phi}(k) \\ &= \sum_{k=0}^{n-1} \lambda^{n-k} \mathbf{\Phi}^H(k)\mathbf{\Phi}(k) + \mathbf{\Phi}^H(n)\mathbf{\Phi}(n) \\ &= \lambda \mathbf{R}(n-1) + \mathbf{\Phi}^H(n)\mathbf{\Phi}(n). \end{aligned} \tag{3.84}$$

We define the cross-correlation vector of size $N_c \times 1$:

$$\begin{aligned} \mathbf{p}(n) &= \mathbf{\Theta}^H(n)\mathbf{\Lambda}\mathbf{y}(n) \\ &= \sum_{k=0}^{n} \lambda^{n-k}\mathbf{\Phi}^H(k)y(k) \\ &= \sum_{k=0}^{n-1} \lambda^{n-k}\mathbf{\Phi}^H(k)y(k) + \mathbf{\Phi}^H(n)y(n) \\ &= \lambda\mathbf{p}(n-1) + \mathbf{\Phi}^H(n)y(n). \end{aligned} \tag{3.85}$$

Defining the recursive solution:

$$\mathbf{b}(n+1) = \mathbf{R}^{-1}(n)\mathbf{p}(n) = \mathbf{P}(n)\mathbf{p}(n), \tag{3.86}$$

where defining $\mathbf{P}(n) = \mathbf{R}^{-1}(n)$ and applying the inversion lemma to calculate $\mathbf{R}^{-1}(n)$ yields to:

$$\mathbf{P}(n) = \lambda^{-1}\mathbf{P}(n-1) - \frac{\lambda^{-2}\mathbf{P}(n-1)\mathbf{\Phi}^H(n)\mathbf{\Phi}(n)\mathbf{P}(n-1)}{1+\lambda^{-1}\mathbf{\Phi}(n)\mathbf{P}(n-1)\mathbf{\Phi}^H(n)}. \tag{3.87}$$

Now defining the gain $\mathbf{g}(n)$:

$$\mathbf{g}(n) = \frac{\lambda^{-1}\mathbf{P}(n-1)\mathbf{\Phi}^H(n)}{1+\lambda^{-1}\mathbf{\Phi}(n)\mathbf{P}(n-1)\mathbf{\Phi}^H(n)} \tag{3.88}$$

Then applying (3.88) to $\mathbf{P}(n)$ defined in (3.87) we get:

$$\mathbf{P}(n) = \lambda^{-1}\mathbf{P}(n-1) - \lambda^{-1}\mathbf{g}(n)\mathbf{\Phi}(n)\mathbf{P}(n-1). \tag{3.89}$$

To rewrite the recursive weight update algorithm:

$$\begin{aligned} \mathbf{g}(n) &= \frac{\lambda^{-1}\mathbf{P}(n-1)\mathbf{\Phi}^H(n)}{1+\lambda^{-1}\mathbf{\Phi}(n)\mathbf{P}(n-1)\mathbf{\Phi}^H(n)} \\ \mathbf{P}(n) &= \lambda^{-1}\mathbf{P}(n-1) - \lambda^{-1}\mathbf{g}(n)\mathbf{\Phi}(n)\mathbf{P}(n-1) \\ e(n) &= y(n) - \mathbf{\Phi}^T(n)\mathbf{b}(n) \\ \mathbf{b}(n+1) &= \mathbf{b}(n) + \mathbf{g}(n)e(n). \end{aligned} \tag{3.90}$$

We define initial conditions as $\mathbf{p}(0) = 0$, $\mathbf{R}(0) = \delta\mathbf{I}$, where $\mathbf{I}$ is identity matrix. The typical value of δ is usually set as a small positive value equal to $\delta = 10^{-3}$. Then we can define:

$$\mathbf{P}(0) = \mathbf{R}^{-1}(0) = \delta^{-1}\mathbf{I}. \tag{3.91}$$

To show the relationship between LS solution and RLS algorithm lets set $\lambda = 1$, we get:

$$\mathbf{R}(n) = \mathbf{\Theta}^H(n)\mathbf{I}\mathbf{\Theta}(n). \tag{3.92}$$

$$\mathbf{p}(n) \;=\; \mathbf{\Theta}^H(n)\mathbf{I}\mathbf{z}(n). \tag{3.93}$$

and using:

$$\begin{aligned} \mathbf{R}(n)\mathbf{b}(n) &= \mathbf{p}(n) \\ \mathbf{\Theta}^H(n)\mathbf{I}\mathbf{\Theta}(n)\mathbf{b}(n) &= \mathbf{\Theta}^H(n)\mathbf{I}\mathbf{z}(n). \end{aligned} \tag{3.94}$$

we get:

$$\mathbf{b}(n) = \left(\mathbf{\Theta}(n)\mathbf{\Theta}^H(n)\right)^{-1}\mathbf{\Theta}(n)\mathbf{z}(n). \tag{3.95}$$

We recognize (3.95) for $n = N$ the LS solution for the block of N samples.

Introducing a forgetting factor λ leads to an adaptive algorithm. RLS converges faster and is more precise than LMS. The RLS algorithm is more complex than LMS.

3.6.5 Comparison of RLS and LMS Complexity

Lets assume that the evaluation of the inner product $\mathbf{\Phi}^T(n)\mathbf{b}(n)$ requires N complex multiplications and $(N-1)$ complex addition for each iteration. The multiplying the scalar by the vector requires N complex multiplications. Using this procedure, we can compute the complexity of both LMS and RLS algorithms [2]. The comparison can be found in Table 3.1.

Tab. 3.1: Comparison of complexity for each iteration step n [2] for LMS and RLS.

Algorithm	Multiplications	Additions	Divisions
LMS	$2N+1$	$2N$	-
RLS	N^2+5N+1	N^2+3N	1

From the Table 3.1 it is observed that the RLS algorithm has higher complexity than LMS algorithm. We need to point out, that RLS has better performance than LMS.

RLS updates the inverse covariance matrix with each new sample and forms a Kalman-like coefficient update. Modified fast versions are available (Fast-RLS), but these, like LMS, suffer from poorly conditioned covariance matrices and tend to instability and divergence.

3.6.6 Identification of Parameters For Multi-stage Models

There exists variety of different approaches (presented in section 3.4.2) involving multistage modeling or DPD.

Unfortunately all parameters cannot be estimated simultaneously, because then it is a nonlinear process. Several non-linear optimization techniques can be used. One possible solution is to divide the tasks to several steps. The solution of identification of multi-stage model of PA in several steps can be seen in Fig.3.17.

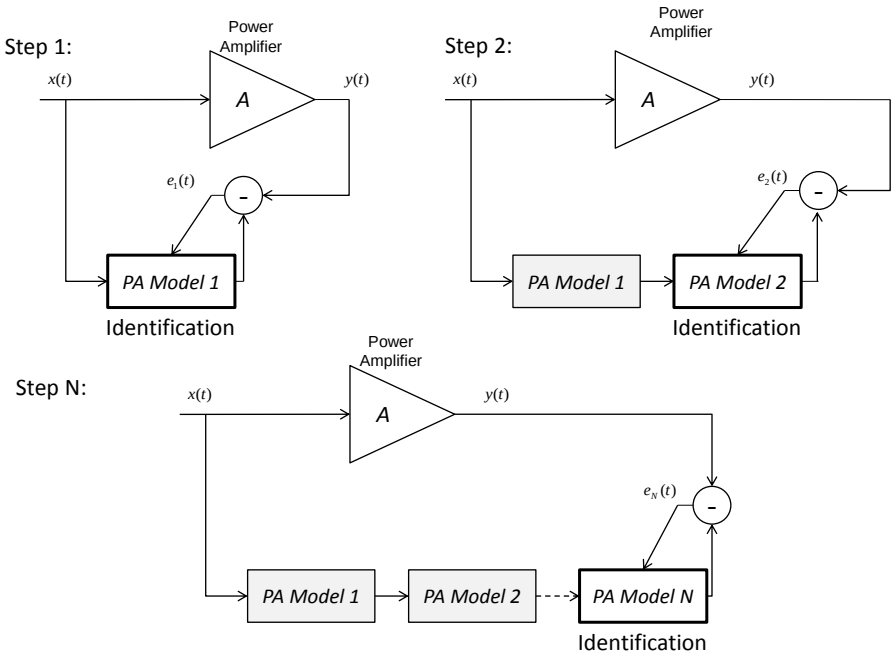

Fig. 3.17: Principle of steps for PA identification using N multi-stage models.

First we identify the model of PA. The next step is to add another block with PA model (denoted in Fig.3.17 as PA Model 2). As the input of this block we use output signal from previously estimated model (denoted as PA Model 1). We can repeat this steps until Nth model is estimated.

In the Fig.3.18 we would like to present multistage DPD indirect learning architecture. As mentioned before, we cannot identify all the coefficients simultaneously for the case of Fig.3.18, therefore all the blocks have to be identified in several stages.

In order to use indirect learning approach, first we estimate the coefficients of DPD1 (denoted in Fig.3.18). The next step is to consider DPD1 and PA as one block. Then we estimate the new DPD2 again using indirect learning approach

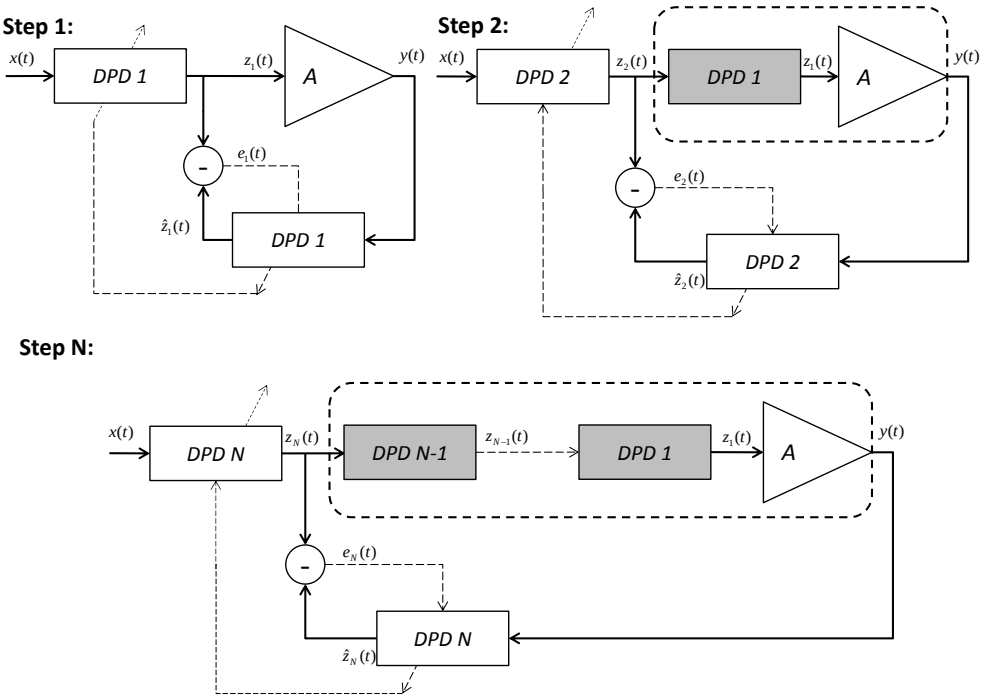

Fig. 3.18: Principle of adaptive indirect algorithm for DPD using N multi-stage models.

(where DPD1 has set coefficients that have been already estimated in step 1). We can repeat this procedure until the required number of blocks N is archived.

Using multistage models bring interesting properties, because we can combine several series in order to improve the performance.

3.6.7 Kalman Filtering

In order to estimate adaptively coefficients of DPDs and PA models, there have been proposed approaches based on Kalman filtering [47]. For example such propositions can be found in [48, 49].

Kalman filter is recursive adaptive filtering technique developed for real-time filtering of time series. The technique was originally developed for linear system, however there also exists Extended Kalman Filter (EKF) [50] designed for nonlinear systems. The drawback of EKF is the calculation of analytical derivations of nonlinear system, which can be complex [50]. Unscented Kalman filter (UKF) has also been proposed for DPD [51].

The Kalman filter uses a state model which describes the future evolution of system for a given input. In identification, the coefficients are updated recursively at each iteration. The coefficients are updated by the Kalman gain which is multiplying the estimation error between the actual output and the model output.

There exist several publications trying to reduce the complexity of Kalman filtering. For example in order to reduce the computational complexity of classical Kalman Filtering, a sliding time window Kalman filtering has been proposed in [52].

One of the disadvantages could be based on necessity to know the statistical properties of the signal in order to estimate covariance matrices.

For the rest of the thesis the Kalman filtering based algorithms are not used.

3.7 Conclusion

In this chapter several models suitable for DPD and for PA modeling have been presented. First the transition from RF models to filtered baseband equivalent models have been presented and explained. Further only baseband equivalent models have been discussed due to their suitability for DPD. We have divided baseband models to several groups according to their capabilities: Static and quasi-static models, dynamical models. We have also briefly discussed special group of models that allows to separate the model (or DPD) into several stages: two-stage and multi-stage models (can be Static, quasi-static and dynamical). In practice they can be realized by

parallel or cascade structures.

As for model-based approaches (models with linear dependency with respect to their coefficients), orthogonal polynomial models, dynamic distortion reduction and generalized memory polynomials based on simplified Volterra series are a common choice due to their simple complexity, stability of solution and ease of implementation [32]. In terms of performance it is not simple to distinguish between models. In general we may say, that every model outperforms others in different applications.

Next section has presented several methods suitable for identification of the models. There have been presented one one-shot solution and adaptive methods. One may choose method according to needs of Pa modeling or DPD systems. For example in case of high requirements for adaptivity but low complexity, LMS or RLS can be good compromise.

One of the problems is determination of structure of the models. For example for GMP there are eight parameters to be estimated. We would like to point out that using multi-stage models, the estimation of structure is a very important issue. For example using three-stage GMP models (or DPD), 24 parameters defining the structure need to be estimated.

For the case of using neural networks we believe that estimation of such models may bring difficulties. One of the main difficulties could be related with adaptiveness.

In the following chapters we would like to present personal contributions on DPD and PA modeling.

4 IMPROVEMENTS AND PERSONAL CONTRIBUTIONS ON THE PA AND DPD MODELS AND IDENTIFICATION

This chapter presents several personal improvements and contributions to the field of PA modeling and DPD. First sections gives an overview of test signals and PAs that are used for measurements and simulations. Then next section is dedicated to the modeling of the measured PAs with Volterra based series. Next we bring results on linearization of measured PAs also with Volterra based series [126, 127].

We then focus on adaptive algorithms. We will compare adaptive algorithms for several test signals. We propose a new adaptive algorithm called Fractional Least Square algorithm.

The next section is dedicated to the determination of optimal order of structures of series. We propose to use integer genetic algorithm to solve this determination question.

Finally the last section compares modeling several amplifiers using neural networks.

4.1 Test Signals Used For Measuring PAs

In order to test power amplifiers we have generated several test signals. These test signals corresponds to the two applications of the AMBRUN project: tactical communication and broadcast.

For the smart PA from Thales we have used Multiplexed signals composed of several elementary signals described later.

For the PA from TeamCast we have used OFDM (DVB or DAB) signals signals.

We present these signals in the following paragraphs. First let us define the elementary signals used in multiplexes:

4.1.1 Test Signal Type 64 QAM

- Carrier Frequency = fixed at 200 MHz
- Shaping filter = Root Raised Cosine
- Roll off factor = 0.6
- Bit rate = 150 kbps, 3 Mbps

4.1.2 Test Signal Type GMSK

- Type = GMSK modulation
- Shaping filter = Gaussian
- BT = 0.3
- Data rate = 24 kpbs
- Frequency deviation = 6 kHz

This GMSK signal used in multiplexes is characterized by frequency hopping:

- Frequency hopping = 300 hops/s
- Channel spacing = 25 kHz
- No spectrum overlapping

4.1.3 Test Signal Type OFDM

- 1536 sub-carriers
- Total bandwidth of 1536 kHz
- The guard interval is 246 ms long
- Inner modulation is 64-QAM

The transmitted signal is similar to digital audio broadcast (DAB) standard.

All the signals for multiplexes are placed in bursts that last 3.3 ms. The burst is composed from zeros (1.1 ms) and from useful signal (2.2 ms). For each burst, the frequencies of hopping signals changes.

4.1.4 Definition of Multiplex 1 (MUX1)

According to signal definition by Thales in the MUX1 we can use up to three GMSK signals. These three GMSK signal are frequency hopping without overlapping of spectrum. The channel distance between carriers is 25 kHz minimum. The bandwidth of overall signal is limited to 20 MHz. These three carriers have all of the same power.

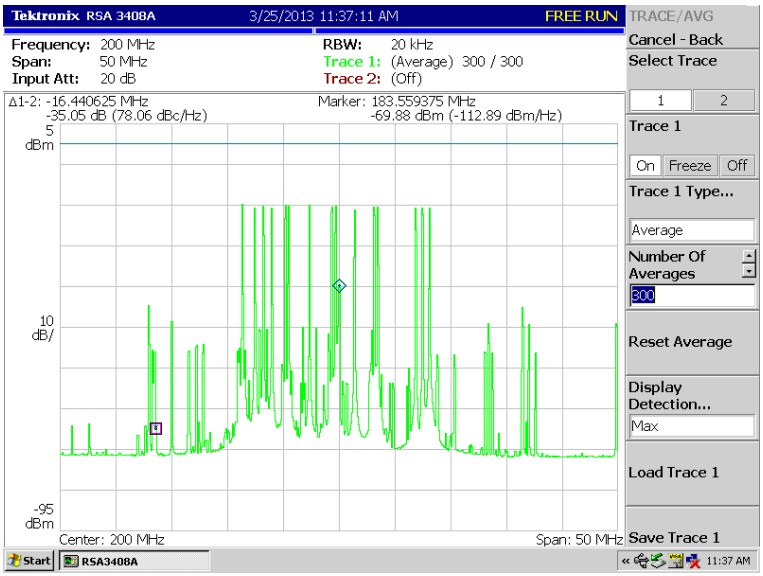

Fig. 4.1: Spectrum of Multiplex 1 measured at the output of PA with inserted 40dB attenuator.

Figure 4.1 shows the spectrum of a MUX 1 signal measured with real-time spectrum at the output of PA on several bursts.

4.1.5 Definition of Multiplex 2 (MUX2)

The Multiplex 2 is composed of one GMSK signal with frequency hopping and a 64 QAM signal (with fixed position centered at carrier frequency). GMSK signals jump in a band of 10 MHz while the minimum frequency distance between the two signals corresponds to the spectral bandwidth of a QAM channel (depending on the bit rate). GMSK signal power is close to the compression point of PA. The average power of the 64QAM is below the GMSK signal.

Figure 4.2 shows the spectrum of a MUX 2 signal measured with real-time spectrum at the output of PA on several bursts.

4.1.6 Definition of Multiplex 3 (MUX3)

The Multiplex 3 is composed of a GMSK signal with frequency hopping and an OFDM signal DAB type simultaneously. GMSK signals jump in a bandwidth of 15 MHz. The minimum frequency distance between the two signals corresponds to the spectral spacing of a DAB channel depending on bit rate that is used. GMSK signal power is close to the compression point of the PA.

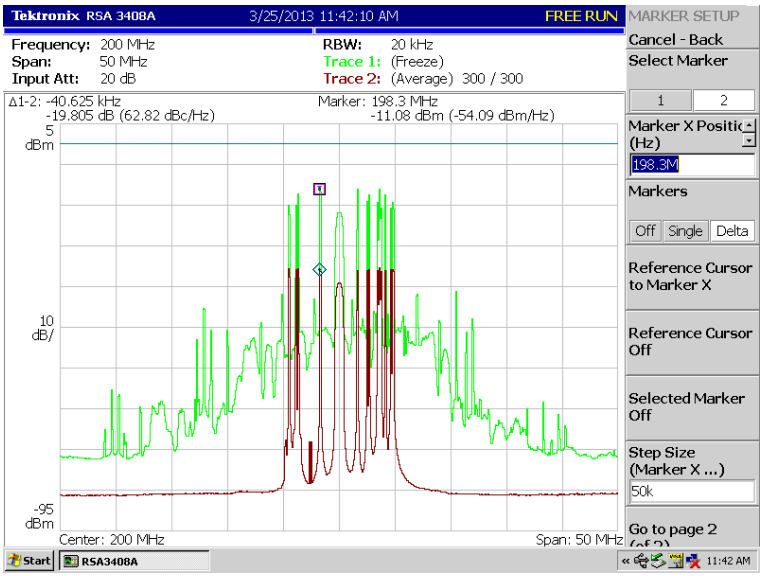

Fig. 4.2: Spectrum of Multiplex 2 measured at the input and output of PA with inserted 40dB attenuator.

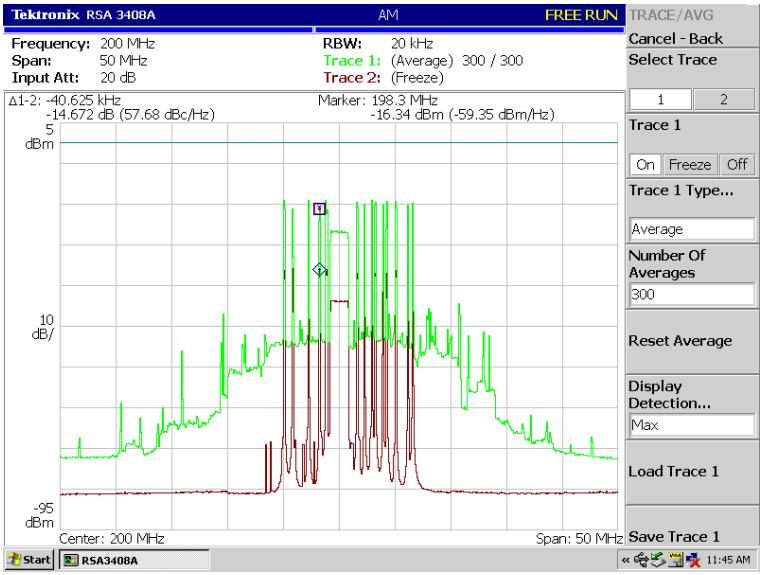

Fig. 4.3: Spectrum of Multiplex 3 measured at the input and output of PA with inserted 40dB attenuator.

Figure 4.3 shows the spectrum of a MUX 1 signal measured with real-time spectrum at the output of PA on several bursts.

4.1.7 Wideband OFDM Signals

We have also tested the PA from Thales with an OFDM signal with 1536 carriers of 40 MHz bandwidth.

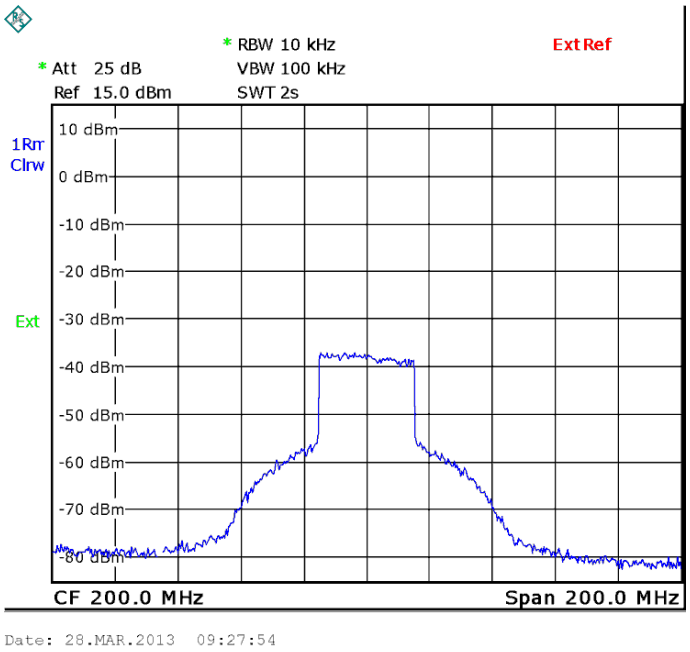

Fig. 4.4: Spectrum of OFDM Wideband signal measured at the output of PA with inserted 40dB attenuator. The bandwidth of signal is 40 MHz.

Figure 4.4 shows the spectrum of OFDM wideband signal at the output of the amplifier. One can observe that the gain of the amplifier is not constant over the entire band of the signal.

4.2 Devices under tests

Several power amplifiers with different input signals have been measured. The list of devices:

Amplifier A1 from TeamCast:

- The PA is Doherty
- RF Transistors are LDMOS NXP BLF888A
- Frequency range: 460 - 860 MHz
- Output power option: 75 W_{rms}, 100 W_{rms} for DVB-T (approximatively can deliver 500 W_{Peak})

- OFDM signal with bandwidth 8 MHz was used and with oversampling rate 8

Amplifier A2 from TeamCast:

- The PA is Doherty
- RF Transistors are LDMOS NXP BLF888B
- Frequency range: 460 - 860 MHz
- Output power option: 120 W_{rms} for DVB-T
- OFDM signal with bandwidth 8 MHz was used and with oversampling rate 8

Amplifier B from TeamCast:

- The PA is Doherty
- RF Transistors are LDMOS
- Frequency range: 620 - 700 MHz
- Output power: 200 W_{rms} for DVB-T (approximatively 2000 W_{Peak})
- OFDM signal with bandwidth 8 MHz was used and with oversampling rate 8

Smart amplifier from THALES:

- The class can be changed from class A to deep class AB
- We have chosen to work on three different operating points
- Transistors are LDMOS (2 x PD55008 and 2 x PD55035)
- Frequency range: 30 - 512 MHz
- Output power: 20 W_{rms} for continuous wave
- The amplifier is driven by FPGA that is controlled by remote PC.
- Controllable input attenuator (made from PIN Diodes)
- As an input signals, several multiplexes were used with different bandwidths (several hopping GMSK, 64 QAM + several hopping GMSK, OFDM + several hopping GMSK, or only OFDM). These signals are described in the previous section 4.1.

The Smart amplifier from Teamcast was measured on our testbenches located at ESIEE Paris. Other amplifiers were measured by TeamCast and Thales Colombes and they data have been supplied to us.

4.3 Modeling the PAs using Volterra Series derived models

In this section we would like to present results for modeling the power amplifiers using Volterra derived series. In order to test the models, we use real measured data obtained by testbench assembled at ESIEE and also data given by Thales and TeamCast. Several test and measurements have been conducted, but only the main ones are presented. A closer description of used amplifiers is given in previous Section 4.2. An orders used for PA modeling and DPD are not chosen randomly. They are based on optimal orders selection. Closer explanation will be given is Section 4.8.

4.3.1 Modeling The Amplifier A1 - 75W

This amplifier was measured by TeamCast company that provided us input and output baseband signals. The average output of this amplifier was 75W. For the modeling, 32768 samples were used. The estimation of model structure for OMPS, DDR and DDR2 can be deduced directly from Fig.4.5 that give the obtained results for M smaller than 4 and K smaller than 10.

First we modeled the PA with OMPS where an order of nonlinearity K=5 and a memory depth M=2 were set. For this test we used 15 coefficients with an overall NMSE=-28.47dB. The results can be seen in Fig.4.6.

The PA was then tested with DDR of first order. The order of nonlinearity was se to K=7 and memory depth M=2. We need to estimate 18 coefficients. The error was: NMSE=-28.51dB. The results can be seen in Fig.4.7.

The DDR of second order (DDR2) was used in order to model the power amplifier A1. The order of nonlinearity K=7 and a memory depth M=2 were set. We have used 30 coefficients with NMSE= -28.55dB. The model of PA can be seen in Fig.4.8.

The order for GMP were set as follows: $Ka = 5, La = 3, Kb = 2, Lb = 2, Mb = 2, Kc = 3, Lc = 2, Mc = 2$. For this configuration we have to estimate 35 coefficients. The calculated error was NMSE=-28.55dB. The GMP model of PA can be seen in Fig.4.9.

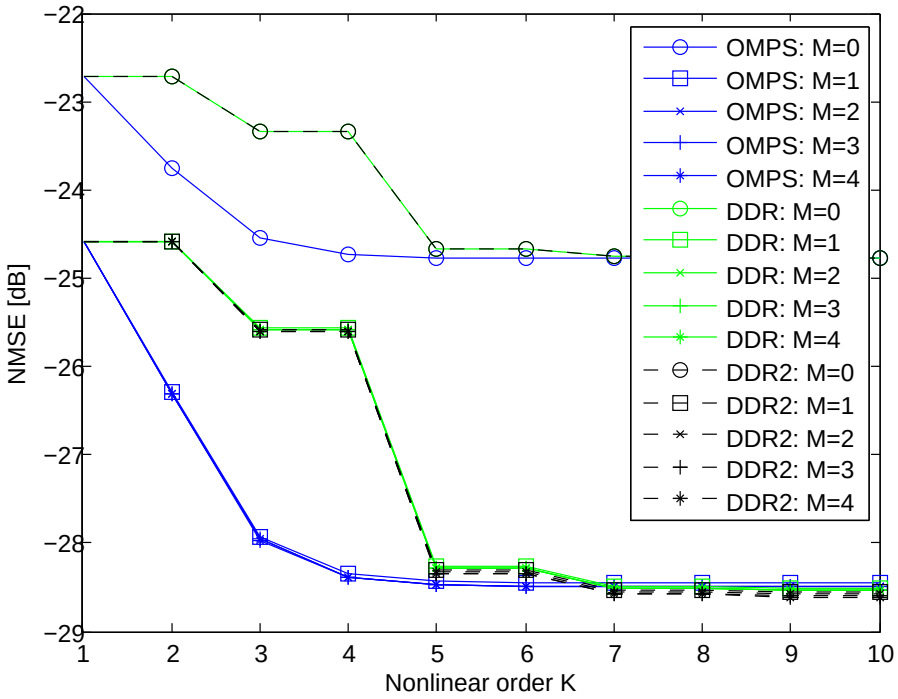

Fig. 4.5: Exhaustive search of optimal model parameters (OMPS, DDR and DDR2) of the amplifier A1 (75W).

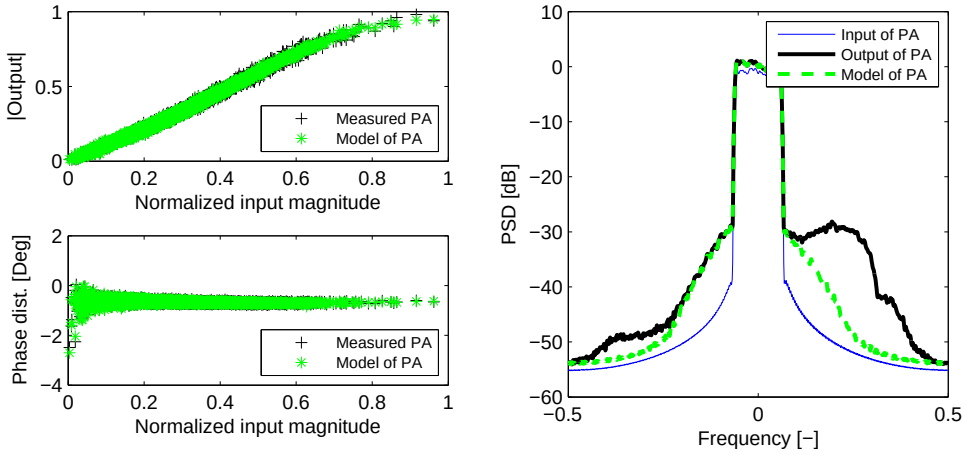

Fig. 4.6: Modeling the amplifier A1 (75W) with OMPS with order of nonlinearity K=5 and memory depth M=2. The calculated error is: NMSE=-28.47dB.

4.3.2 Modeling The Amplifier A1 - 100W

The average output of this amplifier is 100W. The data set was given by TeamCast. For modeling the PA 32768 samples were used. The estimation of model structure for OMPS, DDR and DDR2 can be deduced directly from Fig.4.10. We choose following orders for OMPS: $K = 5$ and $M = 2$, and for DDR and DDR2: $K = 7$ and

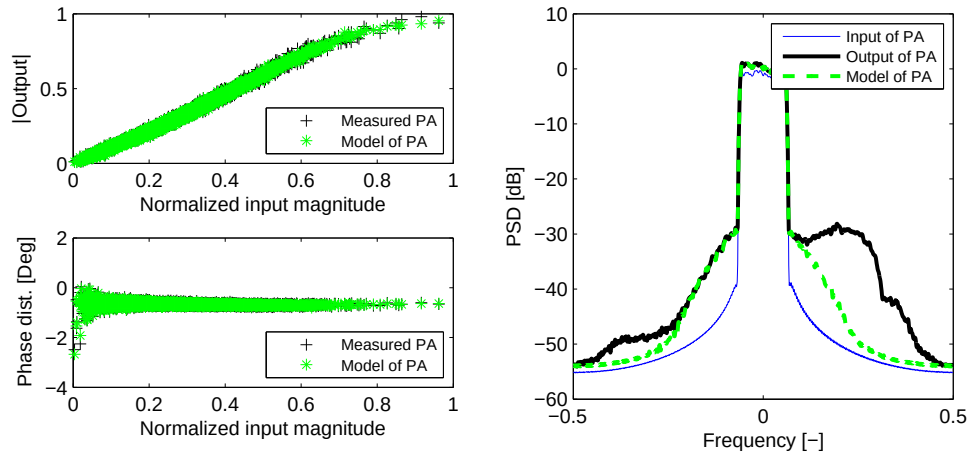

Fig. 4.7: Modeling the amplifier A1 (75W) with DDR1 with order of nonlinearity K=7 and memory depth M=2. The calculated error is: NMSE=-28.51dB.

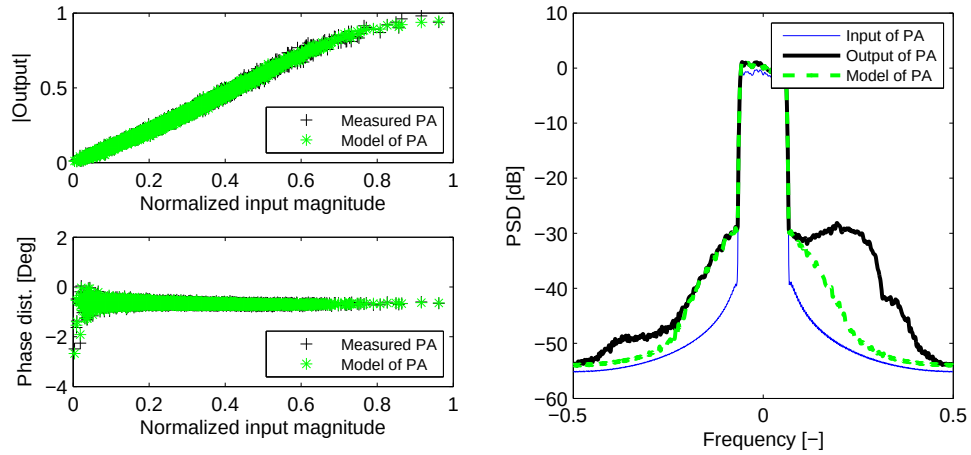

Fig. 4.8: Modeling the amplifier A1 (75W) with DDR2 with order of nonlinearity K=7 and memory depth M=2. The calculated error is: NMSE=-28.55dB.

$M = 2$.)

First we modeled the PA with OPMS where the order of nonlinearity K=5 and memory depth M=2 was set. For this test we used 15 coefficients with an overall NMSE=-28.21dB. The results can be seen in Fig.4.11.

The PA was then tested with DDR of first order (DDR1). The order of nonlinearity was se to K=7 and memory depth M=2. We need to estimate 18 coefficients. The error was: NMSE=-28.23dB. The results can be seen in Fig.4.12.

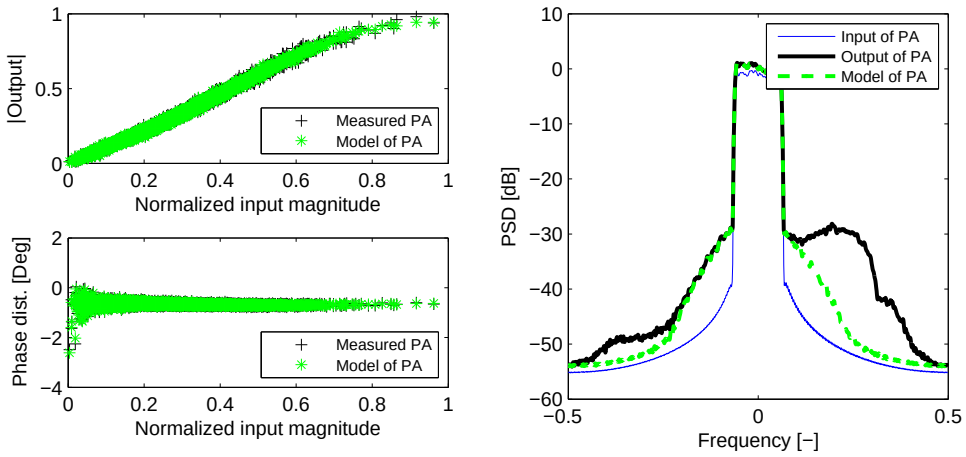

Fig. 4.9: Modeling the amplifier A1 (75W) with GMP with orders: $Ka = 5, La = 3, Kb = 2, Lb = 2, Mb = 2, Kc = 3, Lc = 2, Mc = 2$. The calculated error is: NMSE=-28.55dB.

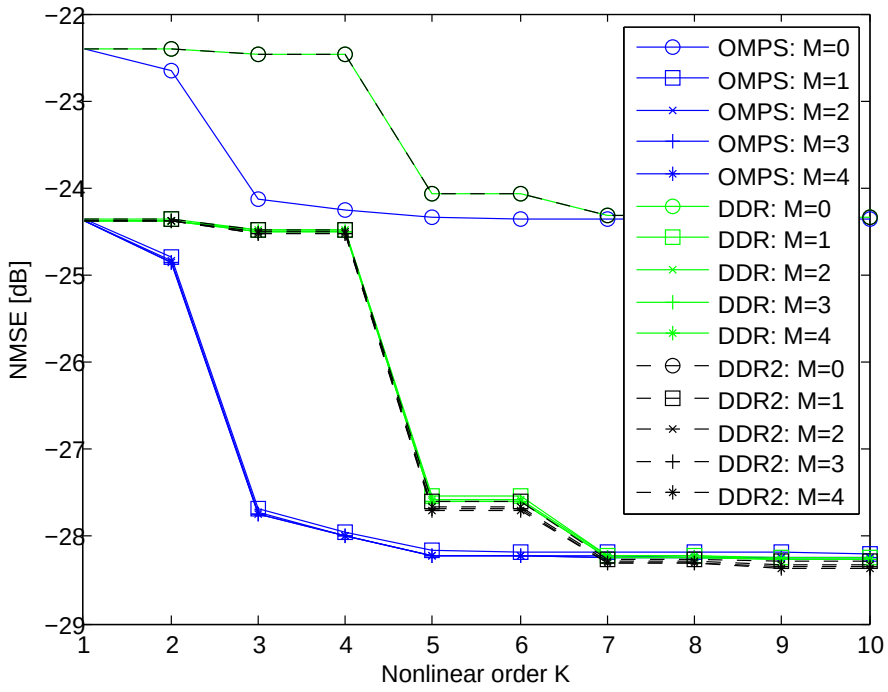

Fig. 4.10: Exhaustive search of optimal model parameters (OMPS, DDR and DDR2) of the amplifier A1 (100W).

The DDR of second order (DDR2) was used in order to model the power amplifier A1. The order of nonlinearity K=7 and memory depth M=2 were set. We have used 30 coefficients with NMSE= -28.29dB. The model of PA can be seen in Fig.4.13.

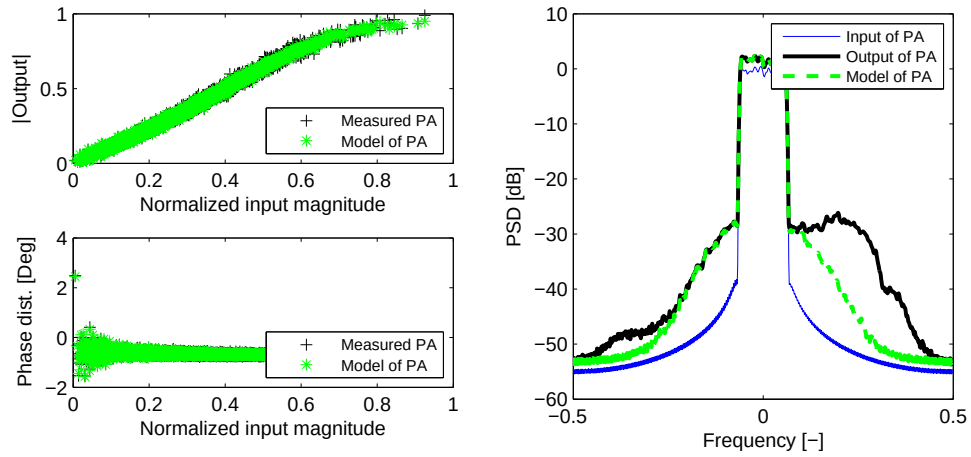

Fig. 4.11: Modeling the amplifier A1 (100W) with OMPS with order of nonlinearity K=5 and memory depth M=2. The calculated error is: NMSE=-28.21dB.

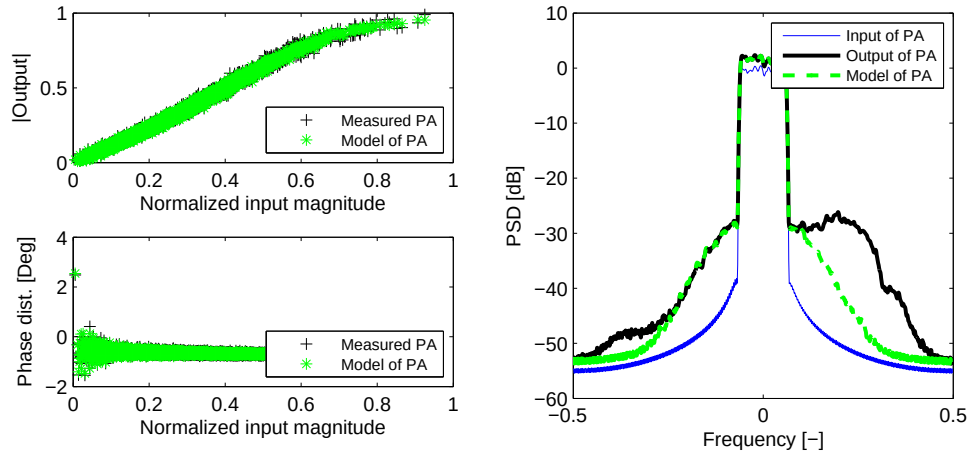

Fig. 4.12: Modeling the amplifier A1 (100W) with DDR1 with order of nonlinearity K=7 and memory depth M=2. The calculated error is: NMSE=-28.23dB.

The order for GMP were set as follows: $Ka = 5, La = 3, Kb = 2, Lb = 2, Mb = 2, Kc = 3, Lc = 2, Mc = 2$. For this configuration we have to estimate 21 coefficients. The calculated error was NMSE=-28.31dB. The GMP model of PA can be seen in Fig.4.14.

4.3.3 Modeling The Amplifier A2 - 120W

The average output of this amplifier is 120W. The data set was given by Team-Cast. For modeling the PA 32768 samples were used. The estimation of orders for OMPS, DDR and DDR2 can be deduced directly from Fig.4.15. We choose following

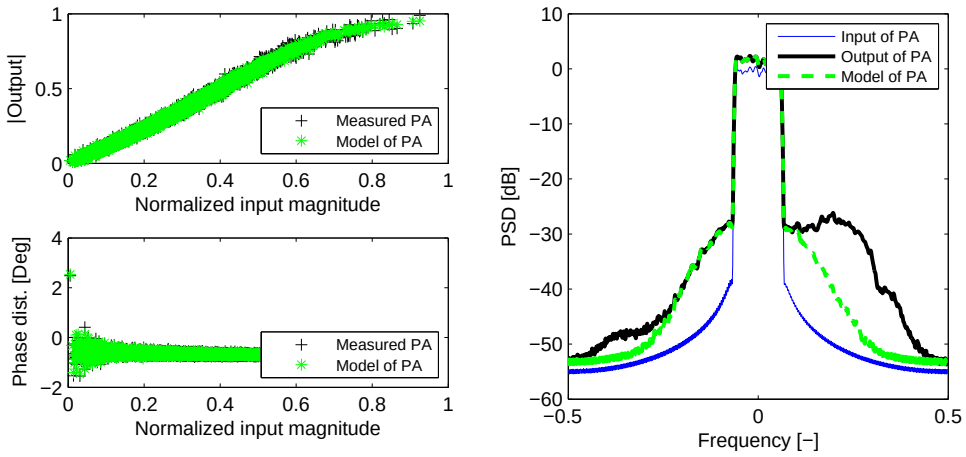

Fig. 4.13: Modeling the amplifier A1 (100W) with DDR2 with order of nonlinearity K=7 and memory depth M=2. The calculated error is: NMSE=-28.29dB.

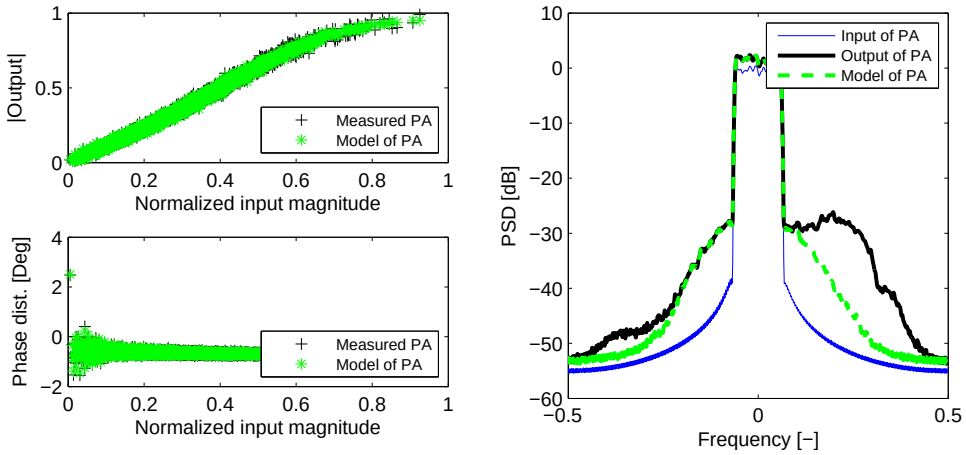

Fig. 4.14: Modeling the amplifier A1 (100W) with GMP with orders: $Ka = 5, La = 3, Kb = 2, Lb = 2, Mb = 2, Kc = 3, Lc = 2, Mc = 2$. The calculated error is: NMSE=-28.24dB.

orders for OMPS: $K = 6$ and $M = 3$, and for DDR and DDR2: $K = 11$ and $M = 3$.)

First we modeled the PA with OMPS where an order of nonlinearity K=6 and a memory depth M=3 was set. For this test we used 24 coefficients with an overall NMSE=-39.17dB. The results can be seen in Fig.4.16.

The PA was then tested with DDR of first order. The order of nonlinearity was se to $K = 11$ and memory depth $M = 3$. We need to estimate 39 coefficients. The error was: NMSE=-39.76dB.

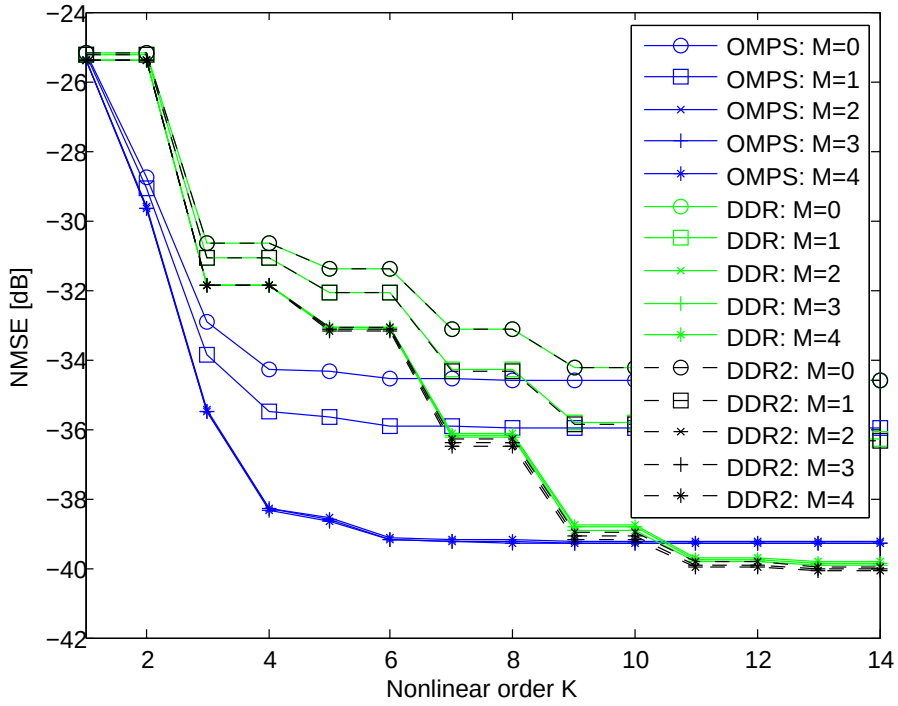

Fig. 4.15: Exhaustive search of optimal model parameters (OMPS, DDR and DDR2) of the amplifier A2 (120W).

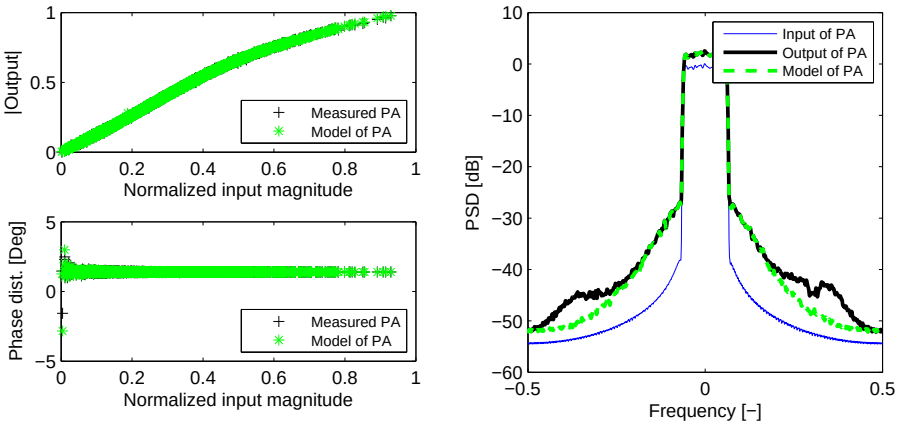

Fig. 4.16: Modeling the amplifier A2 (120W) with OMPS with order of nonlinearity K=6 and memory depth M=3. The calculated error is: NMSE=-39.17dB.

The DDR of second order (DDR2) was used in order to model the power amplifier A2. The order of nonlinearity $K = 11$ and memory depth $M = 3$ were set. We have used 69 coefficients with NMSE= -39.94dB. The model of PA can be seen in Fig.4.17.

The order for GMP were set as follows: $Ka = 7, La = 3, Kb = 3, Lb = 3, Mb =$

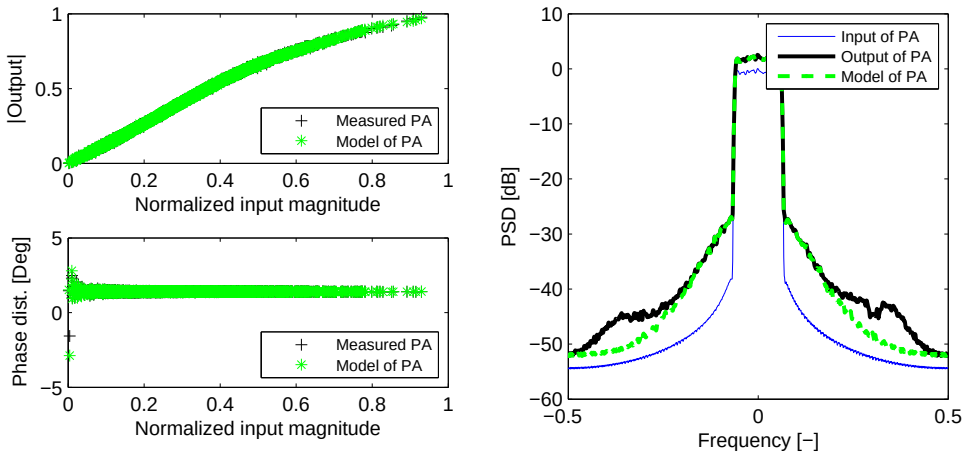

Fig. 4.17: Modeling the amplifier A2 (120W) with DDR2 with order of nonlinearity $K = 11$ and memory depth $M = 3$. The calculated error is: NMSE=-39.94dB.

$2, Kc = 3, Lc = 5, Mc = 4$. For this configuration we have to estimate 99 coefficients. The calculated error was NMSE=-39.99dB. The GMP model of PA can be seen in Fig.4.18.

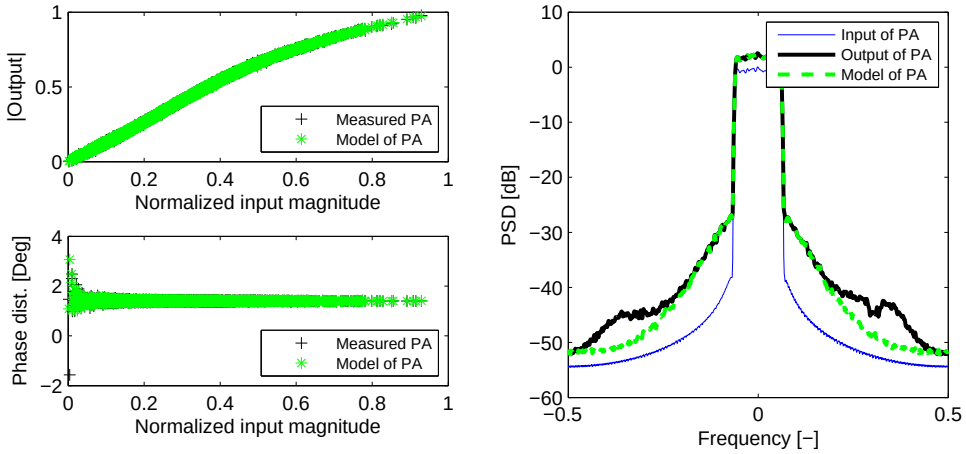

Fig. 4.18: Modeling the amplifier A2 (120W) with GMP with orders: $Ka = 7, La = 3, Kb = 3, Lb = 3, Mb = 2, Kc = 3, Lc = 5, Mc = 4$. The calculated error is: NMSE=-39.99dB.

4.3.4 Modeling The Amplifier B

This amplifier was measured by TeamCast. It is designed for DVB-T applications. The carrier frequency was set to 666MHz. For the modeling we used 196 608 samples. The optimal orders for OMPS, DDR and DDR2 have been directly deduced from exhaustive search plotted in Fig.4.19. For the OMPS we set orders: $K = 8$ and $M = 2$. For the DDR and DDR2 we set: $K = 13$ and $M = 4$.

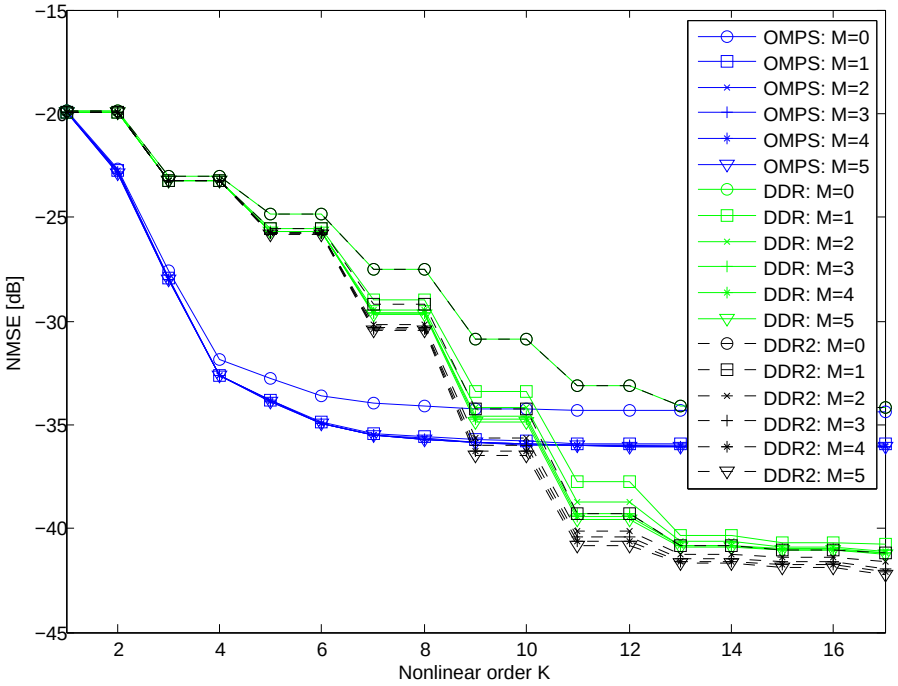

Fig. 4.19: Exhaustive search of optimal model parameters (OMPS, DDR and DDR2) of the amplifier B.

First let us model this PA with PMS or OMPS (because we use low order of structure, we will obtain similar results). Setting order of nonlinearity $K = 8$ and memory depth $M = 2$ (24 coefficients). The error between modeled output of PA and measured output is NMSE=-35.64dB. The results are plotted in Fig.4.20.

The amplifier B was then tested with DDR of first order. The order of nonlinearity was se to $K = 13$ and memory depth $M = 4$. We need to estimate 59 coefficients. The error was: NMSE= -40.83dB.

We have tested the DDR2 model with $K = 13$ and $M = 4$. This model has 107 coefficients. The error between modeled and measured output was NMSE=

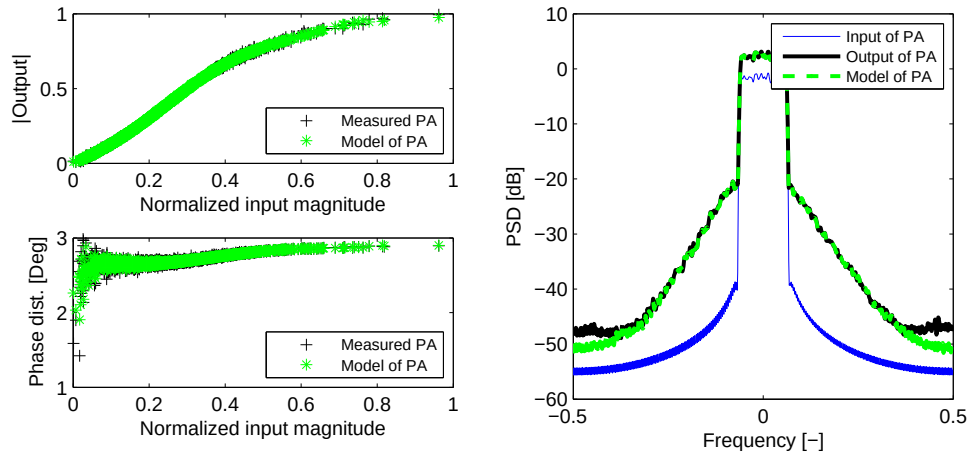

Fig. 4.20: Modeling the amplifier B with PMS/OMPS with order of nonlinearity $K = 8$ and memory depth $M = 2$. The calculated error is: NMSE= -35.64dB.

-41.58dB.

The order for GMP were set as follows: $Ka = 10, La = 3, Kb = 1, Lb = 3, Mb = 1, Kc = 5, Lc = 5, Mc = 3$. For this configuration we have to estimate 108 coefficients. The calculated error was NMSE=-41.75dB.

We may see that for modeling the amplifier A1 (75W and 100W) all proposed models give similar NMSE. Therefore the OMPS (or GMP) are good choice due to low complexity. In the case of modeling power amplifier A2 and more obviously power amplifier B, the OMPS can not achieve the same results as other proposed models. For this case GMP is a good compromise between complexity and performance. In contradistinction to DDR models the GMP can be better adjusted, but finding proper order is more complicated.

4.3.5 Modeling The Smart Amplifier - MUX1

This amplifier was measured in the laboratory located at ESIEE. The PA was produced by Thales. As input signal was used MUX1 described earlier. The polarization of PA was set to high (see Section 4.2). This configuration was measured at double channel testbench. Therefore we have measured the input signal of PA and the output signal of PA. As described in chapter 7, preprocessing has been done. The comparison of modeling results can be seen in Table 4.1. The optimal estimation of orders for models (OMPS, DDR and DDR2) can be found in Fig.4.21.

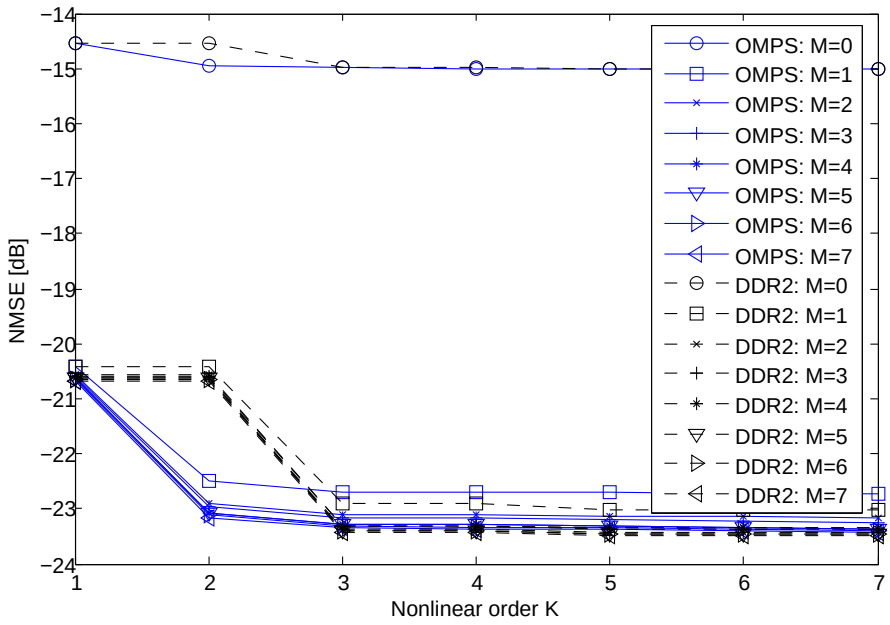

Fig. 4.21: Exhaustive search of optimal model parameters (OMPS, DDR and DDR2) of the Smart Amplifier.

Tab. 4.1: Modeling the Smart PA with high polarization and with MUX1 as input signal. Comparison table of NMSEs and number of coefficients for different models.

Model	**Orders**	$NMSE$ **[dB]**	No. of coef.
OMPS	K=3, M=3	-23.17	12
DDR1	K=3, M=3	-23.25	11
DDR2	K=3, M=3	-23.31	17
GMP	Ka=3, La=3, Kb=1, Lb=1, Mb=1, Kc=1, Lc=6, Mc=8	-23.02	58

The graphical results of AM/AM, AM/PM and PSD for GMP are in Fig.4.22.

4.3.6 Modeling The Smart Amplifier - MUX2

As a input signal was used MUX2 described in previous section. The polarization of PA was set to low. This configuration was measured at double channel testbench. The comparison of modeling result can be seen in Table 4.2 and the optimal orders estimation of models (OMPS, DDR and DDR2) can be found in Fig.4.23.

The graphical results fo GMP are in Fig.4.24.

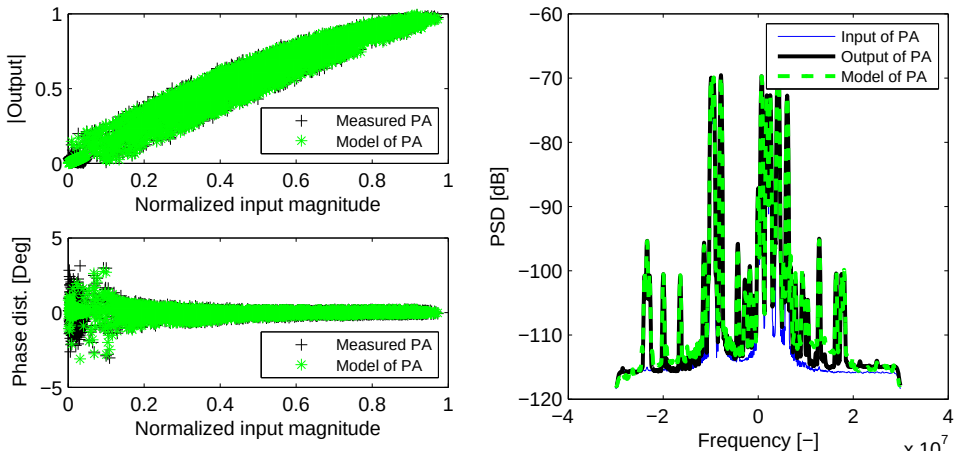

Fig. 4.22: Modeling the Smart amplifier with GMP with structure as follows: $Ka = 3, La = 3, Kb = 1, Lb = 1, Mb = 1, Kc = 1, Lc = 6, Mc = 8$. The calculated error is: NMSE= -23.02dB.

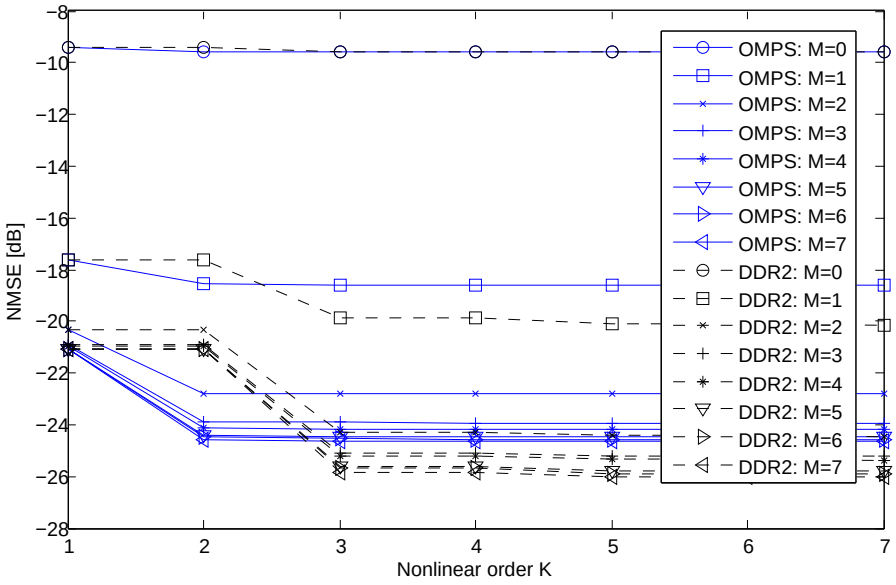

Fig. 4.23: Exhaustive search of optimal model parameters (OMPS, DDR and DDR2) of the Smart Amplifier.

4.3.7 Modeling The Smart Amplifier - MUX3

For this configuration a MUX3 signal is used in order to model the PA. The polarization of PA was set to low. The comparison of modeling results can be seen in Table 4.3 and the optimal orders estimation of models (OMPS, DDR and DDR2) can be found in Fig.4.25

Tab. 4.2: Modeling the Smart PA with low polarization and with MUX2 as input signal. Comparison table of NMSEs and number of coefficients for different series.

Series	**Orders**	$NMSE$ **[dB]**	No. of coef.
OPMS	K=2, M=3	-23.87	8
DDR1	K=4, M=5	-25.17	17
DDR2	K=4, M=5	-25.59	27
GMP	Ka=3, La=13, Kb=1, Lb=1, Mb=1, Kc=2, Lc=5, Mc=3	-25.68	70

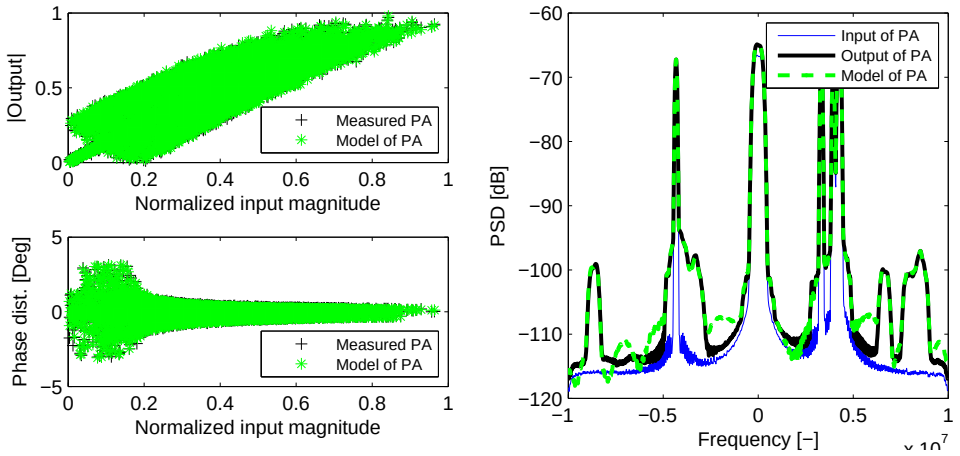

Fig. 4.24: Modeling the Smart amplifier with GMP with structure as follows: $Ka = 3, La = 13, Kb = 1, Lb = 1, Mb = 1, Kc = 2, Lc = 5, Mc = 3$. The calculated error is: NMSE=-25.68dB.

Tab. 4.3: Modeling the Smart PA with low polarization and with MUX2 as input signal. Comparison table of NMSEs and number of coefficients for different series.

Series	**Orders**	$NMSE$ **[dB]**	No. of coef.
OPMS	K=2, M=3	-23.51	8
DDR1	K=3, M=4	-23.65	14
DDR2	K=7, M=2	-23.67	22
GMP	Ka=3, La=3, Kb=3, Lb=1, Mb=1, Kc=1, Lc=6, Mc=8	-23.71	60

The graphical results fo GMP are in Fig.4.26.

We can see, that modeling the Smart amplifier for MUX1 signal can be done using all of the proposed models. This amplifier is quite linear with small memory effects. For modeling this PA, DDR1 has best the results with respect to complexity and performance. For the MUX 2 we can see, that the amplifier is linear, but with higher memory effect. Therefore one have to use higher memory orders. We can

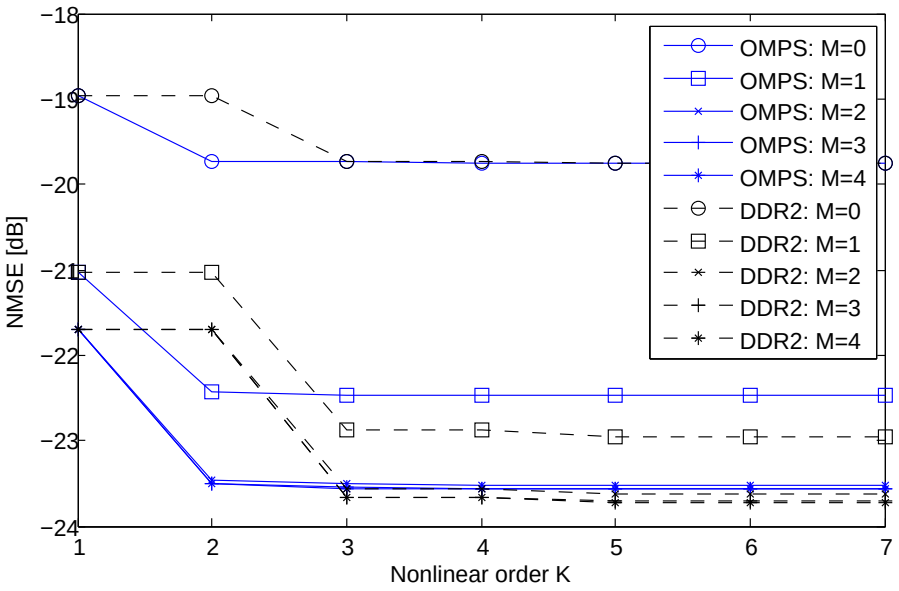

Fig. 4.25: Exhaustive search of optimal model parameters (OMPS, DDR and DDR2) of the Smart Amplifier.

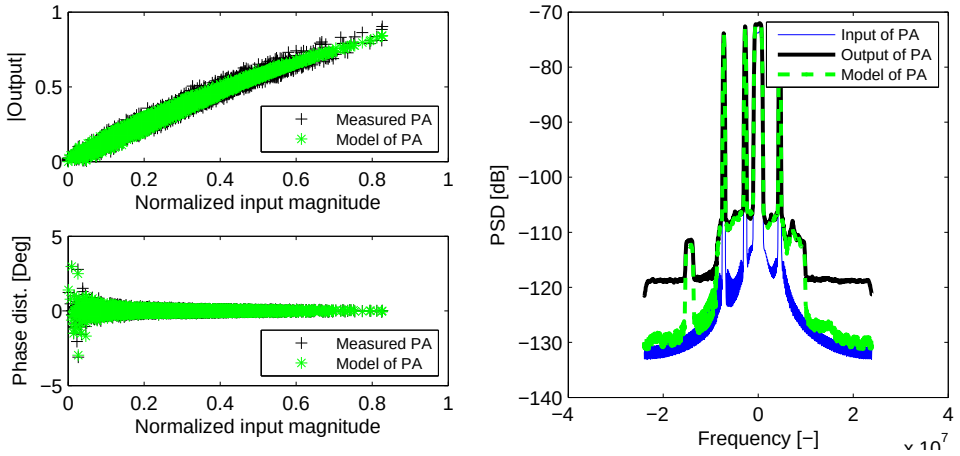

Fig. 4.26: Modeling the Smart amplifier with GMP with structure as follows: $Ka = 3, La = 3, Kb = 3, Lb = 1, Mb = 1, Kc = 1, Lc = 6, Mc = 8$. The calculated error is: NMSE= -23.71dB.

also observe that OMPS has worse results of NMSE. For the MUX3 GMP have best NMSE, but with higher complexity. For this PA the OMPS is best compromise between complexity and performance.

4.4 Linearizing the PAs using Volterra Series derived models

In this section we present results for linearization of power amplifiers using indirect learning approach. The configuration of PAs is similar to that of the previous section.

4.4.1 Linearization of Amplifier A1 (75W)

The results of linearization of the Amplifier A1 (75W) can be seen in Table 4.4. The orders of linearization series have been estimated as a compromise between complexity and performance. The exhaustive search can be found in the Fig.4.27

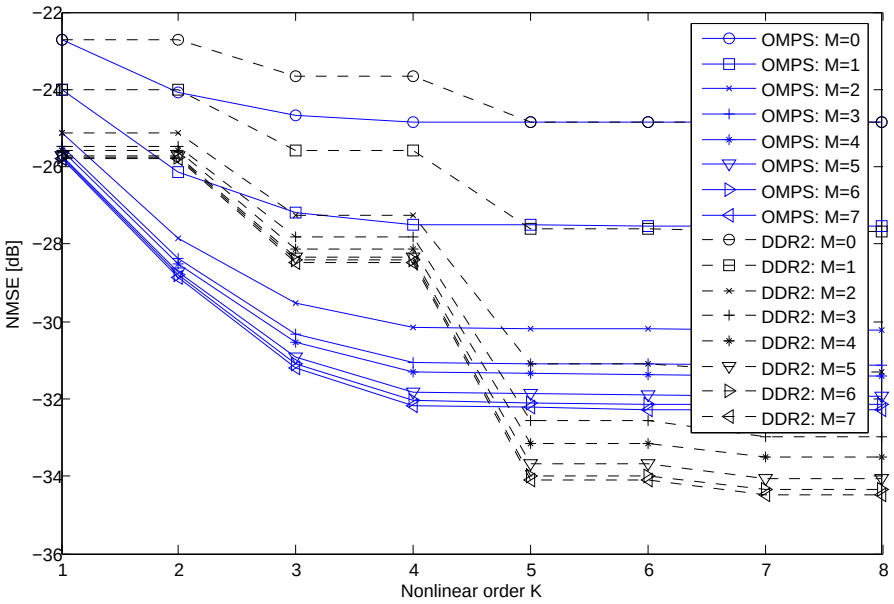

Fig. 4.27: Exhaustive search of optimal linearization parameters (OMPS, DDR and DDR2) of the amplifier A1 (75W).

Tab. 4.4: Linearization of amplifier A1 (75W).

Series	**Orders**	$NMSE$ **[dB]**	No. of coef.
OPMS	K=4, M=5	-31.83	24
DDR1	K=5, M=6	-32.93	33
DDR2	K=5, M=6	-33.98	57
GMP	Ka=4, La=3, Kb=2, Lb=3, Mb=3, Kc=3, Lc=4, Mc=4	-34.15	78

In the Fig.4.28 we may observe the linearization of amplifier A1 (75W) linearized by GMP with orders: $Ka = 4, La = 3, Kb = 2, Lb = 3, Mb = 3, Kc = 3, Lc = 4, Mc = 4$. One can see, that the GMP (but also OMPS, DDR and DDR2) does not achieve to fully linearize the right asymmetrical side lobe of the spectrum.

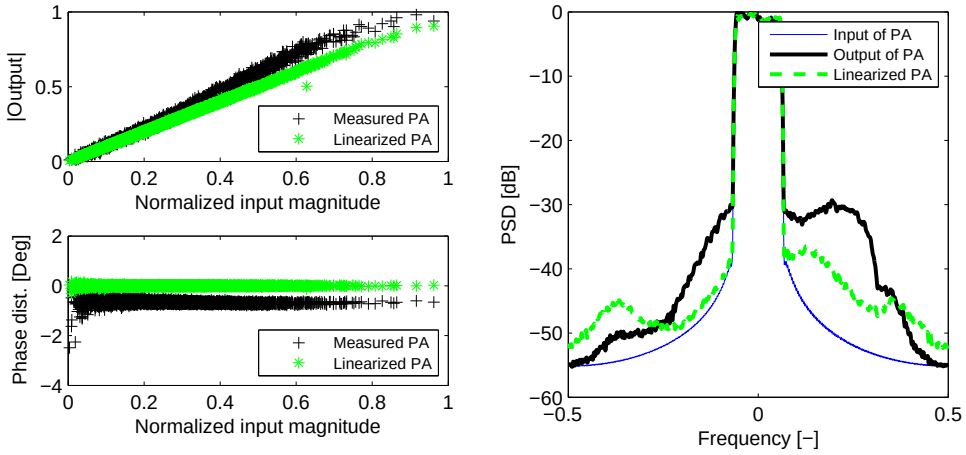

Fig. 4.28: Linearization the amplifier A1 (75W) with GMP with orders: $Ka = 4, La = 3, Kb = 2, Lb = 3, Mb = 3, Kc = 3, Lc = 4, Mc = 4$. The calculated error is: NMSE= -34.15dB.

4.4.2 Linearization of Amplifier A1 (100W)

The results of linearization the amplifier A1 (100W) are presented in Table 4.5. The corresponding AM/AM, AM/PM and PSD results for GMP (with orders: Ka=5, La=3, Kb=2, Lb=2, Mb=2, Kc=1, Lc=2, Mc=2) are presented in Fig.4.30.

Tab. 4.5: Linearization of amplifier A1 (100W).

Series	**Orders**	$NMSE$ **[dB]**	No. of coef.
OPMS	K=4, M=6	-31.32	28
DDR1	K=7, M=7	-32.43	53
DDR2	K=7, M=7	-33.90	95
GMP	Ka=5, La=3, Kb=2, Lb=10, Mb=3, Kc=3, Lc=2, Mc=7	-34.44	117

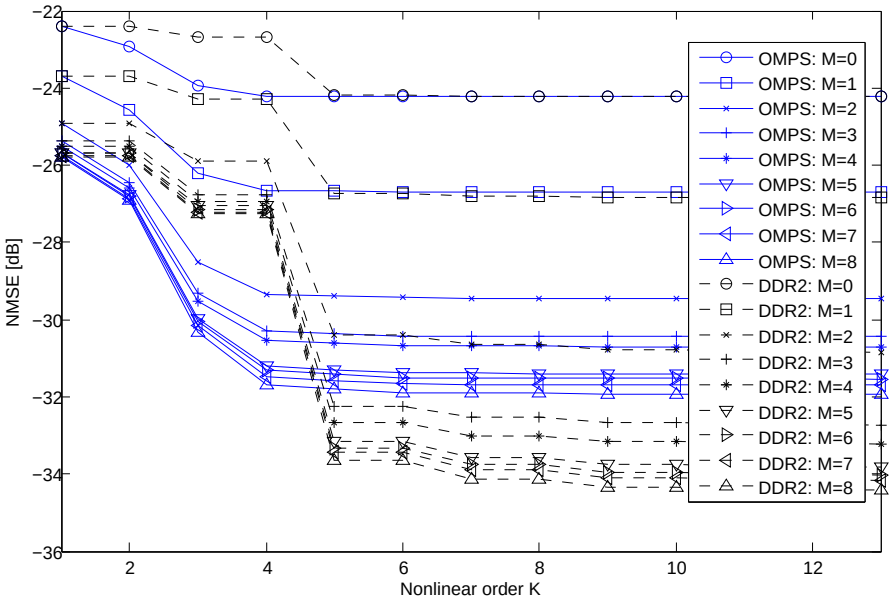

Fig. 4.29: Exhaustive search of optimal linearization parameters (OMPS and DDR2 (similar orders as DDR)) of the amplifier A1 (100W).

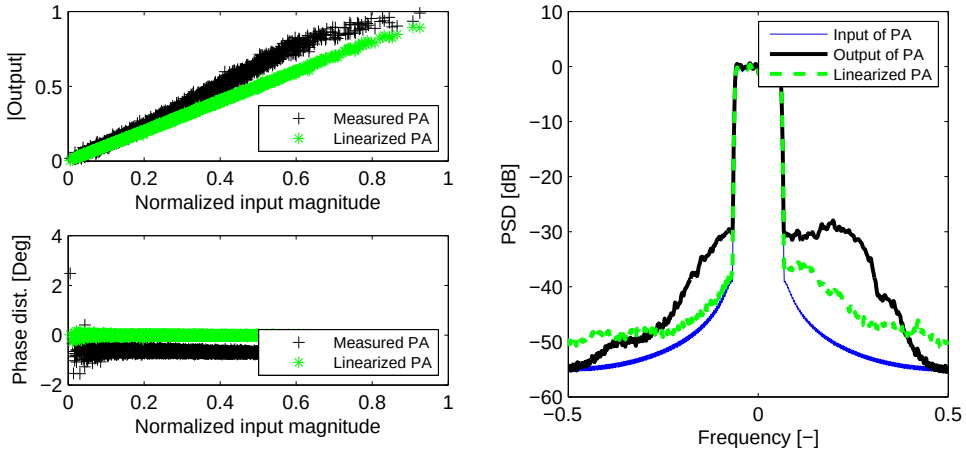

Fig. 4.30: Linearization the amplifier A1 (100W) with GMP with orders $Ka = 5, La = 3, Kb = 2, Lb = 10, Mb = 3, Kc = 3, Lc = 2, Mc = 7$. The calculated error is: NMSE= -34.44dB.

4.4.3 Linearization of Amplifier A2 (120W)

In this subsection we would like to present results of linearizing the power amplifier A2. The summary can be found in Table 4.6. The exhaustive order estimation can be seen in Fig.4.31.

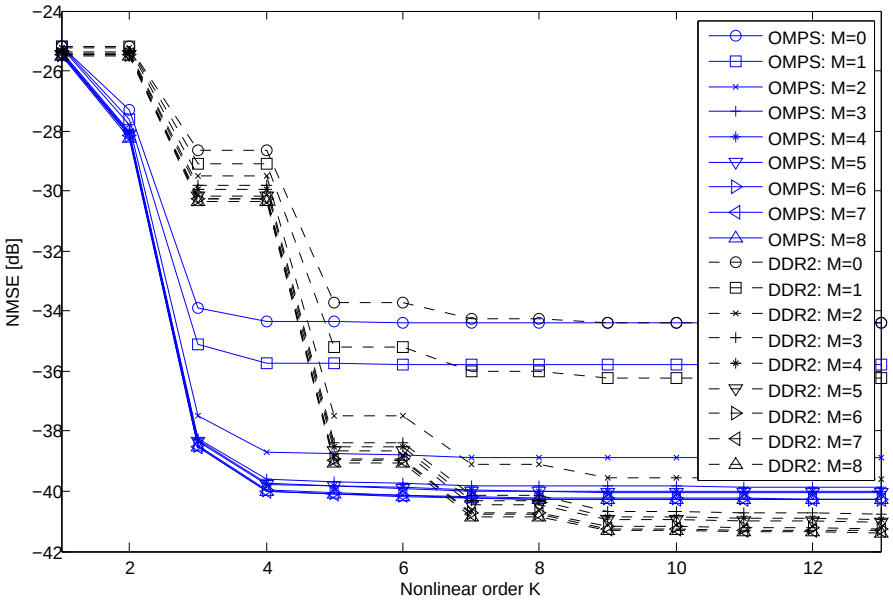

Fig. 4.31: Exhaustive search of optimal linearization parameters (OMPS and DDR2 (similar orders as DDR)) of the amplifier A2 (120W).

Tab. 4.6: Linearization of amplifier A2 (120W).

Series	**Orders**	$NMSE$ **[dB]**	No. of coef.
OPMS	K=4, M=4	-39.73	20
DDR1	K=9, M=5	-40.68	50
DDR2	K=9, M=5	-40.94	90
GMP	Ka=5, La=3, Kb=2, Lb=10, Mb=3, Kc=2, Lc=2, Mc=5	-41.27	95

4.4.4 Linearization of Amplifier B

The results can be found in Table4.7. Linearized amplifier using GMP with orders: $Ka = 9, La = 2, Kb = 3, Lb = 3, Mb = 3, Kc = 3, Lc = 4, Mc = 3$, can be found in Fig.4.33. The order selection is closer described in Fig.4.32.

Tab. 4.7: Linearization of amplifier B.

Series	**Orders**	$NMSE$ **[dB]**	No. of coef.
OPMS	K=5, M=2	-33.30	15
DDR1	K=13, M=3	-40.43	46
DDR2	K=7, M=2	-40.88	82
GMP	Ka=9, La=2, Kb=3, Lb=3, Mb=3, Kc=3, Lc=4, Mc=3	-41.03	81

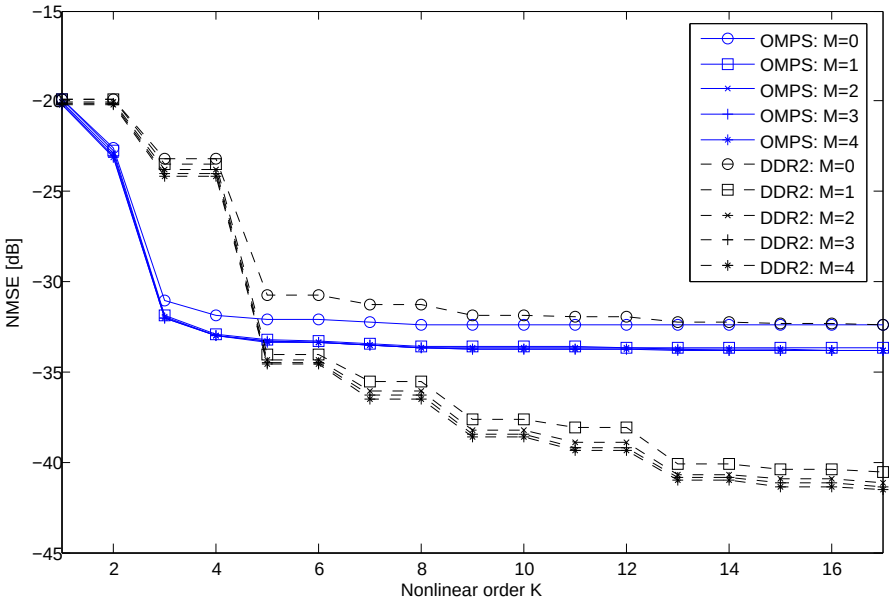

Fig. 4.32: Exhaustive search of optimal linearization parameters (OMPS and DDR2 (similar orders as DDR)) of the amplifier B.

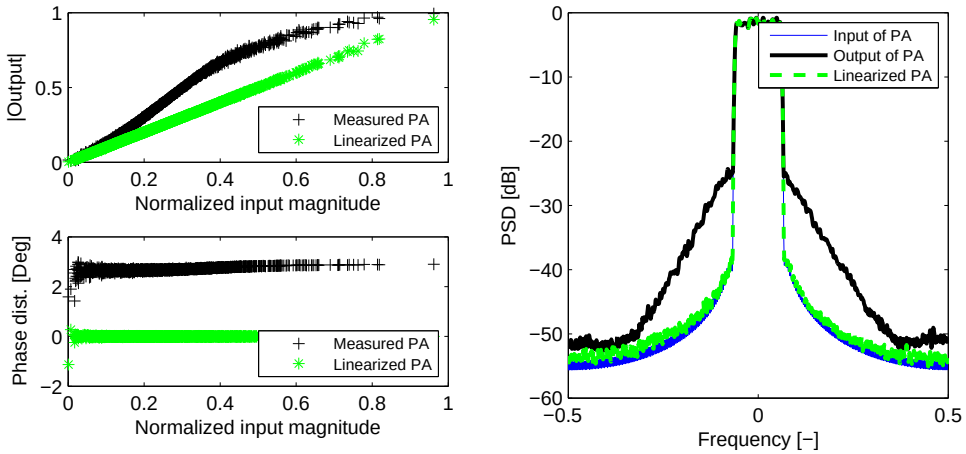

Fig. 4.33: Linearization the amplifier B with GMP with orders $Ka = 9, La = 2, Kb = 3, Lb = 3, Mb = 3, Kc = 3, Lc = 4, Mc = 3$. The calculated error is: NMSE= -41.03dB.

We may see, that for linearization of amplifiers A1 (75 and 100W), A2 and B the OMPS have limitations. One can see that we are not successful in linearizing the asymmetrical spectrum of amplifier A1. The order of nonlinearities is higher and the memory depth is also high. For linearization usually GMP and DDR2 are the best compromise between performance and complexity.

4.4.5 Linearization of Smart amplifier - MUX1

In this section we would like to present the linearization of the Smart power amplifier with Multiplex 1 as an input signal. This signal is specific, because it consists of several bursts with frequency hopping. The results can be found in Table.4.8. The order selection of linearization is described in Fig.4.34. The linearization is performed on block made of $960 \cdot 10^3$ samples.

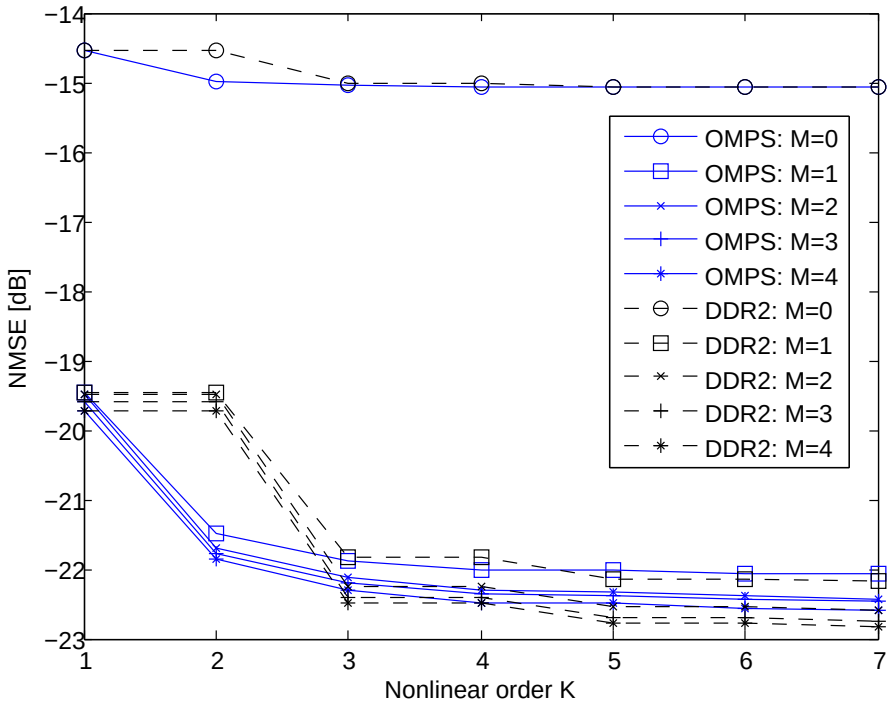

Fig. 4.34: Exhaustive search of optimal linearization parameters (OMPS and DDR2 (similar orders as DDR)) of the Smart amplifier with MUX1.

Tab. 4.8: Linearization of Smart amplifier for MUX1.

Series	**Orders**	$NMSE$ **[dB]**	No. of coef.
OPMS	K=4, M=3	-22.35	16
DDR1	K=5, M=3	-22.31	18
DDR2	K=5, M=3	-22.69	30
GMP	Ka=4, La=3, Kb=2, Lb=3, Mb=2, Kc=3, Lc=4, Mc=2	-23.37	48

4.4.6 Linearization of Smart amplifier - MUX2

In this subsection we present results for postdistortion of Smart amplifier with Multiplex 2 as an input signal of PA. The corresponding result can be found in Table 4.9. The order selection can be deduced from Fig.4.35. For the calculation the block of $320 \cdot 10^3$ samples have been used.

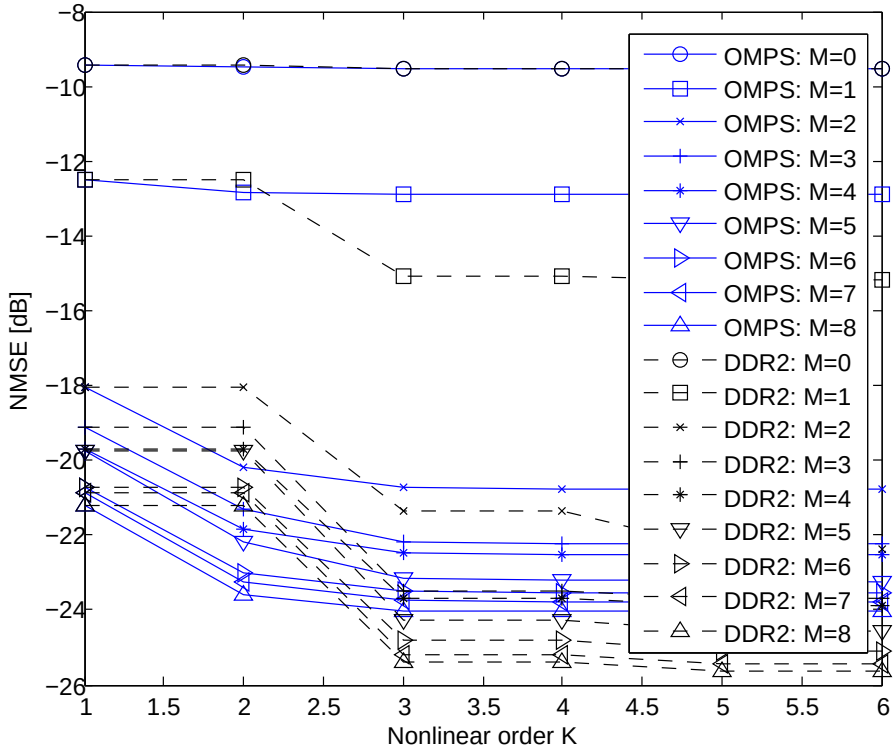

Fig. 4.35: Exhaustive search of optimal linearization parameters (OMPS and DDR2 (similar orders as DDR)) of the Smart amplifier with MUX2.

Tab. 4.9: Linearization of Smart amplifier for MUX2.

Series	**Orders**	$NMSE$ **[dB]**	No. of coef.
OPMS	K=3, M=8	-24.01	27
DDR1	K=3, M=8	-24.90	26
DDR2	K=3, M=8	-25.40	42
GMP	Ka=3, La=5, Kb=1, Lb=1, Mb=2, Kc=2, Lc=4, Mc=5	-25.54	57

4.4.7 Linearization of Smart amplifier - MUX3

In the Table 4.10 one can observe results for linearization the Smart PA with MUX3 as an input signal of PA. The optimal order estimation can be obtain from Fig.4.36. Buffer of size $350 \cdot 10^3$ is used for the calculation.

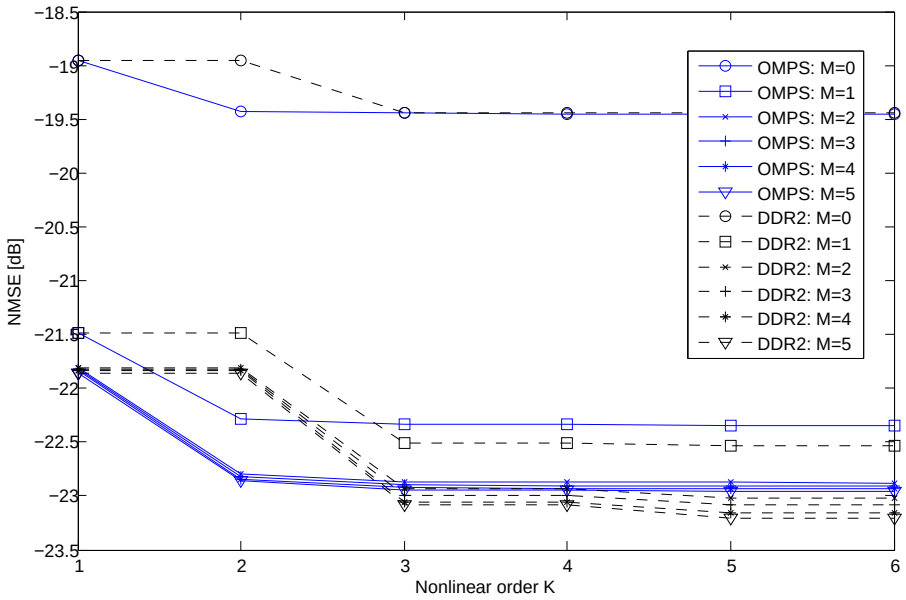

Fig. 4.36: Exhaustive search of optimal linearization parameters (OMPS and DDR2 (similar orders as DDR)) of the Smart amplifier with MUX3.

Tab. 4.10: Linearization of Smart amplifier for MUX3.

Series	**Orders**	$NMSE$ **[dB]**	No. of coef.
OPMS	K=2, M=3	-22.83	8
DDR1	K=3, M=3	-22.89	11
DDR2	K=3, M=3	-23.00	17
GMP	Ka=5, La=7, Kb=1, Lb=2, Mb=2, Kc=2, Lc=2, Mc=2	-22.83	47

Linearization of Smart amplifier with MUX1 and MUX2 signals can be done using OMPS, DDR, DDR2 and GMP. We can see, that the performance of evaluated models is similar. Linearization of Smart amplifier with signal called MUX3 perform better for high memory order with relatively low order of nonlinearity. Linearization of the Smart amplifier with signal MUX3 using DDR2 models has the best performance whilst preserving a low complexity.

4.5 Number Of Coefficients For Volterra Derived Series

In this subsection we would like to present analytical formulas necessary in order to obtain number of coefficients N_c. We have expressed this formulas for PMS, OMPS, DDR1, DDR2 and GMP. The results can be found in Table 4.11.

Tab. 4.11: Analytical estimation of coefficients for presented series

Series	Used Constants	Number of Coefficients
PMS	K,M	$K(M+1)$
OPMS	K,M	$K(M+1)$
DDR1	K,M	KM
DDR2 (Simplified)	K,M	$2MK + \left(\frac{K+1}{2}\right) - M$
GMP	$K_a, L_a, K_b, L_b, M_b, K_c, L_c, M_c$	$K_aL_a + K_bL_bM_b + K_cL_cM_c$

4.6 Results Using Adaptive Algorithms

In order to evaluate the performance of adaptive algorithms we calculate the NMSE between the model output and real measured data. For the DNA the NMSE is evaluated on each block of data. But for the RLS and LMS, averaging over 20 previous NMSEs is applied.

For the simulation we have used TeamCast PA described in Section 4.2 operating on carrier frequency 800MHz. The input signal of the PA is a broadcast OFDM signal. The model of predistorter was OMPS with orders $K = 7, Q = 2$.

For the simulations we have used 98304 captured baseband samples. The whole vector of samples was created by concatenating six blocks of 16384 samples. It is the reason of the discontinuity occurrence. We take advantage of this discontinuity in order to demonstrate the adaptiveness of algorithms. In Fig.4.37 we may observe discontinuity of signal.

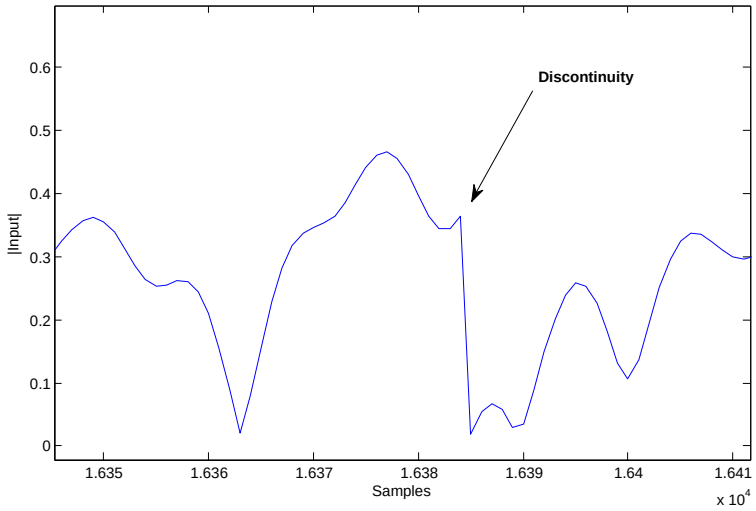

Fig. 4.37: Discontinuity of measured input signal of PA.

The dependency of NMSE on the buffer size for DNA can be seen in the Fig.4.38. The constant μ was set to 0.2 to have an important damping. We may see "spikes" caused by discontinuities of measured samples.

In the Fig. 4.39 we can observe the same NMSE dependency on the buffer size in the case where $\mu = 1$ (no averaging between successive blocks).

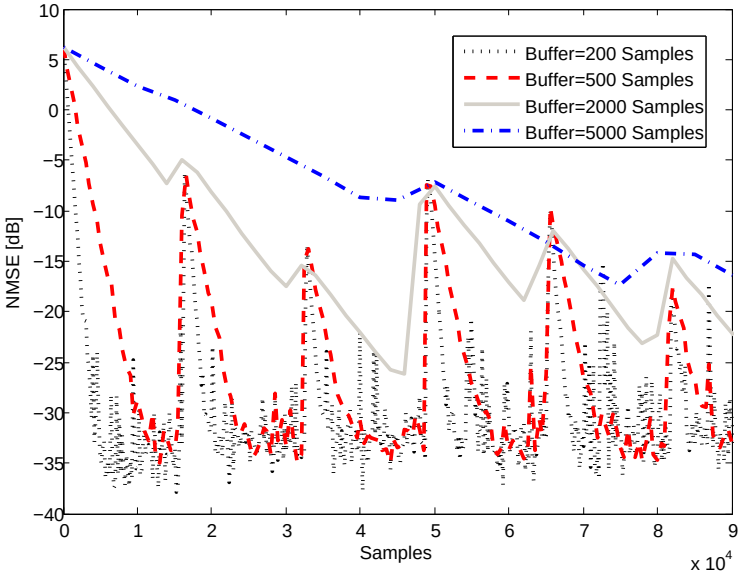

Fig. 4.38: NMSE dependency for the DNA algorithm on the buffer size with $\mu = 0.2$.

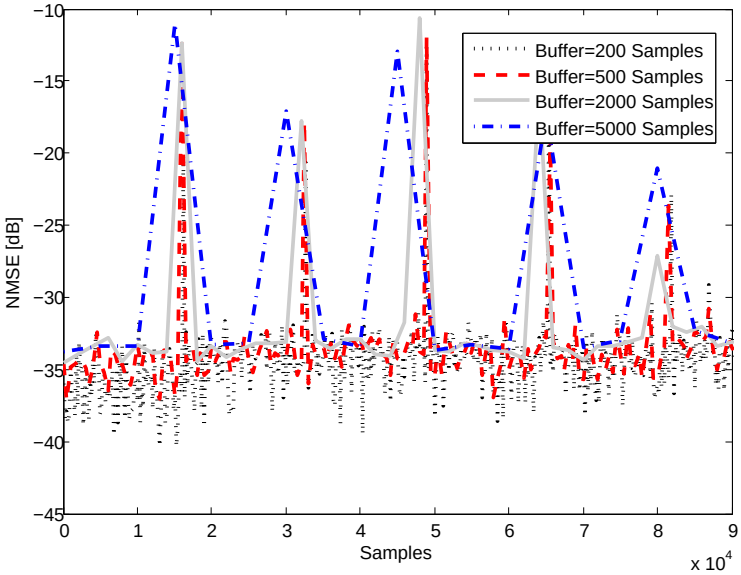

Fig. 4.39: NMSE dependency for the DNA algorithm on the buffer size with $\mu = 1$. For $\mu = 1$, there is no damping (no averaging between successive blocks).

We present in Fig.4.40 the results to RLS algorithm for $\lambda = 1$, $\lambda = 0.9$ and $\delta = 10^{-3}$. One may observe that for $\lambda = 1$ the algorithm is not adaptive.

In Fig.4.41 we can see the results using LMS. For the $\mu = 0.5$ the adaptivity is limited. We can see slow rate of convergence. For the $\mu = 0.1$ the LMS is adaptive but performance is lower than RLS.

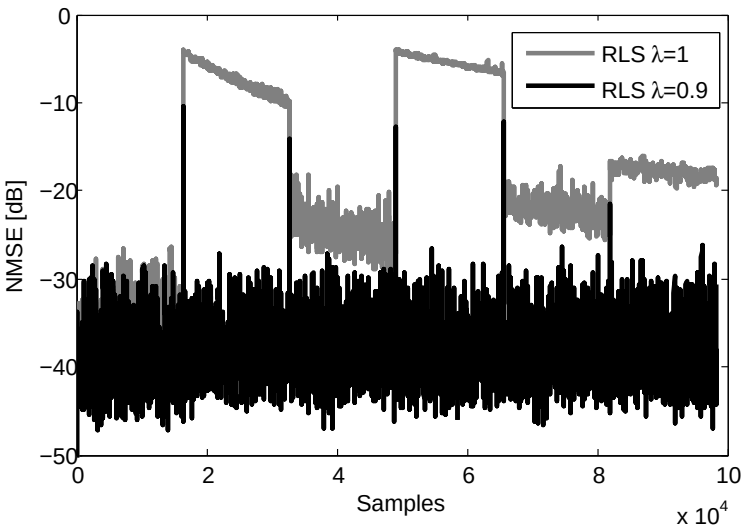

Fig. 4.40: The NMSE for the RLS algorithm with different λ.

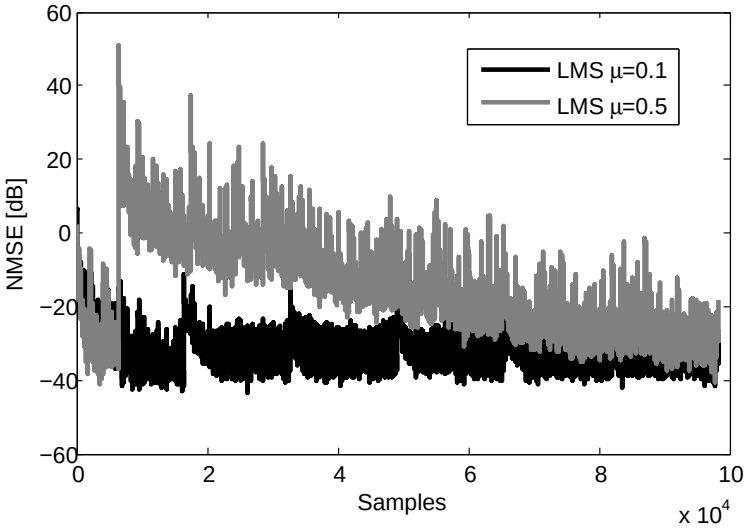

Fig. 4.41: The NMSE for the LMS algorithm with different μ.

Then we have taken under inspection the multiplexed signal denoted as MUX3 (presented in Section 4.1), which has changing power levels due to GMSK bursts combined with OFDM signal.

The whole test signal corresponds to real measurements. For the simulations, we have taken 450000 test samples. The varying real and imaginary parts of the input complex baseband filtered signal of power amplifier can be seen in Fig.4.42.

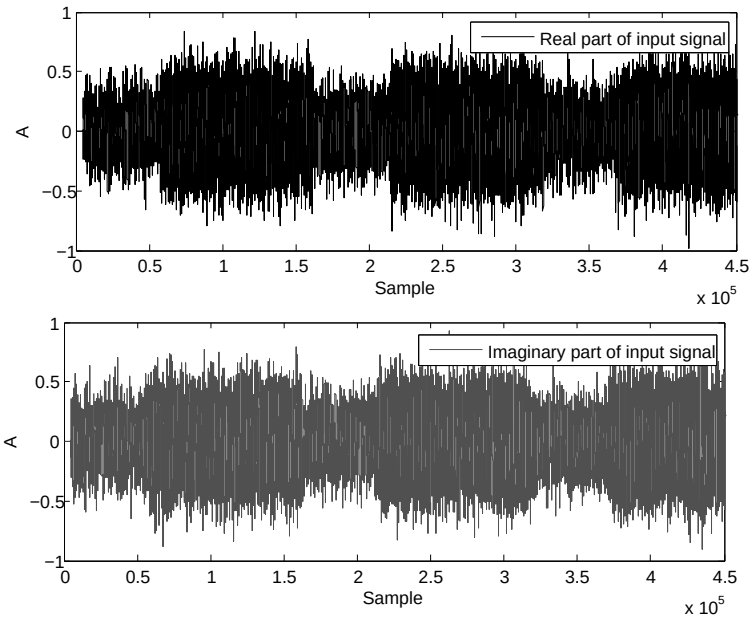

Fig. 4.42: Real and imaginary part of the complex baseband filtered signal denoted as MUX3.

For this real measurements based test we have used OMPS as the DPD with the nonlinear order K=7 and memory depth M=2.

In Fig.4.43 we can observe evolution of error for LMS algorithm with different values of μ. One may observe a short divergence for the $\mu = 0.5$ at the end of sequence. It is due to wrong setup of μ.

In the Fig.4.44 we can see similar situation as in Fig.4.43 but for the RLS algorithm. We can see, that RLS is able to track the variations of the signal with $\lambda = 0.9$ and has better performance than LMS algorithm.

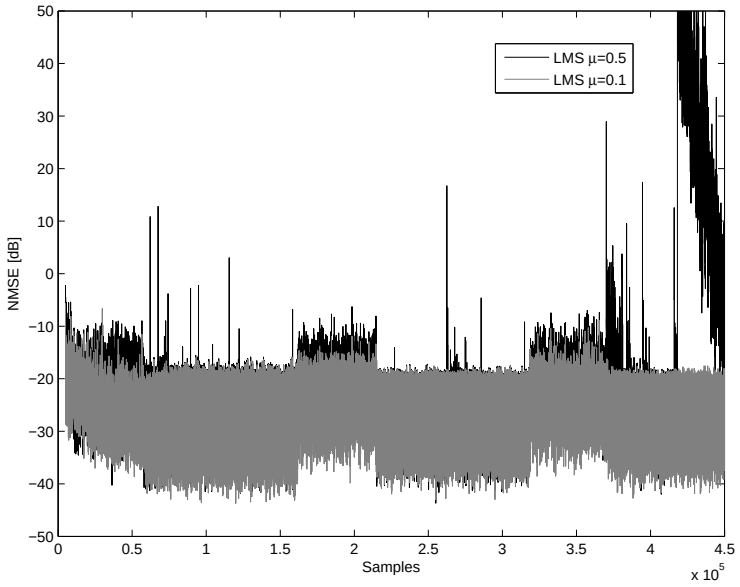

Fig. 4.43: NMSE for the LMS algorithm with different μ calculated on signal denoted as MUX3. The value $\mu = 0.5$ is chosen intentionally for demonstrating the temporal divergence of the solution due to variation in the signal.

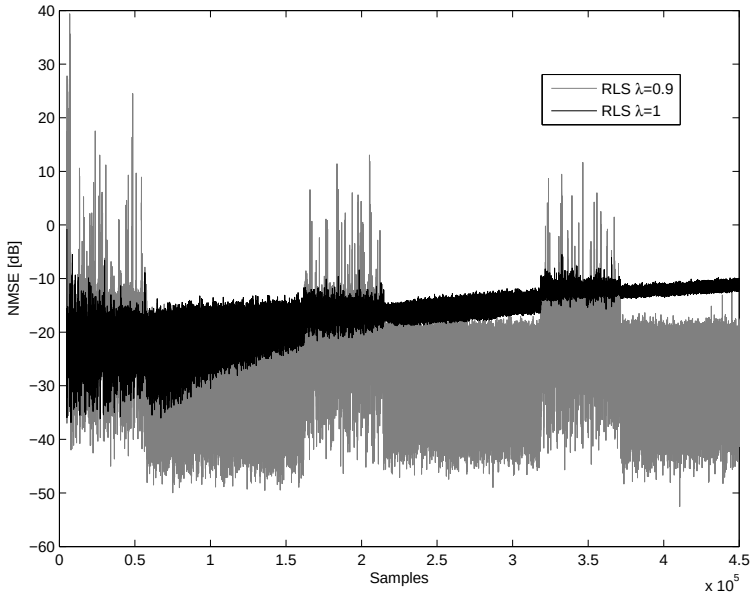

Fig. 4.44: NMSE for the RLS algorithm with different λ calculated on signal denoted as MUX3.

4.7 Fractional Least Mean Square Algorithm

In this section we would like to propose an adaptive method suitable for solving the convex linear problems. The most popular and simplest adaptive algorithm is the LMS, however the LMS shows some serious problems such as slow convergence

rate and delay in identification of unknown systems. The Fractional Least Mean Square algorithm (FLMS) algorithm has capability to outperform the LMS. The FLMS was already proposed for solving convex linear problems, but was not used for calculating DPDs or PA models. The FLMS is an algorithm, which is based on the concept of fractional order calculus. Usage of Riemann-Liouville differential operator is closely described in Part II.

Let us define a line vector $\mathbf{\Phi}(t)$ as:

$$\mathbf{\Phi}(n) \quad = \quad [\Phi_{1,0}(x(n)), ..., \Phi_{K,Q}(x(n))], \tag{4.1}$$

with (for example using PMS):

$$\Phi_{k,q}(x(n)) \quad = \quad |x(n-q)|^{k-1}x(n-q). \tag{4.2}$$

The cost function $\mathbf{J}$ for the error e is given by:

$$J(n) = E[e(n)e^*(n)] = \sum_{n=0}^{N} |e(n)|^2. \tag{4.3}$$

Where the calculation of vector $\mathbf{b}$ for FLMS is defined as

$$\mathbf{b}(n+1) = \mathbf{b}(n) - \mu_1 \frac{\partial J(n)}{\partial \mathbf{b}(n)} - \mu_2 \frac{\partial^v J(n)}{\partial^v \mathbf{b}(n)}. \tag{4.4}$$

By taking the fractional derivative using Riemann-Liouville differential operator of order v we get:

$$\frac{\partial^v J(n)}{\partial^v \mathbf{b}(n)} = \mu_2 e \mathbf{\Phi}^H(n) \frac{\mathbf{b}^{(1-v)}(n)}{\Gamma(2-v)}. \tag{4.5}$$

Therefore the iterative FLMS solution of row vector $\mathbf{b}$ can be expressed as:

$$\mathbf{b}(n+1) = \mathbf{b}(n) + \mu_1 e \ \mathbf{\Phi}^H(n) + \mu_2 e \ \mathbf{\Phi}^H(n) \frac{\mathbf{b}^{(1-v)}}{\Gamma(2-v)}, \tag{4.6}$$

where Γ is a Gamma function, v represents fractional order of the system and μ_1 and μ_2 are the convergence constants.

In the Fig.4.45 we may see the comparison in convergence speed for LMS, FLMS and RLS. The RLS does have fastest convergence speed, but also high computational complexity. The FLMS converges faster than LMS, but still has bigger error than RLS.

For the presented experimental results we have used Smart PA described in Section 4.2 with wideband OFDM signal. In order to use indirect adaptive approach,

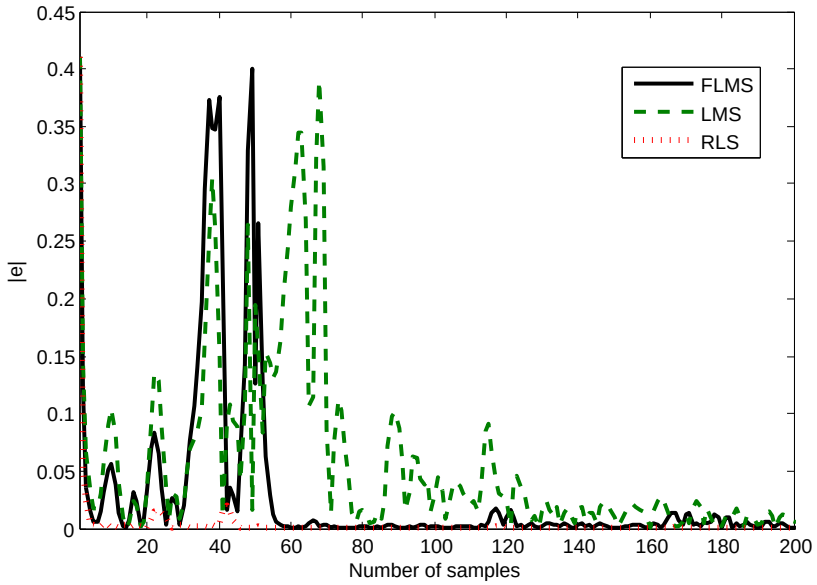

Fig. 4.45: Comparison of convergence speed for LMS, FLMS and RLS.

first we have modeled the memoryless PA with OMPS with order of nonlinearity K=5 and memory level M=0. For the presented results in Fig.4.45 we have used odd terms with maximal order of nonlinearity K=3 and memory depth M=0. As a DPD function we have used OMPS. The whole estimation was done on 5000 samples.

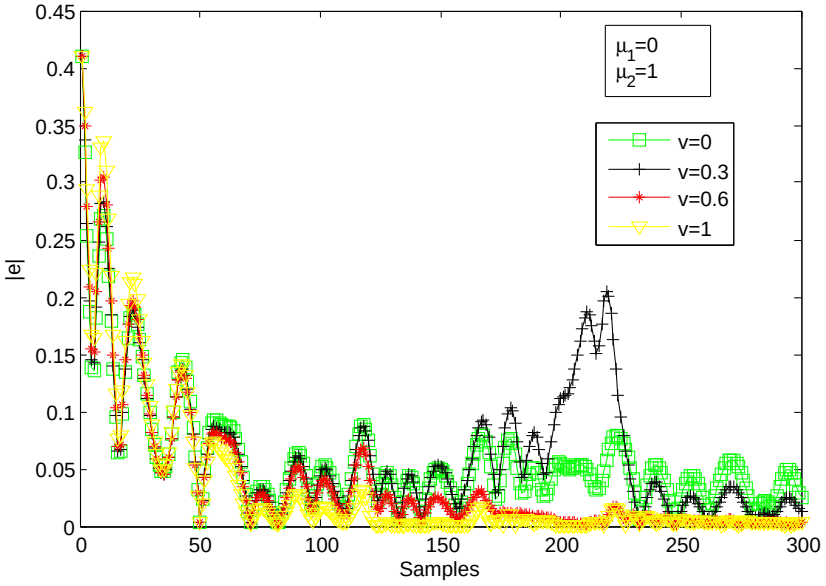

Fig. 4.46: The influence of parameter v on the error where constants are fixed as follows: $\mu_1 = 0$ and $\mu_2 = 1$.

The influence of constant v can be seen in the figure 4.46. In this figure, weight

parameter μ_1 (equivalent to LMS μ) is set to 0 and weight parameter for fractional part is: $\mu_2 = 1$.

For the FLMS the setup was: $\mu_2 = 0.5$, $\mu_2 = 0.5$ and $v = 0.8$. LMS parameters were: $\mu_2 = 0.5$ and RLS initial parameters: $\delta = 1e - 3$ and $\lambda = 1.00$.

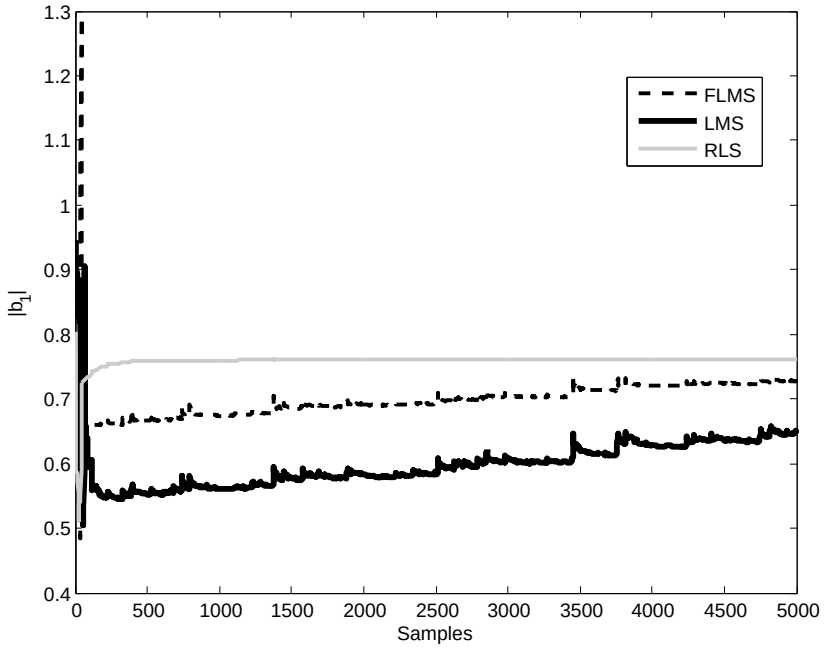

Fig. 4.47: Comparison of convergence of $|b_1|$ for LMS, FLMS and RLS.

The convergence of magnitude of first coefficient b_1 can be seen in the Fig.4.47. We may observe the fastest converge of the RLS algorithm. The second fastest algorithm is FLMS. Therefore we may say that FLMS is a certain compromise between complexity and speed of convergence.

The FLMS can converge faster than LMS, but the complexity is higher. We may see, that fractional part of the equation contributes to the calculation with depending on the fractional parameter v and on weight μ_2.

4.8 Optimal Order Estimation for Modeling and Predistortion of Power Amplifiers

We have shown in the previous sections, that modeling or linearizing the PA can be successfully done by using any of the proposed models. The coefficient estimation has been also shown. In this section we would like to focus on the determination of optimal orders of the proposed models.

In general the criteria for optimal order is performance with respect to complexity.

In the following section we will focus on OMPS and GMP models. In the case of OMPS there are two orders to estimate: order of nonlinearity and memory depth. Likewise for the GMP there are eight parameters describing the structure of models. These models can be applied for PA modeling or calculation of a predistorter as shown in Fig.4.48 with: on the left the principle of PA modeling and on the right the approach used for predistortion called indirect learning approach.

In the case of DPD, we consider a normalization gain G [53]. Let us denote by $u(t)$ the complex input of a nonlinear system and by $z(t)$ the corresponding complex output visualized in Fig.4.48.

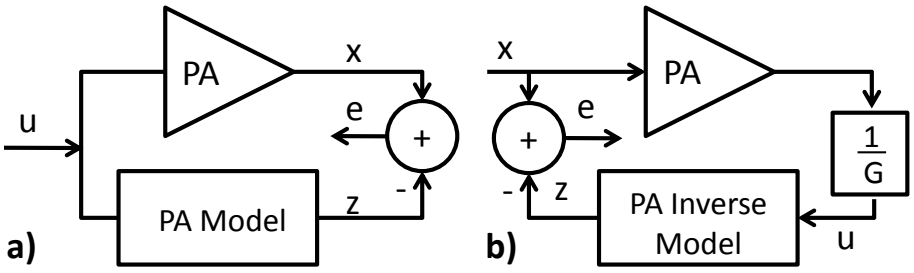

Fig. 4.48: Schematic of minimizing problem between measured and modeled signals. Left denoted as a) is PA modeling and right b) is postdistortion.

4.8.1 Determination of model structure

The determination of model structure consists in finding the right orders of the model such as non-linearity orders and memory orders. The model structure can be determined by an exhaustive search consisting in testing all the possible order values up to a fixed maximum and selecting the structure that leads to a good model accuracy (small value of criterion J) while keeping a reasonable complexity. Simply

setting the orders of the structure high enough to guarantee good performance is not sufficient, because in addition to high complexity it can also be connected with numerical instability.

This exhaustive search may be acceptable for models with a small number of orders, e.g. PMS model that has only 2 parameters K and M, but it becomes very fastidious for models with a greater number of orders.

In the case of PMS, setting K from 1 to 17 and M from 1 to 5, the exhaustive search represents only 85 tests (each one requiring to solve of a system of linear equations (6)). But in the case of GMP model, there are 8 orders to determine. Setting all orders for GMP from 1 to 10 it would represent 10^8 search operations. Therefore we propose to apply stochastic integer genetic algorithm in order to determine model structures.

4.8.2 Integer Genetic Algorithm

Genetic algorithm (GA) is a heuristic search often used in artificial intelligence, that copy the process of natural evolution. It is based on the idea of evolution theory that individuals having a high value of quality will survive to the next generation with greater probability [54].

To perform the integer optimization we have used standard GA with functions for generating integer population and integer mutations. Basically we are trying to obtain a vector of integer numbers representing the structure of model based on fitness function defined later.

The algorithm selects a group of individuals, called parents, in the current population that is at the beginning generated as random vectors of integer numbers.

The fundamental approach of operations made during basic operations can be seen in Fig.4.49. We may describe each operation as follows:

Selection: identifies statistically the best individuals (based on fitness function described later) of a population and eliminate the unsatisfactory [54] (for example in the Fig.4.49 is Individual 3 unsatisfactory). It generates parents for further processing. The next step is to create two types of children for the next generation,

The applied GA algorithm is described by:

generation=1;
Generate initial random integer population **P** made of individuals **I**;
while *generation* $\leq$ *max generations* **do**
    Evaluate the fitness function for all individuals;
    for *i=1 with step 2 to population size (Create new population)* **do**
        Selection (Find the best individuals);
        Crossover;
        Integer Mutation;
    end
    generation=generation+1;
    if *One of the stopping criterie == TRUE* **then**
        Stop optimization;
    end
end

Algorithm 1: Overview of simplified genetic algorithm

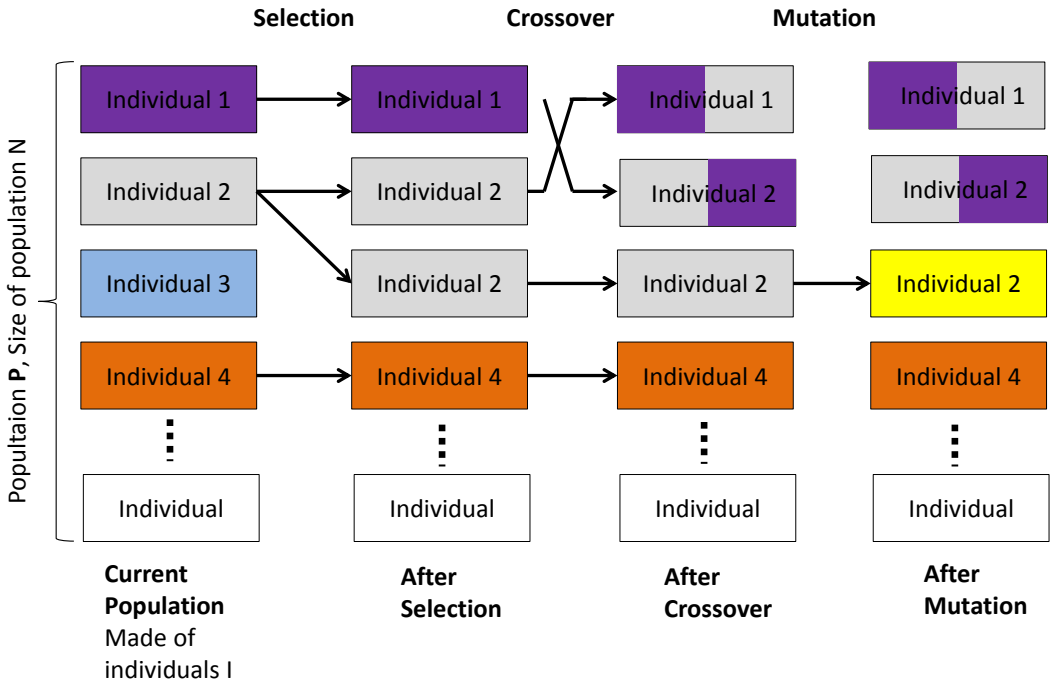

Fig. 4.49: The basic GA operations: One generation (current population) recalculated using a selection, crossover and mutation to new set of individuals.

where mutation is done after crossover just with certain probability.

Crossover: is a process of taking two parent solutions and producing offspring.

Basically we can represent parents by binary numbers, subdividing them into the groups and combine them with each other. Note that it is necessary to obtain as a result integer set. Because we use integer set we have two options. We may use the binary approach, or we may use round function after crossover.

Mutation: is analogous to biological mutation. Mutation alters one or more gene values in a chromosome (binary representation). We have to ensure the mutation will be integer.

The algorithm uses a several stopping criteria (maximal number of generations achieved, fitness function is met, etc.). Among them we have also added stall criteria: when the fitness function varies less than tolerance for certain number of generations, the criteria is used.

Where $\mathbf{P}$ is a matrix of individuals representing the structure of DPD. The initial population is usually generated by random estimate or can be set from previous fast estimation.

4.8.3 Fitness functions

We have defined a fitness function with the aim to achieve a compromize between accuracy and complexity of the model.

To evaluate the accuracy of the model, we use normalized mean square error (NMSE) in decibels. For two signals $\mathbf{x}$ and $\mathbf{z}$, the NMSE is defined as:

$$NMSE(\mathbf{x}, \mathbf{z})[dB] = 10 \log \left(\frac{(\mathbf{x} - \mathbf{z})^H (\mathbf{x} - \mathbf{z})}{\mathbf{x}^H \mathbf{x}} \right). \tag{4.7}$$

Instead of NMSE, we can employ adjacent channel power ratio (ACPRs) to improve performance in out-band spectral area or EVM to improve modulation properties, or combination of both.

To evaluate the complexity of the model, we simply used the total number of coefficients L. We are aware that it is not a perfect measure of the complexity, but the higher the number of coefficients is, the more complex the model is. We defined the fitness function as a weighted combination of these two criteria as follows:

$$f(\mathbf{I}, L) = NMSE + \alpha \; L, \tag{4.8}$$

where **I** is an integer vector of parameters determining the structure of model. Parameter L is number of coefficients used in structure. A α is a balance of the solution by complexity.

We are aware of existence of the Akaike information criterion [55], but we believe that we will obtain similar results.

4.8.4 Results

In order to evaluate the proposed method for predistortion we used data from amplifier A2 operating from 460 MHz to 860 MHz described in the Section 4.2. First we do the exhaustive search for PMS model structure (K and M). From Fig.4.50, we see that a good compromise between performance and complexity is obtained with $K = 8$ and $M = 2$. this result will be used as a reference to evaluate the genetic algorithm.

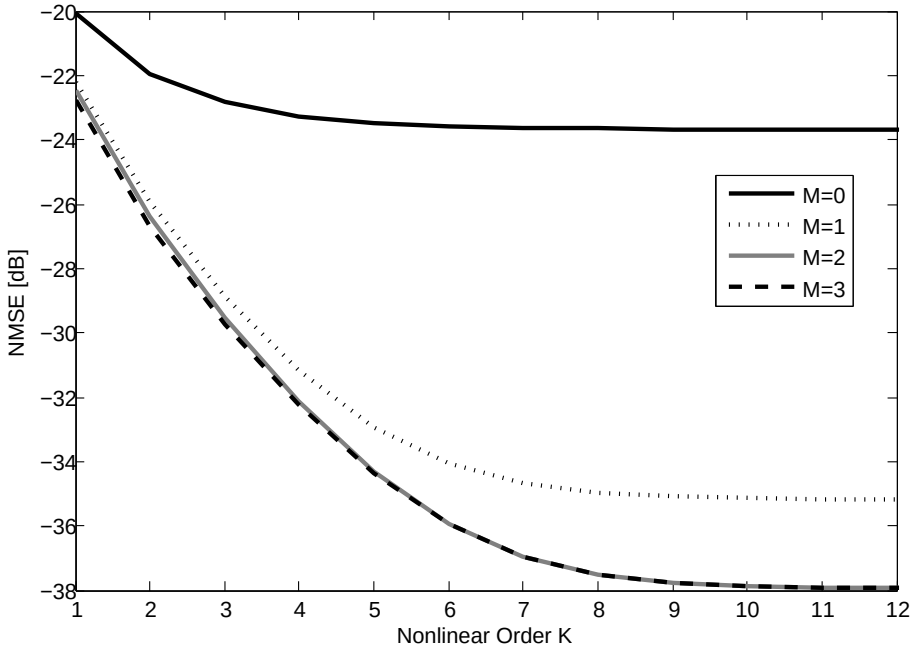

Fig. 4.50: Exhaustive search of the parameter space for K and M for PMS.

We have executed the GA algorithm with different values of the ponderation coefficient α. In Fig.4.51 we show the influence of α on the obtained NMSEs (left axis) and number of coefficients (right axis) after convergence of the GA algorithm. We can observe that value of α is not highly sensitive. For our algorithm we set

$\alpha = 0.2$ according to Fig.4.51, where the number of coefficients for PMS start to rise.

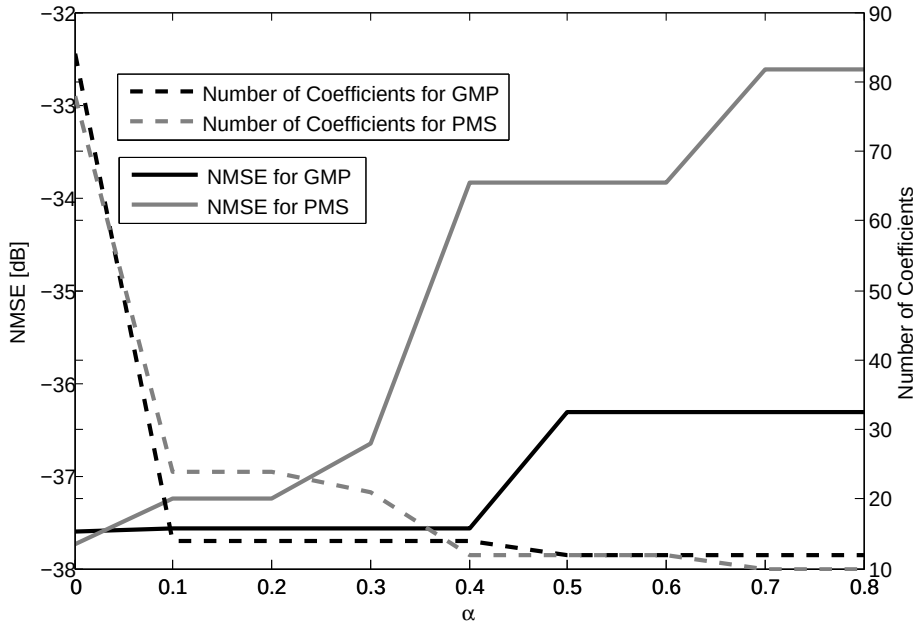

Fig. 4.51: NMSE dependency of GMP and PMS and corresponding number of coefficients for different values of α.

For the genetic algorithm the parameters were: number of generations 100, and population size of 20 individuals, stall condition : 40 generations. The upper boundary condition was set to $K = 13$ and $M = 8$ for PMS model and to $K_a = 7, L_a = 3, K_b = 3, L_b = 3, M_b = 5, K_c = 3, L_c = 3, M_c = 5$ for GMP model. For PMS model, the genetic optimization results are $K = 8$ and $M = 2$ that represents 24 coefficients and $NMSE = -37.25dB$. These results correspond to the reference derived from Fig.4.50.

For the same setup of genetic algorithm for GMP we found $K_a = 7, L_a = 2, K_b = 2, L_b = 0, M_b = 2, K_c = 2, L_c = 0, M_c = 0$ with $NMSE = -37.56dB$. That represents overall 14 coefficients. From Fig.4.51 we can see, that GMP is a very interesting model maintaining low complexity with good performance. Its drawback is determining the model structure, but it can be solved thanks to proposed GA algorithm.

Fig.4.52 shows the different power spectral densities of the PA output without predistortion and with PMS and GMP model predistortion.

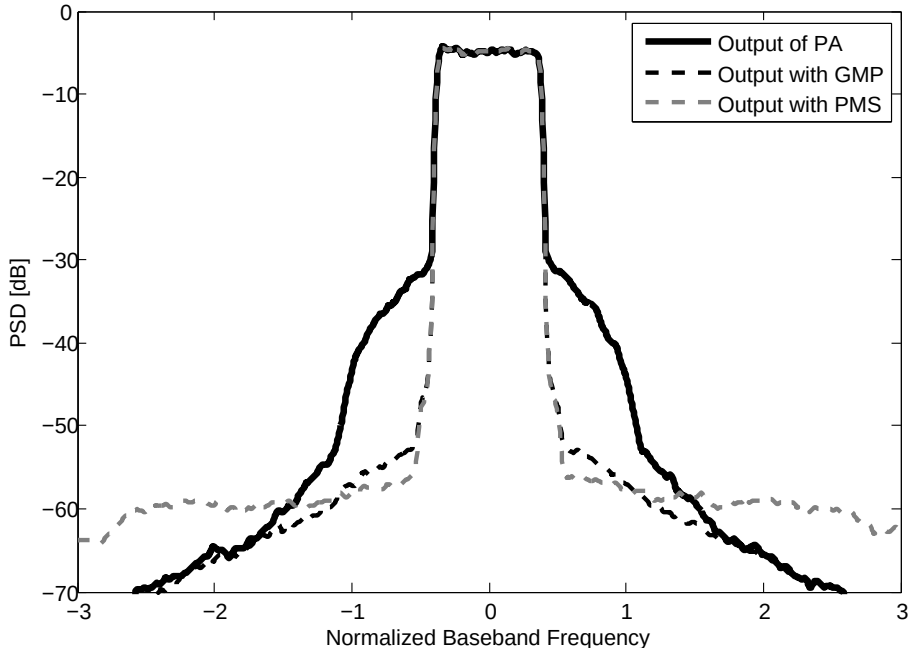

Fig. 4.52: Overall power spectrum density where for PMS $K = 8$ and $M = 2$ and for GMP $K_a = 7, L_a = 2, K_b = 2, L_b = 0, M_b = 2, K_c = 2, L_c = 0, M_c = 0$ and for $\alpha = 0.2$.

4.8.5 Conclusion on Optimal Order Estimation

In this section we have proposed an integer genetic algorithm and a fitness function for automatic estimation of model structure for different modeling and predistortion series.

The fitness function achieves a compromise between complexity and performance. It is known, that genetic algorithms can be easily implemented to several systems such as FPGAs [56]. The results were compared with exhaustive search. In the case of GMP with presented configuration exhaustive search represents 42525 evaluations of fitness function, the GA only 2000 respectively.

The method has proved to find close to optimal solutions in reasonable amount of time both for memory polynomial models and generalized memory polynomial models.

4.9 Neural Network DPD and PA modeling

In this section we would like to briefly present results obtained by different approaches. In the first section we present baseband DPD that uses two separated networks.

In the next subsection we present possible realization of predistortion with implemented memory compensation.

4.9.1 Two Networks Baseband Approach

There exists a possible memoryless models of neural network baseband predistortion. The input is divided into real and imaginary parts. Therefore we use two separated neural networks. Thus the correction is made for each branch separately.

The complex baseband signal at the output $y(t)$ of PA is divided to real and imaginary parts. Then it is compared with real and imaginary part of complex baseband PA input signal. The instantaneous errors of each branch control the calculation of weights separately.

A possible improvement is presented in the Fig.4.53. The model has a memory effect compensation.

The neural networks are popular because of their simplicity. Nevertheless as we can see in the Fig.4.54 the performance in the terms of angle predistortion is not perfect. More often, the AM/AM and AM/PM correction functions affect each other, and thus an iterative approach for the calculation gives more better. Better results would be achieved using complex numbers neural networks. A feedforward neural networks with two layers was used with 8 inputs and with 20 neurons in the hidden layer.

4.9.2 Neural Network Baseband Approach With Memory

Due to separation of real and imaginary parts for the separated neural networks presented in previous section, the DPDs or PA models are not able to track mutual dependencies. Therefore we would like to present a NN (neural network) approach compensating or modeling memory effects. Let us introduce notations for DPD and

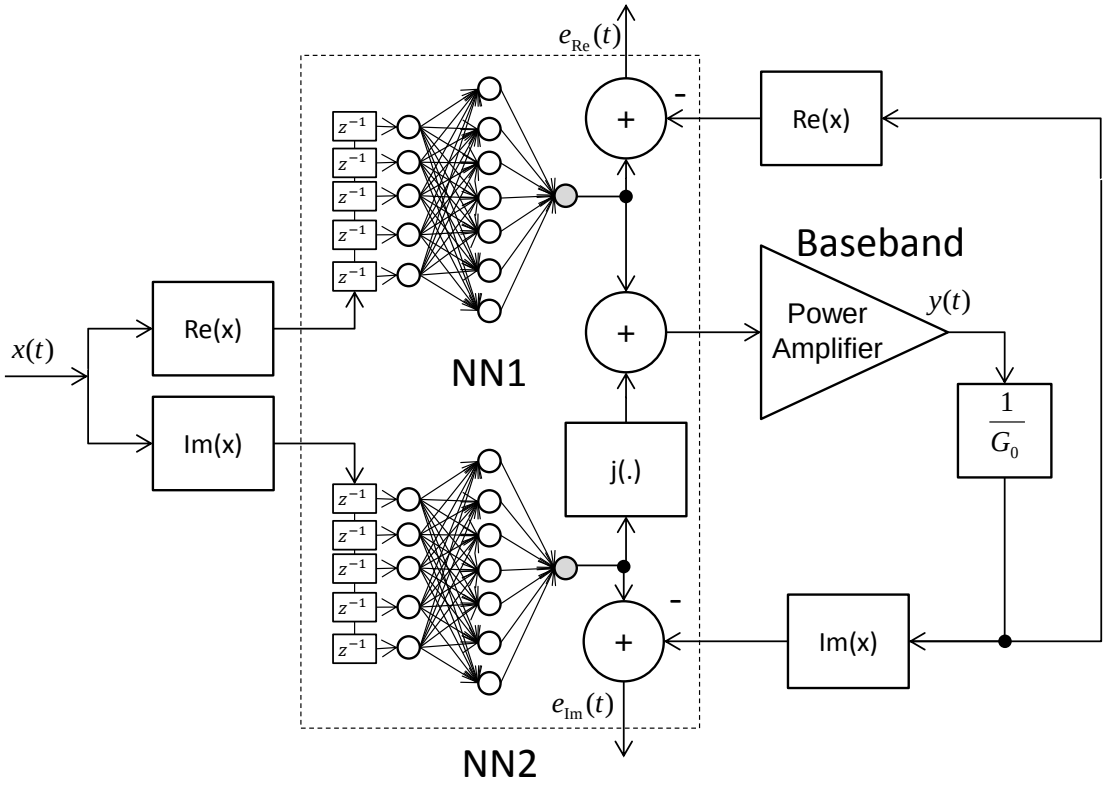

Fig. 4.53: Simulation model of memory neural network used as predistortion.

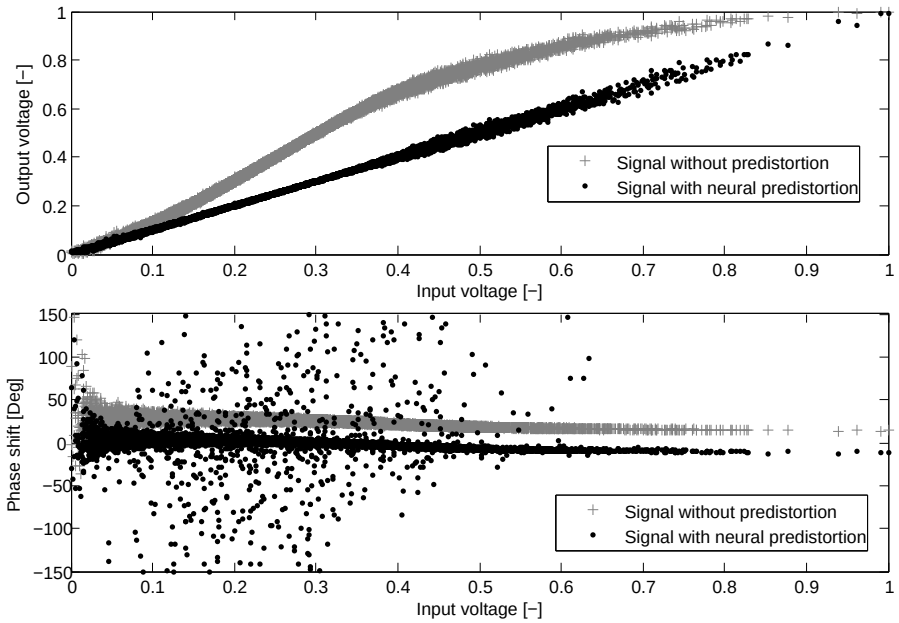

Fig. 4.54: Evaluation of predistortion with feedforward networks, 7 inputs and memory order of 3.

PA modeling as in Fig.4.55 using NN.

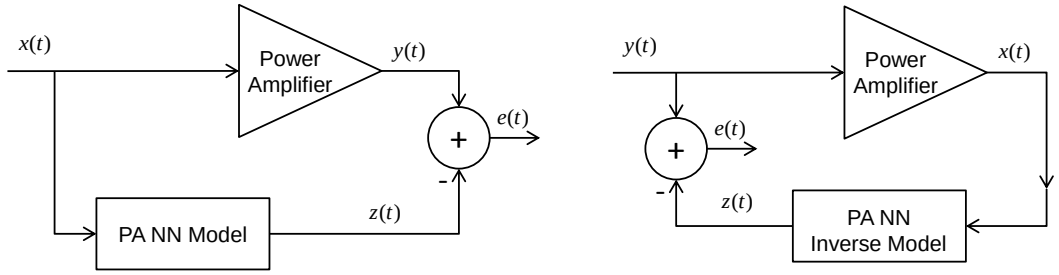

Fig. 4.55: The notations for DPD and PA modeling using neural networks (NN).

In order to introduce memory of order M to neural networks let us arrange input row vector $\mathbf{x}_{in}(t)$ of size $4(M+1)$ using complex baseband input signal $x(t)$ as follows:

$$\mathbf{x}_{in}(t) = [x(t), x(t \pm 1), \ldots, x(t \pm M)]\,. \tag{4.9}$$

Because the NNs are not primarily designed to operate with complex numbers, let us arrange input column vector of neural network of size $2(M+1)$ as:

$$\mathbf{x}(t) = [\mathrm{Re}(\mathbf{x}_{in}(t)), \mathrm{Im}(\mathbf{x}_{in}(t))]^T\,. \tag{4.10}$$

Similarly we arrange vector $\mathbf{y}(t)$ of size 2×1 as follows:

$$\mathbf{y}(t) = [\mathrm{Re}(y(t)), \mathrm{Im}(y(t))]^T\,. \tag{4.11}$$

Denoting the complex output of neural network $z(t)$ we minimize error:

$$e(t) = z(t) - y(t), \tag{4.12}$$

where assuming the NN has two outputs $z_1(t)$ and $z_2(t)$:

$$z(t) = z_1(t) + j\ z_2(t) \tag{4.13}$$

and $y(t)$ is a complex baseband signal.

The principle schematic of the proposed neural network (feedforward network) is given in the Fig.4.56. For designing the feedforward neural network we have used build-in MATLAB toolbox. For training the network Levenberg-Marquardt algorithm was used.

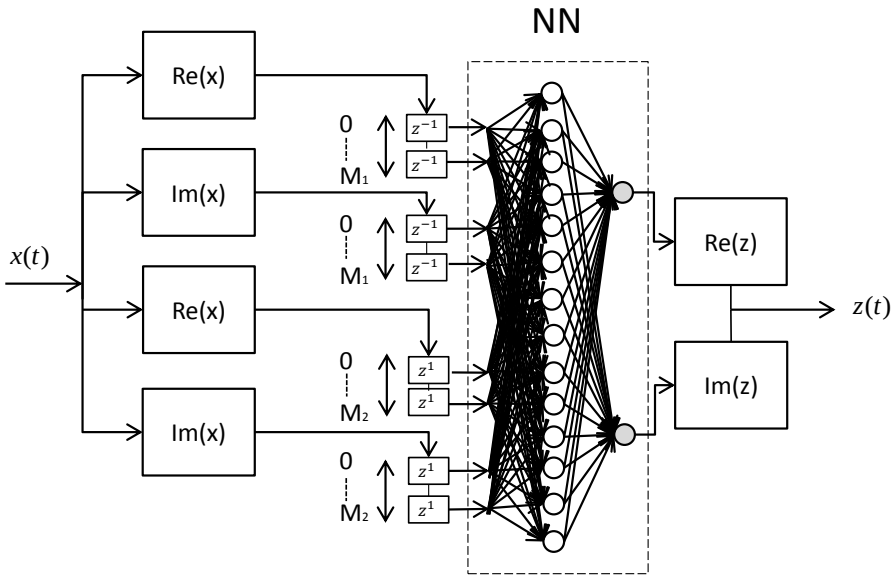

Fig. 4.56: Principle of memory feedforward neural network with: $2(M_1+1)+2(M_2+1)$ inputs, 14 neurons in hidden layer and two output neurons.

In order to test the proposed solution we have used TeamCast power amplifier data with average output power 75W and with OFDM input signal of PA.

The comparison of performances for modeling of the PA with different network configurations are presented in Table4.12 and in Table4.13.

Tab. 4.12: Table of results modeling the PA a using single neural network with 10 neurons in hidden layer.

Memory order	**Number of hidden layers**	**NMSE [dB]**
1	1	-28.11
2	1	-28.45
3	1	-28.42
5	1	-28.33
10	1	-28.15
2,-2	1	-28.41
10,-10	1	-28.00

The results using neural network as predistortion can be seen in Fig.4.57.

In order to test the DPD, the network was modified according to Fig.4.55. Re-

Tab. 4.13: Table of results for PA modeling using a single neural network with memory order 2 and with two hidden layers.

Neurons in hidden layer 1	Neurons in hidden layer 2	NMSE [dB]
1	0	-3.11
2	0	-24.58
5	0	-26.99
10	0	-28.33
50	0	-28.52
5	2	-27.45
5	5	-28.34
10	2	-28.44
10	10	-28.50

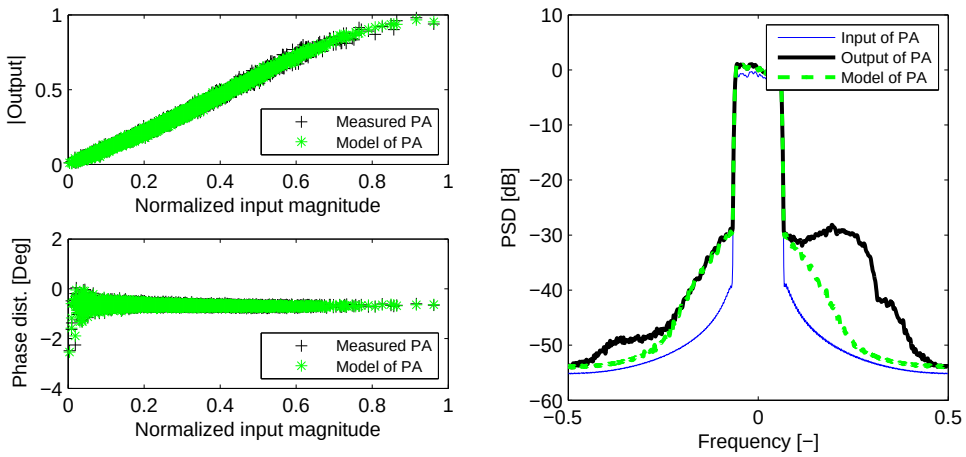

Fig. 4.57: Model of amplifier A1 (75W) using single neural network with one hidden layer with 10 neurons, memory order 10 and the NMSE=-28.34 dB.

sults estimated with this DPD can be found in Table.4.14. For the DPD a single network with one hidden layer with 10 neurons was used.

The linearization of amplifier A (75W) by single neural network with 10 hidden neurons and with memory depth 10 can be seen in the Fig.4.58. The error between the input and the linearized output is NMSE=-33.08 dB.

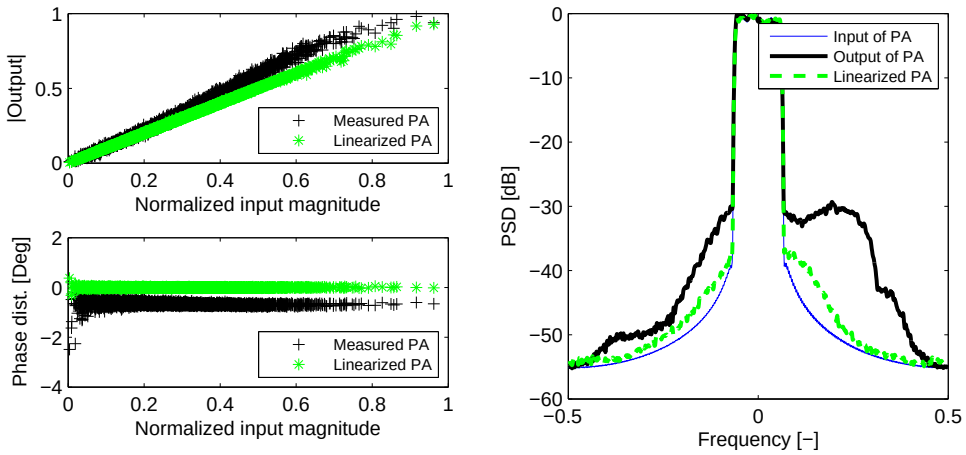

Fig. 4.58: Linearization of amplifier A1 (75W) using single neural network with one hidden layer with 10 neurons, memory order 10, -10 and the NMSE=-37.61 dB.

Tab. 4.14: Table of results for DPD using a single neural network with 10 neurons in hidden layer.

Memory order	**Number of hidden layers**	**NMSE [dB]**
1	1	-27.29
2	1	-29.00
3	1	-31.09
5	1	-31.71
10	1	-32.20
10,-10	1	-37.61

4.10 Conclusion

First we have introduced several signals used for measuring and simulating the PAs. Then we discuss the modeling and linearization techniques in terms of performance and number of coefficients.

Then have compared capabilities of adaptive algorithms. In terms of adaptiveness the RLS has the best performance (that can be compared with DNA). In terms of complexity, LS and DNA are good choices.

We have proposed and analysed a new adaptive algorithm called fractional LMS that take advantage of fractional order derivatives. The performance is better than LMS (speed of convergence) and complexity is lower than RLS.

The next section present optimal estimation of model structure. In the case of GMP, eight parameters needs to be estimated. Therefore we propose an integer genetic algorithm, that is able to find good structure compromising between complexity and performance.

In the last section we present results using neural networks for predistortion and modeling. In terms of performance, the NNs are good. In some situation are even better than Volterra derived models, but their adaptiveness is limited.

5 INFLUENCE OF DELAY MISMATCH ON DIGITAL PREDISTORTION FOR POWER AMPLIFIERS

In this chapter we would like to evaluate influence of delay, inserted in the return path, on the precision of estimation of coefficients. Hence, evaluate the performance od DPD when delay is inserted in the feedback path [128].

Fig. 5.1 shows an adaptive baseband digital predistorter. In order to follow the time evolution of the PA as a function of temperature, for example, the DPD may be updated periodically. To do this, a return channel is introduced which takes a part of the PA output signal thanks to a coupler. Signal is frequency down-converted and digitized. This result in a baseband signal that is an image of the PA output, that can be used to update the DPD. But first it has to be synchronized with $x(t)$ or $z(t)$ since the delay introduced by the components in the direct and return path is unknown.

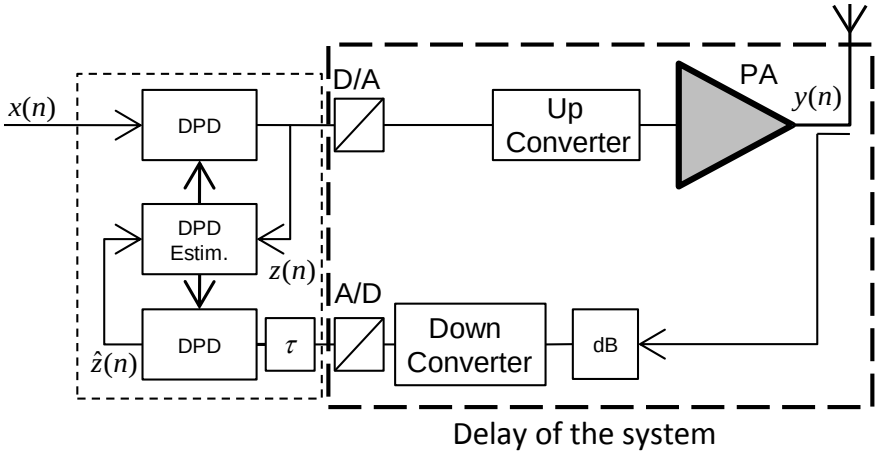

Fig. 5.1: Digital predistortion principal layout with inserted delay.

The estimation of the time offset between two signals is usually done by correlation, the precision obtained is on the order of a sample. The question is whether to refine the precision for a fraction of samples or to use different techniques to compensate for this delay by fractional resampling or interpolation by methods such as Farrow filters described for example in [57], [58] and [59].

5.1 Upper Limit of Power Error Due to a Time Shift

The error $e(t)$ due to a time lag τ of a signal $z(t)$ can be written as:

$$e(t) = z(t) - z(t-\tau). \tag{5.1}$$

Assuming the lag τ small and using limited development of order of 1, we can write:

$$e(t) = z(t) - z(t-\tau) \approx z(t) - z(t) + \tau z'(t) = \tau z'(t). \tag{5.2}$$

With this approximation, we can calculate an upper bound of the average power of the error:

$$E\left(\left|e^2(t)\right|\right) \approx E\left(\tau^2 \left|z'(t)\right|^2\right) = \tau^2 E\left(\left|z'(t)\right|^2\right), \tag{5.3}$$

$$E\left(\left|e^2(t)\right|\right) \approx \tau^2 \int_{-\infty}^{+\infty} S_{z'}(f)df = 4\pi^2\tau^2 \int_{-\infty}^{+\infty} f^2 S_z(f)df, \tag{5.4}$$

$$E\left(\left|e^2(t)\right|\right) \leq 4\pi^2\tau^2 max\left(S_z(f)\right)\frac{2B^3}{3}. \tag{5.5}$$

Where B is the bandwidth of the baseband signal $z(t)$, $S_z(f)$,$S_{z'}(f)$ respectively are the power spectral densities of the signal and of its derivative. Similarly, we can write:

$$E\left(\left|z^2(t)\right|\right) = \int_{-B}^{+B} S_z(f)df = 2Bmean\left(S_z(f)\right). \tag{5.6}$$

Where $mean\left(S_z(f)\right)$ represents the mean value of the power spectral density of $z(t)$. Therefore we can deduce the boundary for normalized mean square error between the signal and the same signal delayed by τ:

$$NMSE = \frac{E\left(\left|z(t) - z(t-\tau)\right|^2\right)}{\left|z(t)\right|^2} \leq \frac{4\pi^2}{3}\frac{max\left(S_z(f)\right)}{mean\left(S_z(f)\right)}B^2\tau^2. \tag{5.7}$$

And when the power spectral density is nearly a constant over the entire band of the signal (for an OFDM signal for example) we obtain:

$$NMSE \leq \frac{4\pi^2}{3}B^2\tau^2. \tag{5.8}$$

For a given time lag, the NMSE deteriorates especially as the bandwidth is large. So for a DVB-T signal with B = 4MHz, an oversampling factor equal to 8 and a delay equal to $Ts/2$ the NMSE is not better than only -18dB.

5.2 Used Methodology

To evaluate the influence of a time lag on the performance of the predistorter, we introduced misalignments τ at the output of PA. Then we used signals with misalignment $y(t \pm \tau)$ for the calculation of the DPD coefficints.

For the DPD, we have used OMPS models defined in equation (3.36) and GMP models presented in equation (3.40).

For the performance evaluation we used normalized mean square error (NMSE) between the output of the cascade: misalignment τ + DPD + PA and the original signal. The principle of estimation can be seen in Fig.5.2 - on the right.

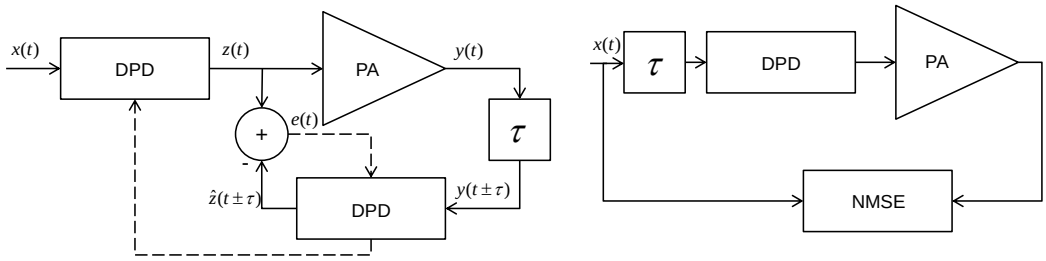

Fig. 5.2: Left: introducing the time misalignment τ at the output of PA and calculation of DPD. Right: Calculation of NMSE, where DPD has coefficients estimated on the left schematics.

Note that in order to obtain fair error, we need to introduce misalignment before the DPD, because the DPD is trained on misaligned sequence and compensate the misalignment. As presented in the Fig.5.3 the NMSE performance calculated on the same signal with its delay copy ($NMSE[x(t), x(t \pm \tau)]$) degrades, therefore we have calculated the NMSE as on Fig.5.2.

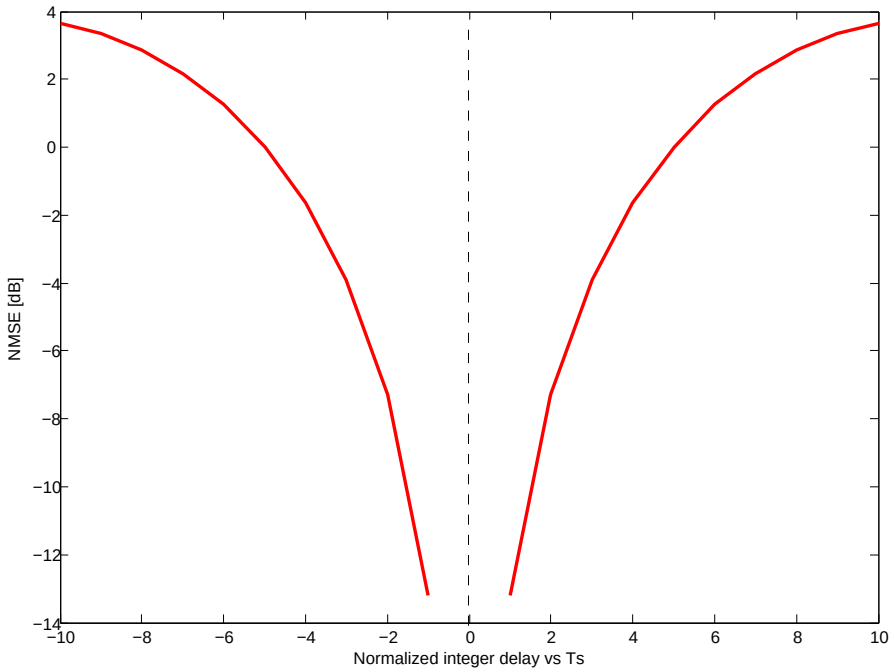

Fig. 5.3: NMSE of input signal and its integer time shifted copy.

5.3 Experimental Results

We present results measured on Doherty amplifier UHF NXP LDMOS using BLF888A transistor (75W) The more detailed description is in the Section 4.2. The amplifier has been modeled with orthogonal polynomials with nonlinearity order K = 7 and a memory depth M = 2 (the choice of structure corresponds to optimal values).

We present here the results for a DPD with the order of non-linearity $K = 7$ and a memory depth of M in the range: $0 \leq M \leq 10$.

5.3.1 Influence of Integer Misalignment

we have tested the influence of temporal integer misalignment evaluated in terms of NMSE for the signals $z(t)$ and $\hat{z}(t \pm \tau)$.

We see Fig.5.4 the influence of a time offset in the range $[-10T_s, 10T_s]$ where T_s is a sampling period and positive values are corresponding to a time advance. The model used for DPD is a polynomial memory orthogonal model. We set K = 7 and varies the memory M between 0 and 10. In the example discussed here, for the absence of time shift a memory of order M=2 is sufficient enough to linearize the PA.

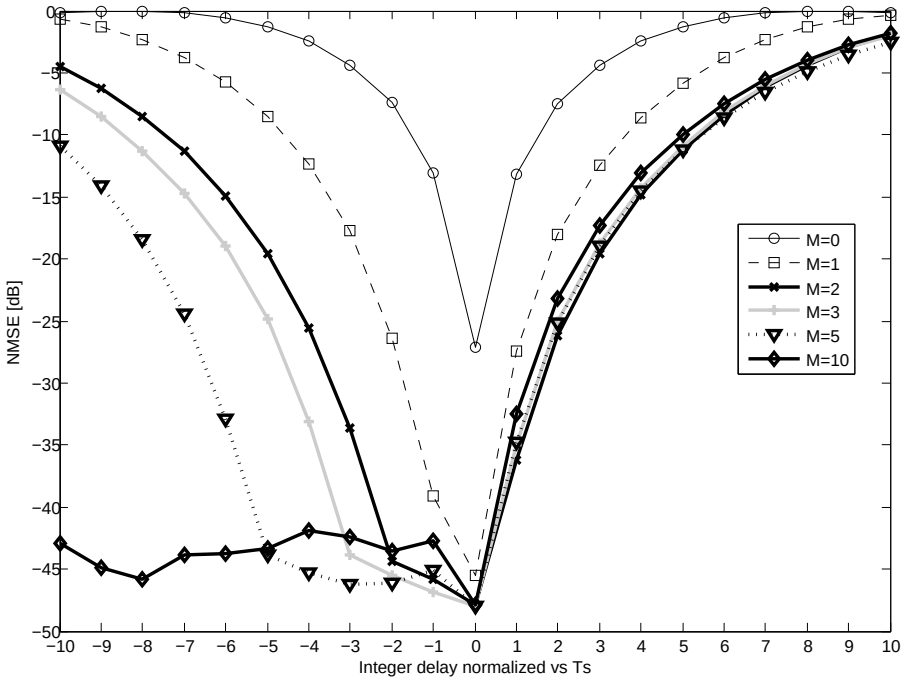

Fig. 5.4: Effect of integer delay for different memory length of the DPD with OMPS.

We can observe that DPD with polynomial memory is able to compensate for both non-linearities and delay of an integer number of samples or if that delay is smaler than its memory depth. For example, for $M = 5$ and $|\tau| \leq 5Ts$, the NMSE is degraded less than 4dB. DPD compensates at least partially. But for the $|\tau| \geq 5Ts$ DPD can no longer compensate for the delay and NMSE degrades very rapidly over 20dB (for $7Ts$). We can observe in Fig.5.4 that DPD can not compensate for advances.

Fig.5.5 shows the same analysis in the case of a DPD using the GMP model. We have denoted the memory depth M (where the parameters are: $L_a = L_b = L_c = M_b = M_c = M$). It is observed that the GMP model behaves as polynomials memory: it tends to compensate for non-linearities and delays that have a shorter length than its memory depth but also it can not compensate for advances.

5.3.2 Influence of Fractional Misalignment

We then tested the influence of a fractional time shift τ with a normalized value $\frac{\tau}{Te}$ included between -0.5 and 0.5.

Figs. 5.6 and 5.7 show the effect of the fractional shift on the NMSE. Respec-

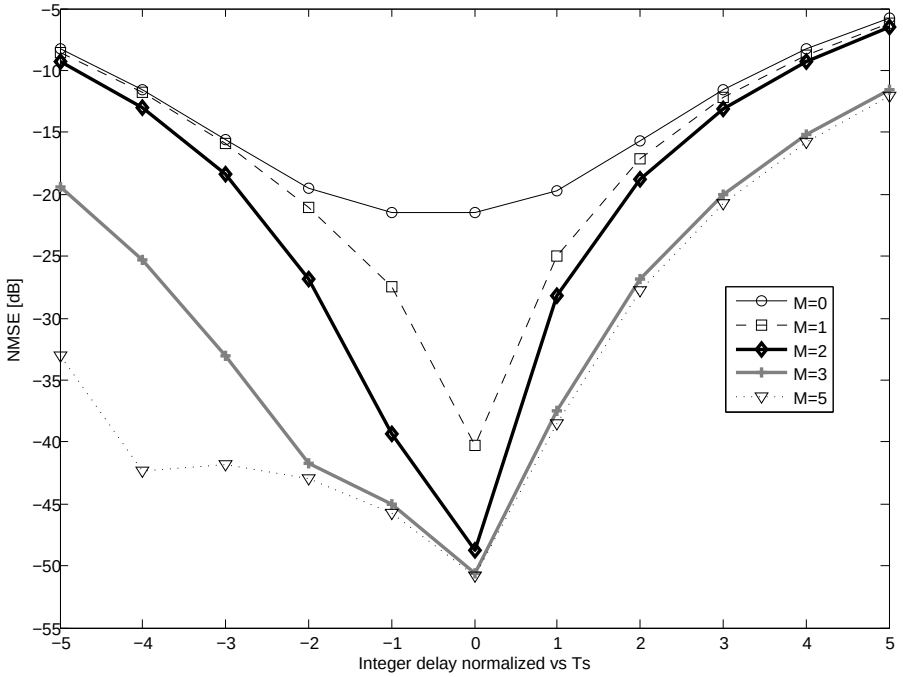

Fig. 5.5: Effect of integer delay for different memory length of the DPD with GMP, where $M = L_a = L_b = L_c = M_b = M_c$.

tively for the two models of DPD for different values of the memory depth.

We observe that the DPD for the two presented models is able to properly compensate for the fractional time shifts: delay as well as advance, as soon as the memory depth is ≥ 3. The NMSE degradation is less than 3 dB for M=3 and $|\tau|/Ts \geq 0.3$. But when $M = 1$ (or $M = L_a = L_b = L_c = M_b = M_c$), the memory depth of DPD is too low and NMSE degrades rapidly with the fractional difference, typically more than 10 dB for $|\tau|/Ts \geq 0.3$. Also note that, without time lag, the GMP DPD gives better results than the DPD with polynomial memory but in the presence of a fractional time shift the two types of DPD lead to very similar results for $M \geq 3$.

5.3.3 Influence of Misalignment using PMM

After analyzing the results of the effect of a time shift on the NMSE in the presence of a correction DPD, we found that the results are asymmetrical for the polynomials memory models and GMP.

It has been shown the that DPD is able to compensate the delay of an integer

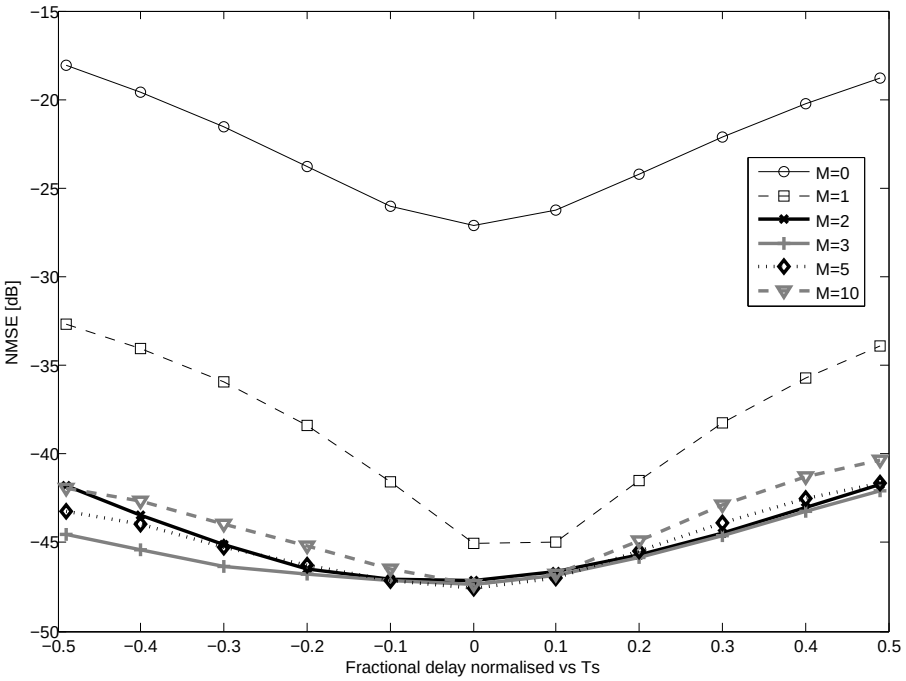

Fig. 5.6: Effect of fractional delay for different memory length of the DPD with OMPS.

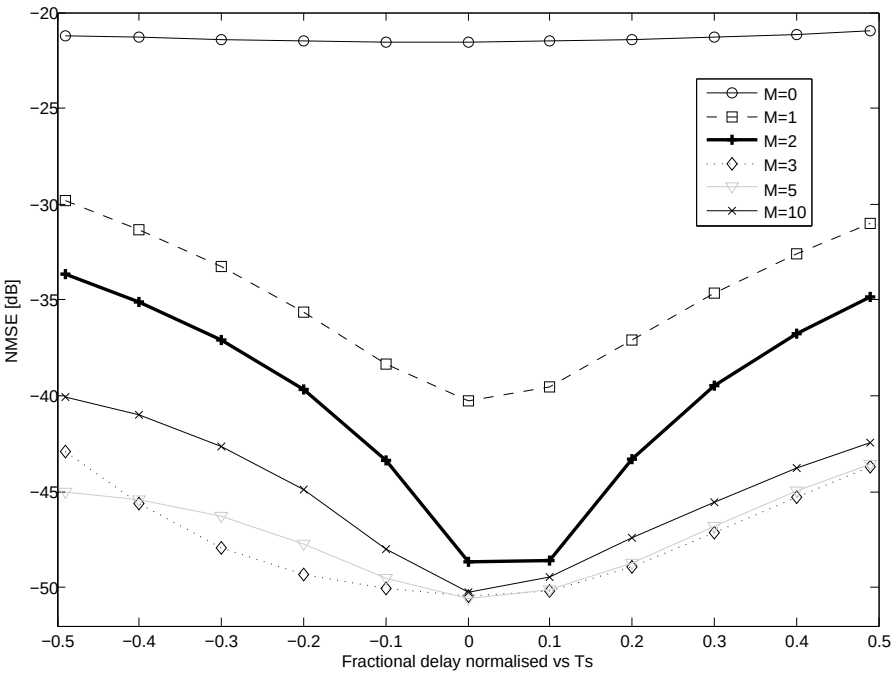

Fig. 5.7: Effect of fractional delay for different memory lengths of the DPD with GMP, where $M = L_a = L_b = L_c = M_b = M_c$.

number of samples but not an advance.

We propose a new model for the predistortion function model that we called polynomial memory modified (PMM).

We propose a new model able to compensate for delay and advance. It can be written as:

$$\begin{aligned} y(t) &= \sum_{k=0}^{K_a-1}\sum_{l=0}^{L_a-1} a_{k,l}x(t-l)|x(t-l)|^k \\ &+ \sum_{k=0}^{K_b-1}\sum_{l=0}^{L_b-1} b_{k,l}x(t+l)|x(t+l)|^k, \end{aligned} \tag{5.9}$$

where K_a, K_b is the order of non-linearity and L_a, L_b are the memory depths representing the delay and advance direction respectively.

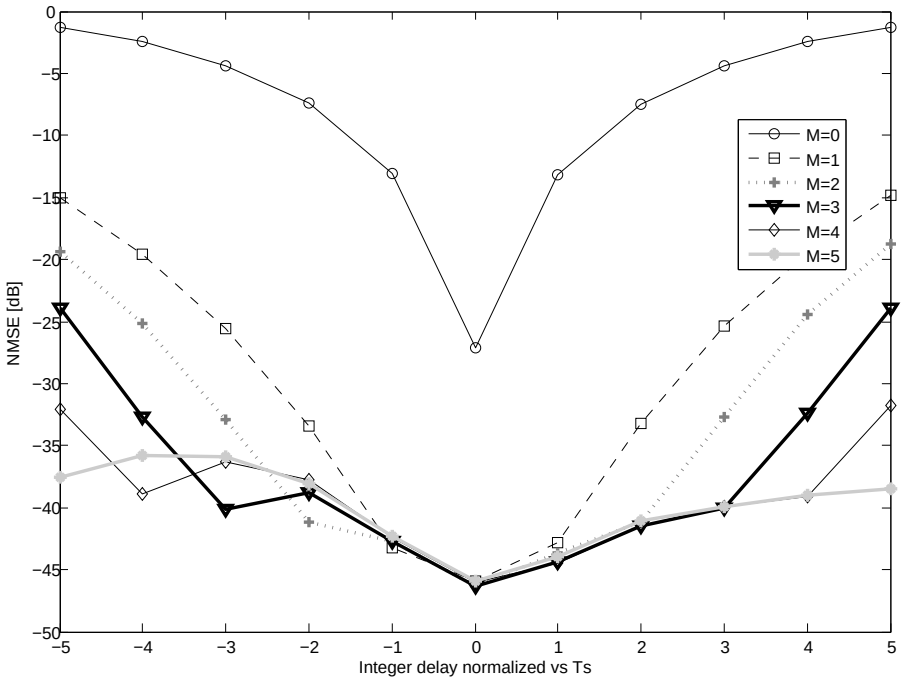

Fig. 5.8: Effect of fractional delay for different memory length of the DPD with PMM.

Fig. 5.8 shows the results obtained with the new PMM model and illustrates the effect on the NMSE of a shift equal to an integer number of samples for different values of memory. We note $L_a = L_b = M$.

Fig. 5.9 shows the results for fractional shift. It is observed that the new model is able to compensate for the delays as well as for advances when the depth of DPD

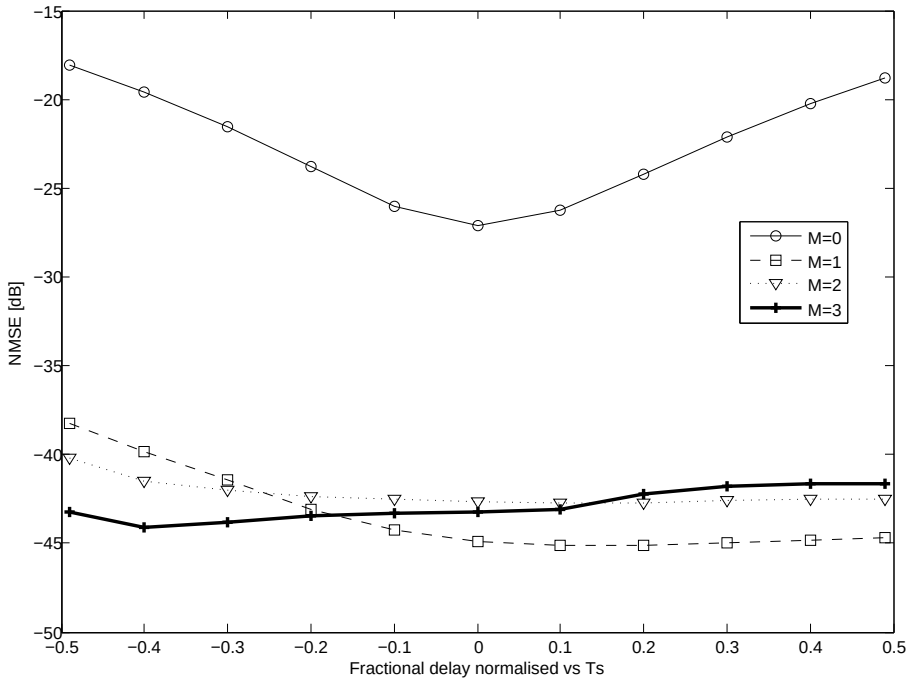

Fig. 5.9: Effect of fractional delay for different memory length of the DPD with PMM.

memory is sufficient to correct both the memory effect of the amplifier and the misalignment. This model still requires some improvements in terms of numerical robustness.

5.4 Conclusion

In this chapter we present overview of influence of misalignment in the DPD systems. The misalignment is inserted in the return path. We have evaluated the influence on the precision of estimation of coefficients. The evaluation have been done using integer and fractional misalignments. The DPDs with memory are able to compensate the misalignment well. In the case of fractional delay with memory order ≥ 3 the predistortion is able to compensate the misalignment.

In the case of integer delay the OMPS and GMP are able to compensate the same delay as is the memory order. Unfortunately they are not able to compensate the advance. Then we present new series called PMM that is able to compensate the delay and the advance.

6 ON MULTIPLE SOLUTIONS IN ADAPTIVE INDIRECT DIGITAL PREDISTORTION

Several models usually derived from Volterra series have been proposed. The most commonly used of these models have a linear dependency in respect to their coefficients. Therefore the estimation of the coefficients, in the case of a least square criterion (for the indirect learning approach), can be achieved by solving a linear system of equations. To obtain solution by least-squares criterion, usually pseudo-inversions of matrices are needed. In this section we would like to focus especially on the case of online adaptive solution (sample by sample) used in the adaptive indirect learning architectures. We would like to demonstrate the existence of multiple solutions for coefficient estimation using the simplest adaptive system and propose a criterion based on gain error instead of signal error [128].

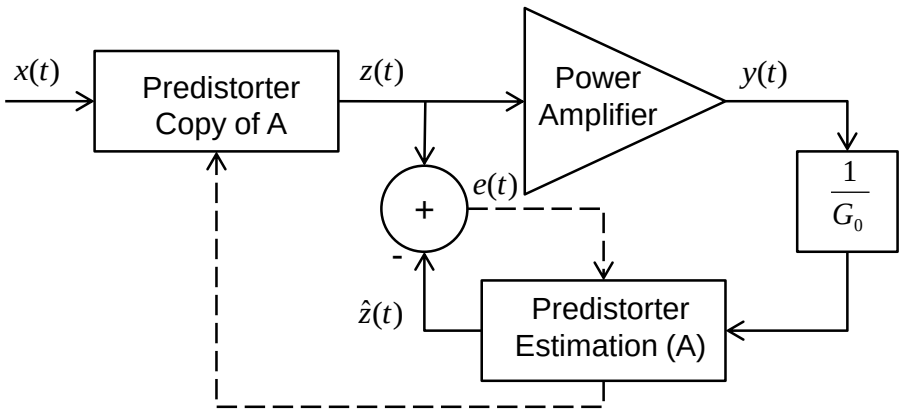

Fig. 6.1: Principal layout of the indirect learning architecture for the digital baseband predistorter.

6.1 Multiple solutions

In this section we would like to demonstrate on a simple example the existence of multiple solutions, for coefficient estimation in the adaptive systems (outlined in Fig.6.1), even for the simplest linear case of PA represented only by gain a. We use a DPD with a polynomial model defined as:

$$z(t) \;=\; \sum_{k=1}^{K} b_k |x(t)|^{k-1} x(t). \tag{6.1}$$

In this example we set order of nonlinearity to $K = 1$, which yields to:

$$z(t) \;=\; b\; x(t), \tag{6.2}$$

and as mentioned before the simple linear power amplifier is defined only by gain a as:

$$y(t) \;=\; a\; z(t), \tag{6.3}$$

where $z(t)$ is defined in discrete time t and is the complex output of the predistorter and $x(t)$ is a complex input. Constant K is the non-linear order of polynomial series and $\mathbf{b}$ is the complex coefficient vector (for this particular example is it one dimensional vector, hence it is a scalar).

Using adaptive predistortion as presented in indirect learning architecture in a loop with DPD estimation in Fig.6.1 and employing (6.2) with $K = 1$, after convergence we can directly write error criteria for least squares solution as:

$$e = z - \hat{z} = bx\left(1 - \frac{ab}{G_0}\right), \tag{6.4}$$

where G_0 stands for gain normalization. The quadratic error criteria function is defined as:

$$J = \sum_{t=1}^{N} |e(t)|^2 = \sum |x(t)|^2 |b|^2 \left|1 - \frac{ab}{G_0}\right|^2 = |b|^2 \left|1 - \frac{ab}{G_0}\right|^2 \sum |x(t)|^2. \tag{6.5}$$

Setting the first derivative of criteria function J equal to zero, we get local extrema.

$$\frac{\delta J}{\delta b} = b\left(1 - \frac{ab}{G_0}\right)\left(1 - \frac{a^* b^*}{G_0} - \frac{a^* b^*}{G_0^*}\right) \sum |x(t)|^2 = 0 \tag{6.6}$$

Solving system (6.6) we get three complex extrema located in:

$$\left\{ b_1 = 0, b_2 = \frac{G_0}{a}, b_3 = \frac{G_0^*}{2a} \right\}. \tag{6.7}$$

Where for the predistortion we cannot use solution denoted as b_1 which leads to $y(t) = 0$, even if the criteria is equal to 0. Solution denoted as b_2 is then global

minim of (6.6), that is only suitable for predistorter.

We believe that for standard solving approaches (such as adaptive algorithms for example as LMS or recursive least square approach so-called RLS) solutions obtained in (6.7) can occur, because they depend directly on criteria derivatives. The consideration above hold generally for indirect learning adaptive systems architectures and not only for polynomial series.

There also exists result b_3 that is obviously global maximum where the derivative for equation (6.6) is equal to $\frac{\delta J}{\delta b} = 0$.

6.2 Gain based solution

In this section we propose a modified error criteria resulting in solution that avoids unwanted solutions. Out error criteria is based on gain as:

$$e = 1 - \frac{\hat{z}}{z}, \tag{6.8}$$

where division by zero is undefined $z \neq 0$. After convergence ($b(n+1) \approx b(n)$) and some arrangements we get

$$e = 1 - \frac{\hat{z}}{z} = 1 - \frac{ab}{G_0}. \tag{6.9}$$

Thus the quadratic error criteria function for N samples is defined as

$$J = \sum_{t=1}^{N} |e(t)|^2 = N \left| 1 - \frac{ab}{G_0} \right|^2. \tag{6.10}$$

Derivative of the quadratic error criteria function and setting to zero we get

$$\frac{\delta J}{\delta b} = N \left(1 - \frac{ab}{G_0} \right) = 0. \tag{6.11}$$

Solving (6.11) we get one unique solution

$$\left\{ b = \frac{G_0}{a} \right\}. \tag{6.12}$$

In (6.9) we have presented simple example of modified criterion that proved to avoid the zero solution in the loop of adaptive indirect learning architecture.

6.2.1 Matrix notation

Achieving more general definition let us define polynomial series:

$$\begin{aligned} z(t) &= \sum_{k=1}^{K} b_k |x(t)|^{k-1} x(t) \\ &= \sum_{k=1}^{K} b_k \varphi_k x(t) = \Phi \mathbf{b}, \end{aligned} \tag{6.13}$$

Defined for N samples by:

$$\begin{aligned} \varphi_k(x(t)) &= |x(t)|^{k-1} x(t), \\ \mathbf{b} &= [b_{1,0}, b_{2,0}, ..., b_1, ..., b_K]^T, \\ \mathbf{\Phi}(t) &= [\varphi_1(x(t)), ..., \varphi_K(x(t))], \\ \mathbf{z} &= [z(1), z(2), ..., z(N)]^T, \\ \mathbf{U} &= [\mathbf{\Phi}(1), \mathbf{\Phi}(2), ..., \mathbf{\Phi}(K)] \end{aligned} \tag{6.14}$$

We consider the input signal $x(t)$ and output signal $y(t)$ as sequence of finite N samples, where t is a integer number and can be expressed as $t = 1, 2, ..., N$.

Then definition of the modified error criteria is:

$$e = 1 - \frac{\hat{z}}{z}, \tag{6.15}$$

where $\hat{z}$ and z are postdistorted and predistorted signals.

Defining the desired gain matrix $\mathbf{G}_D$ (when everything is normalized, the desired gain is unitary) is a vector defined as:

$$\mathbf{G}_D = \begin{pmatrix} 1 \\ \vdots \\ 1 \end{pmatrix} \tag{6.16}$$

Defining the diagonal matrix $\mathbf{D}$:

$$\mathbf{D} = \begin{pmatrix} \frac{1}{z(1)} & 0 & 0 \\ 0 & \ddots & 0 \\ 0 & 0 & \frac{1}{z(N)} \end{pmatrix}, \tag{6.17}$$

and using expression:

$$\mathbf{z} = \mathbf{U}\ \mathbf{b}, \tag{6.18}$$

we get error criteria matrix defined as:

$$\mathbf{E} = \mathbf{G}_D - \mathbf{DUb}. \tag{6.19}$$

Now we define LS quadratic error criteria function:

$$\mathbf{J} = \mathbf{E}^H\mathbf{E} = (\mathbf{G}_D^H - \mathbf{b}^H\mathbf{U}^H\mathbf{D}^H)(\mathbf{G}_D - \mathbf{DUb}), \tag{6.20}$$

Derivation of the quadratic criteria function $\mathbf{J}$ and setting to zero we get:

$$\frac{\delta\mathbf{J}}{\delta\mathbf{b}} = \mathbf{U}^H\mathbf{D}^H\mathbf{DUb} - \mathbf{U}^H\mathbf{D}^H\mathbf{G}_D = 0. \tag{6.21}$$

Then we can express matrix solution for adaptive indirect gain based system as:

$$\mathbf{b} = \left[\mathbf{U}^H\mathbf{D}^H\mathbf{DU}\right]^{-1}\mathbf{U}^H\mathbf{D}^H\mathbf{G}_D \tag{6.22}$$

To bring complete summary of our new matrix method, one can control the adaptivity by introduction of a damping. One of the well known methods is the damped Newton algorithm (DNA) which is usually compared with adaptive approach. For this purpose, the solution can be rearranged as

$$\mathbf{b}_{k+1} = \mathbf{b}_k + \mu\left[\mathbf{U}^H\mathbf{D}^H\mathbf{DU}\right]^{-1}\mathbf{U}^H\mathbf{D}^H\mathbf{E}. \tag{6.23}$$

6.3 Numerical Simulations

The complexity of higher orders of predistortion architectures is too high. To obtain analytic solutions for the problem of multiple solutions (stability points) is nearly impossible. Therefore we demonstrate such assumptions numerically. For the simulations, third order polynomial model with omitted even term of PA was used for PA modeling:

$$y(n) = a_1 z(n) + a_2 z(n)\left|z(n)\right|^2, \tag{6.24}$$

where $a_1 = 2$ and $a_2 = -0.88$ are the real valued coefficients of PA and $z(n)$ is the predistorted signal as defined in Fig.6.1.

A third order model of predistorter and postdistorter with omitted even terms was used.

In adaptive systems we consider recursive least squares (RLS) adaptive algorithm. Embedding criteria (6.4) of (6.15) we define

$$\mathbf{g}(n) = \mathbf{P}(n)\ \mathbf{U}(n)^*\left[\lambda + \mathbf{U}(n)^H\mathbf{P}(n)\left(\mathbf{U}(n)^*\right)^{-1}\right] \tag{6.25}$$

where

$$\mathbf{P}(n+1) = \frac{\mathbf{P}(n)}{\lambda} - \frac{1}{\lambda}\ \mathbf{g}(n)\ \mathbf{U}(n)^H(n)\ \mathbf{P}(n), \tag{6.26}$$

then we express

$$\mathbf{b}(n+1) = \mathbf{b}(n) + \mathbf{g}(n)\ \mathbf{e}(n), \tag{6.27}$$

where forgetting factor is set to $\lambda = 0.9$ and the initial value for $\mathbf{P} = \delta^{-1}\mathbf{I}$. The value of $\delta = 10^{-3}$ and $\mathbf{I}$ is square identity matrix of size K. For more informations regarding RLS algorihm refer to chapter 3.6.4.

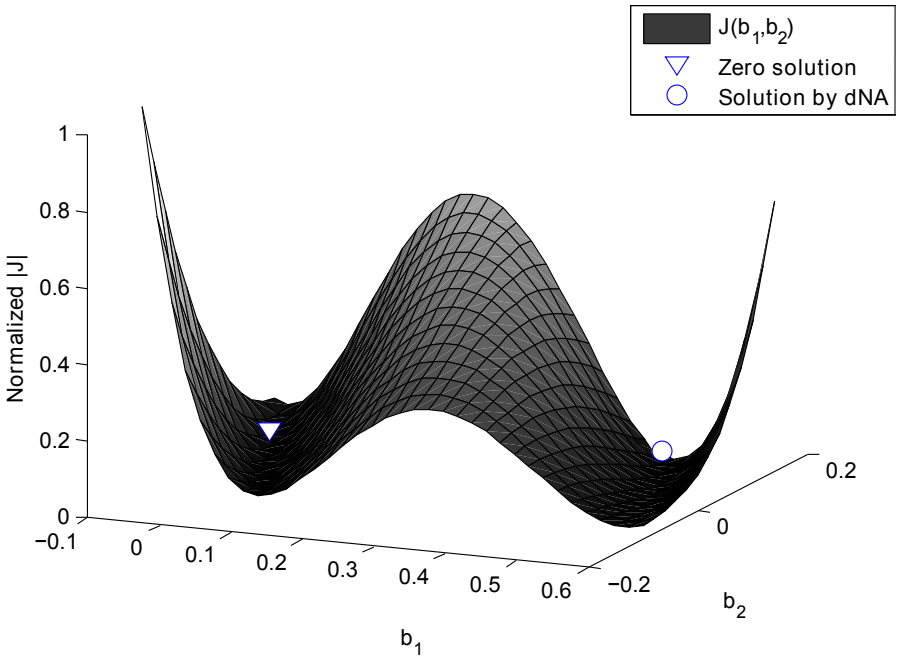

Fig. 6.2: The simulation of criteria function with standard solution (marked as circle) and zero solution (marked as triangle).

Two criteria functions **J** with PA model defined in (6.24) are evaluated by exhaustive search. Using the exhaustive search: with step of $h = 0.01$ in the range $-2 \leq b_1 \leq 2$ and $-2 \leq b_2 \leq 2$, we need to evaluate all possible solutions of criteria function. Such setup yields approximatively to 160800 evaluations.

In Fig.6.2 we use a normalized criteria function defined in (6.4). We can see, that there already exists two minim and one maximum. Unfortunately we can see in the Fig.6.2 that there exists global minim in the origin on the criteria function (denoted as zero solution).

To remove global minimum from the origin we have modified the criteria as in (6.4). Therefore by exhaustive search we can see the shape of normalized quadratic criteria function **J** in the Fig.6.3. In the figures there are two solutions also marked. One in the origin and the second one estimated on the block of data by damped Newton method. In the Fig.6.3 we can see, that there is undefined region of function **J** for the zero solution. It is the region, where the criteria function (6.15) can't be

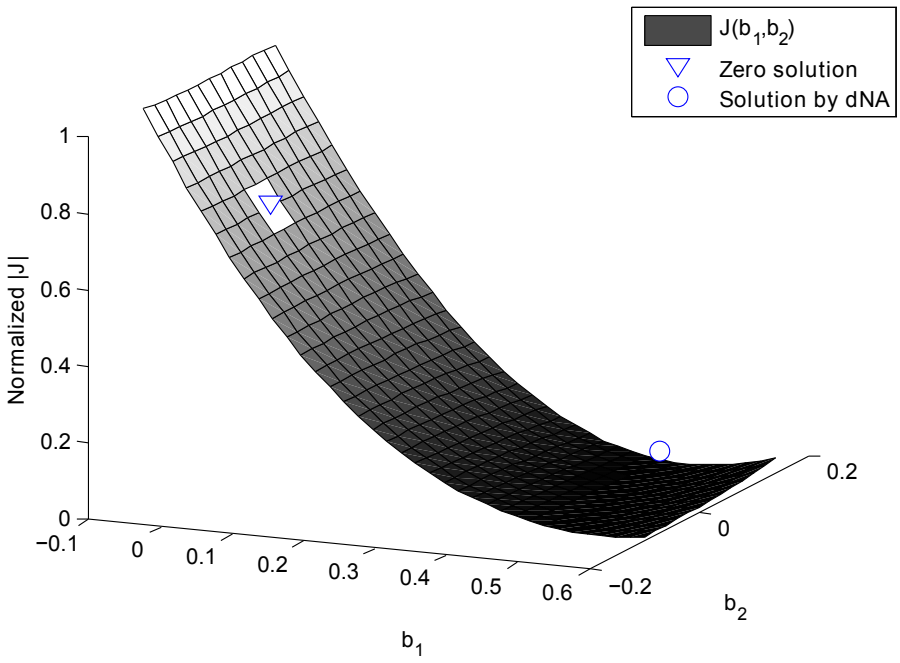

Fig. 6.3: The simulation of criterium function with gain based error with eliminated solution (marked as triangle) and standard solution (marked as circle).

evaluated (for real and complex numbers) because division by 0 is performed.

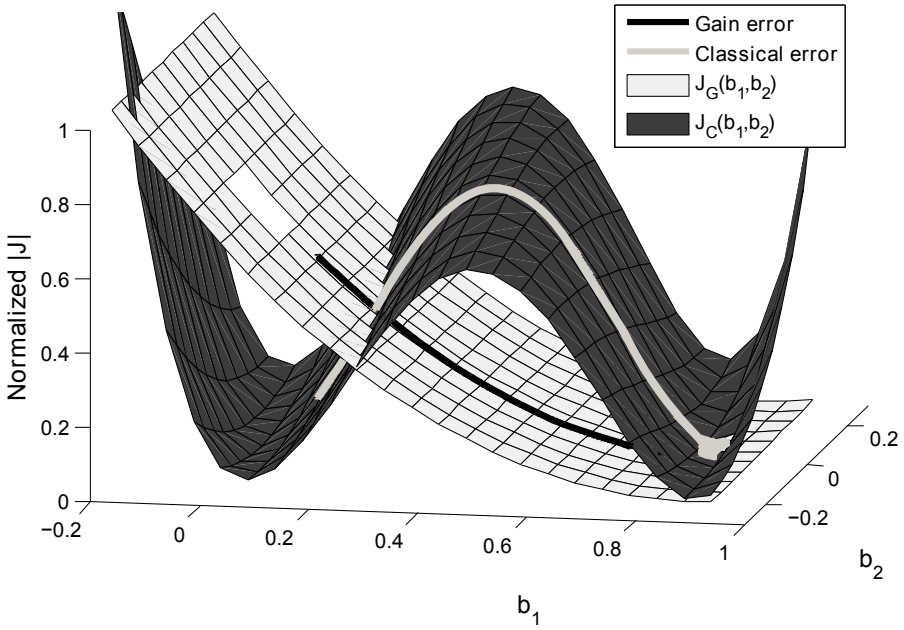

Fig. 6.4: The simulation using RLS, with traces of solutions (on the criteria functions) for the initial solution $b_1 = 0.1$ and $b_2 = 0$.

Now we present results obtained by adaptive RLS algorithm. First as showed in the Fig.6.4 we set the initial solution estimation to point $b_1 = 0.1$. We can see there shapes of criteria functions with traces (evolution of solutions) of solutions. In the case of both criteria functions the final result are nearly the same.

Next we set the initial guess to $b_1 = -0.1$ and $b_2 = 0$ expecting the classical solution to fail. As we can see the traces in the Fig.6.5 our expectations have been confirmed with both criteria functions $|J| \to 0$.

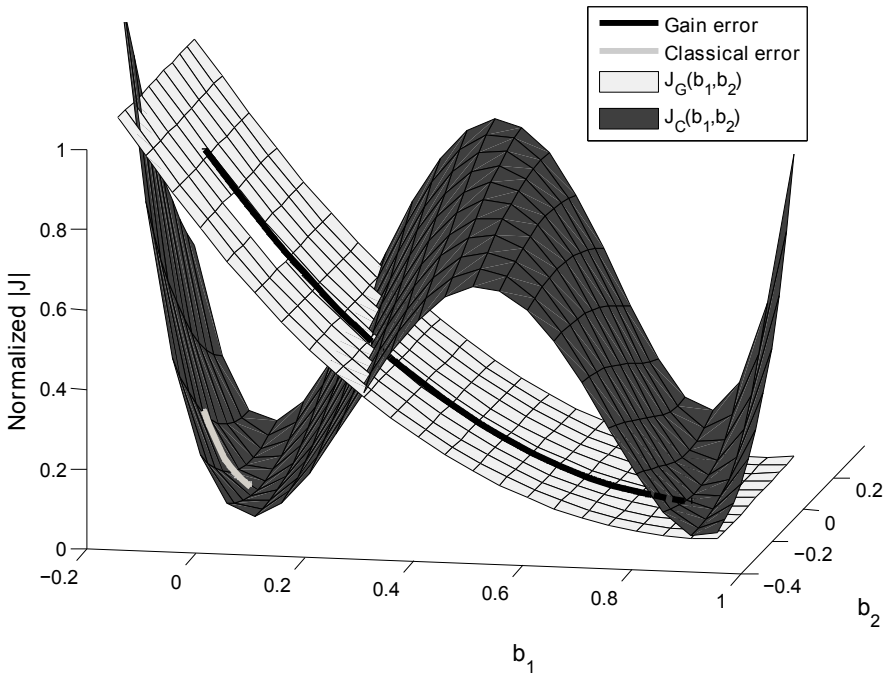

Fig. 6.5: Convergence to zero solution of typical approach compared with gain approach. The simulation using RLS, with traces of solutions (on the criteria functions) for the negative initial solution $b_1 = -0.1$ and $b_2 = 0$.

To prove the concept, we are comparing evolution of magnitude of first coefficient b_1. As standard value, we plot solution obtained by damped Newton block solution performed on matrices.

In the plot there are two different initial conditions $b_1 = -0.1$ and $b_2 = 0$ versus $b_1 = 0.1$ and $b_2 = 0$. In the case of negative value of initial value, the standard solution reaches the zero solution. It is obvious that gain based criterium reach all time the value of damped Newton block solution (Fig.6.6).

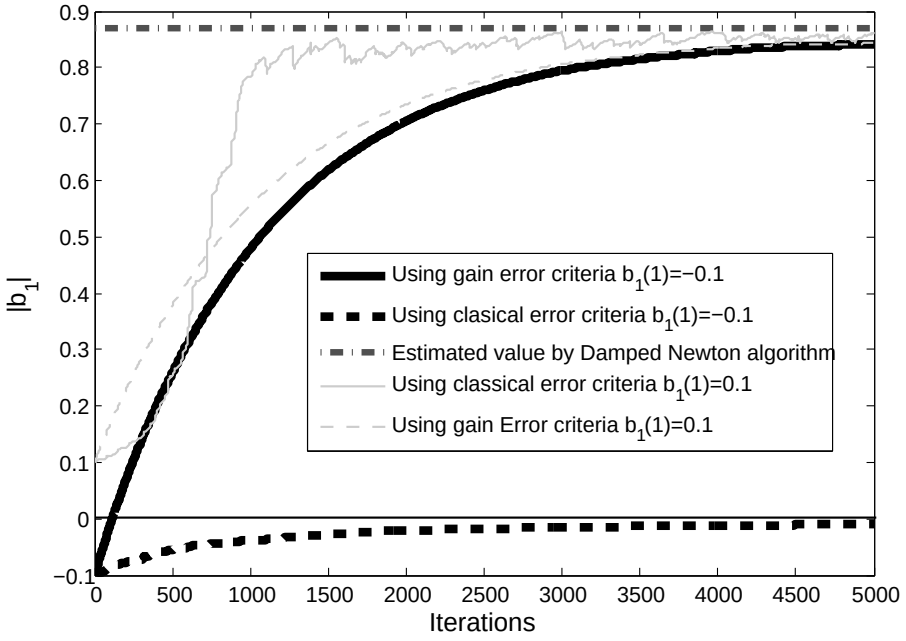

Fig. 6.6: The convergence of first coefficient $|b_1|$ for different initial values.

We have to be aware, that the initial value of $b_1 = 0$ and $b_2 = 0$ is undefined for the proposed gain based criterium. In the case of standard criterium the final solution after convergence will be $b_1 = 0$ qnd $b_2 = 0$.

6.4 Experimental Results

Because presented idea uses just simple polynomial model of PA, we have decided to prove the concept on real system. Therefore we considered a Doherty UHF power amplifier using NXP BLF888A UHF RF power LDMOS transistor for DVB-T applications (470 MHz to 860 MHz) with output power P1dB 100W. For the experiments OFDM-like signal was used with oversampling rate 8. For modeling the PA, we have employed a memory polynomial model with nonlinearity order $K = 17$ and the memory depth of $M = 2$. The modeled PA AMAM and AMPM characteristics can be seen in Fig.6.7.

The power spectral density of input signal and PA model output signal can be seen in Fig.6.8.

To evaluate our ideas we used this model of PA and memoryless DPD with nonlinear order $K = 5$. We used adaptive RLS algorithm, where the initial guess was set

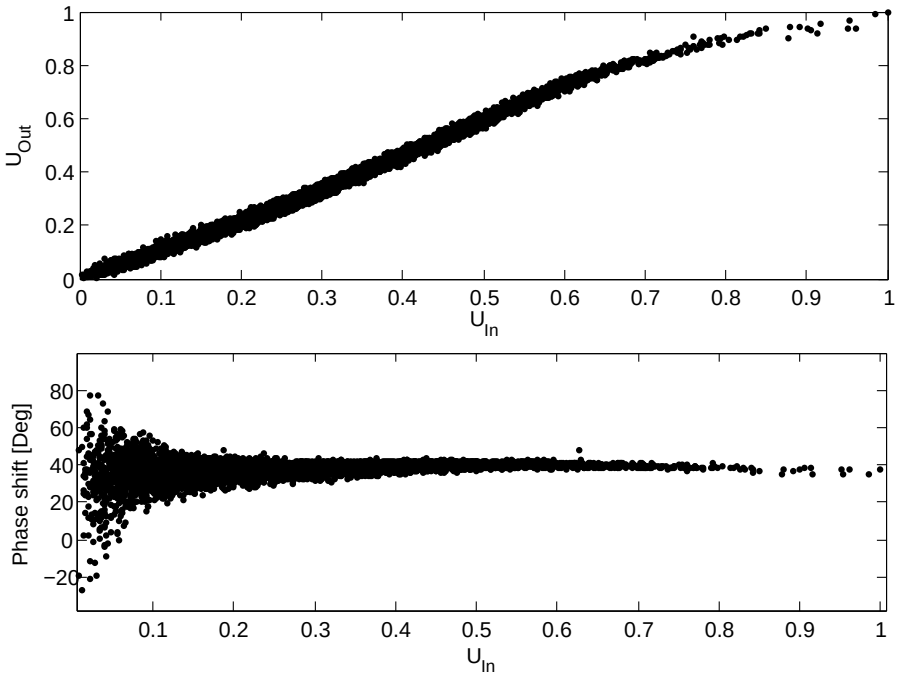

Fig. 6.7: The AM-AM plot(Top) and Phase shift (Bottom) for model of PA using orthogonal polynomials with polynomial order of $K = 17$ and memory depth of $M = 2$.

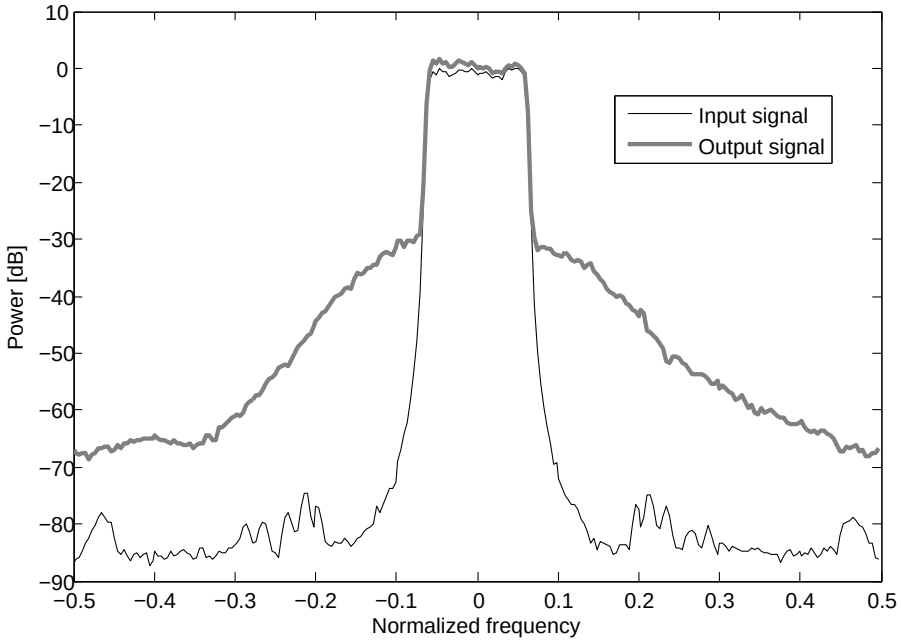

Fig. 6.8: Power spectral density of input and output signal for model of PA using orthogonal polynomials with polynomial order of 17 and memory depth of 2.

as $\mathbf{b}_{init} = [-0.001, 0, 0, 0, 0]$. First standard criteria was used. In the Fig.6.9 we can

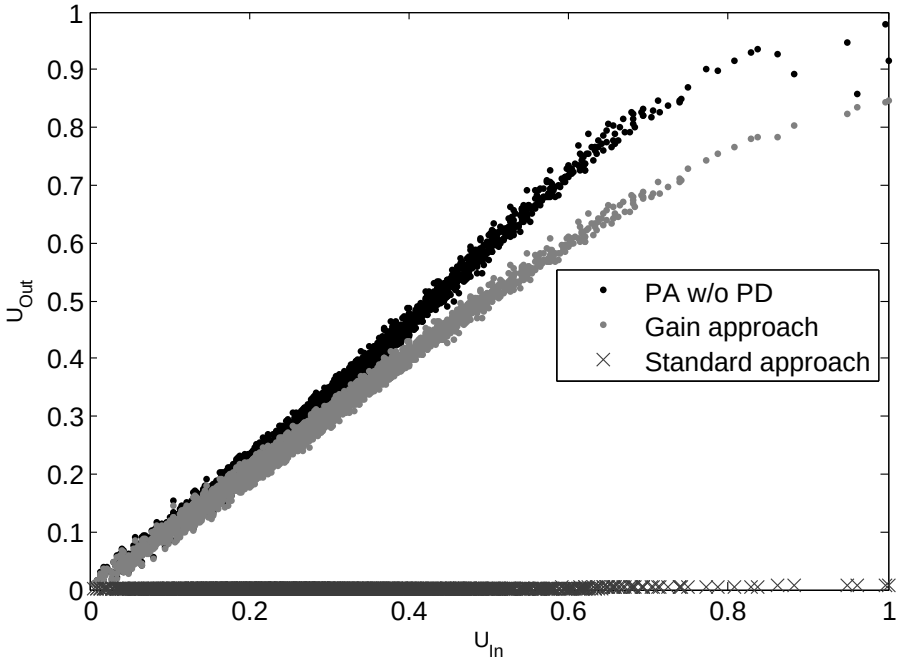

Fig. 6.9: The AM-AM plot for different approaches and PA without any predistortion. As initial value for $\mathbf{b}_{init} = [-0.001, 0, 0, 0, 0]$ was used. The RLS algorithm was utilized with 2700 iterations.

see that predistortion fails. The result is a set of dark gray points. The estimated coefficients were close to zero solution. Then we have employed gain based criteria to RLS. The results are marked as light gray points in the Fig.6.9.

6.5 Conclusion

For the design of real DPD we believe, that using standard indirect approach for calculation of coefficients for DPD could lead to multiple solutions that meets the error criteria. In this chapter we have demonstrated the possible existence of multiple solutions for predistorters using indirect approach. First we took simple mathematical models of DPD and PA and we have proved the concept. Then we have derived matrix notation of indirect approach.

In order to overcome problems with convergence we have proposed new criteria based on gain. We have evaluated and compared both criteria. The gain based criteria tends to avoid wrong solutions. We would like to point out, that for more complex systems with higher orders in standard criteria definition, there exist more

possible solutions, where the first derivation is equal to zero. Some of them could be maxima.

A practical way to overcome such multiple solutions is to compare histograms of input power and in the case of change update the coefficients. Such solution can be found for example in some current commercial FPGA implementations.

7 TESTBED MEASUREMENTS

In this chapter the measurement testbed is presented. The testbed was assembled at ESIEE in order to perform measurements. Measuring the physical layer of a wireless radio transmission can be done in the following way: Firstly, a transmitter generates the signal-samples to be transmitted. Secondly, these samples are transmitted in real-time and captured by the receiver. Thirdly, the received signal is aligned, post-processed and evaluated on the PC.

First we have assembled a testbench using real-time spectrum analyzer and generator. Such setup had problems with down-conversion and with bandwidths.

Therefore we have assembled another test-bench using a high speed digital oscilloscope in order to be able to analyze fundamental and harmonic signals of RF signal. As a last upgrade of testbench, we have added measurements of generated signals (input of PA).

7.1 Setup with Real-Time Spectrum Analyzer

The measurement setup consisted of a N5182A MXG RF Vector Signal Generator (VSG) and a RSA3408A 8GHz Real-Time Spectrum Analyzer(RTSA) (Fig.7.2). The VSG contains a build-in analog mixer and is practically capable to generate any signal within its frequency and bandwidth limitations. Also the RTSA has a mixer and is capable to down-convert the RF signal practically to baseband. Both devices were connected over LAN using VISA communication protocol. The output of PA was attenuated with 40 dB attenuator.

The experimental setup can be seen in Fig.7.1.

The final data were processed using MATLAB. The output power of the Device Under Test (DUT) in our case PA, was attenuated with 40 dB attenuator.

Fig.7.3 presents the spectrum of a wideband OFDM signal with strong nonlinear distortion in adjacent channels.

In order to test the test bench, a 64 QAM signal was generated with a data rate of 3Mbps, an output power 5dBm for the generator (input of PA), a sampling

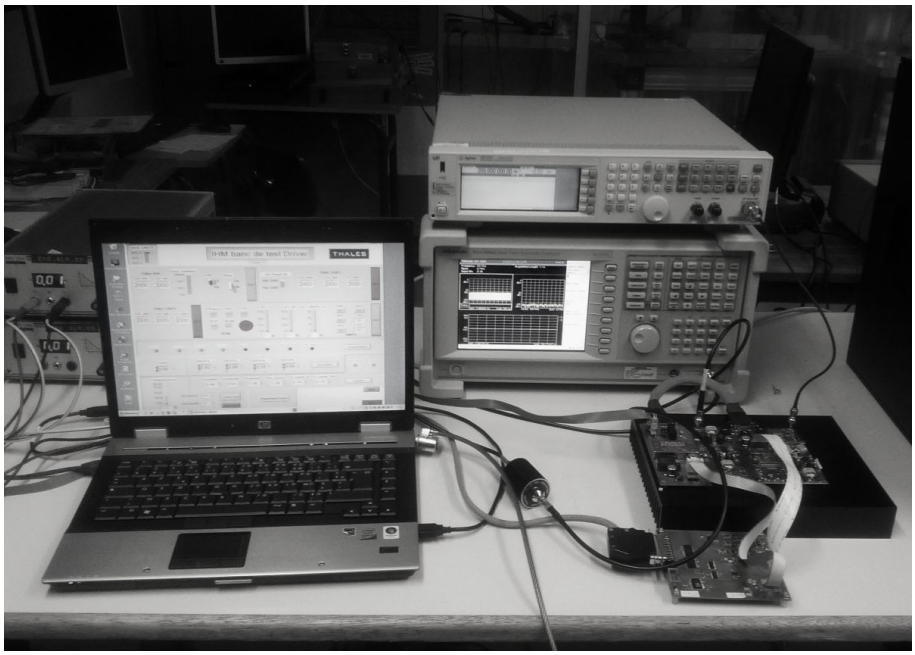

Fig. 7.1: Setup of experimental test bench. There is a N5182A MXG RF Vector Signal Generator, RSA3408A 8GHz Real-Time Spectrum Analyzer and computer driven PA.

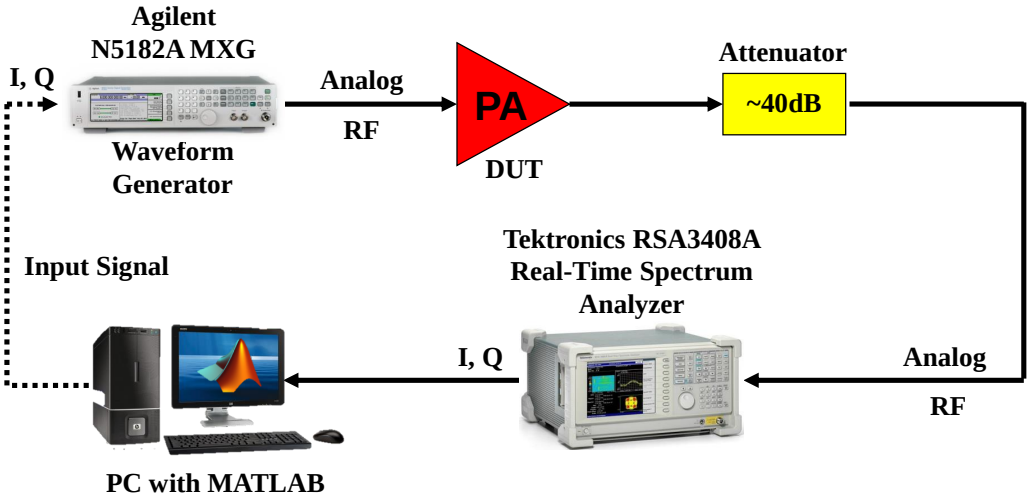

Fig. 7.2: Layout of measurement testbed using RSA3408A Real-Time Spectrum Analyzer.

frequency 24 MHz and a center carrier frequency 200 MHz.

The DUT was the Smart PA from Thales driven by PC as described previously. The quite nonlinear AM/AM characteristics with memory effect can be seen in the Fig.7.4. Also after demodulation (before quantization) we can see the deformation

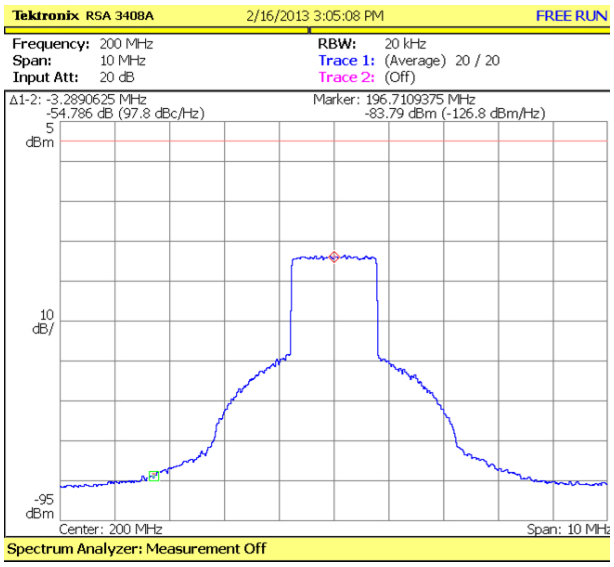

Fig. 7.3: Example of the output screen of PA with wideband OFDM input signal and distortion in adjacent channels.

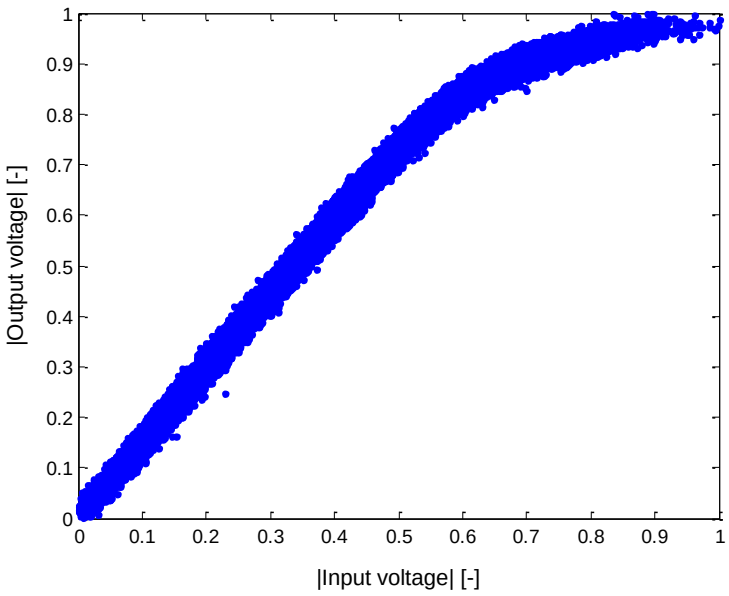

Fig. 7.4: The AM/AM characteristics for 64QAM.

of constellation points in constellation diagram in Fig.7.5. The PSD of input and output baseband signals are in the Fig.7.6.

The overall EVM was calculated as 6.4%. In the Fig.7.6 we can see the different noise floor for the input (Matlab signal) and for the output signal (Measured). The Matlab input has nearly 20dB better dynamical range. Such difference influence the performance of modeling and linearization of PA.

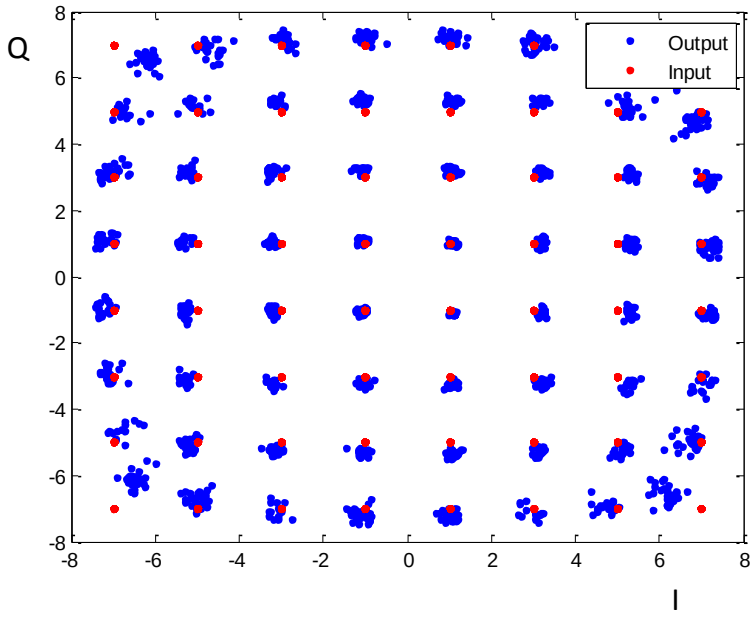

Fig. 7.5: The constellation diagram for 64QAM with EVM=6.4%.

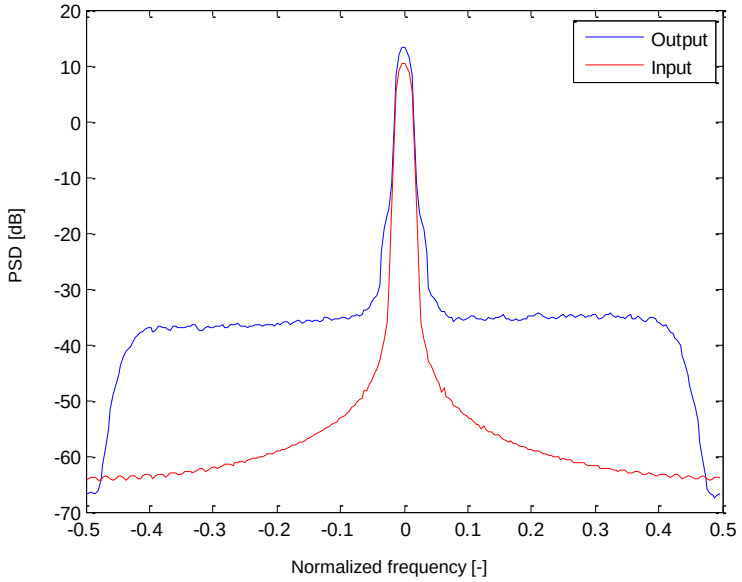

Fig. 7.6: The PSD characteristics for 64QAM.

The RSA3408A has a limitation for real-time measurements of span 20MHz which is not enough for modern wideband signals. Due to transmitted signal imperfection of analog down-conversion certain errors are added.

This setup of testbench is sufficient within 20MHz of bandwidths. But for larger

bandwidths it cannot be used. Therefore we have assembled a new setup with a digital oscilloscope.

7.2 Wideband platform - Setup with Digital Storage Oscilloscope

Due to previously described limitation of bandwidth and imperfections, the digital oscilloscope Agilent DSO81204B capable of capturing a bandwidth of 12GHz with sampling frequency 40GSa/s was used (Fig.7.7).

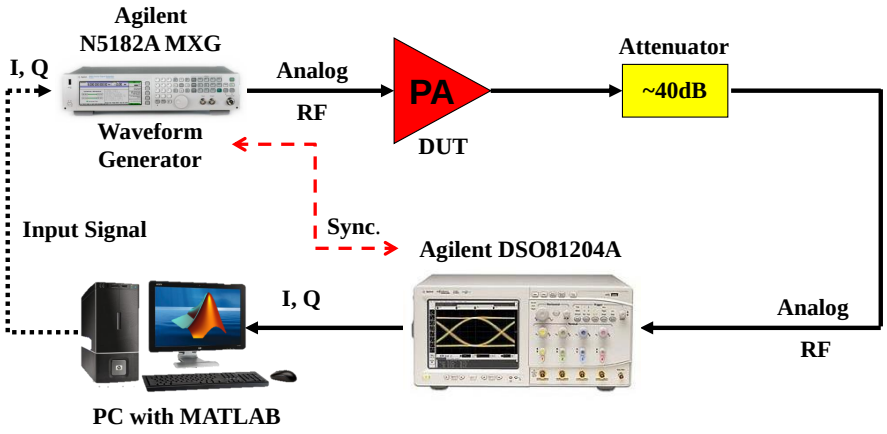

Fig. 7.7: Experimental test-bench using digital oscilloscope DSO81204B.

Characteristics of the DSO 81004B: 12GHz bandwidth, sample rate up to 40GSps, noise floor: 342 μV @ 5 mV/div.

We performed measurements directly from the output of the amplifier without analog frequency conversion. An advantage of this approach is to allow us to analyze not only the signal around the carrier frequency but also the higher order harmonics if the sampling frequency is chosen high enough. The sampling frequency is more than twice the center frequency. The center frequency was set to 200 MHz. The layout of testbench can be seen in Fig.7.8.

The development of the new testbench needed writing the command interface of the oscilloscope Matlab, to read 16-bit words and convert them to float data format, to setup sampling frequency to 500MHz or 1GHz, filtering and frequency

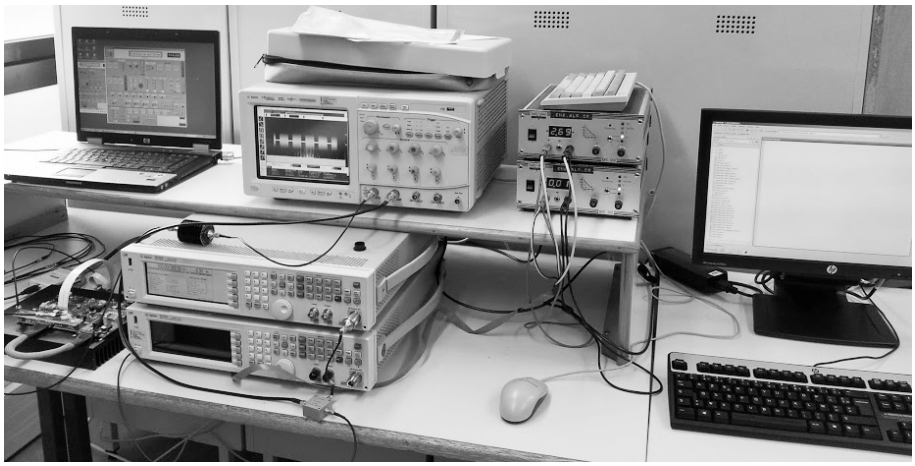

Fig. 7.8: Experimental test-bench using digital oscilloscope DSO81204B and N5182A MXG RF Vector Signal Generator.

down-conversion in Matlab, to recover the signal around the fundamental or harmonic frequencies.

In order to simplify the synchronization of two signals (output of PA recorded by the oscilloscope and input signal generated by Matlab), we have introduced a sequence of zeros between the repetition periods of the MXG signal generator as can be seen in Fig.7.9.

In order to validate this second bench, we first made measurements without PA. Fig.7.11 shows the power spectral density of the digitized signal with sampling frequency 500 MHz. We also plot a window of recorded signal by the oscilloscope.

Figure 7.10 shows the power spectral density and AM/AM characteristics of baseband signals after frequency down-conversion and filtration in Matlab (left) and power spectral density of RF signal before down-conversion.

We would like to point out that we may observe in the Fig.7.11 the difference of noise floor for measured and generated signal. Such difference could lead to deterioration of modeling performance.

Fig. 7.9: Screen from oscilloscope displaying RF signal with zero gaps.

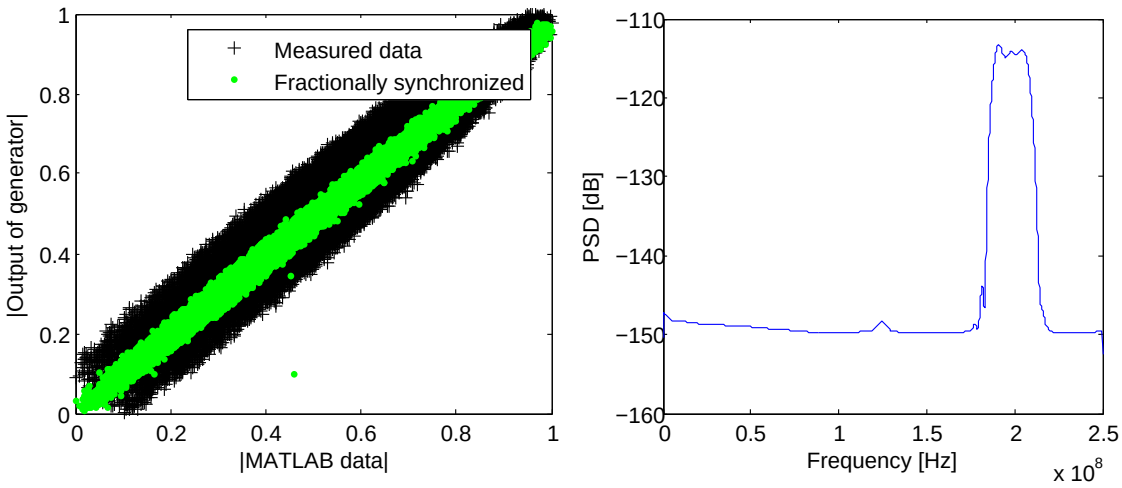

Fig. 7.10: AM/AM characteristics of testbench (without PA) in baseband (left). The green points are fractionally synchronized ($\tau = -0.19F_s$). On the right is power spectral density of RF signal with sampling frequency 500 MHz.

7.2.1 Imperfections in The Measurement System

Carrier Frequency offset

We observed and estimated a frequency shift of the carrier frequency generated by the arbitrary generator MXG. The value of the carrier was not exactly equal to the

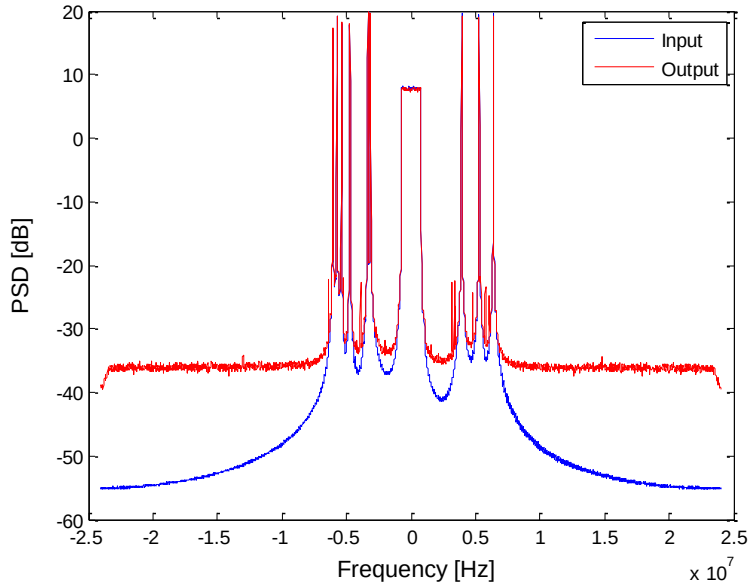

Fig. 7.11: Power spectral density of baseband signals without PA.

theoretical value of 200 MHz. The difference was typically just a few Hz (we have estimated the shift up to 44 Hz for some measurements). Figure 7.12 gives example of difference between the theoretical phase baseband signal and the measured signal. The slope of the line corresponds to the carrier offset. In this specific case we have estimated the shift to be 40Hz. After estimating this shift we have corrected it.

Influence of Automatic Gain Correction ALC (Automatic Level Control)

The arbitrary waveform generator has an automatic gain correction ALC (automatic leveling circuitry). ALC may distort the signals that are made of burst of signals. Figure ref.7.13 illustrates the effect of ALC on the multiplexed signals.

Basically the incorrect ALC setup can create a sudden unleveled condition that may create a spike in the RF output, potentially damaging a DUT or connected instrument. Such spikes can be seen in the Fig.7.13. Properly setup ALC of the MXG generator can be seen in the Fig.7.14.

Without Filter at Output of Power Amplifier

In the experimental testbench there is not any filter at the output of PA. Thus for a 200 MHz carrier frequency and sampling frequency 500MHz, we may expect aliasing of higher harmonics (the second harmonics 400MHz will fold at 100MHz). In fact it is not a problem since there is no spectrum overlap and we can recover the useful

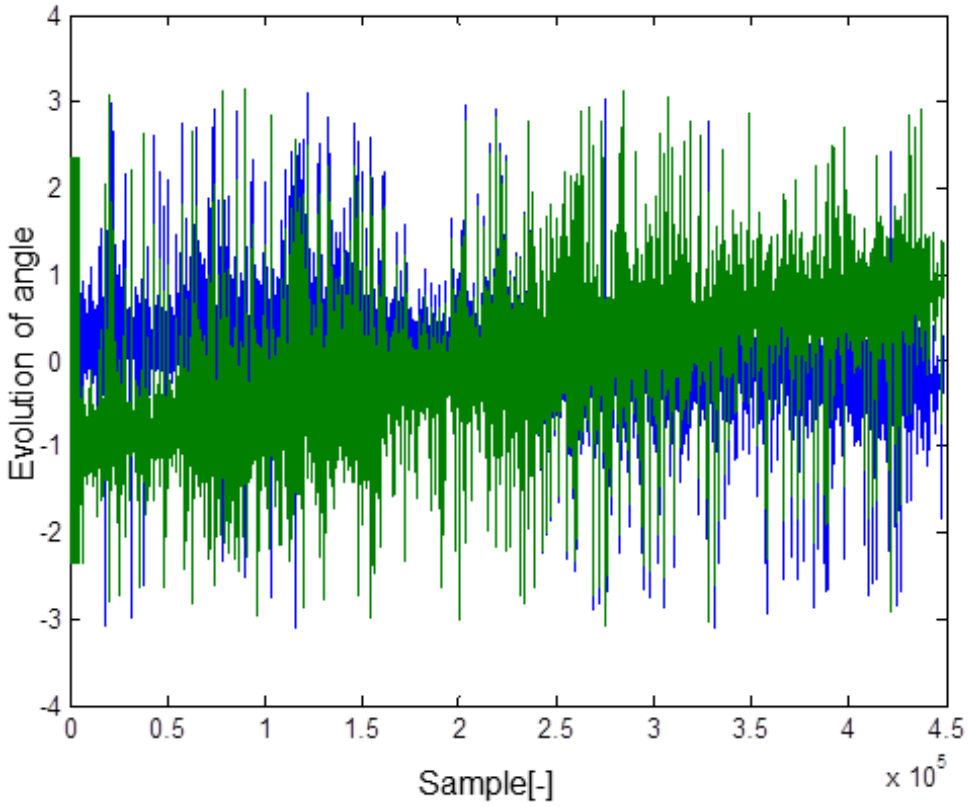

Fig. 7.12: Wrong carrier frequency of a down-converter (green) and corrected (blue). Slope due to a shift in the value of the carrier (40Hz shift).

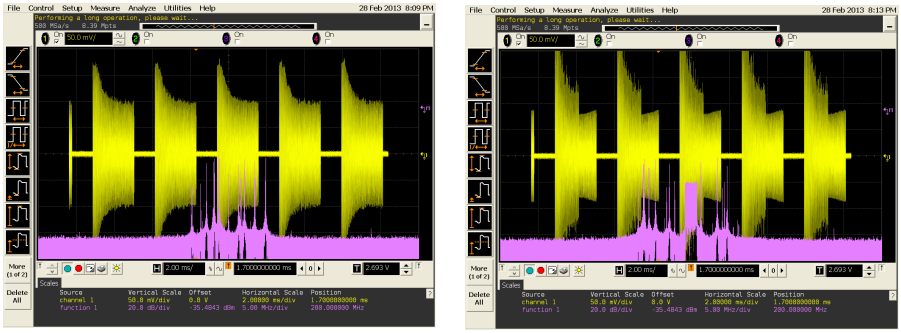

Fig. 7.13: Influence of wrong ALC setup on the output signal of MXG.

signal by filtering (in Matlab).

We may observe in Fig.7.15, the RF spectrum, sampled with sampling frequency 1 GHz, the main carrier around 200 MHz, additional harmonics around 400 MHz and harmonics close to DC components.

Fig. 7.14: Properly setup ALC and its influence on the output signal of MXG.

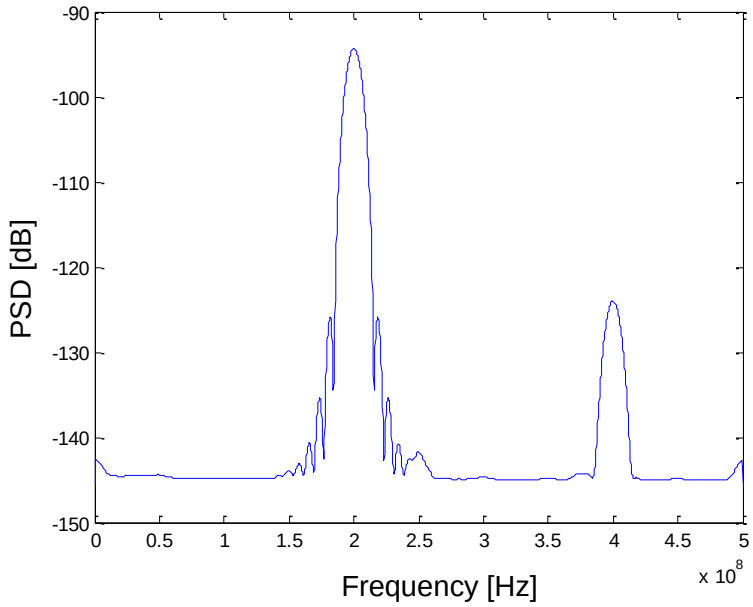

Fig. 7.15: RF spectrum of output of smart PA with distortions.

7.2.2 Two Channel Measurement Modification of Testbench

Due to previously mentioned problems such as with different dynamical range, or artifacts generated due to imperfections of input signals and output signals, the testbench was modified in order to allow the capture of two channels. First channel is used to capture the generated signal by MXG and second channel captures the output of PA. The fundamental layout can be seen in the Fig.7.16.

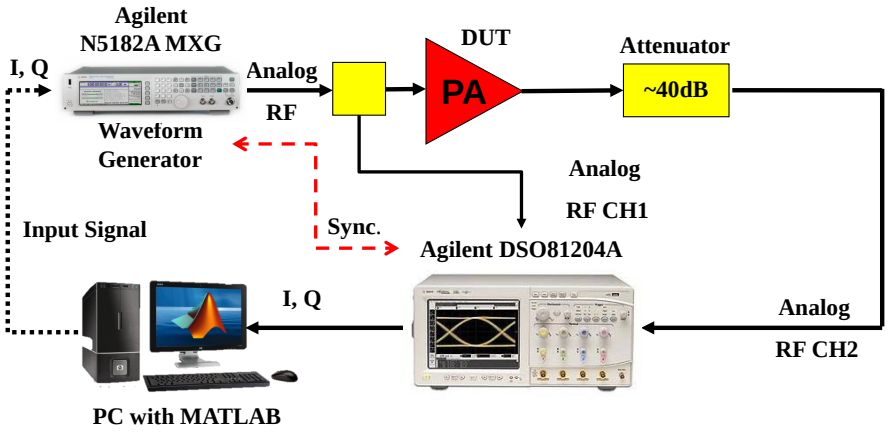

Fig. 7.16: Modified configuration of testbench to capture input of the PA.

As we may see, the input signal is divided by power divider (Mini-Circuits 15542) to provide signal to PA and to oscilloscope. Of course the input power of generator has to be modified.

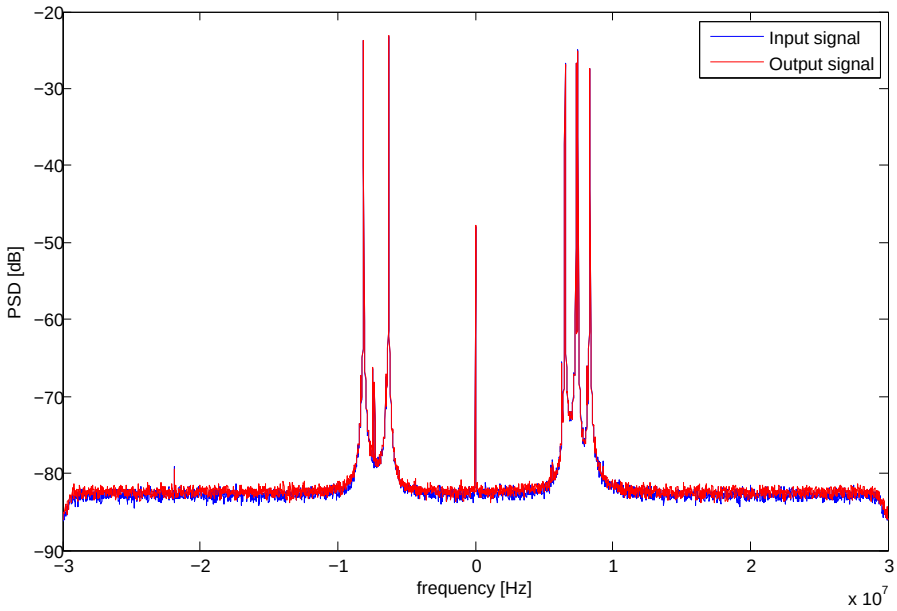

Fig. 7.17: Power spectral density of input and output signals of multiplex composed by frequency spaced GMSK signals. The setup is without PA.

Figure 7.17 presents power spectral density of input and output signal of the multiplex composed by frequency spaced GMSK signals. The presented measurements are without PA. We may observe quite strong local oscilator (LO) leakage that is generated by MXG. Usually if any of the LO leaks into the RF path, then

it will self-mix and produce a DC offset. The DC offset can rail the PA stages. Fortunately the LO leakage was observed only when the center frequency of a signal was not corresponding to the carrier frequency. The dynamical range is nearly 60dB.

7.3 Conclusion

In this chapter we have presented power amplifiers that have been measured and used for simulations. In order to measure the devices, the testbench was assembled. The first testbech used realtime spectrum analyzer with build-in down-converter. The bandwidth of this analyzer was not sufficient enough in order to measure wide-band signals.

The next testbench, for wideband, we have assembled was with oscilloscope with high sampling rate. The whole RF signal was retrieved. The down-conversion was done in MATLAB.

Because the dynamical range of generated signal (and distortions) play important role, the testbench was modified in order to also capture the input signal of PA.

8 CONCLUSIONS AND PERSPECTIVES OF PART I

The purpose of this chapter is to summarize the work on power amplifiers. The work focuses on PA modeling and PA predistortion.

The second chapter has introduced the concept of ideal power amplifiers. The parameters for the evaluation of communication systems performance have been presented too. It also gave a basic survey of general linearization techniques.

In the third chapter several models suitable for DPD and for PA modeling have been presented. First the transition from RF models to filtered baseband equivalent models have been presented and explained. Further only baseband equivalent models have been discussed due to their suitability for DPD. We have divided baseband models to several groups according to their capabilities: static and quasi-static models, dynamical models. We have also briefly discussed the special group of models that allows to separate the model (or DPD) into several stages: two-stage and multi-stage models (can be static, quasi-static and dynamical). In practice they can be realized by parallel or cascade structures.

As for model-based approaches (models with linear dependency with respect to their coefficients), orthogonal polynomial models, dynamic distortion reduction and generalized memory polynomials based on simplified Volterra series are a common choice due to their low complexity, stability of solution and ease of implementation.

Next section have presented several methods for identification of the models: one-shot solution and adaptive methods. One may choose methods according to needs of PA modeling or DPD systems. For example in case of high requirements for adaptivity but low complexity, LMS is a good compromise. In the case of good performance and adaptiveness, RLS outperforms presented approaches.

In the fourth chapter first we have introduced power amplifiers and several signals used for measuring and simulating the PAs. In the next section we do an exhaustive evaluation of Volterra based models for modeling PAs.

The next section bring an exhaustive evaluation of linearization of the same PAs as was used for modeling. We also discuss modeling and linearization techniques in terms of performance and number of coefficients.

In terms of performance it is not simple to distinguish between models. In general we may say, that every model outperforms others in different applications. GMP and DDR allow better NMSE performance than OMPS, but they are more complex to identify. DDR and GMP are very close but often GMP achieves a better compromise between number of coefficients and NMSE.

The capabilities of adaptive algorithms are then discussed. In terms of adaptiveness the RLS has the best performance (that can be compared with DNA). In terms of complexity, LS is a good choice.

The fractional LMS that takes advantage of fractional order derivatives is introduced. The performance is better than LMS (speed of convergence) and complexity is lower than RLS.

The next section focuses on optimal estimation of model structure. In the case of GMP, eight integer parameters needs to be determined. Therefore we propose an integer genetic algorithm, that is able to find good structure with respect to complexity.

One of the problems is determination of structure of the models. For example for GMP there are eight parameters to determine. We would like to point out that using multi-stage models, the estimation of structure is a very important issue. For example using three-stage GMP models (or DPD), 24 parameters defining the structure needs to be estimated, which represents if we consider only integers between 0 and 10 10^{24} possibilities.

Then we show results using neural networks for predistortion and modeling. In terms of performance, the NNs are very good. Due to training difficulties, their adaptiveness is limited.

In the fifth chapter we bring overview of influence of misalignment in the DPD systems. We have evaluated the influence on the precision of estimation of coefficients. The evaluation have been done using integer and fractional misalignments. The DPDs with memory are able to compensate fractional misalignment partially. In the case of fractional delay with memory order ≥ 3 the predistortion is able to compensate the misalignment.

In the case of integer delay the OMPS and GMP are able to compensate a delay of the same order as the memory length. Unfortunately they are not able to compensate an advance. Then we present a new model called polynomial memory modified series (PMM) that is able to compensate the delay and the advance.

In the sixth chapter we have demonstrated the existence of multiple solutions for predistorters using indirect approach. First we took simple mathematical models of DPD and PA and we have proven the concept.

In order to overcome problems with convergence we have proposed a new criterion based on an error of gain instead of the common error of signal. We have evaluated and compared both criteria. The gain based criterion tends to avoid wrong solutions. We would like to point out, that for more complex systems with higher orders in standard criteria definition, there exist more possible solutions, where the first derivation of the criterion is equal to zero. Some of them could be maxima.

In the seventh chapter we describe the testbench that was designed to measure real PAs. The first testbench used real-time spectrum analyzer with build-in down-converter. The bandwidth of this analyzer was not sufficient to measure wideband signals.

We have realized another testbench, for wideband signals with high sampling rate oscilloscope. The whole RF signal was retrieved. The down-conversion was done in MATLAB.

Because the dynamical range of generated signal (and distortions) play important role, the testbench was modified in order to capture even the input signal of PA.

Perspectives:

One of the perspectives that points out this thesis is the automatic determination of structures of multistage DPDs. And with the determination of multistage structures (also single stage structures) are closely related with their hardware implementations. Implementation of GA is well known, thus modification to integer GA is also possible. The whole concept of an automatic order determination of structure of DPD and calculation of coefficients adaptively can be challenging.

Another challenging area is adaptive hardware implementation of DPD to DSP, FPGA or ASIC for wideband non-stationary signals. The requirements for processing unit and for the ADCs/DACs can be high. For example in the 802.11ac standard the bandwidth of signal can be up to 160 MHz. Oversampling increases this bandwidth additionally three to five times. From there we may realize requirements for adaptive DPD systems.

In the thesis we have proposed a new model: polynomial memory modified series (PMM). As mentioned in the thesis there are stability issues. Its stability can be for example improved by applying an orthogonalization.

Another potentially interesting area are power amplifiers with asymmetrical spectral properties. Such power amplifiers are not well modeled or linearized with current low order Volterra derived series.

Part II

Advanced methods for non-linear systems

9 INTRODUCTION

The idea of deterministic non-linear series has influenced thinking in many research fields of science. Especially the paradigm of chaotic behavior. It is well known, that complex dynamical mathematical objects show rich and surprising structures [60, 61, 62]. Most catching for researchers over forty years in applied sciences is the fact that deterministic systems provide striking explanation for irregular behavior and anomalies in many systems which does not seem to be implicitly stochastic[63].

With a recent massive progress in the overall personal computer performance it turns out that even very complicated multi-level dynamical systems can be modeled and analyzed, in a reasonable amount of computational time. Many of these discovered events have been recently observed and proved by means of the artificial experiments. The excitement about chaos theory rises from the perception that it captures the complex disorganized order of the real world [64]. Meaning that chaotic signal from the macroscopic point of view represents total disorder [65].

Looking closely certain deterministic properties can be revealed. The absence of long-term predictability [66, 67] and the presence of infinitely many unstable periodical orbits makes almost any chaotic subsystem an ideal candidate for the ultra-fast encrypted communication channels. The basic obstacle to be removed in this area lies in the lack of sophisticated algorithms for the higher-order dynamical motion quantification. Due to the absence of closed-form analytical solution of the non-linear dynamical systems the existing routines are based on the numerical analysis and linearizion of continuous vector field near equilibrium points. On the other hand, great efforts are being made to exploit ideas from chaos theory in cases where the system is not necessarily deterministic but the data display more structure than can be captured by traditional methods.

10 MATHEMATICAL MODELS AND TIME SERIES ANALYSIS

In this chapter several methods for analyzing the non-linear dynamical systems have been presented. Fist section deals with mathematical model analysis. Such methods are usually useful in the case of known mathematical models.

Otherwise in the case of having only measurements, different methods have to be applied. Such method have been presented in second part of this chapter.

10.1 Mathematical Model Analysis

The dynamics of linear systems is governed by the paradigm that small causes lead to small changes of a solution. Linear equations can lead to exponentially decaying (growing) or damped periodically oscillating solutions, where all irregular behavior has to be introduced by some random external conditions.

Chaos theory has simply demonstrated that there is no need of being one of the parameters random or stochastic [68], to produce irregular and complicated behavior.

Usually the model of autonomous system is given by the set of ordinary differential equations. The closed-form solution for such set of the equations is impossible to obtain analytically. Actually for modern computer technology it is impossible to find a analytical solution, but even if the solution is be obtained, it probably won't be intelligible.

10.1.1 Poincare Sections

The purpose of a Poincare section is to detect some sort of structure in the attractor. It can be defined as an intersection of a state space orbit of a continuous dynamical system with a certain lower dimensional subspace, transversal to the flow of the system.

A Poincare sections can be interpreted as a discrete dynamical system with a state space that is one dimension smaller than the original continuous dynamical

system.

$$P : U \to S, \tag{10.1}$$

where P is Poincare map for certain orbit on the Poincare section S and U is an open and connected neighborhood of point on the orbit.

10.1.2 Bifurcation Analysis

Bifurcation analysis is used to find certain points, where the system exhibits periodic, aperiodic and chaotic behavior (be aware that there exist also different bifurcation analysis.).

One of the most used methods is made of marginal sight (set) of Poincare sections, by perturbing chosen parameter of the mathematical model. Such typical plot can be seen in the Fig.10.1.

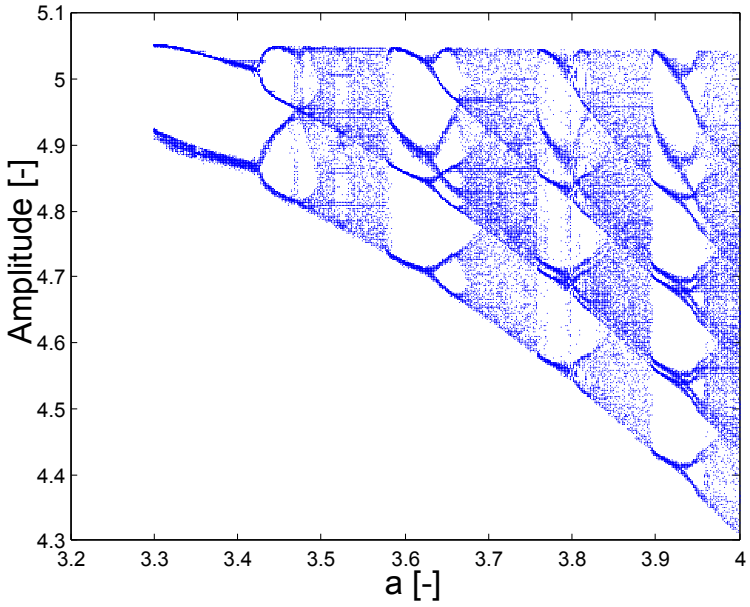

Fig. 10.1: Bifurcation analysis of single Hindamarsch-Rose neural model [135, 131].

10.1.3 Lyapunov Exponents

Detecting and quantifying chaotic behavior has become very important task for the non-linear dynamical systems. Almost every article dealing with non-linear systems

is using Lyapunov exponents for its analysis [69, 70, 71].

These exponents are used to describe the average exponential rate of divergence or convergence of near arbitrary trajectories in the phase state space. They are also called characteristic exponents. Exponents can be regarded as a measure of sensitivity to initial conditions.

Lyapunov exponents are real numbers that can be advantageously used to classify non-chaotic and chaotic systems. If the system is in an unstable state, one can see that two nearby trajectories of each are moving away faster than a polynomial rate. Any system containing at least one positive Lyapunov exponent is defined to be chaotic. The LE can be defined as:

$$LE[\mathbf{x}_0, \mathbf{y}_0 \in T_{x(t)}\Re^3] = \lim_{t\to\infty} \frac{1}{t} \frac{\|D_x\phi(t, \mathbf{x}_0)\mathbf{y}_0||}{\|\mathbf{y}_0\|}, \tag{10.2}$$

where $Tx(t)$ is a tangent space in the point on the fiducial trajectory and $D_x\phi(t, \mathbf{x}_0)\mathbf{y}_0$ is solution of the linearized system.

In order to preserve the orthogonal base of vectors in each iteration step, a Gram-Smith orthogonalization procedure is added to the standard routine for LE calculation.

By sorting and indexing LEs in descending order the mentioned metric dimension called Kaplan-Yorke dimension can be calculated as:

$$D_{KY} = k + \frac{\sum_{i=1}^{k} LE_i}{\|LE_{k+1}\|}, \tag{10.3}$$

where k is the largest integer representing the $k+1$ state variables. This formula is in accordance with two fundamental mechanisms of chaos generation, i.e. folding and stretching of the state space trajectories.

From definition of the dissipative systems the sum of all LEs has to be negative. It is obvious from that the most common approach for LE evaluation for three dimensional dynamical systems described by ordinary differential equations is based on the numerical integration of the twelve differential equations. The linearization matrix is calculated in each point on the trajectory [72], thus it necessary to have the knowledge about Jacobi matrix (JM) in the symbolic form.

The approach is based on the divergence of neighboring trajectories compared with the fiducial trajectory. The solution was first presented in [73]. It is a method for identifying just the largest Lyapunov exponent, since the quantifying property is sufficient enough. Over time interval $t_2 - t_1$, the rate of divergence of two points that evolve from a spacing D_1 to a spacing D_2, may be characterized by a quantity:

$$Q = \frac{ln\left(\frac{D_2}{D_1}\right)}{t_2 - t_1}. \tag{10.4}$$

Because the separation must be kept small comparing with the size of the attractor, a new neighbor has to be set periodically for subsequent estimates of the divergence rate. After n repetitions of stretching and re-normalizing the spacing the rates are weighted by fraction of time between each re-normalization. Then they are added to yield an experimental value for the largest Lyapunov exponent as:

$$\lambda_1 = \sum_{i=1}^{n-1} \left\{ \left[\frac{(t_{i+1} - t_i)}{\sum_{i=1}^{n-1}(t_{i+1} - t_i)} \right] \left[\frac{ln\left(\frac{D_{i+1}}{D_i}\right)}{(t_{i+1} - t_i)} \right] \right\}. \tag{10.5}$$

Since

$$\sum_{i=1}^{n-1}(t_{i+1} - t_i) = t_n - t_1, \tag{10.6}$$

we have

$$\lambda_1 = \frac{\sum_{i=1}^{n-1}\left(\frac{D_{i+1}}{D_i}\right)}{t_n - t_1}. \tag{10.7}$$

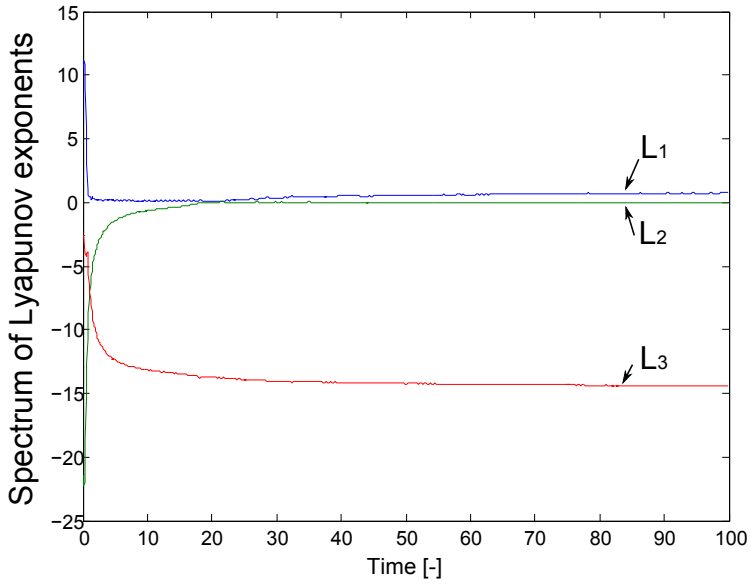

Fig. 10.2: The spectrum of Lyapunov exponents for the system (17.1).

The estimated spectrum of Lyapunov exponents for the Lorenz system 17.1 of ordinary differential equations of third order is in the Fig.10.2.

This method cannot be used if the vector field is discontinuous, especially if the repeated jump functions are involved in the mathematical model [74], since JM contains extreme values [75, 76, 69]. Such system was presented in [142]. In the article, there are values in the matrix, both infinity (positive as well as negative) and zero [69, 63].

If the transition between two states of the sign function is omitted the standard procedure returns the incorrect results. It is because the linearized flow is uniquely determined by three real negative eigenvalues and form stable node local geometry near the fiducial point. Having this configuration each edge of the volume cube shrinks suggesting that the system possess three negative LEs.

In practice the transition event is not neglected and the corresponding derivative depends on the numerical integration step size. If the extreme values substituted into the Jacobi matrix the entire procedure tends to diverge and fails.

10.2 Time Series Approach

One rarely has complete information about all of the degrees of freedom in a complex dynamical system. There are quite few conventional approaches for analyzing time series.

For example for quantifying the behavior, calculation of a correlation dimension can be used. The correlation dimension gives us an estimate of the system complexity [77]. But the methods for dynamical analysis of experimental data have been still developing.

In order to estimate all variables, first the reconstruction of dynamics has to be done. The standard method of reconstruction consists of estimating the degree of freedom, called embedding dimension m, reconstruction of dynamics and of determination of certain invariant quantities.

10.2.1 Reconstruction Of Dynamics

The reconstruction of a vector state space which is equivalent to the generating state space of the system from a scalar time series is the basis of almost all of the methods. The simplest method to embed scalar data is usage of method of delays.

This can be done by reconstructing the pseudo phase-space from a scalar time series, by using delayed copies of the original time series as components of the reconstruction matrix. It involves sliding a window of length m through the data to form a series of vectors, stacked row-wise in the matrix. Each row of this matrix is a point in the reconstructed phase-space. Setting $\{X_1 \cdots X_n\}$ represent the time series, the reconstruction matrix is then represented as:

$$\mathbf{X} = \begin{pmatrix} X_0 & \cdots & X_{(m-1)\tau} \\ \vdots & \ddots & \vdots \\ X_n & \cdots & X_{n+(m-1)\tau} \end{pmatrix}, \tag{10.8}$$

where m is the embedding dimension and τ is the embedding delay (in samples). Fixing an optimal value of m and τ requires domain specific knowledge about the time series being analyzed.

10.2.2 Embedded Dimension

In fact there exists several methods for estimating the embedded dimensions. If the attractor is embedded in spaces of increasingly higher dimension it exhibits an increasingly complex structure as it unfolds. This process continues, until the structure's correlation dimension saturates. At this point the fully attractor is revealed.

Another possibility is take advantage of symplectic geometry process, performing symplectic transforms [78].

10.2.3 Time Delay τ

For choosing the time delay τ the geometrical argument has to be applied and the attractor should be unfolded. It means that the extension of the attractor in all space dimensions should be roughly the same. Statistics such as fill factor or displacement from diagonal are employed to evaluate this argument quantitatively.

Despite this definition the most natural approach is utilizing the autocorrelation function to the time series. It is intimately related to the shape of the state space attractor. Investigating the ellipsoid set containing normally distributed points in the state space.

The lengths of semi-axes of the optimal approximation have been given by the square root eigenvalues of the auto-covariance matrix. In the two dimensional space the two eigenvalues are equal if the autocorrelation function vanishes at the time lag used for the construction of the matrix.

Because there is no simple rule for choosing τ in all cases, investigators has to adjust τ until the results seems satisfactory. Autocorrelation based methods have the advantage of short calculation time using the fast Fourier transform (FFT) algorithm.

$$R_{ff}(\tau) = (f(t) * \hat{f}(-t))(\tau) = \int_{-\infty}^{\infty} f(t)\hat{f}(t-\tau)dt \approx 0. \tag{10.9}$$

10.2.4 Demonstration of Time Series Analysis

For analyzing the time series the equations (17.1) have been chosen as the generating system. This system has bee chosen, because it is well known and it has been precisely studied by many researchers [79].

Particularly the first variable was stored and the others were discarded. In the real valued measurements, the system under study gives usually one observable, thus the only information about the system, is noisy one-dimensional signal sampled with a finite precision [67]. According to Taken's embedding theorem [80], we can use time series $x_1, x_2, ..., x_n$ to construct a trajectory matrix $X_{m\times d}$ by time delay coordinates method described by (10.8).

The different attractors can be seen in Fig.10.3 for different embedded lag τ. The most appropriate estimation to preserve the dynamics seems to be $\tau = 8$.

To estimate the embedded dimension m a symplectic geometry method is used to determine the appropriate number of variables from a scalar time series. Symplectic geometry has a certain measure and can keep the essential character of the primary time series unchanged when performing symplectic similar transforms. More about this theory can be found in [78]. When using the symplectic geometry approach,

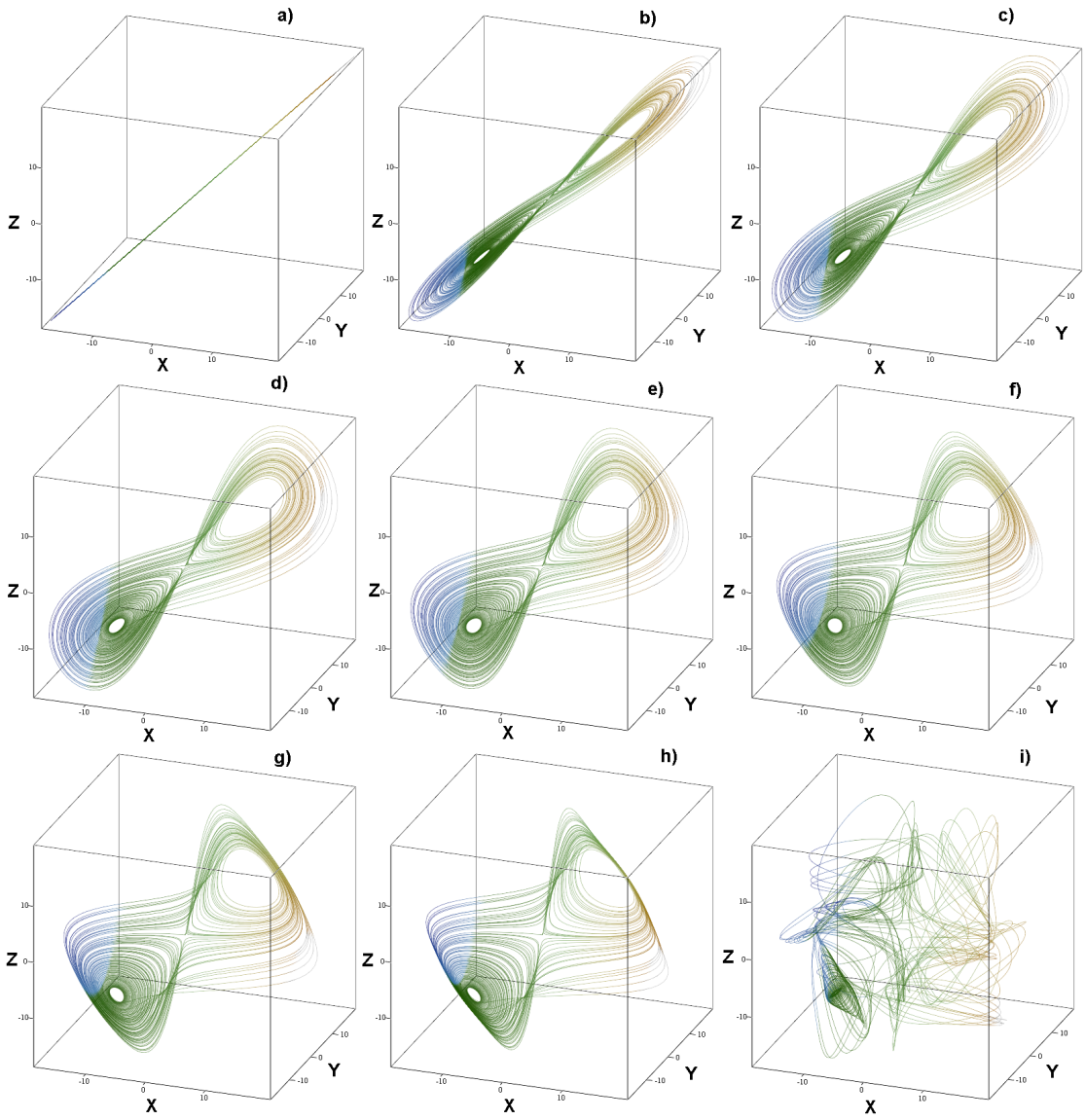

Fig. 10.3: Different lag τ *a*) $\tau = 0$, *b*) $\tau = 2$, *c*) $\tau = 4$, *d*) $\tau = 6$, *e*) $\tau = 8$, *f*) $\tau = 10$, *g*) $\tau 12$, *h*) $\tau = 14$, *i*) $\tau = 98$.

the embedded dimension of system (17.1) was estimated to be $m = 4$. In fact that is not exactly correct result, but using higher order of system can also lead to same behavior.

Using method described in [73] for estimation of the largest Lyapunov exponent for the time series, the exponent was estimated as $\lambda_1 = 0.663$. For comparison estimated largest Lyapunov exponent from the ODEs is equal to $\lambda_1 = 0.703$. Different method for quantification chaotic attractors were presented in [129].

10.3 Conclusion

In this chapter the concept of mathematical model analysis was briefly discussed. First one of the oldest method called Poincare sections for quantification of the motion is presented. This method is not very accurate, but can be used also for time series approach. One of the main issues is the setup of intersection planes.

The next section presents bifurcation analysis. The method is often used in order to investigate the stability of the systems.

The last section presents quantifier so-called Lyapunov exponents. The LE are one of the most widely used for investigation of the mathematical systems. As will be presented later, there exist cases, where the quantifier is limited.

In the next section reconstruction of attractor dynamics is introduced. It is very useful tool, because in real-valued measurements the availability of state variables is highly limited. One of the main issues that hast to be overcome is the estimation of parameters for reconstruction.

In the next section the estimation of embedded dimension is presented.

The next section presents one of the methods for estimation of τ that is used for reconstruction of dynamics of attractor.

The last section presents example of time series analysis, on the well known Lorenz attractor, applying the previously presented tools.

11 FRACTIONAL ORDER SERIES

A classical description of dynamical processes and models in the real physical systems is usually based on the description by the differential equations. But there exists phenomenons that can not be described by the classical integer derivatives therefore it is necessary to apply the non-integer fractional calculus [81, 82, 83, 84, 85, 125].

$$\frac{D^n\ f(x)}{Dx^n}, \tag{11.1}$$

where n can be a real number. Such calculus is an extension of derivatives and integrals to non-integer orders. In fact there exist several definitions of derivatives and integrals. The well known is Riemann-Liouville definition, Caputo's definition, Oldman and Spanier and many others.

One of the mainly used definition is the fractional Grunwald Letnikov (GL) differ-integral defined as:

$${}_aD_t^{\alpha}\ f(t) = \lim_{h\to 0} \frac{1}{h^{\alpha}} \sum_{j=0}^{\left[\frac{t-a}{h}\right]} (-1)^j \binom{\alpha}{j} f(t-j\ h), \tag{11.2}$$

where:

$$\left[\frac{t-a}{h}\right] \to \mathbb{Z}. \tag{11.3}$$

Such definition is elegant general operator since assuming for positive index, one get differentiation:

$$f^1(x) = \lim_{h\to 0} \frac{f(x+h)-f(x)}{h}, \tag{11.4}$$

$$\begin{aligned} f^2(x) &= \lim_{h\to 0} \frac{f^1(x+h)-f^1(x)}{h} \\ &= \lim_{h\to 0} \frac{\lim_{h_2\to 0} \frac{f(x+h_1+h_2)-f(x+h_1)}{h_2} - \lim_{h_2\to 0} \frac{f(x+h_2)-f(x)}{h_2}}{h_1}, \end{aligned} \tag{11.5}$$

$$h_1 = h_2 = h, \tag{11.6}$$

$$f^2(x) = \lim_{h\to 0} \frac{f(x+2h)-2f(x+h)+f(x)}{h^2}. \tag{11.7}$$

Continuing for n time we have:

$$f^n(x) = D^n\ f(x) = \lim_{h\to 0} \frac{1}{h^n} \sum_{j=0}^{n} (-1)^j \binom{n}{j} f(x - j\ h), \tag{11.8}$$

$$\binom{n}{j} = \frac{n!}{j!(n-j)!} = \frac{\Gamma(n+1)}{j!\ \Gamma(n-m+1)}. \tag{11.9}$$

Therefore differentiation in fractional order is:

$${}_aD^n\ f(t) = \lim_{h\to 0} \frac{1}{h^n} \sum_{j=0}^{\left[\frac{t-a}{h}\right]} (-1)^j \frac{\Gamma(n+1)}{j!\ \Gamma(n-m+1)} f(t - j\ h). \tag{11.10}$$

For negative n the process will be integration:

$$\begin{aligned} \binom{-n}{j} &= \frac{-n(-n-1)(-n-2)\dots(-n-j+1)}{j!} \\ &= (-1)^j \frac{n(n+1)(n+2)\dots(n+j-1)}{j!} \\ &= (-1)^j \frac{(n+j-1)!}{j!\ (n-1)!} \to (-1)^j \frac{\Gamma(n+j)}{j!\ \Gamma(n)}. \end{aligned} \tag{11.11}$$

Therefore for the integration we write:

$${}_aD^{-n}\ f(x) = \lim_{h\to 0} h^n \sum_{j=0}^{\left[\frac{x-a}{h}\right]} \frac{\Gamma(n+j)}{j!\ \Gamma(n)} f(x - j\ h). \tag{11.12}$$

The part $\left[\frac{x-a}{h}\right]$ is the integer part of the fraction (floor function). Definitions (RL, GL, Caputo) are equivalent. Fractional calculus allows more compact representation and problem solution for some spatially distributed systems.

Unfortunately many of the results in the fractional calculus are given in the language of advanced analysis and are not easily readable for general engineering and science community.

Probably the first physical system to be recognized as demonstrating the fractional properties is the semi infinite lossy (RC) transmission line.

In fractal order series the fractional real numbers as the differential operators are used. Usually the simplest circuit synthesis of ODEs involves integrator synthesis. Creating integrator with fractional capacitor leads to solution of fractional order systems.

The relation for the explicit numerical approximation of the qth derivative at the points $kh(k = 1, 2, ...)$ has the following form:

$$({}_{k-L_m/h})D^{\alpha}_{t_k} f(t) \approx h^{-\alpha} \sum_{i=0}^{k} c_i^{(\alpha)} f(t_{k-i}), \tag{11.13}$$

where Lm is the memory length, $tk = kh$, h is the time step of calculation, and $c_i^{(\alpha)}(i = 0, 1, ...)$ are binomial coefficients [83]. They can be obtained as follows:

$$\begin{aligned} c_0^{(\alpha)} &= 1, \\ c_i^{(\alpha)} &= (1 + \frac{1+\alpha}{i}) c_{i-1}^{(\alpha)}. \end{aligned} \tag{11.14}$$

Then the solution of fractional differential equation can be obtained as:

$$({}_{\alpha})D^{\alpha}_{t} y(t) = f(y(t), t), \tag{11.15}$$

then without using short therm memory principle:

$$y(t_k) = f(y(t_k), t_k) h^{\alpha} - \sum_{i=1}^{k} c_i^{\alpha} y(t_{k-i}). \tag{11.16}$$

There are several mathematical definitions that solve these problems. Fortunately, the Laplace transform is still applicable and works as one would expect. Upon considering all the initial conditions to be zero, the Laplace transform of the Riemann - Liouville fractional derivative satisfies:

$$L\left\{ \frac{d^{\alpha} f(t)}{dt^{\alpha}} \right\} = s^{\alpha} L\left\{ f(t) \right\}. \tag{11.17}$$

Then, the fractional integral operator of order α can be represented by the transfer function:

$$F(s) = \frac{1}{s^{\alpha}}. \tag{11.18}$$

In the Fig.11.1 there is solution for the system of equations (17.1) with different fractional integrators.

In the Fig.11.2 we can see the dependency of the system on the order of integration. Obvious and revolutionary is, that autonomous system of order approx. 2.73 can exhibit chaotic behavior even for the Lorenz system (17.1).

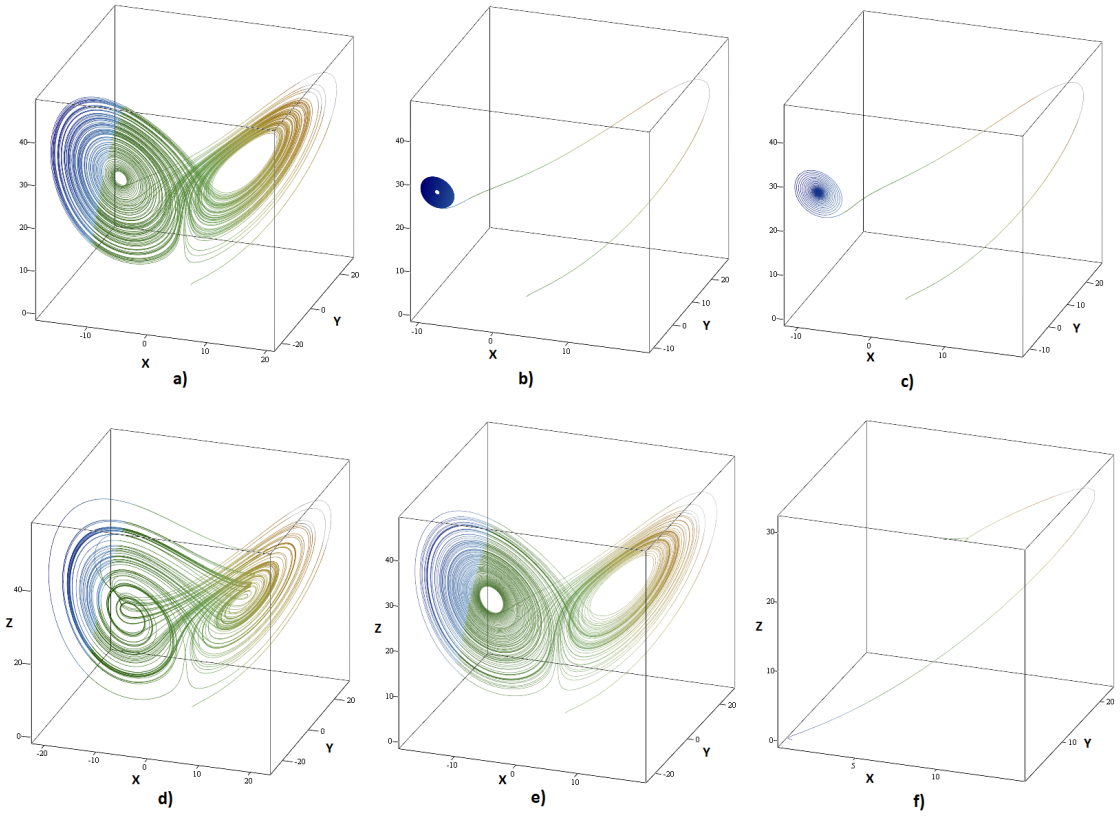

Fig. 11.1: Different fractal integrators $a)\alpha = 1$, $b)\alpha = 0.99$, $c)\alpha = 0.98$, $d)\alpha = 1.1$, $e)\alpha = 0.993$, $f)\alpha = 0.6$.

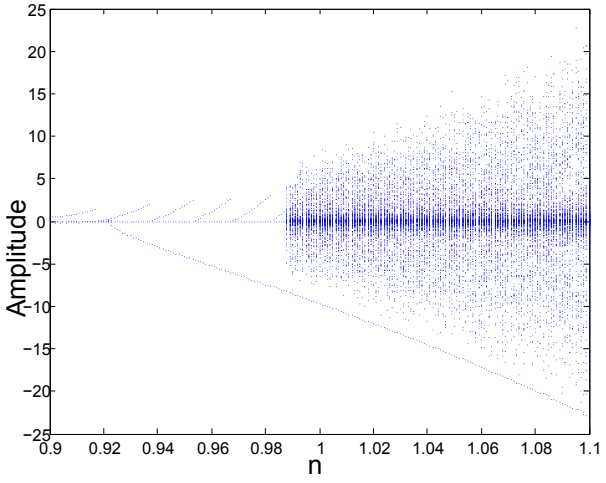

Fig. 11.2: Bifurcation diagram for the perturbed fractional order n.

11.1 On Fractional Autonomous Algebraically Simple Low Order Chaotic Flow

A classical description of dynamical processes and models in the real physical systems is usually based on the description by the differential equations. But there exists phenomenons that can not be described by the classical integer derivatives therefore it is necessary to apply the non-integer fractional calculus [81, 82, 83, 84, 85]. In fractal order series the fractional real number as the differential operators are used.

Usually the simplest circuit synthesis of ODEs involves the integrator synthesis. Creating integrator with fractional capacitor [143] leads to solution of fractional order systems.

The fractional calculus is more than 300 years old, but still yield many unanswered problems.

The algebraically simple mathematical model presented in [70] has been chosen:

$$\begin{aligned} \dot{x} &= -y \\ \dot{y} &= x + z \\ \dot{z} &= xz + 3y^2. \end{aligned} \tag{11.19}$$

The system (11.19) has an unstable point located in the origin. The careful analysis has shown, that the system is extremely sensitive to the initial condition. For the simulations we have set the $\mathbf{I}_c = [0.1, 0, 0]^T$.

In the Fig.11.3-11.6 there are different values of the integrator constants α. We can see the dependency of the system on the order of integration. Obvious and revolutionary is, that autonomous system of order less than 3 can exhibit chaotic behavior. We can see, that lowering the order od integrators, the behavior is affected. Mathematically it means, that the order of autonomous chaotic oscillator is lower than 3.

The bifurcation diagram where the perturbed parameter is the real integration constant is presented in the Fig.(11.7).

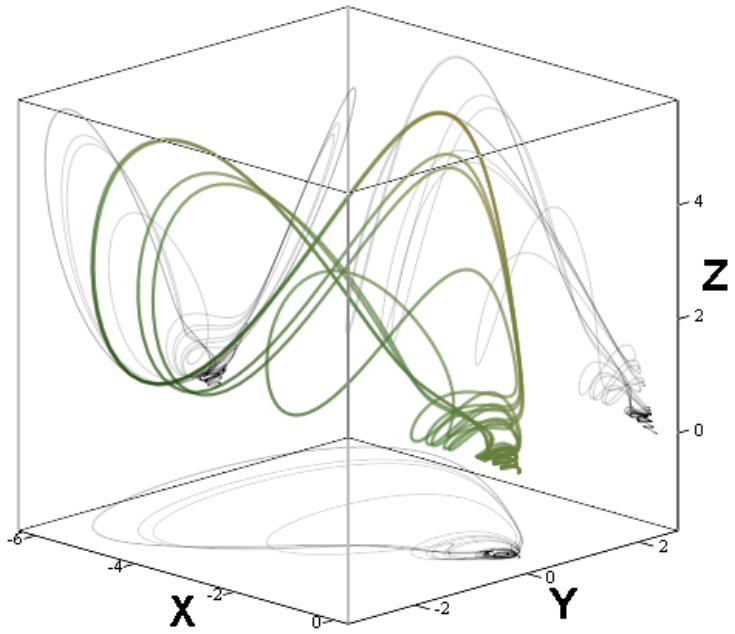

Fig. 11.3: Numerically simulated system with $\alpha_1 = 1, \alpha_2 = 1, \alpha_3 = 1$.

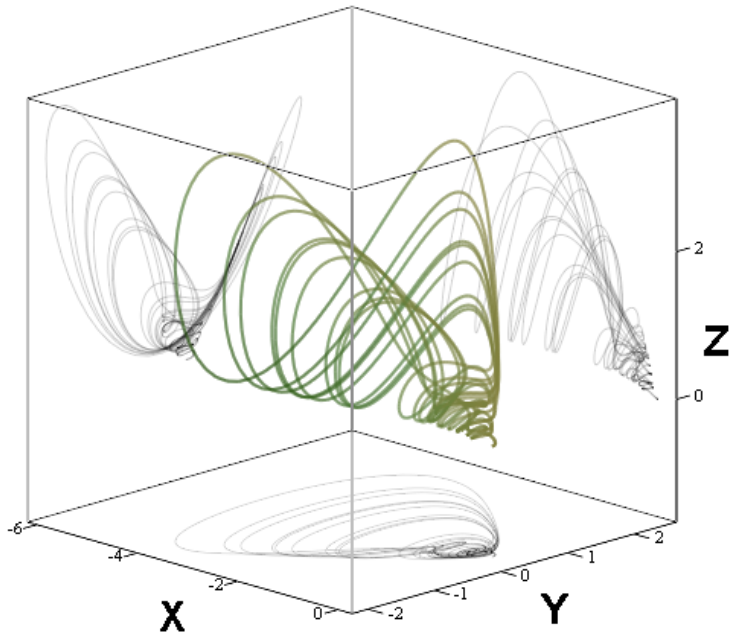

Fig. 11.4: Numerically simulated system with $\alpha_1 = 1, \alpha_2 = 1, \alpha_3 = 0.9$.

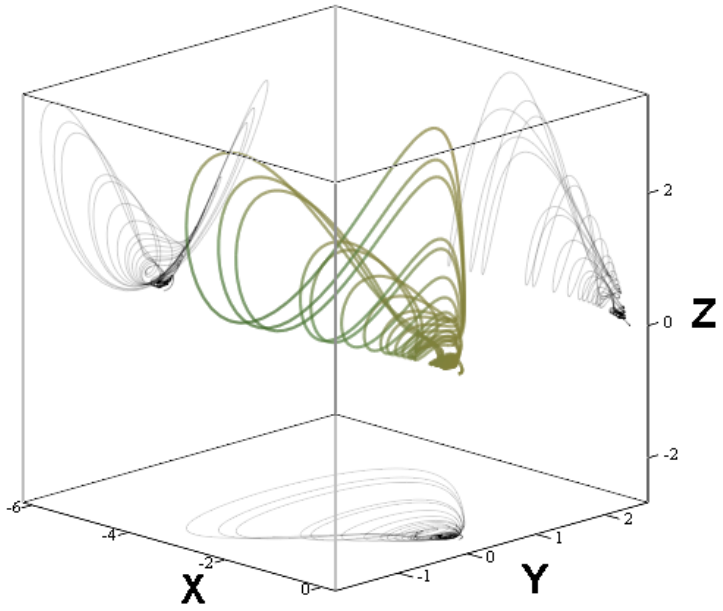

Fig. 11.5: Numerically simulated system with $\alpha_1 = 1, \alpha_2 = 1, \alpha_3 = 0.8$.

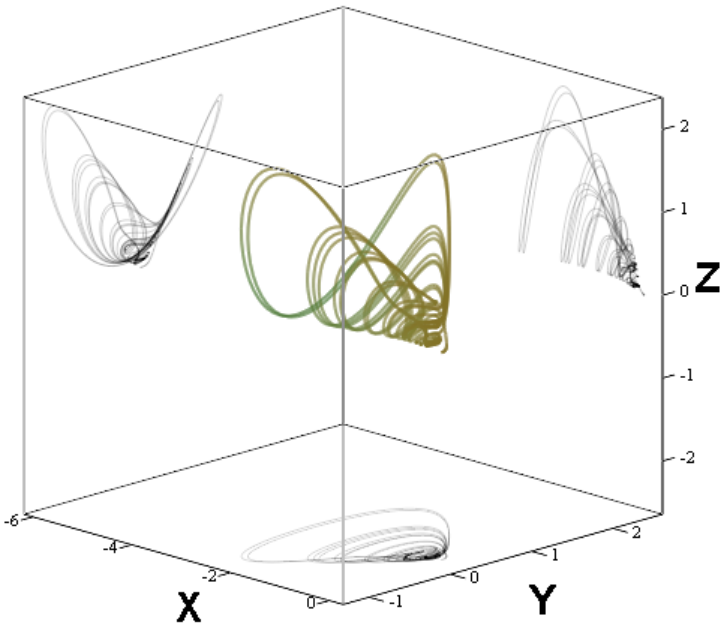

Fig. 11.6: Numerically simulated system with $\alpha_1 = 1, \alpha_2 = 1, \alpha_3 = 0.7$.

11.1.1 Lowest Possible Differential Order

In this subsection we would like to present the lowest possible mathematical order of system (11.19). In the Fig. (11.8) there is presented autonomous chaotic flow

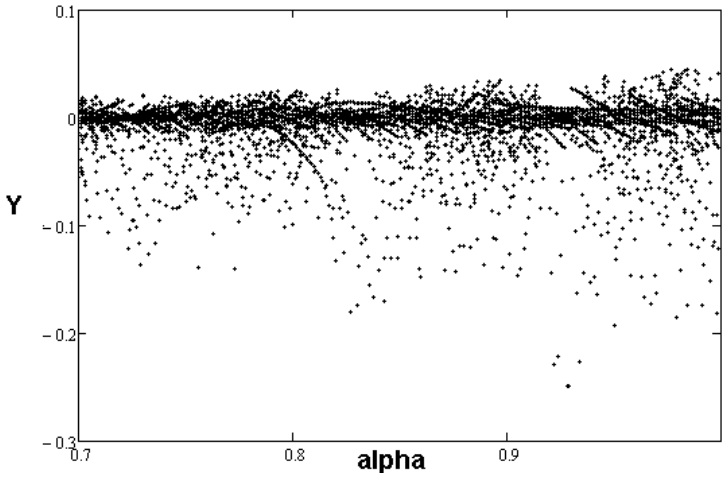

Fig. 11.7: Bifurcation diagram where $\alpha_1 = 1, \alpha_2 = 1$ and α_3 is perturbed.

with order 2.46.

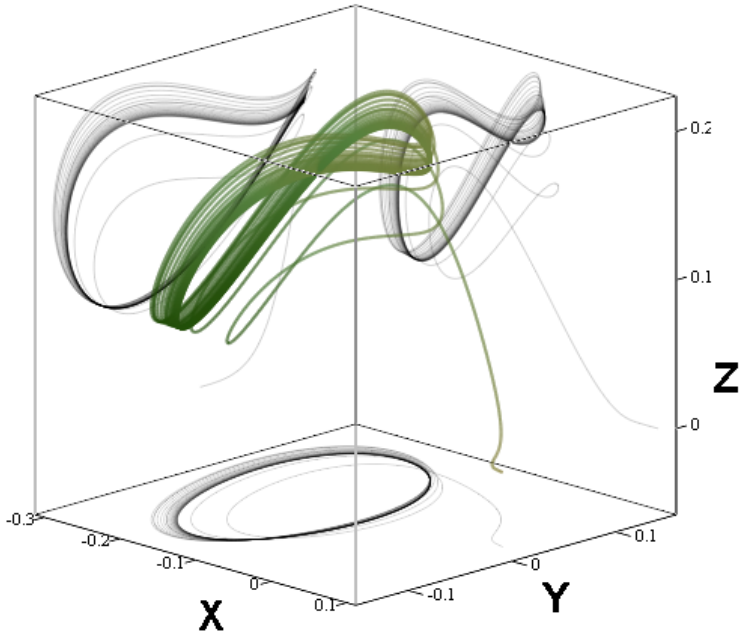

Fig. 11.8: Bifurcation diagram where $\alpha_1 = 0.86, \alpha_2 = 1$ and $\alpha_3 = 0.6$.

We believe that it is the lowest possible order for the system (11.19).

11.2 Conclusion

It is known that avoiding fractional integrators the third order of autonomous dynamical systems is the minimum order to produce chaos. Generating chaotic behavior in less than third order autonomous systems is quite delicate process. The whole system is extremely sensitive as for the initial conditions as for the realization. To obtain chaotic behavior, the whole system has to be perfectly balanced. With the growing order of the system, the presence of chaotic behavior is more probable [141].

Probably the first physical system to be recognized as demonstrating the fractional properties is the semi infinite lossy (RC) transmission lines [85]. Another example of using fractional order circuits can be found in [86, 87], where the author utilize the fractional-order two-port circuit element in different filtering applications.

12 ANALYSIS AND IMPLEMENTATION OF DYNAMICAL SYSTEM WITH PERIODICAL DISCRETE JUMPS

Recently, the discovery of a new interesting dynamical system has been reported by the authors and its practical implementation as an electronic circuit has been already verified [142]. This system so-called GP[142, 119] can be expressed by the following set of the dimensionless differential equations:

$$\begin{aligned} \dot{x} &= -a_x\ x \pm \text{sign}[\sin(b_y y)] \\ \dot{y} &= -a_y\ y \pm \text{sign}[\sin(b_z z)] \\ \dot{z} &= -a_z\ z \pm \text{sign}[\sin(b_x x)], \end{aligned} \tag{12.1}$$

where dots denote the derivatives with respect to time and the dissipative constants $-a_x \leq 0$, $-a_y \leq 0$, $-a_z \leq 0$. The constants $b_x > 0$, $b_y > 0$, $b_z > 0$ are called complexity parameters. Note that it is a modified mathematical model known as a generator of the so-called labyrinth chaos [68], that has a cyclically symmetrical vector field and that is invariant under the trivial changes of the state variables.

It turned out that sine function can be directly replaced by cosine function without the essential changes of the global dynamics.

The main difference between (12.1) and original dynamical system describing auto-catalytic processes in chemistry is the discontinuity of the vector field.

Since there is no closed-form analytic solution of the equations (12.1) the analysis is restricted to the numerical integration process and the associated routines. The most widely used and general quantifier of the dynamical motion is a calculation of some metric dimension of the state space attractor. Such method is known as Kaplan-Yorke dimension and is based on the knowledge of a spectrum of the Lyapunov exponents (10.1.3). The definition formula can be also written as [71]:

$$LE[\mathbf{x}_0, \mathbf{y}_0 \in T_{x(t)}\mathbb{R}^3] = \lim_{t\to\infty} \frac{1}{t} \frac{\|D_x\phi(t, \mathbf{x}_0)\mathbf{y}_0|}{\|\mathbf{y}_0\|\|}, \tag{12.2}$$

where $T_{x(t)}$ represents a tangent space in the fiducial point and $D_x\phi(t, \mathbf{x}_0)\mathbf{y}_0$ is a solution of the linearized system. By sorting and indexing LEs in descending order the mentioned metric dimension can be calculated as:

$$D_{KY} = k + \frac{\sum_{i=1}^{k} LE_i}{\|LE_{k+1}\|}, \tag{12.3}$$

where k is the largest integer for which the numerator in (12.3) is still a positive number.

It is obvious from (12.2) that the most common approach for LE evaluation for three dimensional original systems is based on the numerical integration of the twelve differential equations [69]. The linearization matrix is calculated in each point on the trajectory, thus it necessary to have the knowledge about Jacobi matrix (JM) in the symbolic form.

Using the concept of the box-counting method the capacity dimension can be established using the formula:

$$D_C = \lim_{\varepsilon \to \infty} \frac{N(\varepsilon)}{\ln(\frac{1}{\varepsilon})}. \tag{12.4}$$

This method can not be considered as accurate and precise since these features strongly depend on the chosen size of the volume cubes, which is necessary to be as small as possible. Decreasing edges lead to the necessity of using a huge number of the cubes and subsequently to the large demands on the personal computer performance, especially accessible memory. It is worth nothing that this is very time consuming approach.

Moreover there is a probability that several points on the state space orbit fall into one volume cube and some information about attractor geometry is lost. This drawback is partially solved by other calculation techniques involving probabilities like dimension spectrum and its derivatives, information [63] and correlation dimensions [77]. Thus this method can not be effectively used for the dynamical systems with the large state space attractors.

To end the discussion about suitable method for our purpose there are still some possibilities to quantify dynamical motion using the knowledge of some state variables as time-domain waveforms [64]. The utilization of some method for deriving largest LE from the time series is extremely sensitive to the routine parameters and does not provide precise results.

The above mentioned problems are the main reasons for the discovery of the novel method for metric dimension calculation. Two principles for evaluation of JM in the symbolical form will be addressed in the next section. Then we brings some information about the concept of new rough quantifier of the dynamical motion

different from the conventional metric dimensions together with some practical examples. Then we will discuss the possibilities to model GP system by using lumped analog and mixed electronic circuits. The experimental verification via the oscilloscope screen-shots has been also presented.

The last section covers some perspectives for future work and opens the virtual space for solving the residual problems.

12.1 Numerical Analysis

To obtain a brief insight into the global dynamics of equations (12.1) the numerical integration has been performed. To do this program Mathcad and build-in fourth-order Runge-Kutta method has been used with final time $t_m = 1000$ and time step $t_\Delta = 0.1$.

The initial conditions were chosen to be $\mathbf{x}_0 = (0.1, 0, 0)^T$ and the results are given in Fig. 12.1, Fig. 12.2, Fig. 12.3, Fig. 12.4, Fig. 12.5 and Fig. 12.6 as the three-dimensional perspective views.

Rough approximation of sign functions means that only two harmonics are used in Fourier series. On the contrary, five harmonics are taken into account for soft approximation of sign functions.

Obviously there have been no significant changes in the global dynamics or attractor shape. Note that for small values of a_x, a_y and a_z the corresponding state attractors are bounded in very large state space volume.

The major property of chaotic solution is its extreme sensitivity to the changes of the initial conditions. This is demonstrated by a time dependence of the absolute error of the selected state variable. The initial conditions for reference system have been slightly different $\mathbf{x}_1 = (0.101, 0, 0)^T$.

The exponential divergence of both state trajectories is visible in Fig. 12.7 and Fig. 12.8. A very useful tool for brief dynamical system analysis is the so-called Poincare sections. These state space subsets allow reducing the order of studied system by one. In the case of three state variables the flow is reduced to the map on the plane, see Fig. 12.9, Fig. 12.10 and Fig. 12.11. For each simulation in this

chapter the complexity parameters were $b_x = b_y = b_z = 10$.

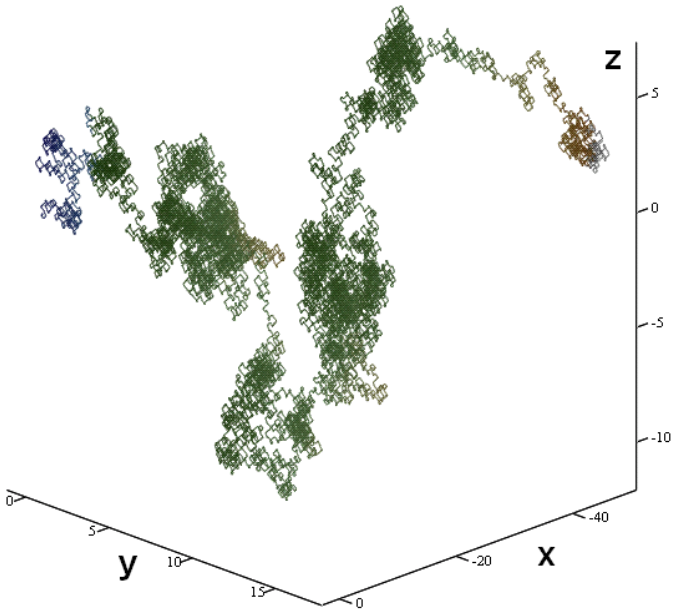

Fig. 12.1: Typical attractors of GP system with uniform parameters $a_x = a_y = a_z = 0$.

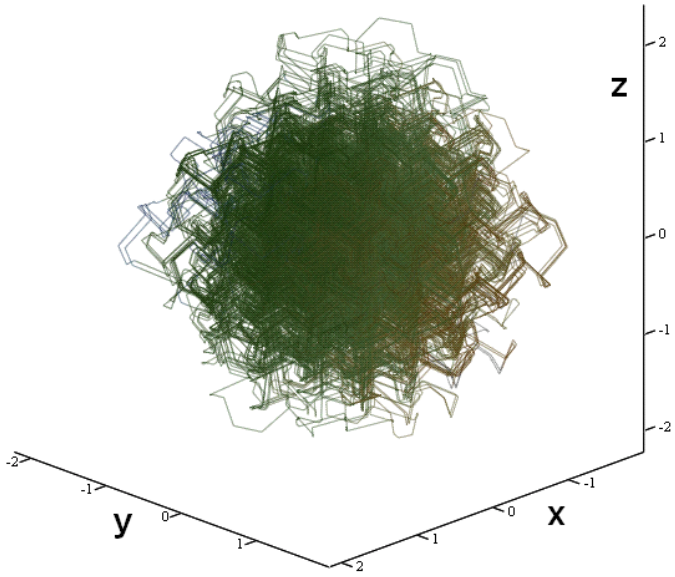

Fig. 12.2: Typical attractors of GP system with uniform parameters $a_x = a_y = a_z = 0.3$.

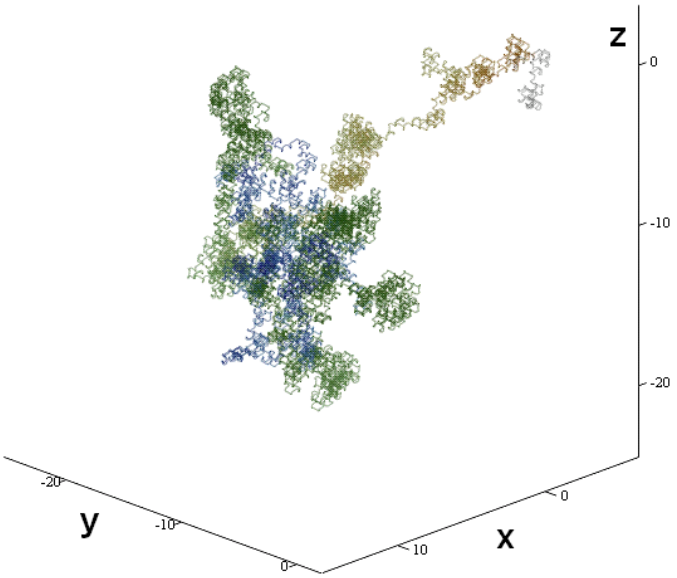

Fig. 12.3: Typical attractors of GP system with rough approximation of the sign function (see text) and uniform parameters $a_x = a_y = a_z = 0$.

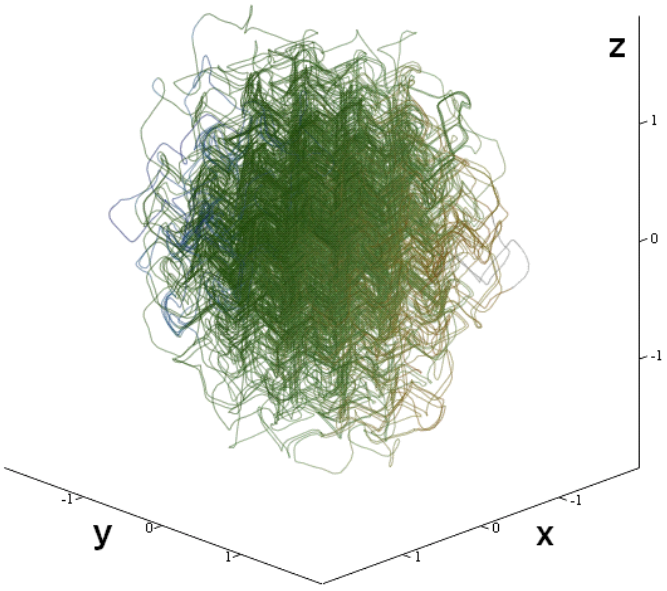

Fig. 12.4: Typical attractors of GP system with rough approximation of the sign function (see text) and uniform parameters $a_x = a_y = a_z = 0.3$.

12.2 Calculation Methods

As mentioned in the first section of this chapter the key problem of system (12.1) quantification is in the symbolical form of the JM. The sign function can be split into segments with zero partial derivative A_0 and regions with positive infinity $+A_\infty$ and negative infinity partial derivative $-A_\infty$. The associated characteristic polynomial

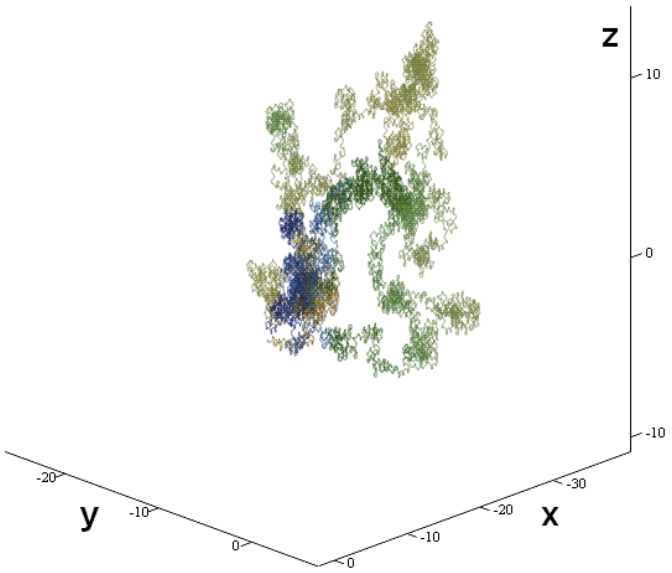

Fig. 12.5: Typical attractors of GP system with soft approximation of the sign function (see text) and uniform parameters $a_x = a_y = a_z = 0$.

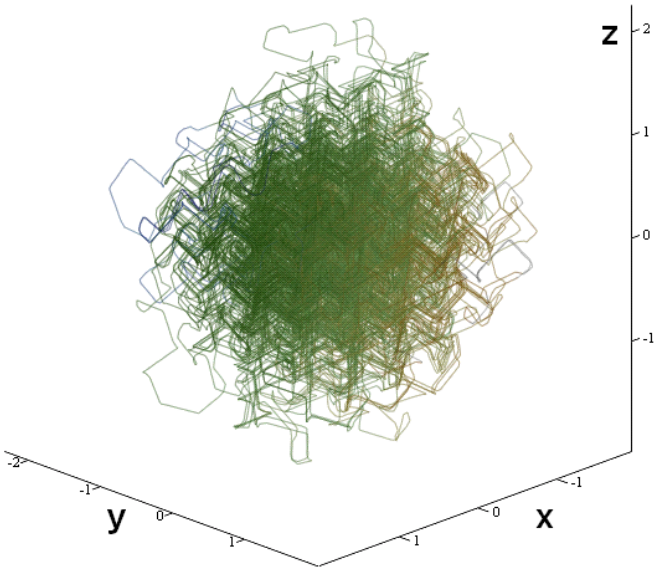

Fig. 12.6: Typical attractors of GP system with soft approximation of the sign function (see text) and uniform parameters $a_x = a_y = a_z = 0.3$.

becomes:

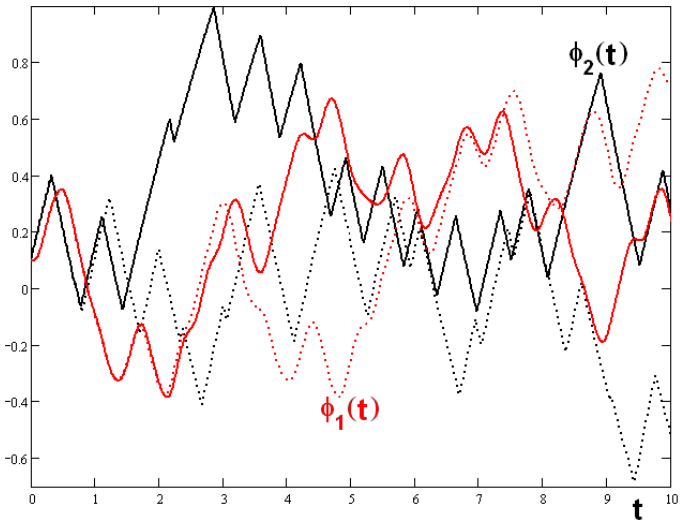

Fig. 12.7: Sensitivity to the changes of the initial conditions for original Thomas system (red curve) and GP system (black flow) and uniform parameters $a_x = a_y = a_z = 0$.

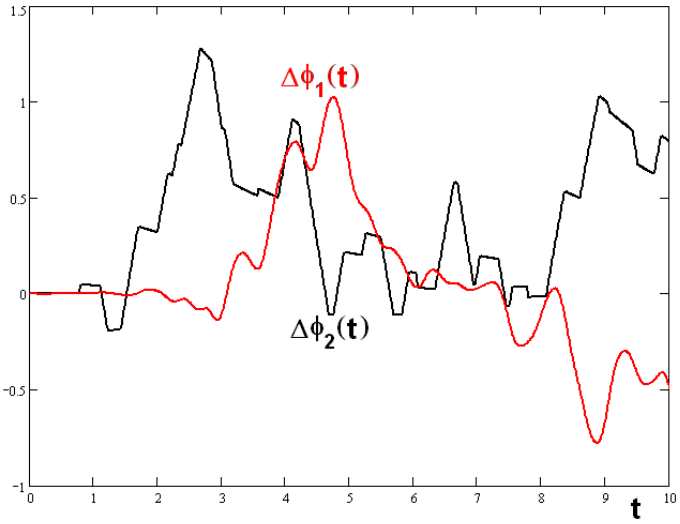

Fig. 12.8: Sensitivity to the changes of the initial conditions for original Thomas system (red curve) and GP system (black flow) and uniform parameters $a_x = a_y = a_z = 0.3$.

$$\begin{aligned} \det(\lambda \cdot \mathbf{E} - \mathbf{J}) &= \begin{pmatrix} \lambda - a_x & -\varphi_x & 0 \\ 0 & \lambda - a_y & -\varphi_z \\ -\varphi_x & 0 & \lambda - a_z \end{pmatrix} \\ &= (\lambda - a_x)(\lambda - a_y)(\lambda - a_z) - \varphi_x\varphi_y\varphi_z = 0, \end{aligned} \tag{12.5}$$

where $\varphi = 0$ inside each segment of the vector field and $\varphi = \pm\infty$ on the bound-

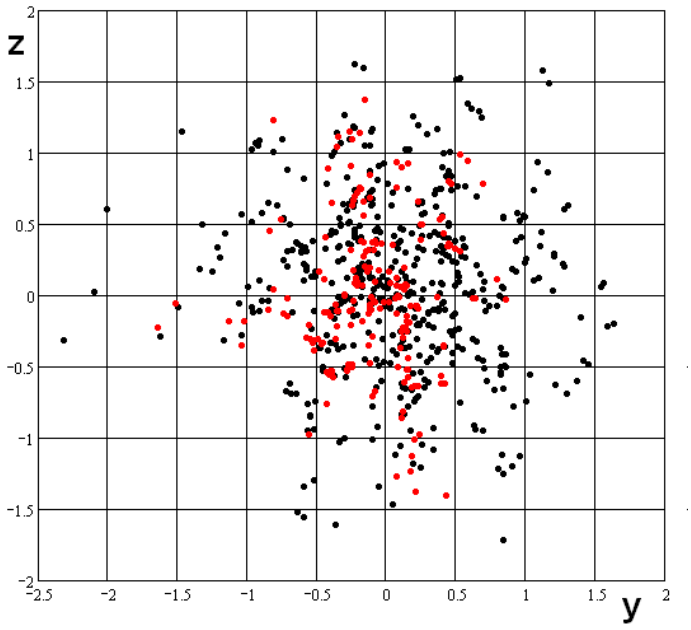

Fig. 12.9: Attractor visualization using different Poincare sections corresponding to the planes $x = 0$,$y = 0$ and $z = 0$ for original Thomas system (red dots) and GP system (black dots) and uniform parameters $a_x = a_y = a_z = 0.3$.

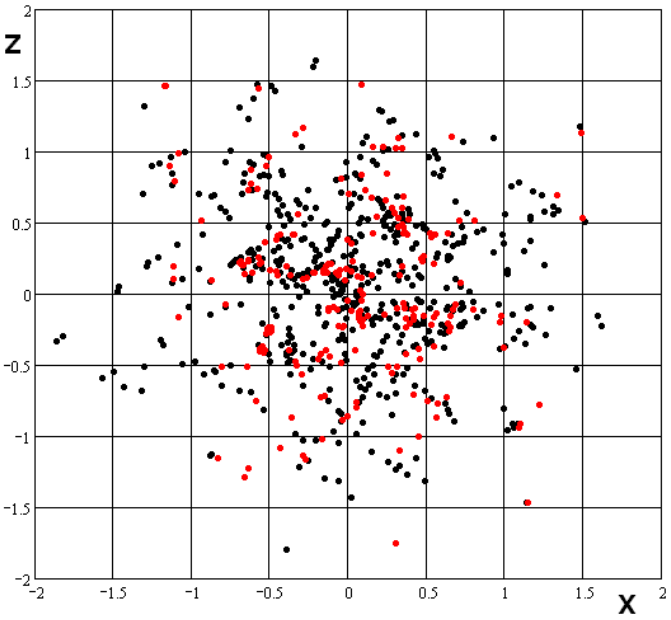

Fig. 12.10: Attractor visualization using different Poincare sections corresponding to the planes $x = 0$,$y = 0$ and $z = 0$ for original Thomas system (red dots) and GP system (black dots) and uniform parameters $a_x = a_y = a_z = 0.3$.

aries. The idea about the individual state variables time dependence is provided in Fig. 12.12 and Fig. 12.13 for $z(t)$.

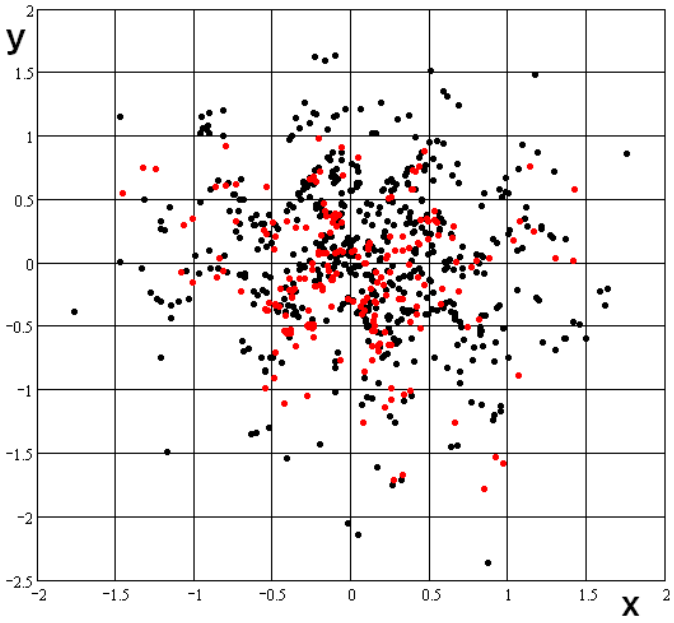

Fig. 12.11: Attractor visualization using different Poincare sections corresponding to the planes $x = 0$,$y = 0$ and $z = 0$ for original Thomas system (red dots) and GP system (black dots) and uniform parameters $a_x = a_y = a_z = 0.3$.

The dynamics of GP system is compared with the smooth Thomas system [68] in the sense of third differential equation (12.1) which evolves accordingly to the following analytic formula (using separation of the variables):

$$\frac{dz}{dt} = a_z z + f(x) \Rightarrow z(t) = \frac{1}{a_z}[e^{a_z t} - f(x)], \tag{12.6}$$

where $f(x) = \text{sign}[sin(bx)]$ and $g(x) = sin(bx)$. This solution can be interpreted as increasing if $f(x) = 1$ and decreasing if $f(x) = -1$ with uniform ratio proportionally to parameter a_z. A more comprehensible image about dynamical motion governed by the last equation (12.1) is shown in Fig.12.14 and Fig.12.15. The raising and falling segments with size $k\pi/bx$ and $k\pi/bx$ where $k \in (-\infty, +\infty)$ is a natural number are also clarified in these Monge projections.

The most straightforward approach to avoid problems with infinity is to expand the periodical sign function into the Fourier series. It is well known that the square wave, if generated by sine function, can be expressed as:

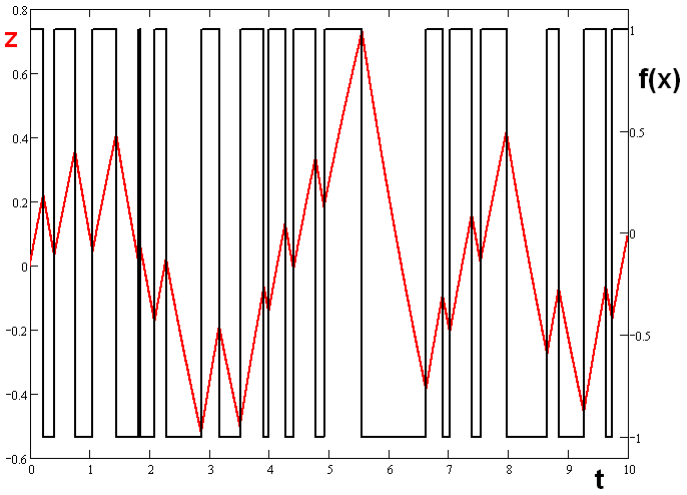

Fig. 12.12: The state variable z(t) waveform of GP system with uniform parameters $a_x = a_y = a_z = 0.3$.

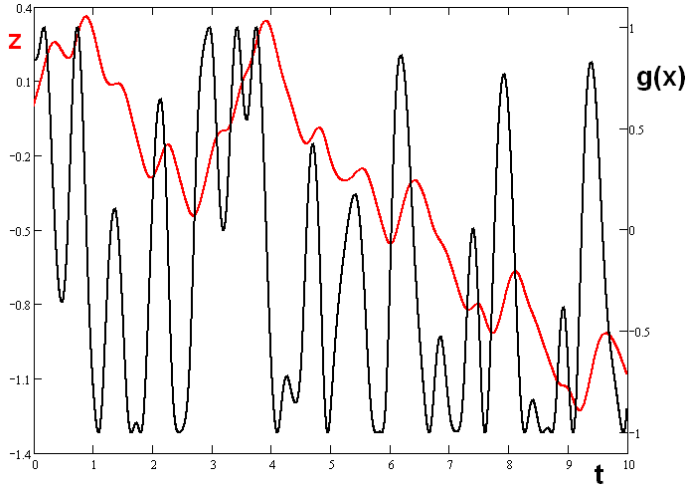

Fig. 12.13: The state variable z(t) waveform of Thomas system with uniform parameters $a_x = a_y = a_z = 0.3$.

$$f(bx) = \frac{4}{\pi} \sum_{n=1}^{k} \frac{1}{2n-1} \sin[b(2n-1)x], \tag{12.7}$$

where k is order of the approximation. Its derivation in the symbolical form:

$$g(bx) = \frac{4}{\pi} \sum_{n=1}^{k} b \sin[b(2n-1)x], \tag{12.8}$$

is adopted inside JM. This approach bears a significant numerical error due to the so-called Gibbs effect [74]. Intuitively speaking, the magnitude of such error

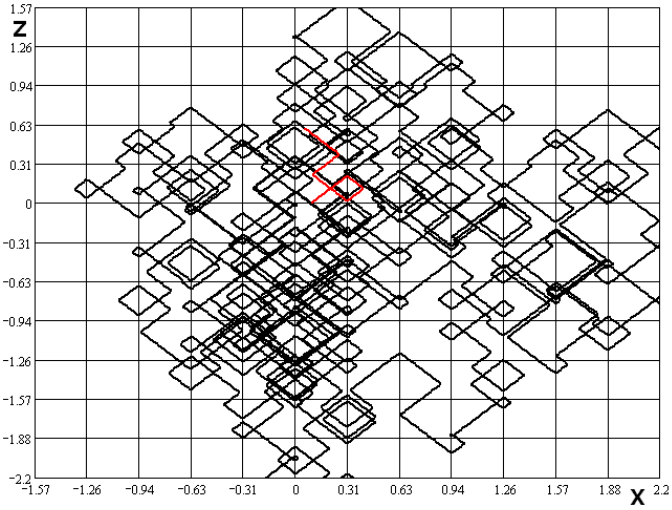

Fig. 12.14: The dynamical motion clarification for the last differential equation using xz plane projection, uniform parameters $a_x = a_y = a_z = 0.1$.

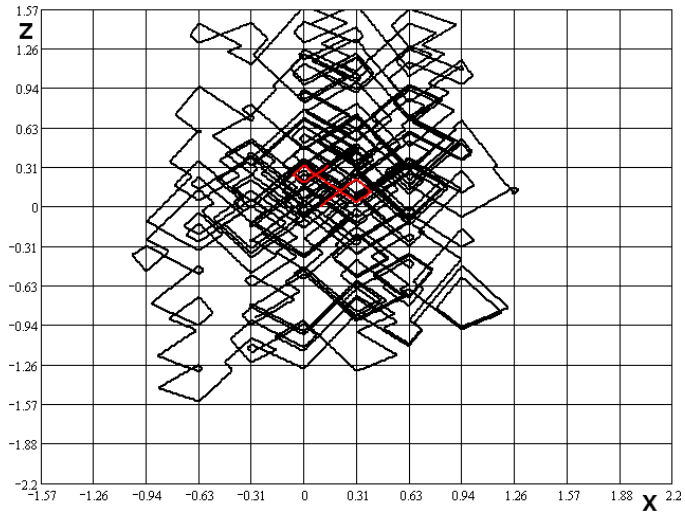

Fig. 12.15: The dynamical motion clarification for the last differential equation using xz plane projection, uniform parameters $a_x = a_y = a_z = 0.3$.

depends on the integration step size. Gibbs effect introduces the fiction of the short-time decreasing volume element expansion and contraction under the dynamical flow. There are some other smooth functions with continuous derivatives that can be utilized like exponential or sigmoid functions.

It turns out that calculating the spectrum of LEs by the usage of the immediate numerical value of the derivative by storing previous values of the corresponding state variable, can not be used.

Extreme values of derivatives causes divergences in computation. Changing the step of numerical integration can avoid the extreme values of derivatives, but causes deviance in the final attractor itself. The topographically scaled contour-surface plots of the largest LE as a function of $a = a_x = a_y = a_z$ and $b = b_x = b_y = b_z$ are provided in Fig.12.16, Fig.12.17, Fig.12.18 and Fig.12.19.

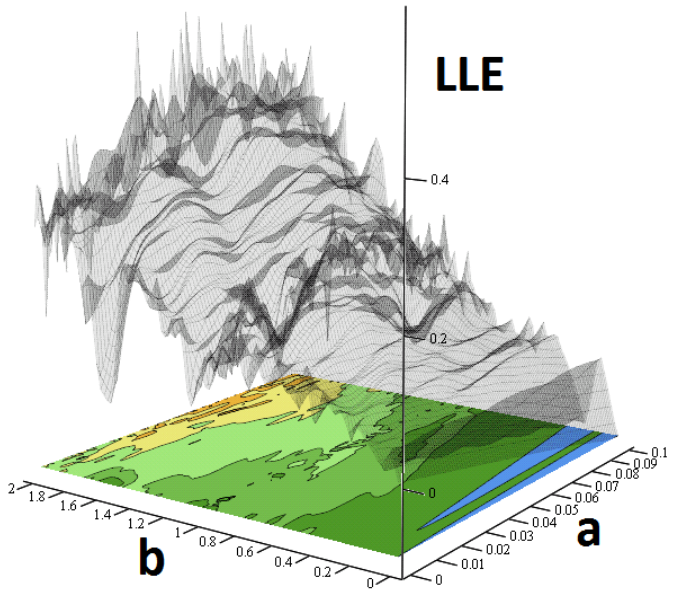

Fig. 12.16: Plot of the largest LE of GP system with uniform parameters $a_x = a_y = a_z \in < 0, 0.1 >$, rough approximation of the sign(.) function. In both plots $b \in < 0, 2 >$.

12.3 Spherical Quantification

There is a lack of suitable methods for quantifying behavior of almost conservative systems with large strange attractors. Therefore we present spherical quantification in order to classify behavior of the attractor.

The proposed approach is based on the fundamental nature of the strange attractors, namely its ergodicity and mixing property. To greatly shorten the computational time the three-body problem should be exchanged by the mathematical operations on the plane, in detail on the surface of the sphere.

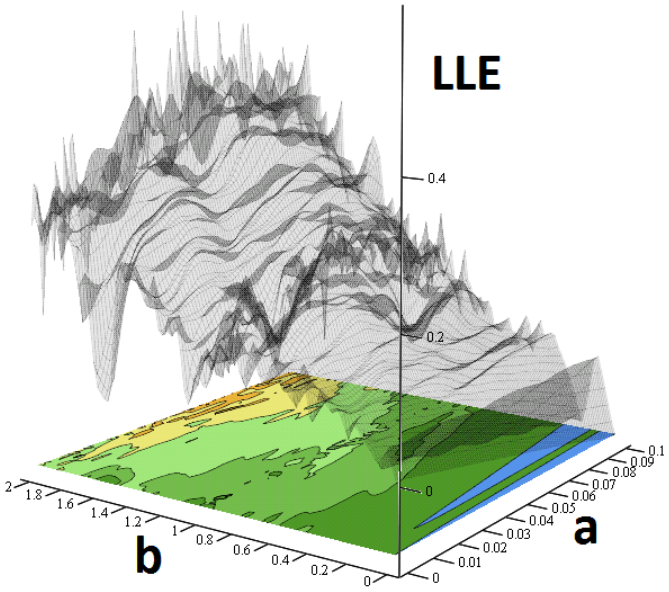

Fig. 12.17: Plot of the largest LE of GP system with uniform parameters $a_x = a_y = a_z \in < 0.25, 0.35 >$, rough approximation of the sign(.) function. In both plots $b \in < 0, 2 >$.

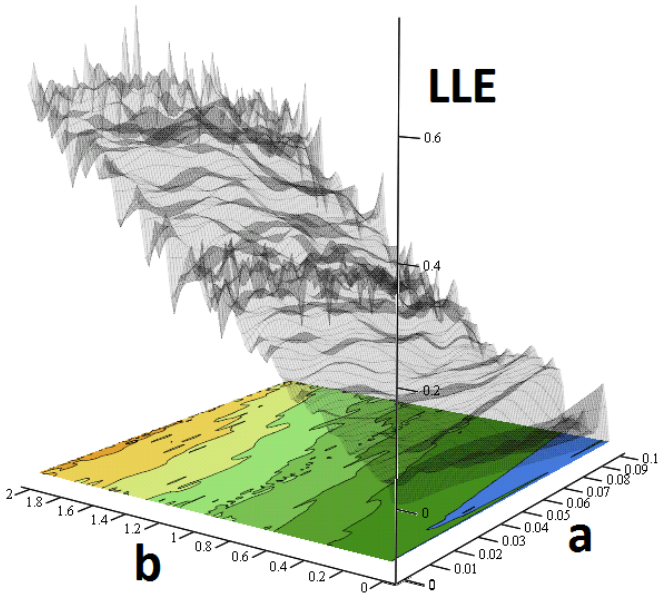

Fig. 12.18: Plot of the largest LE of GP system with uniform parameters $a_x = a_y = a_z \in < 0, 0.1 >$ (left), smooth approximation of the sign(.) function. In both plots $b \in < 0, 2 >$.

The principle of calculation lies in the transformation of the analyzed attractor from the Cartesian coordinates into the sphere. First the surface of $\mathbb{R}^3$ sphere is

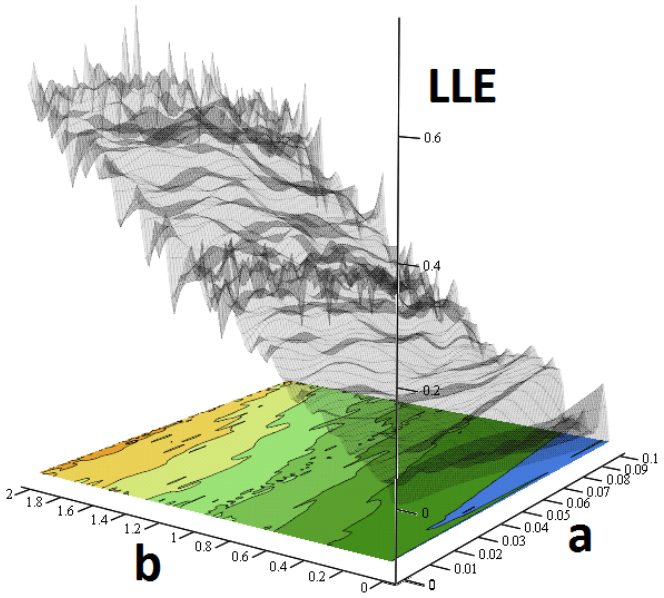

Fig. 12.19: Plot of the largest LE of GP system with uniform parameters $a_x = a_y = a_z \in < 0.25, 0.35 >$, smooth approximation of the sign(.) function. In both plots $b \in < 0, 2 >$.

normalized to have general quantifier. Using the spherical coordinates, the unit sphere can be parameterized by:

$$\begin{aligned} \vec{r}(\theta, \varphi) &= (\cos\varphi \sin\varphi, \sin\theta \sin\varphi, \cos\varphi), \\ \wedge \qquad & 0 \leq \theta \leq 2\pi, 0 \leq \varphi \leq \pi. \end{aligned} \tag{12.9}$$

Than the area A of sphere S is set to be equal to 1 (normalization) can be expressed as:

$$A(S) = \int_S |\vec{r}_u \times \vec{r}_v| du dv = 1. \tag{12.10}$$

Thus for the square radius r^2 of $\mathbb{R}^3$ sphere stands:

$$r^2 = \frac{1}{4\pi}. \tag{12.11}$$

Radius of this sphere is chosen $r = (4\pi)^{-1/2}$ such that the sum of all SP is unity. This globe splits into elemental surface pieces (SP) depending on the $\Delta\varphi$, $\Delta\theta$ angle steps:

$$\theta = \arctan\left(\frac{y}{x}\right), \tag{12.12}$$

$$\varphi = \arccos\left(\frac{z}{r}\right). \tag{12.13}$$

Assuming attractor will fill the entire space of $\mathbb{R}^3$ where integral step limit approaches zero, meaning the likelihood has a continuous uniform distribution $P(x)$ is described:

$$P(x) = \begin{cases} \frac{1}{b-a} & \text{for } a \leq x \leq b \\ 0 & \text{for } x < a \text{ or } x > b \end{cases} \tag{12.14}$$

Than the surface of whole sphere can be expressed as:

$$S_{Sphere} = \int_0^{\pi} \int_0^{2\pi} \frac{1}{4\pi} \sin\theta d\varphi d\theta = 1. \tag{12.15}$$

Considering the discrete time series, the step $\Delta\theta$ and $\Delta\varphi$ needs to be set, otherwise certain SP needs to be deleted to have particular list of SP the complexity of the analyzed attractor.

Following the flow $\Phi(x, y, z)$ of attractor in $\mathbb{R}^3$ of N elements, each SP is indexed by the natural numbers i and j. In the main calculation routine the individual SP occupied by a state trajectory are summarized.

The surface of occupied area on the $\mathbb{R}^3$ sphere can be calculated using the following discrete formula:

$$S_{\Phi} = \sum_{i=1}^{N} \sum_{j=1}^{N} \frac{1}{4\pi} \sin(i\frac{\pi}{N}) 2ij \frac{\pi^2}{N^2}. \tag{12.16}$$

The graphical interpretation of this novel motion quantifier is demonstrated in Fig.12.20, Fig.12.21, Fig.12.22, Fig.12.23, Fig.12.24 and Fig.12.25 for some interesting situations.

There is one serious drawback of this procedure leading to the indispensable numerical errors. The shape and orientation of the state attractor can be right-lined as it is visible in the first two examples. If so, a huge amount of the information about attractor geometric structure is lost. To improve this disadvantage the linear change of the coordinates in order to spread the studied attractor should be performed before transformation on the sphere.

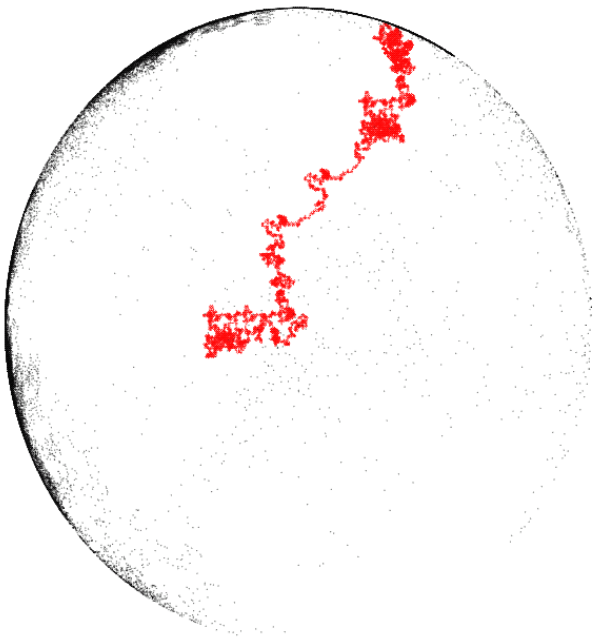

Fig. 12.20: The dynamical motion quantification, analyzed attractor (red) and its projection on sphere (black), GP system with uniform parameters $a_x = 0.1$ and $a_y = a_z = 0$.

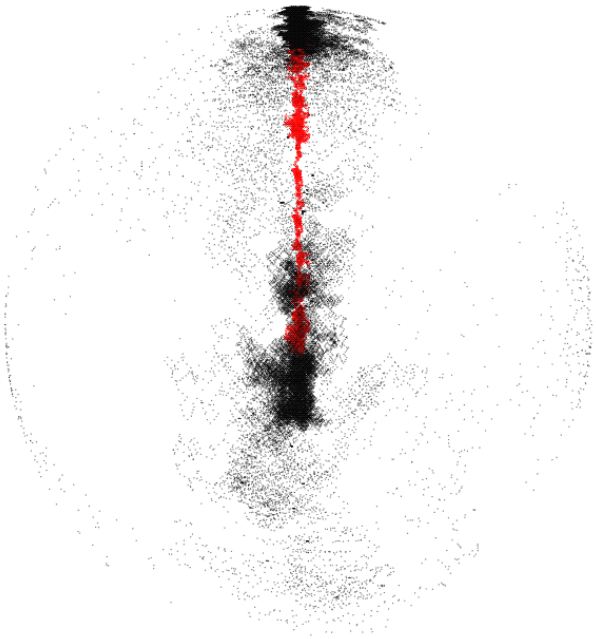

Fig. 12.21: Another view on the dynamical motion quantification, analyzed attractor (red) and its projection on sphere (black), GP system with uniform parameters $a_x = 0.1$ and $a_y = a_z = 0$.

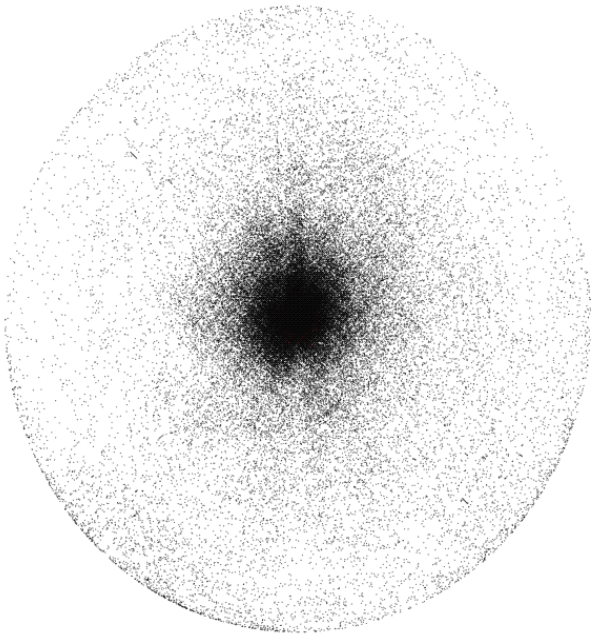

Fig. 12.22: The dynamical motion quantification, analyzed attractor (red) and its projection on sphere (black), GP system with uniform parameters $a_x = a_y = 0.1$ and $a_z = 0$.

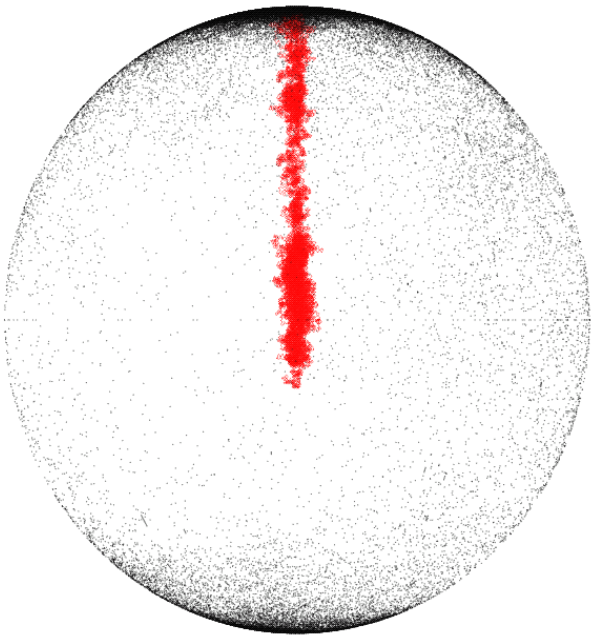

Fig. 12.23: Another different view on the dynamical motion quantification, analyzed attractor (red) and its projection on sphere (black), GP system with uniform parameters $a_x = a_y = 0.1$ and $a_z = 0$.

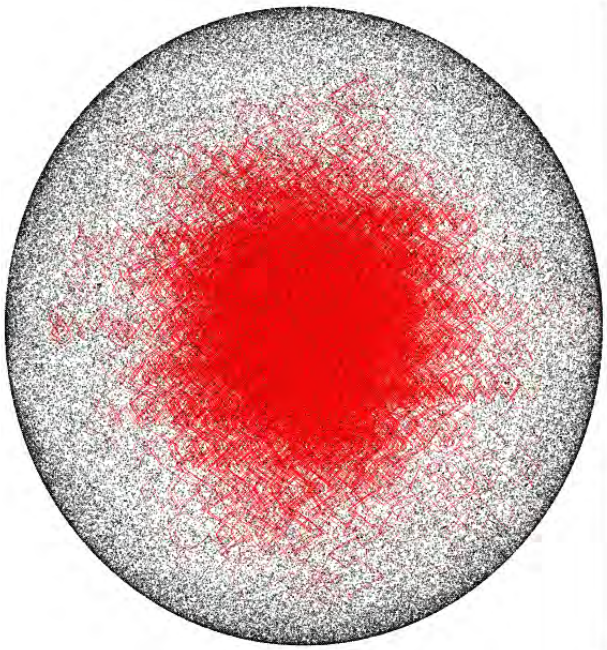

Fig. 12.24: The dynamical motion quantification, analyzed attractor (red) and its projection on sphere (black), GP system with uniform parameters $a_x = a_y = a_z = 0.1$.

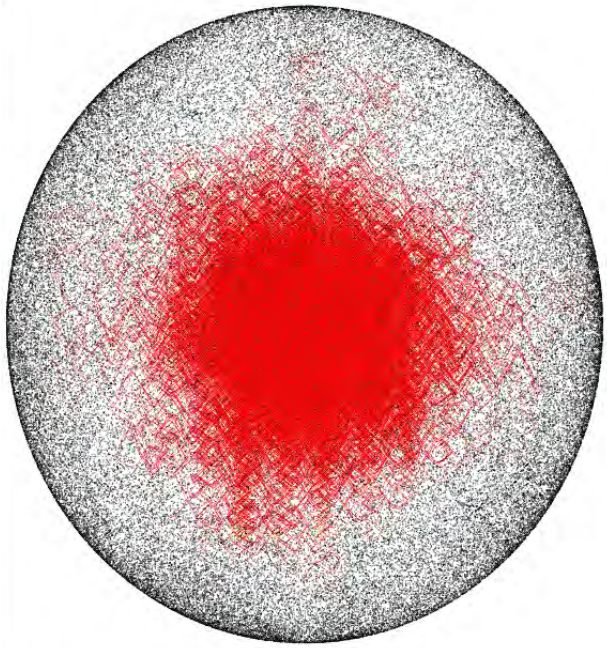

Fig. 12.25: Another different view on the dynamical motion quantification, analyzed attractor (red) and its projection on sphere (black), GP system with uniform parameters $a_x = a_y = a_z = 0.1$.

12.4 Circuitry Implementation

It is well known that synthesis of the electronic circuits is the easiest way how to accurately model the nonlinear dynamical systems. There are three major and widely used systematic approaches: classical circuit synthesis [88, 89], direct implementation of the differential equation [68, 90, 91, 131, 132, 134] and design procedure based on the integrator block schematic [71, 138, 136]. Each mentioned design approach has some advantages and drawbacks.

The circuitry implementation of the continuous time dynamical systems with accessible chaotic behavior is called chaotic oscillator. Due to the stretching mechanism usually caused by single or multiple unstable equilibrium the corresponding circuit must contain one or more active elements [69] supplying energy to the passive parts.

The most straightforward way for practical realization of Thomas dynamical system as well as GP oscillator starts with block schematic with inverting integrators, differential amplifiers (with summation block as a special case) and two-port with desired nonlinear transfer characteristics.

One possible network suitable to model GP system is given in Fig.12.1 and Fig.12.2. The disadvantage of such configuration is clear: a large amount of the active building blocks. The linear part of the vector field is composed of the linear lossy integrators realized by the second generation positive current conveyor (CCII+) with current summation at the input port. CCII+, in particular the integrated circuit AD844, is described by the set of following hybrid equations:

$$i_y = 0 \; u_x = u_y \; i_z = i_x \; u_0 = u_z. \tag{12.17}$$

The purpose of CCII+ is also for easy measurement of the nonlinear function, which is represented by voltage at the output u_0. The principle of the piecewise-constant function is fundamental. The operational amplifiers act as comparators (CMP) without hysteresis effect. The transfer function and integration can be expressed by single equation in Laplace transform:

$$u_0 = -\frac{1}{sC + G} \sum_{k=1}^{i} \frac{u_k}{R_{xk}}, \tag{12.18}$$

where $G = 1/R$, uk are voltages at the output of CMP and i is the number of necessary CMP which is closely related to the dissipation factors a_x, a_y, a_z adjustable by the variable resistors R.

The size of accessible state attractor is upper limited by the dynamical ranges of the OPA, i.e. by supply voltages $V_{cc} = +15V$ and $V_{ee} = -15V$. The breakpoints of the transfer curve are adjusted either by external dc sources or voltage divider made by the resistors R_{di}.

The time-domain simulation of the fully analog GP system is shown in Fig. 12.3 and Fig. 12.4 as the plane projections of the strange state space attractors.

The main drawback of the fully analog oscillator conception is obvious, a huge number of the active elements. The idea behind digital approach is uncovered in Fig.12.26.

The linear part of the vector field remains the same as for previous oscillator. The input signal enters analog-to-digital converter (ADC), goes through processor programmed in C/C++ using KEIL uVision V3.90 and resulting waveform is finally transformed back into the analog form by digital-to-analog converter (DAC).

The slowest operation is computing trigonometric function. The maximum working frequency is about 230 kHz and this boundary has been verified either by numerical study in Mathcad (sampling and quantization mechanism) as well as by experimental measurement.

The selected digital oscilloscope screen-shots are provided in Fig.12.27, Fig.12.28 and Fig.12.29 proving almost one-to-one correspondence between the theoretical expectations and the practical results.

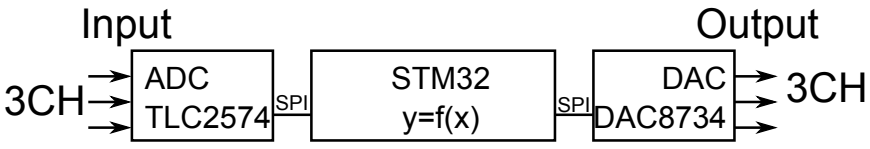

Fig. 12.26: Experimental setup for implementation of GP system by means of six-port with digital signal processing.

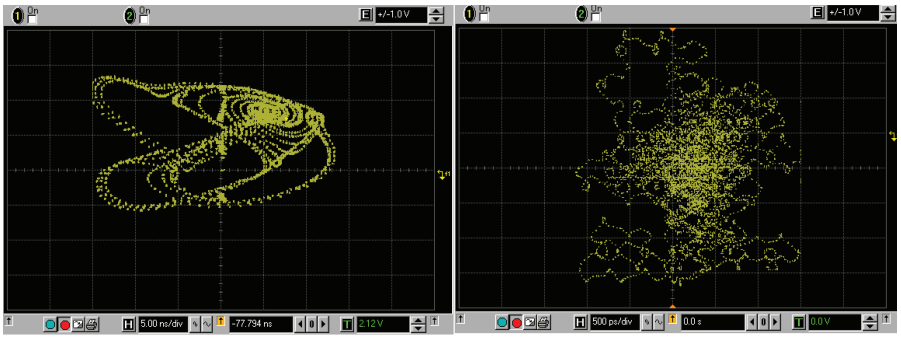

Fig. 12.27: Experimental verification of mixed circuit design of GP system measured by Agilent Infiniium.

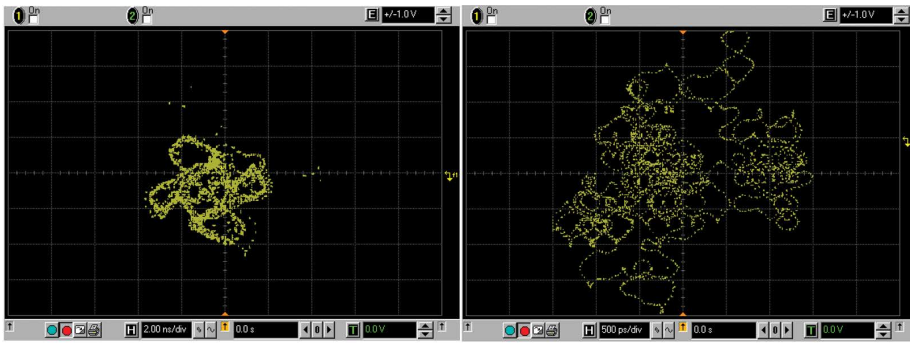

Fig. 12.28: Experimental verification of mixed circuit design of GP system measured by Agilent Infiniium.

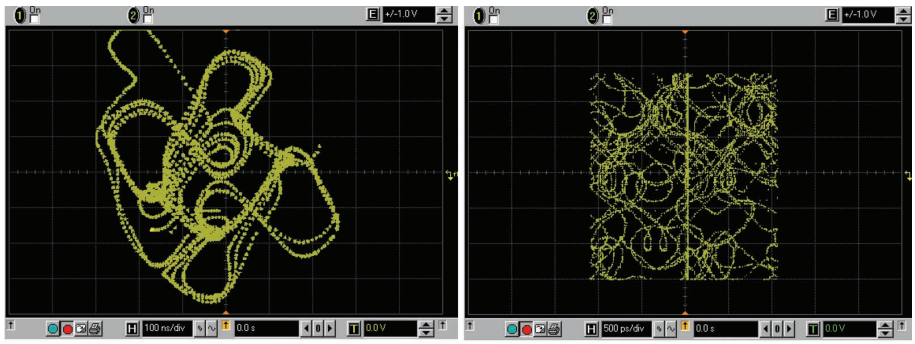

Fig. 12.29: Experimental verification of mixed circuit design of GP system measured by Agilent Infiniium.

After thinking about how to reduce the complexity of the nonlinear network a very simple circuitry has been revealed. The stair-type function can be realized by single ADC, namely by considering its least significant bit. Of course the input voltage range should be adjusted accordingly to the parameter b_x, b_y and b_z. The output voltage level should be also carefully monitored and shifted by negative offset

voltage if necessary. The realization itself can be seen in Fig.12.31 and in Fig.12.32 and its circuit simulations using Orcad Pspice 15 environment in Fig.12.30 and in Fig.12.33

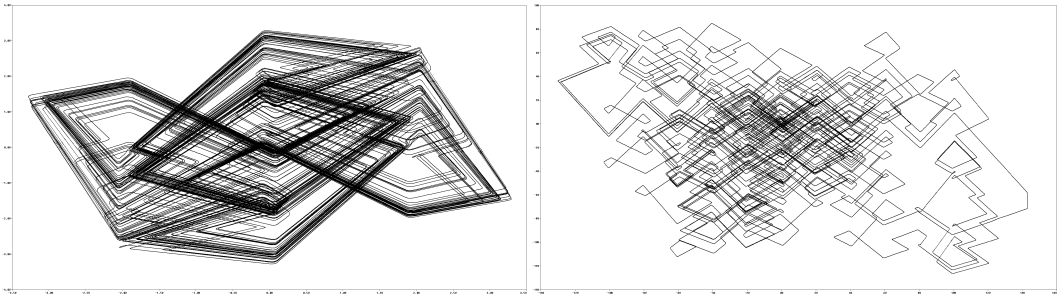

Fig. 12.30: The plane projections of the state space trajectories simulated in Orcad Pspice 15 environment, $b_x = b_y = b_z = 10$ together uniform dissipation parameters $a_x = a_y = a_z = 0.5$ (left) and $a_x = a_y = a_z = 0.2$ (right).

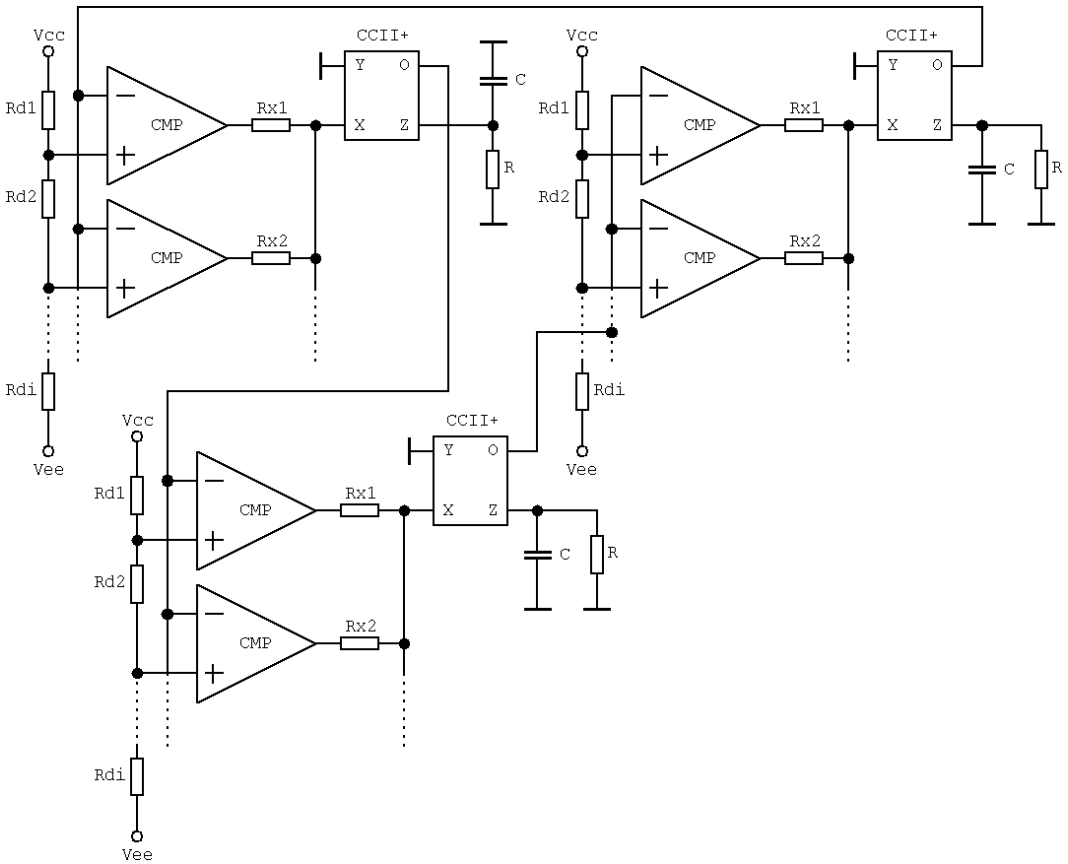

Fig. 12.31: Fully analog implementation of GP system using AD844 (CCII+) and TL084 (OPA).

In this particular case, two ADC blocks have been used. One for positive voltage with positive voltage reference VREF1 and other for negative VREF2. Voltage offset is added by voltage sources VOFF.

In fact, only one ADC can be used with positive and negative voltage dynamical range. Resistors $R_d \sim 1k\Omega$. The parameter b is set directly by the sampling frequency of the converter itself. Values of parameter a_x, a_y and a_z are set by resistors R_x, R_y and R_z.

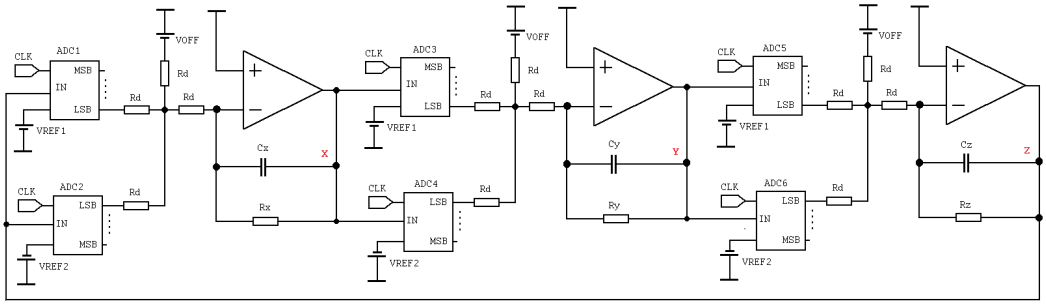

Fig. 12.32: GP system realization by using ADC as core engine for the nonlinear building block.

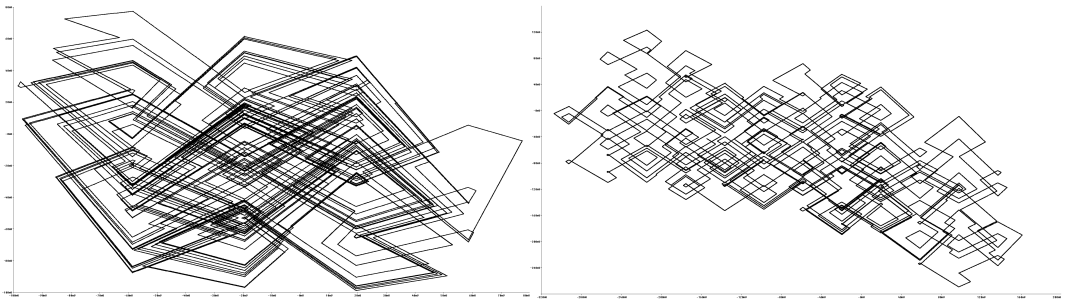

Fig. 12.33: The plane projections of the state space trajectories of ADC realization simulated in Orcad Pspice 15 environment, $b_x = b_y = b_z = 10$ together uniform dissipation parameters $R_x = R_y = R_z = 10k\Omega$ (left) and $R_x = R_y = R_z = 70k\Omega$ (right).

12.5 Conclusion

Several ideas from the area of numerical analysis of the dynamical systems with low dissipation have been suggested and verified. These procedures allow solving the serious problems where standard existing procedures can not be used.

Moreover, the authors believe that GP oscillator models the three-dimensional Brownian-like motion [92] of the single microscopic particle without interactions.

The vector field discontinuity and flow jumping resembles the particle-like behavior known from the quantum theory [93]. There is no doubt that there are a lot of real physical systems with the similar mathematical description.

13 GENERALIZATION OF PIECEWISE-LINEAR APPROXIMATION OF THE CHAOTIC DYNAMICS

Autonomous nonlinear dynamical systems attract increasing interest of mathematicians, physicists as well as design engineers. Several features leads to the necessity of studying and understanding dynamical motion associated with arbitrary-order nonlinear systems.

Firstly the real nature entities are generally nonlinear, however approximately, they can be described by a set of the ordinary differential equations.

Secondly, a dimensionless form of the state description makes any kind of analysis interdisciplinary since one mathematical model can be associated with multiple phenomenon rendering the concrete interpretation of state variables.

Last but not least, nonlinear dynamical systems having at least three degrees of freedom can exhibit unpredictable noise-like behavior called chaos. For better clarification, the so-called chaotic motion is solution extremely sensitive to tiny changes of the initial conditions while forming bounded and dense state space attractors with fractal metric dimension.

The most catching in electrical engineering is the fact that circuitry implementation of the deterministic system can provide striking explanation for irregular behavior and anomalies in many systems which does not seem to be implicitly stochastic. The basic obstacle to be removed in this area lies in the lack of closed form analytical solutions for most of the higher-order nonlinear dynamical systems. This can be overcome by using numerical methods for the analysis and by linearizing the continuous vector field by suitable piecewise-linear (PWL) function.

A lot of simple PWL mathematical functions were already developed. For example let recall same fundamental types as explicit ones presented in [94, 95] or implicitly given published in[96]. The linearization of vector field is not a new idea, but finding the singular solution in order to preserve chaotic or hyper-chaotic motion by optimization algorithms was not proposed. In the case of vector fields with stretching and folding property this task is a little bit tricky.

The least mean square method (or derived procedures) cannot provide satisfac-

tory results, i.e. desired chaotic attractor can be deformed or completely degraded into complex limit cycles. The main difficulty is that the numerical values of PWL function coefficients does not have direct relation to chaotic nature of given dynamical system with smooth polynomial vector field.

Next section will be focused on the individual aspects of behavior quantification and its utilization as a core engine for vector field approximation. Then we brings mathematical models as examples suitable for algorithm verification. Fourth section is aimed to the numerical results proving structural stability of the discovered chaotic attractors. All will conclude by short discussion of next modifications and research challenges in this area.

13.1 Problem Formulation

Following the rules of linear algebra, it is much easier to get insight into global motion and attracting sets of the dynamical system by using PWL approximation of the continuous vector field.

Vector field with several affine segments also represents much simpler model for circuitry realization in which PWL transfer function is composed of diodes, external and controlled voltage or current sources.

It is evident that chaotic oscillator designed in such a way is more accurate (if comparing numerical integrations and the laboratory measurements), has wider dynamical ranges (larger state space volume can be modeled) and operates with higher harmonic frequency components [122]. All these features predetermine chaotic PWL dynamical systems for future practical applications.

As mentioned before minimization of error between the original vector field and its linearized equivalent cannot be done by utilization of some existing method. Some preliminary ideas toward answer to this problem have been demonstrated in [97] where only algebraically simple third-order dynamical systems with single quadratic nonlinearity have been considered. To improve procedure developed by first author and make the final algorithm as universal as possible the dynamical systems with multi-dimensional polynomial functions will be addressed.

Lets suppose there are the significant polynomial nonlinearities in the mathematical model of the dynamical system with immediate impact on equilibria, eigenvalues, eigenvectors or, generally speaking, entire vector field geometry. After successful run of optimization routine these functions will be replaced by PWL counterparts. To ensure the chaotic attractor generated by the PWL system is topologically the same as reference attractor produced by original system precise dynamical behavior quantifier must be defined. One of the most widely used is spectrum of the Lyapunov exponents (LE) defined in section (10.1.3).

In the case of exponential divergence of two neighborhood trajectories (chaos) estimation of LEs is mandatory. Looking at definition of LE it is obvious that LEs are uniquely coupled by the given differential equations, more precisely by Jacobian matrix. The presence or absence of strange attractor is indicated by the largest LE, namely its positive or negative value respectively.

After a number of tests it seems that (13.1) is a fragile routine and many serious problems can be experienced while using it carelessly [144].

If summarizing the biggest issues the first place takes the attribute that the regions of chaos in hyperspace of the system parameters are very small and often surrounded by an unbounded solution. This corresponds to the fact that chaotic or hyper-chaotic waveform is produced by perfectly balanced system.

Routine for calculation LEs is also a subject to numerical errors providing incorrect results for discontinuous [142] or slowly divergent flows. For accurate values of LEs the length of transient motion should be guessed and this kind of behavior omitted. Having LEs numerically calculated we can use Kaplan-Yorke dimension (defined in section 10.1.3)of state space attractor defined as:

$$D_{KY} = D_T + |LE_{DT+1}|^{-1} \sum_{i=1}^{D_T} D_i, \tag{13.1}$$

where D_i are individual LEs sorted in descending order and D_T is a topological dimension.

For studied class of the third-order dynamical systems $D_T = 2$. The fitness function in the main optimization loop is a comparison (absolute difference) between D_{KY} of polynomial and PWL system.

We believe that if the initial guess is close enough to the correct solution and the optimization work properly the zero difference means that both state space attractors are very similar. Since there is no analytic representation of objective function the gradient methods cannot be used and the only remaining option is stochastic approach, for example genetic algorithm, particle swarm method or some deliberated modifications.

Complicated dynamical motion can be quantified differently than using metric dimension. The straightforward method is to implement objective function acting with absolute difference between numerical integration of the original and PWL dynamical system. Positive differences in each integration step are summed and consequent result has to be minimized. This approach is less time-consuming than comparison of D_{KY} but often give confusing outputs.

Another promising method is the calculation of normalized frequency spectrum of the chaotic waveform of original system. In each step of optimization frequency spectrum of PWL system is find out and compared to the reference. The main drawback of such method is evident from the definition term of discrete Fourier transform (DFT):

$$X(k) = \sum_{j=1}^{N} x(j) \left(e^{\frac{-2\pi i}{N}} \right)^{(j-1)(k-1)} \tag{13.2}$$

where analyzed state orbit is represented by vector $x(j)$ and k are a natural numbers up to value N (length of numerical integration).

The disadvantage of this optimization comes directly from the essence of DFT. The resolution of among individual frequency components has lower margin given by length of integration and upper boundary corresponding to sampling frequency, i.e. integration step.

For common values of these integration constants resulting frequency resolution is bad and the similarity between attractors of original and approximated system cannot be recognized. Thus re-sampling is recommended for a given length of the numerical integration. Moreover DFT belongs to the fast algorithms build-in almost any mathematical software or environment dedicated to signal processing.

No matter which one is finally employed the fitness function has to take into account the number and positions of the fixed points and associated eigenvalues of

original system. Discovered PWL system must preserve all these aspects otherwise new attractor can not be geometrically conjugated to the original.

In order to satisfy such requirements and criteria objective function has to be properly extended. If something changes (which should remain unchanged) the penalization of fitness function should be considered; in the case of genetics by excluding particular member from population or using the concept of dead bee in the case of swarm.

Of course length of numerical integration of reference polynomial and novel PWL dynamical system has to be exactly the same for D_{KY} and time-domain quantification.

Before start of searching procedure the ranges of the nonlinear functions input variables must be determined accordingly to the smallest state space volume needed to fully cover desired state space attractor.

It should be noted that the ability to recognize specific limit cycles or, sometimes, quasiperiodic trajectories is limited because each such orbit is characterized by one or two zero LE. This disadvantage is not removed in the case of behavior analysis in time or frequency domain.

All the results mentioned below have been achieved using powerful simulated annealing method [98] implemented in Matlab. For visualization of the numerical verification Mathcad and fourth-order Runge-Kutta method has been utilized with step size 0.01 and number of points 10^5. As a core process of optimization engine the total number of points was lowered to 10^4 and time step was set to 0.1.

Nowadays new aspect begins to play an important role in the choice of proper optimization method. It is a possibility to effectively use multi-core computers and take advantage of parallel processing. As shown in [130] the necessary calculation time can be reduced significantly.

13.2 Dynamical Systems Under Inspection

For experimental validation of proposed algorithm it will be tested by using few dynamical systems of some importance. First one is given by a famous Chua's equa-

tions [99] as follows:

$$\begin{aligned} \dot{x} &= 10\ (y + 0.143\ x - x^3) \\ \dot{y} &= x - y + z \\ \dot{z} &= -16\ y \end{aligned} \tag{13.3}$$

where dots denote time derivatives and x^3 is a cubic polynomial to be replaced by n-th segment scalar PWL function. Note that nonlinear function is odd-symmetrical leading to the analogical simplification of searched PWL function.

Note that linear part of the vector field is defined numerically and these values are excluded from the hyperspace dedicated for optimization.

The main goal is to use as simple approximation as possible. If searching for the parameters of PWL function fails this function will be modified into more complicated form by adding more breakpoints and linear segments defined by its slopes.

One dimensional PWL function can be expressed in following compact form:

$$f(x) = \beta_0 + \alpha_0\ x + \sum_{i=1}^{N} \alpha_i |x - \beta_i|, \tag{13.4}$$

where $f(x)$ is a scalar function of the input state variable x, α_i and β_i are the kernels of approximation, and N is total number of breakpoints.

In the case of (13.3) PWL function is expected into odd-symmetrical form:

$$f(x) = \alpha_0\ x + 0.5(\alpha_1 - \alpha_0)(|x + \beta| - |x - \beta|). \tag{13.5}$$

Using proposed optimization method unknown parameters of function (13.5) have been found as $\alpha_0 = 0.4$, $\alpha_1 = -0.5$, $\beta = 0.4$.

The comparison between old and new chaotic attractor known as double-scroll produced by dynamical system (13.3) is illustrated in Fig. 13.1.

Routine linear analysis of PWL dynamical system yields that total number of the fixed points, its stability indexes and rough position one-per-segment remains

unchanged.

Second example suitable for substituted PWL vector field is Rossler dynamical system [100]. It is described by three first-order differential equation:

$$\begin{aligned} \dot{x} &= -y - z \\ \dot{y} &= x + 0.1\ y \\ \dot{z} &= 0.1 + x\ z - 14\ z. \end{aligned} \tag{13.6}$$

Rossler system produce the so-called funnel attractor; its shape should be kept even after PWL approximation. Since polynomial nonlinearity is no longer one-dimensional the PWL function should be redefined as:

$$f(x) = \alpha_0 + \beta_0\ x + \gamma_0\ y + \sum_{i=1}^{N} \delta_i |\beta_i\ x + \gamma_i\ y + \alpha_i|, \tag{13.7}$$

where α_i, α_i, γ_i and δ_i are parameters to be found during optimization. The suggested search procedure celebrates success with the set $N = 2$, $\alpha_0 = 0$, $\beta_0 = -1$, $\gamma_0 = -3$, $\alpha_1 = -9$, $\beta_1 = 18$, $\gamma_1 = 3$, $\delta_1 = 3$, $\alpha_2 = -0.8$, $\beta_2 = 6$, $\gamma_2 = -1$ and $\delta_2 = -8$.

Note that it is not necessary to calculate individual values to more than one decimal degree. Such knowledge can speed-up optimization especially in the cases where unknowns are coded as genes and sorted as chromosomes. The numerical validation of these coefficients is provided by means of Fig.13.2.

Obviously this PWL approximation is less accurate than it can be by using least means squares or some other method. Nevertheless the main goal is to preserve the chaotic structure of the state space attractor.

Lower picture in the Fig.13.2. represents topographically-scaled surface-contour plot of the largest LE as a function of dissipation constants which appear in the second and third equation of system (13.6).

For clarification, white and yellow color marks the regions of the chaotic solution, green is for trivial and complex limit cycles and dark blue for fixed point solution.

This pattern can differ if it is calculated for the original and the approximated dynamical system. For practical applications final attractor should be situated in the center of the chaotic region in hyperspace of the system parameters.

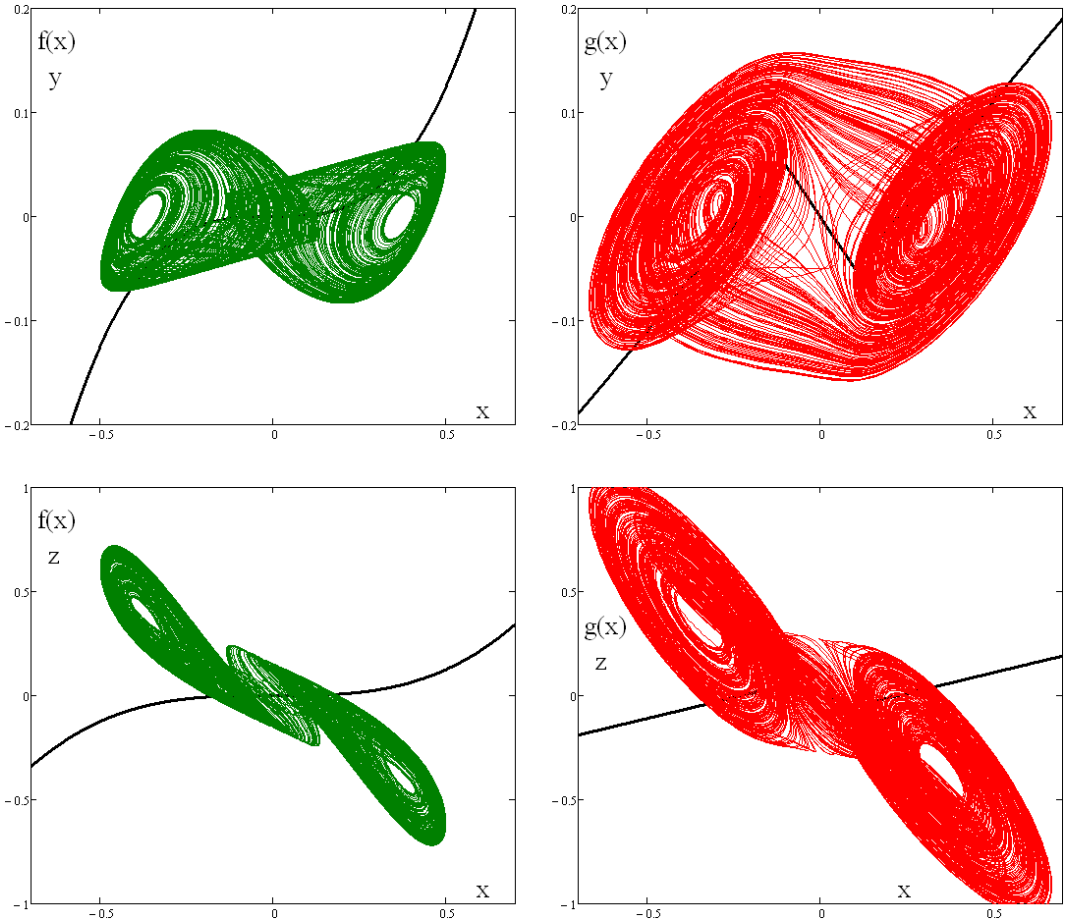

Fig. 13.1: Monge projections of original (left) and novel (right) Chua system in the same scale, polynomial and PWL function.

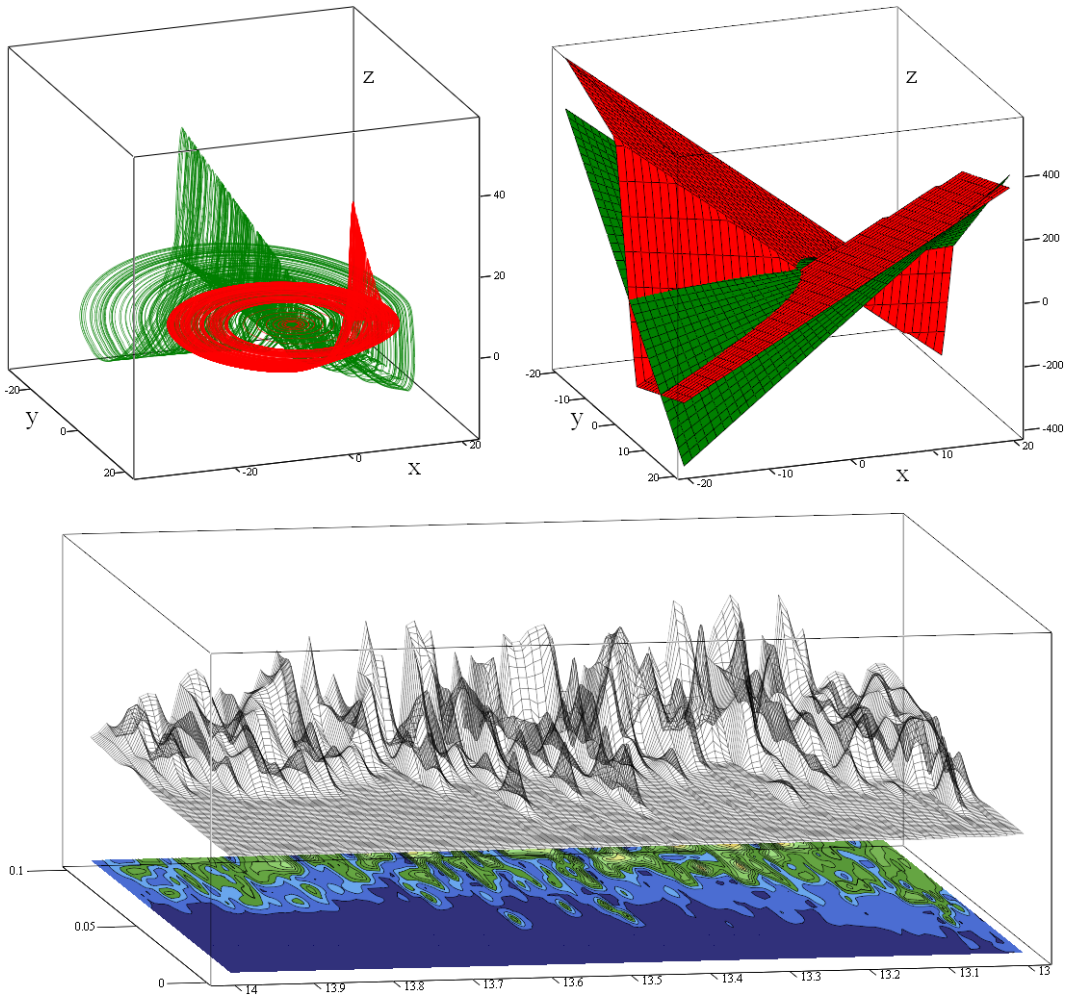

Fig. 13.2: Typical chaotic attractor for Rossler dynamical system and comparison of polynomial and discovered PWL function.

Ultimately, third dynamical system is one of the oldest member of family with possible chaotic solution called butterfly attractor. This set of the differential equations has been named after its inventor Lorenz system [79]:

$$\begin{aligned} \dot{x} &= 10(y - x) \\ \dot{y} &= 28\ x - x\ z - y \\ \dot{z} &= x\ y - 2.667\ z. \end{aligned} \tag{13.8}$$

Now the situation is quite complicated since there are two plane nonlinearities in these equations. It turns out that PWL function term (13.7) with N=2 can be used for both.

Optimization routine converges to following list of values for product of the variables x and y $\alpha_0 = -50$, $\beta_0 = 0$, $\gamma_0 = 0$, $\alpha_1 = -2.5$, $\beta_1 = -4$, $\gamma_1 = 4$, $\delta_1 = -2.5$, $\alpha_2 = 0$, $\beta_2 = 4$, $\gamma_2 = 4$ and $\delta_2 = 2.5$.

Similarly for product of the state variables x and z holds $\alpha_0 = 0$, $\beta_0 = 2$, $\gamma_0 = 1$, $\alpha_1 = -10$, $\beta_1 = 8$, $\gamma_1 = 3$, $\delta_1 = 2.5$, $\alpha_2 = 0$, $\beta_2 = 4$, $\gamma_2 = -1.5$ and $\delta_2 = -5$.

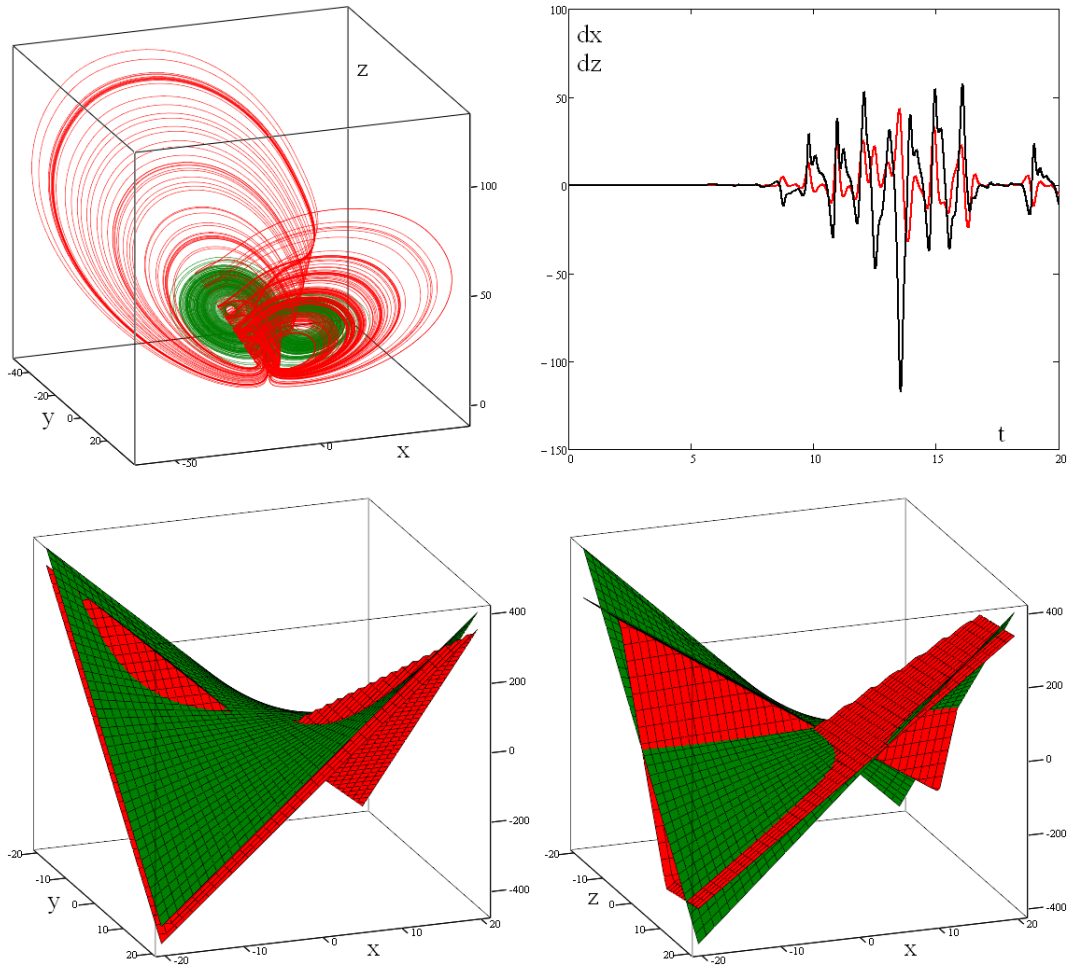

Fig. 13.3: The results for Lorenz dynamical system, comparison of chaotic attractors and nonlinear functions.

Having these PWL approximations the numerical verification can be done proving the correct function of optimization routine, see Fig. 13.3. Here, upper left graph is a time-domain demonstration of the sensitivity to changes of the initial conditions which differs on third decimal place, namely $\mathbf{x}_0 = (0.1, 0, 0)^T$ vs $\mathbf{x}_0 = (0.101, 0, 0)^T$.

Note that new chaotic attractor is much bigger than the original one. Such difference cannot be recognized or eliminated by search routine itself because both

state attractor has the same D_{KY} and, as a consequence, the same metric dimension.

The last tested dynamical system is Hindmarch-Rose model of singular neuron [132]:

$$\begin{aligned} \dot{x} &= y + 2.96\ x^2 - x^3 - z + 2.99 \\ \dot{y} &= 1 - 5\ x^2 - y \\ \dot{z} &= 0.01\left[4\left(x + 1.6\right) - z\right]. \end{aligned} \tag{13.9}$$

In this case the vector field is strongly nonlinear and up to three scalar polynomial functions have to be replaced by PWL characteristics.

This mathematical model has been picked due to its special property; a very long transient spiral motion can be improperly interpreted as limit cycle. Fig.13.4 shows both chaotic attractors and each approximated polynomial function.

Note that there is significant attractor movement without the change of geometrical structure.

First quadratic polynomial can be replaced by PWL function (13.5) with $N = 2$, $\alpha_0 = 0$, $\beta_0 = -8.3$, $\alpha_1 = 1.5$, $\beta_1 = 0$, $\alpha_2 = 2$, $\beta_2 = 1.8$, $\alpha_3 = 2$, $\beta_3 = -1.8$.

Second PWL approximation has formally the same description but with values $N = 2$, $\alpha_0 = 0$, $\beta_0 = -8$, $\alpha_1 = 1.12$, $\beta_1 = 0$, $\alpha_2 = 2$, $\beta_2 = 1.8$, $\alpha_3 = 2$, $\beta_3 = -1.8$.

Cubic polynomial can be interchanged with odd-symmetrical PWL function (13.5) with values $\alpha_0 = 10$, $\alpha_1 = 0.9$, $\beta = 1.2$.

13.3 Conclusion

The main purpose of this chapter is to extend current state-of-the-art in the field of complicated vector field approximations. Discovered method can be marked as general and applicable to dynamical systems with almost any type and number of the nonlinear functions.

This can be handy especially in the case theoretical study of the underlying dynamics. It is well known that dynamical motion in each region of the vector field

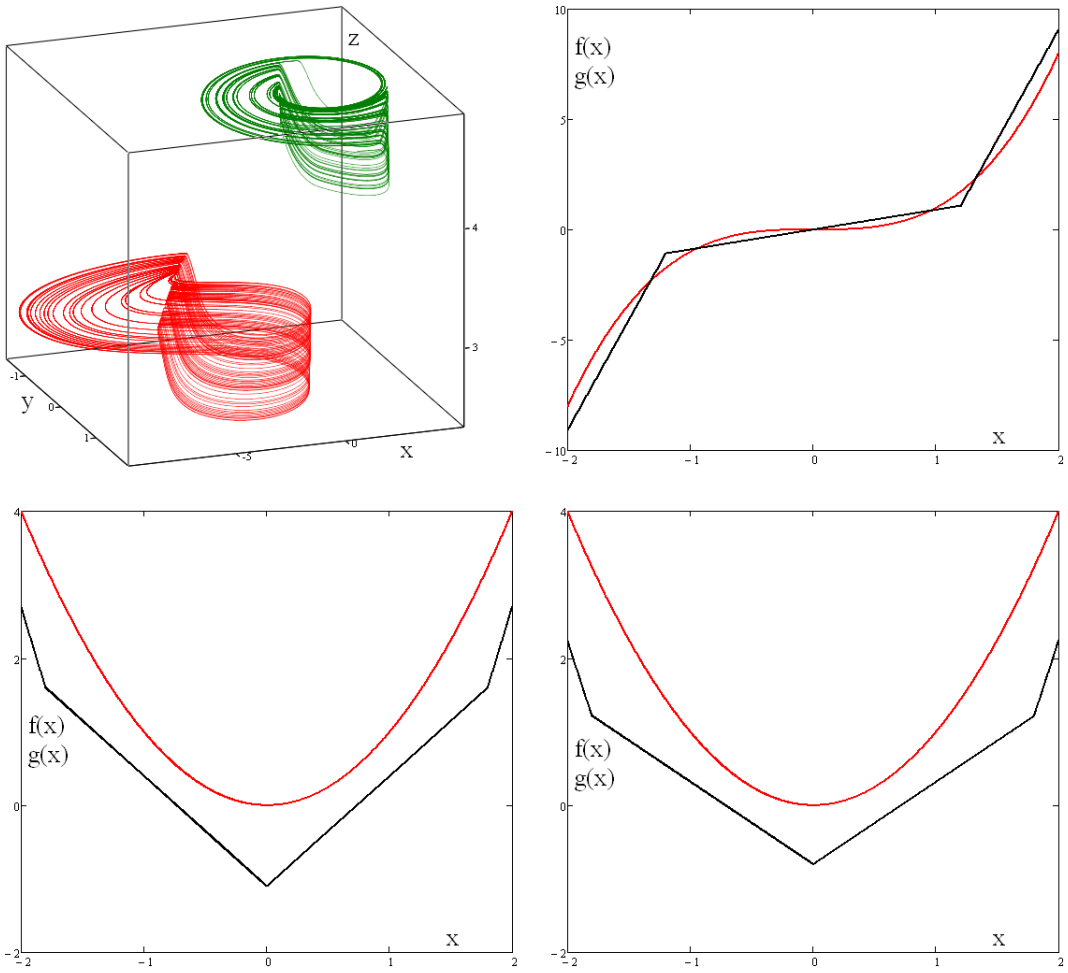

Fig. 13.4: Approximation of mathematical model of neuron, chaotic attractors and nonlinear functions.

can be described analytically.

Proposed algorithm for approximation can be extended for higher-order mathematical models as well as for higher-dimensional nonlinear functions.

There have been also other definitions of the metric dimensions that can be used for motion quantification. For example the capacity (box-counting) dimension has enormous computational time demands which increases drastically for large state space attractors. For example it proves to be worthless if labyrinth chaos [118] is a reference behavior.

14 CHAOTIC OSCILLATORS WITH SINGLE POLYNOMIAL NONLINEARITY AND DIGITAL SAMPLED DYNAMICS

Plenty of the methods for synthesis of the linear, piece-wise linear and nonlinear (polynomial type) analog circuits have been already published. The corresponding results are summarized in the well written paper [89], [101].

The main drawback of such approaches is in that it is quite difficult to implement strongly nonlinear vector fields. This is a problem associated especially with the dynamical systems having cyclically symmetrical vector fields [64], [68].

Another example of problems with the nonlinear transfer function synthesis is the approximation [102] of some trigonometrical functions. To avoid creating the complex analog networks susceptible on the noise presence the better way is to use n-port with internal digital signal processing.

It eventually turns out that the well-known Nyquist sampling theorem is generally not strict enough in the case of the chaotic dynamics.

The sampling frequency should be much higher than the largest distinguishable frequency component associated to the desired state space attractor.

The existence of the chaotic attractor should be proved by the numerical integration process as well as by the precise calculation of the largest Lyapunov exponent [103].

14.1 Overall Numerical Analysis

Assume the third-order differential equation known from the Newtonian dynamics:

$$\dddot{x} + a\ddot{x} + b\dot{x} = f(x) \tag{14.1}$$

where state variable x can be interpreted as position, its first derivative as velocity and second derivative as acceleration. As mentioned above the numerical

integration is a first step to quantify dynamical behavior of any system.

There have been many programs capable to do this. In our case Mathcad and build-in fourth-order Runge-Kutta method has been utilized with final time 600, 10000 integration steps and the initial conditions equal $\mathbf{x}_i = (0.1, 0, 0)^T$. The corresponding results are demonstrated in Fig.14.1-14.2 and Fig.14.3-14.4 for the quadratic and cubic nonlinearity respectively.

System with quadratic nonlinearity generates the so-called single-scroll attractor for the set of parameters $a = 0.8$, $b = 1.1$ and $f(x) = \pm 0.8(x^2 - 1)$.

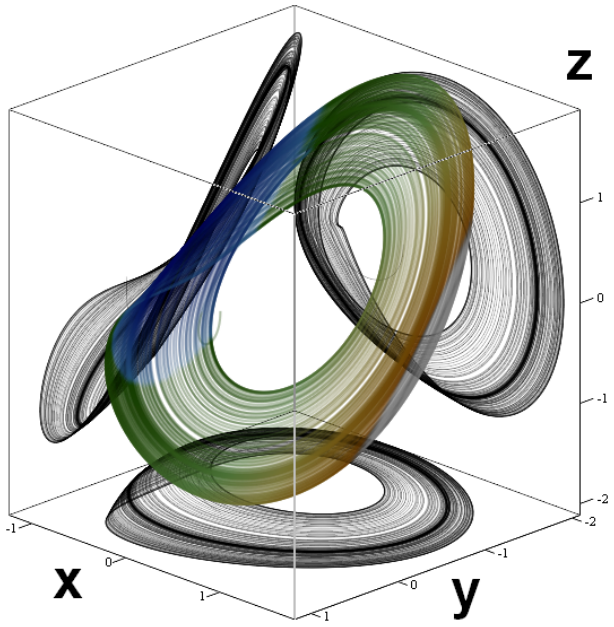

Fig. 14.1: Integration of the typical quadratic chaotic attractors.

Note that there are two mirrored attractors for the different sign in the polynomial function. Similarly system with cubic polynomial is capable to produce double-scroll attractor if $a = 0.7$, $b = 0.9$ and $f(x) = -0.8x(x^2 - 1)$ or dual double-scroll attractor for the set $a = 0.3$, $b = 0.8$ and $f(x) = 0.8x(x^2 - 1)$. It has been verified that at least 7 bits are necessary for vertical sampling to preserve a global behavior.

For horizontal sampling it turns out that each chaotic state space attractor is bounded in the volume $x \in (-3, 3)$ and 7 bits are again sufficient. The sampled chaotic dynamics is visible in Fig.14.5-14.6 and Fig.14.7-14.8.

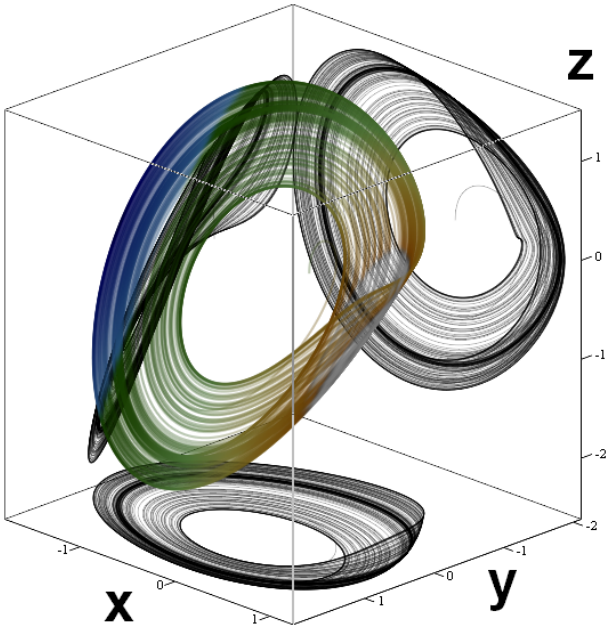

Fig. 14.2: Integration of the typical quadratic chaotic attractors (rotated).

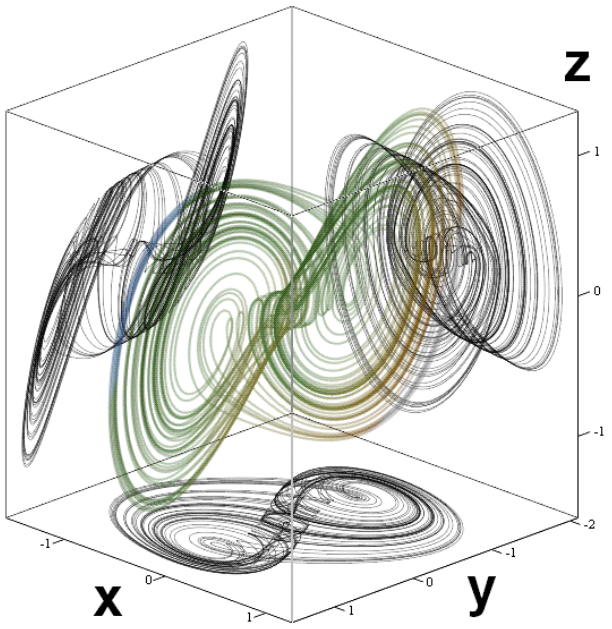

Fig. 14.3: Integration of the typical cubic chaotic attractors.

From the viewpoint of practical implementation the parameters of the nonlinear function will be fixed. To observe some routing to chaos scenario the bifurcation parameter is a and b, represented by variable resistors in the real circuit.

To specify the regions of the system solution sensitive to the small changes of the initial conditions the surface-contour plot of the largest Lyapunov exponent (LE)

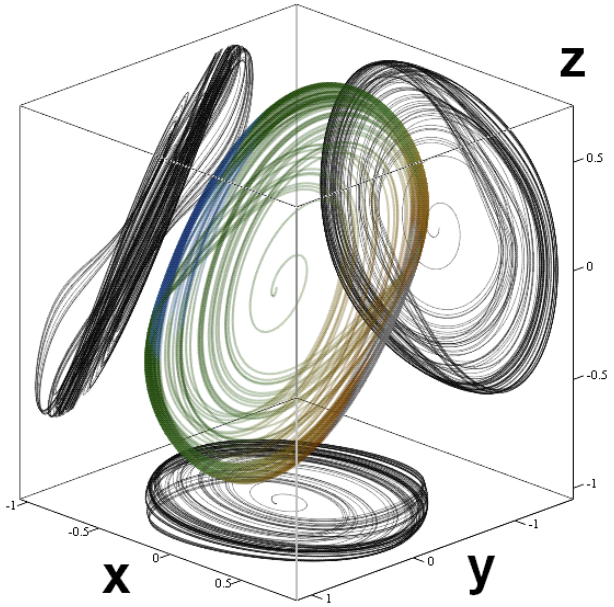

Fig. 14.4: Integration of the typical cubic chaotic attractors (rotated).

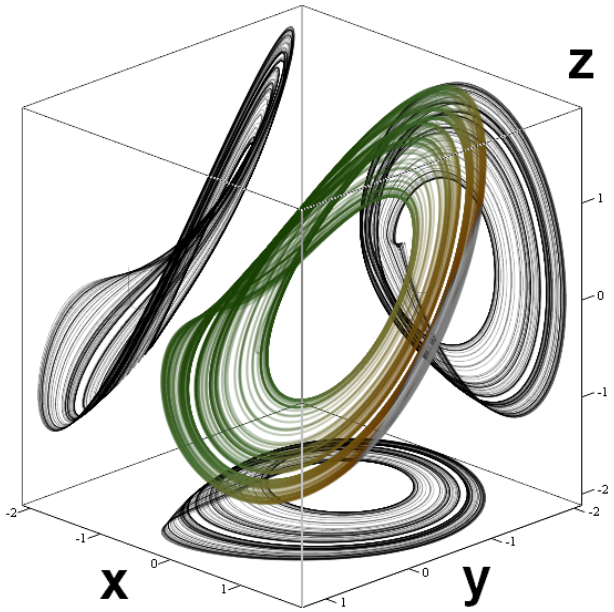

Fig. 14.5: Integration of the sampled quadratic chaotic attractors.

has been created, see Fig.14.9 and Fig.14.10. The individual routine parameters are exactly the same as for the numerical integration discussed above.

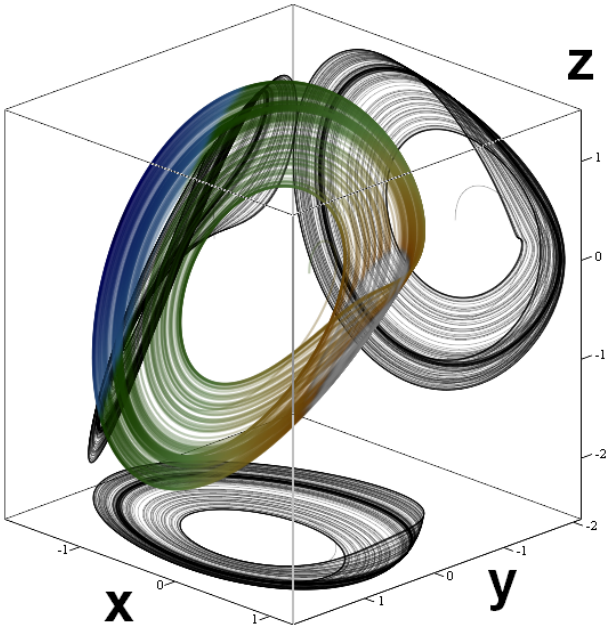

Fig. 14.6: Integration of the sampled quadratic chaotic attractors (rotated).

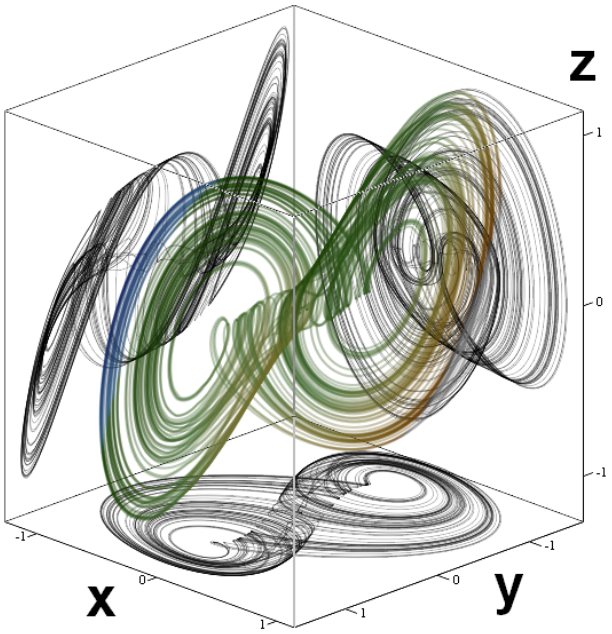

Fig. 14.7: Integration of the sampled cubic chaotic attractors.

14.2 Mixed-mode Circuitry Realization

To simplify the final circuitry implementation and verify the conception of the sampled dynamics the digital two-port network has been designed. The core engine is processor STM32F107 with 516kB memory.

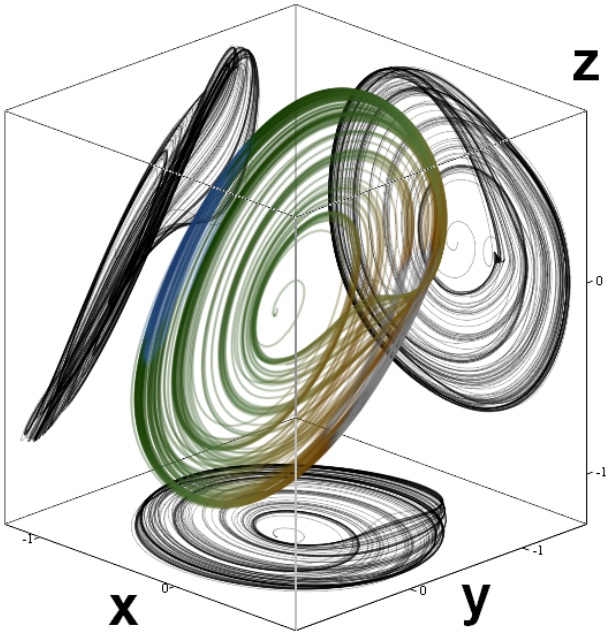

Fig. 14.8: Integration of the sampled cubic chaotic attractors (rotated).

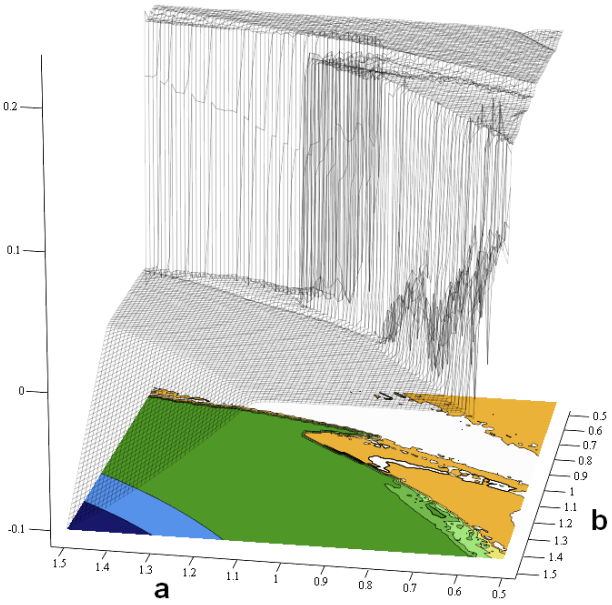

Fig. 14.9: The largest LE for system with quadratic nonlinearity.

This device cooperates with input analog to digital converter TLC2574 and output DAC8734 using SPI bus. KEIL uVision V3.90 has been used as C/C++ software environment. The concrete configuration is provided in Fig.14.11.

The linear part of the vector field is implemented as a cascade connection of the non-inverting integrators with input current summation process.

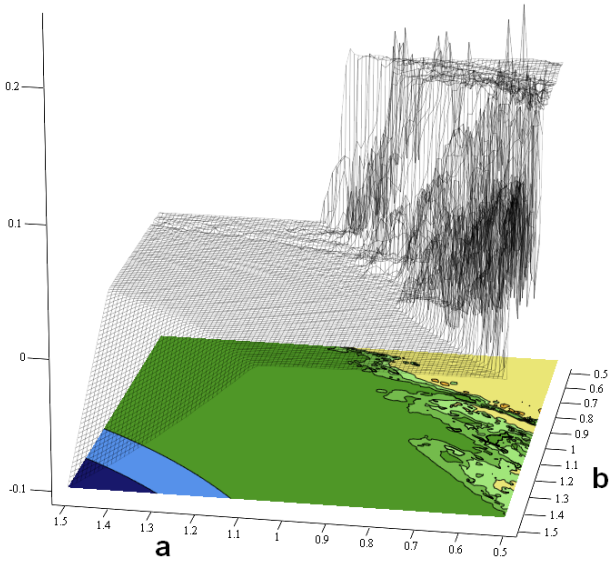

Fig. 14.10: The largest LE for system with cubic nonlinearity.

The individual mathematical operations are realized by means of the positive second generation current conveyors available under notion AD844. This analog building block is described by the following set of the equations:

$$\begin{aligned} V_X &= V_Y \\ I_Y &= 0 \\ I_X &= I_Z \\ V_O &= V_Z \end{aligned} \tag{14.2}$$

The corresponding circuit is given in the Fig.14.12. It is evident that the natural frequency component is given by the time constant $\tau = RC = 10^3 10^{-7}$. The experimental study of chaos evolution can be done through the change of resistors Ra and Rb.

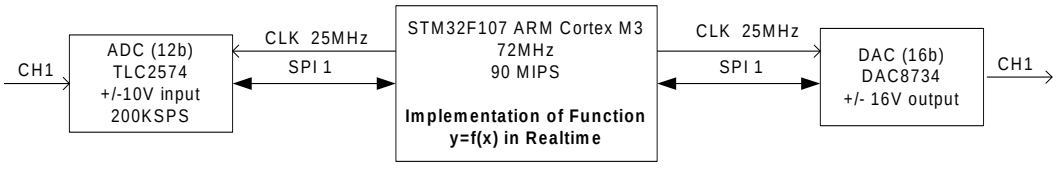

Fig. 14.11: Principal configuration of polynomial digital two-port.

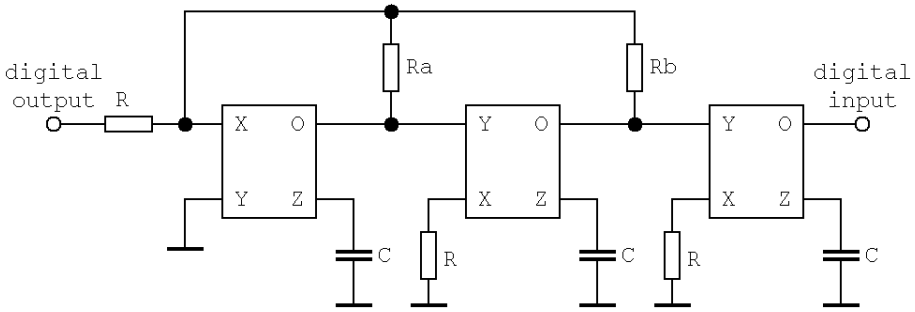

Fig. 14.12: Detailed implementation of the analog part using AD844.

14.3 Experimental Results

The typical state trajectories measured by means of the digital oscilloscope Agilent Infiniium are shown in Fig.14.13 and Fig.14.14 for the quadratic and cubic nonlinearity respectively. These measured results are in good accordance with theoretical expectations, i.e. numerical integration of the given mathematical model. It has been verified that the time constant can not be much lower than $\tau = 10\mu s$.

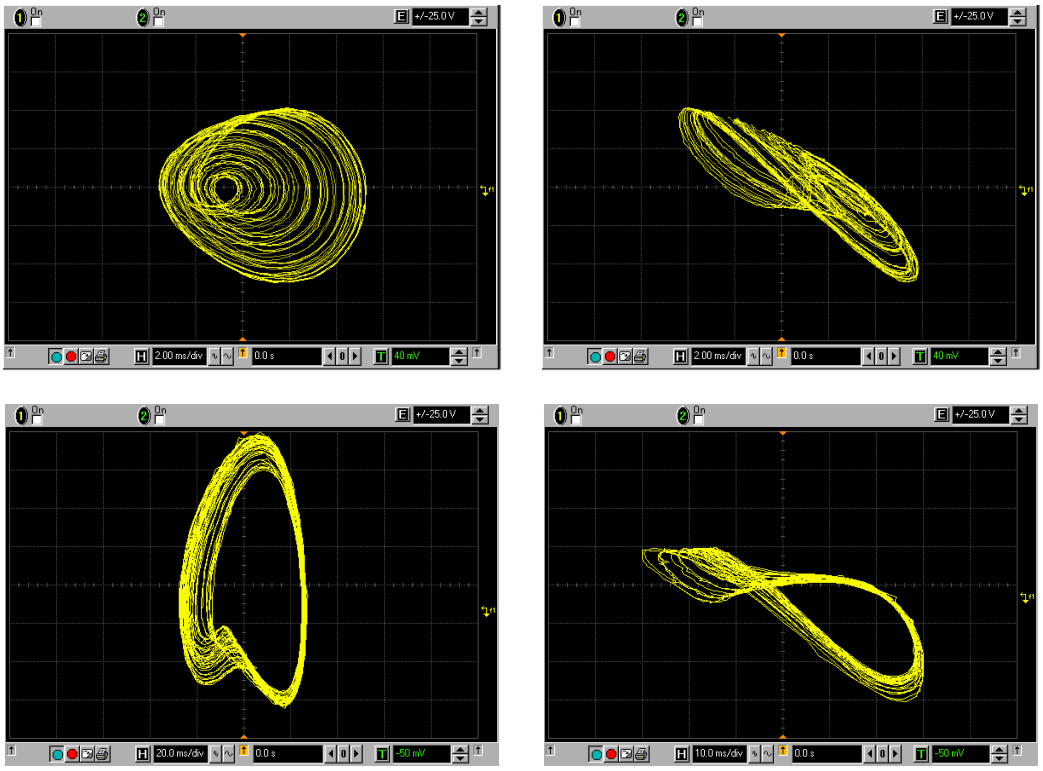

Fig. 14.13: Chaotic attractors for the quadratic polynomial.

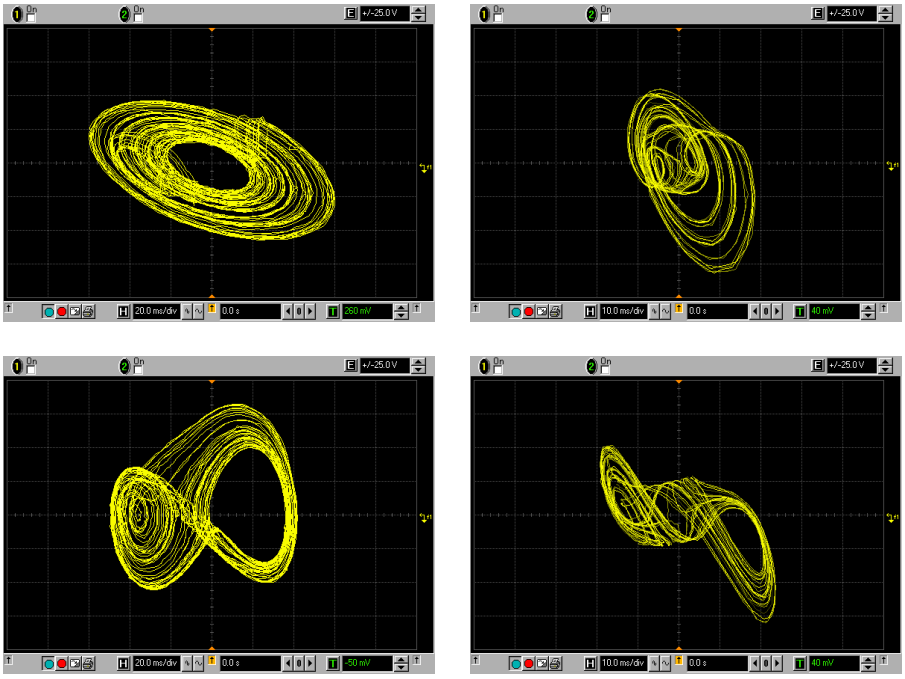

Fig. 14.14: Chaotic attractors for the cubic polynomial.

14.4 Conclusion

It is demonstrated by means of the several examples that it is effective to use mixed analog-digital synthesis even in the case of the chaotic dynamics.

There exist some dynamical systems (for example with cyclically symmetrical vector field) with multiple complex nonlinear functions making its truly analog circuitry implementation almost impossible. The presented approach can be utilized to solve such problem.

15 QUANTIFICATION OF CHAOTIC DYNAMICAL SYSTEMS WITH LARGE STATE ATTRACTORS

The recent discovery of cyclically symmetrical system composed of the differential equations containing signum functions [68], [71] and [69] defined by:

$$\begin{aligned} \dot{x} &= -a_x x \pm \text{sign}[\sin(b_y y)] \\ \dot{y} &= -a_y y \pm \text{sign}[\sin(b_z z)] \\ \dot{z} &= -a_z z \pm \text{sign}[\sin(b_x x)], \end{aligned} \tag{15.1}$$

where $a_{x,y,z}$ and $b_{x,y,z}$ are constants and dots denote the first derivatives of the state variables. The system is so-called GP oscillator. It turns out that there are serious problems during its analysis and using well known mathematical tools. The difficulties are obvious especially in the case of Lyapunov exponents (LE) estimation [63], [77] and [64]. This is caused by extreme numerical values of the derivatives substituted into Jacobi matrix in the main loop of the calculation routine. Moreover there are associated troubles with precision while analytical formulas can not be utilized otherwise the procedure indicates completely incorrect results.

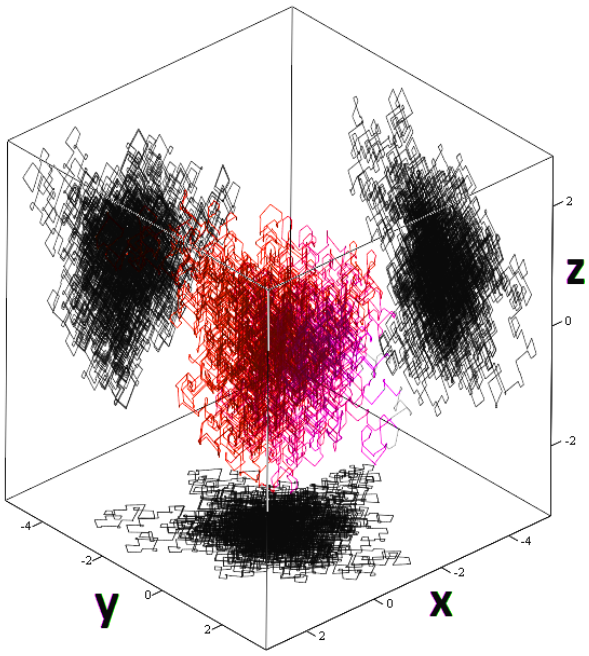

Fig. 15.1: Solution of dynamical system obtained by integration of ODE with Monge's projections, GP system with uniform parameters $a_x = a_y = 0.1$ and $a_z = 0$.

15.1 2-Spherical Quantification

The lack of the suitable methods for quantifying the behavior familiar to the conservative systems with large strange attractors leads the authors to develop different ones. The proposed approach is based on the fundamental nature of the strange attractors, namely ergodicity and mixing property. To reduce the computation time in R^3 demanded by standard box-counting method it should be replaced by the mathematical operations on the plane in R^2, in detail on the surface of a sphere. The principle of calculation is analyzed in the transformation from Cartesian coordinates of the attractor into the spherical coordinates, respectively on the surface of 2-sphere. The surface of 2-sphere has to be normalized to obtain a general quantifier. Using spherical coordinates, the unit sphere can be parameterized by:

$$\begin{aligned} \vec{r}(\theta,\varphi) &= (\cos\varphi\sin\varphi, \sin\theta\sin\varphi, \cos\varphi), && (15.2)\\ 0 &\leq \theta \leq 2\pi, 0 \leq \varphi \leq \pi. && (15.3) \end{aligned}$$

Than the surface S of sphere $Sphere$ is set to be equal to 1 (normalization) can be expressed as:

$$S(Sphere) = \int_{Sphere} |\vec{r}_u \times \vec{r}_v| \mathrm{dudv} = 1. \tag{15.4}$$

Thus for the square radius r^2 of $\mathbb{R}^3$ sphere stands:

$$r^2 = \frac{1}{4\pi}. \tag{15.5}$$

Radius of this sphere is chosen $r = \frac{\sqrt{\pi}}{2\pi}$ such that the sum of all surface pieces (SP) is unity. This globe splits into elemental SP depending on the $\Delta\varphi$, $\Delta\theta$ angle steps:

$$\theta = \arctan\left(\frac{y}{x}\right), \tag{15.6}$$

$$\varphi = \arccos\left(\frac{z}{r}\right). \tag{15.7}$$

Assuming that attractor will fill the entire space of $\mathbb{R}^3$ where integral step limit approaches zero, meaning the like-hood has a continuous uniform distribution $f(x)$ is described as:

$$f(x) = \begin{cases} \frac{1}{b-a} & \text{for } a \leq x \leq b \\ 0 & \text{for } x < a \text{ or } x > b \end{cases} \tag{15.8}$$

Than the surface of whole sphere can be described as:

$$S_{Sphere} = \int_0^{\pi} \int_0^{2\pi} \frac{1}{4\pi} \sin\theta d\varphi d\theta = 1. \tag{15.9}$$

Considering the discrete time series, the step $\Delta\theta$ and $\Delta\varphi$ needs to be set, otherwise certain SP needs to be deleted to have particular list of SP for measuring the complexity of the analyzed attractor. Following the flow $\Phi(x, y, z)$ of attractor in $\mathbb{R}^3$ having N elements, each SP is indexed by the natural numbers i and j. In the main calculation routine the individual SP occupied by a state trajectory are summarized. The surface of occupied area on the $\mathbb{R}^3$ sphere can be calculated using the following discrete formula:

$$S_{\Phi} = \sum_{i=1}^{N} \sum_{j=1}^{N} |\frac{1}{4\pi} \sin(i\frac{\pi}{N}) 2ij \frac{\pi^2}{N^2}|. \tag{15.10}$$

The graphical interpretation of this novel motion quantifier is demonstrated in Fig.15.1-Fig.15.8 for some interesting situations. There is one serious drawback of this procedure leading to the indispensable numerical errors. The shape and orientation of the state attractor can be right-lined as it is visible in the first two examples. If so, a huge amount of the information about attractor geometric structure is lost. To improve this disadvantage the linear change of the coordinates in order to spread the studied attractor should be performed before transformation on the sphere.

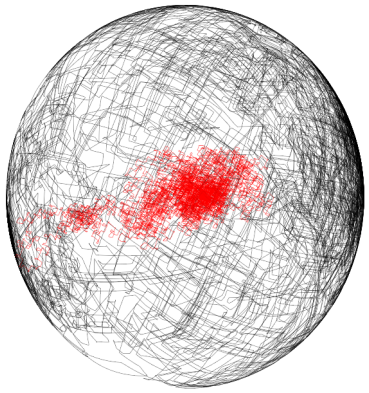

Fig. 15.2: The dynamical motion quantification, analyzed attractor (red) and its projection on sphere (black), GP system with uniform parameters $a_x = 0, a_y = 0.1, a_z = 0.1$ and $b_x = b_y = b_z = 10$.

It is known, that the chaotic systems exhibit special sort of trajectories in state space. Thus the proposed method can be used as quantifier but should not be misinterpreted as metric dimension. There are also certain disadvantages, some of

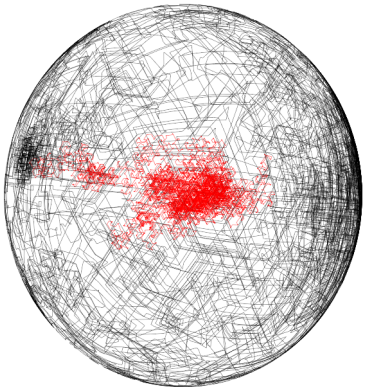

Fig. 15.3: The rotated view on the dynamical motion quantification, analyzed attractor (red) and its projection on sphere (black), GP system with uniform parameters $a_x = 0, a_y = 0.1, a_z = 0.1$ and $b_x = b_y = b_z = 10$.

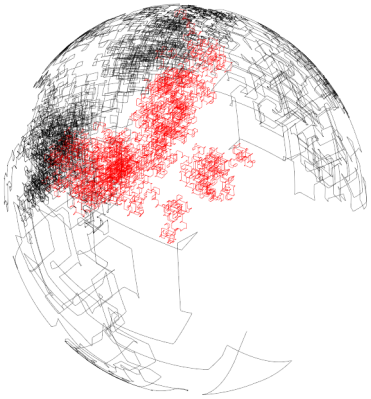

Fig. 15.4: The dynamical motion quantification, analyzed attractor (red) and its projection on sphere (black), GP system with uniform parameters $a_x = 0, a_y = 0.1, a_z = 0$ and $b_x = b_y = b_z = 10$.

them revealed by the authors. Consider the rotation of attractor in Cartesian space. Certain rotation of attractor (very rare cases) can cause problems with transformation. This can be removed using linear coordinate transformation before applying the algorithm.

15.2 General n-spherical Quantification

N-sphere quantification can be considered as a generalization of the surface of an ordinary sphere quantification to an arbitrary dimension. For any natural number n, an n-sphere of radius r is defined as the set of points in $D = (n + 1)$ dimensional

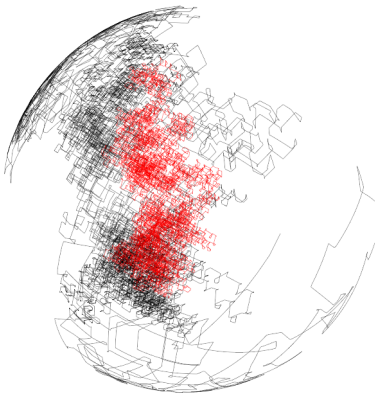

Fig. 15.5: The rotated view on the dynamical motion quantification, analyzed attractor (red) and its projection on sphere (black), GP system with uniform parameters $a_x = 0, a_y = 0.1, a_z = 0$ and $b_x = b_y = b_z = 10$.

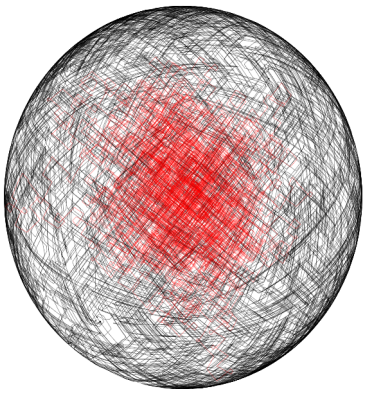

Fig. 15.6: The dynamical motion quantification, analyzed attractor (red) and its projection on sphere (black), GP system with uniform parameters $a_x =_{ay}= a_z = 0.1$ and $b_x = b_y = b_z = 10$.

Cartesian space. The visualization of multidimensional objects is very difficult and provides only a fragment of entire picture. Thus it is left to the readers imagination and skipped in this thesis. The distance r (radius) from a central point is any positive real number. The n-sphere is defined by following term:

$$S^n = \left\{ x \in R^{n+1} : ||x|| = r \right\}. \tag{15.11}$$

It is an n-dimensional manifold in Cartesian space. In particular, a 2-sphere is an ordinary sphere in three-dimensional Cartesian space. Spheres of dimension $n > 2$ are called hyper-spheres.

The surface area of the n-sphere of radius r in $n + 1$ Cartesian space is defined

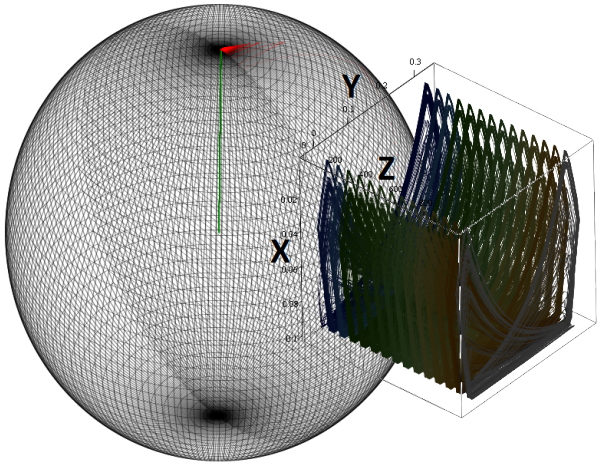

Fig. 15.7: The dynamical motion quantification of periodical solution, analyzed attractor (green and in the extra plot) and its projection on sphere (black and red), GP system with uniform parameters $a_x = 10$ $a_y = a_z = 0.1$ and $b_x = b_y = b_z = 10$.

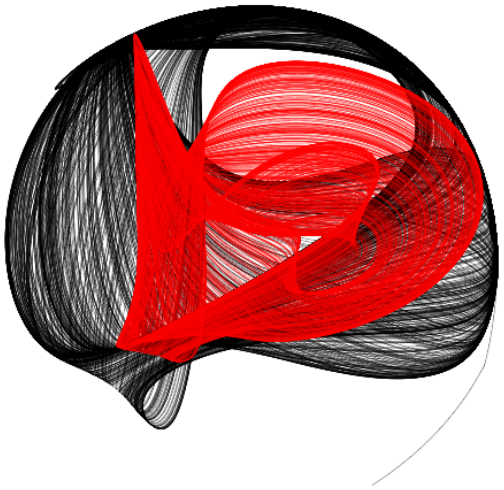

Fig. 15.8: The dynamical motion quantification of periodical solution, analyzed attractor (green and in the extra plot) and its projection on sphere (black and red), The Halvorsen system with parameters $a = 1.3$ and $b = 4$.

as:

$$S^n(r) = \frac{2\pi^{\frac{n+1}{2}}}{\Gamma(\frac{n+1}{2})} r^n = 1, \tag{15.12}$$

where $\forall n \in Z \wedge n \geq 0$, Gamma function $\Gamma(l)$is an extension of the factorial function.

Considering $\frac{n}{2}+1) \geq 0$ is positive real number, the Gamma function reduces to:

$$\Gamma(l) = (l-1)!. \tag{15.13}$$

By defining a coordinate system in an D-dimensional spherical coordinate system from D-dimensional Cartesian space, in which the coordinates consist of a radial coordinate r, $n-2$ angular coordinates $\Theta_1 \ldots \Theta_{n-2}$ with angle ranges $< 0, \pi >$ and another angular coordinate ϕ with range $< 0, 2\pi >$.

The radius of unity surface of n-sphere is defined as:

$$r = \sqrt[n]{\left(\frac{S^n \Gamma(\frac{n+1}{2})}{2\pi^{\frac{n+1}{2}}}\right)}. \tag{15.14}$$

The other angular values can be calculated from Cartesian space consist of $x_1 \ldots x_D$:

$$\begin{aligned}
\Theta_1 &= \text{arccotg}\frac{x_1}{\sqrt{x_D^2 + x_{D-1}^2 + ...x_2^2}} \\
\Theta_2 &= \text{arccotg}\frac{x_2}{\sqrt{x_D^2 + x_{D-1}^2 + ...x_2^3}} \\
&\vdots \\
\Theta_{D-2} &= \text{arccotg}\frac{x_{D-2}}{\sqrt{x_D^2 + x_{D-1}^2}} \\
\varphi &= 2 \cdot \text{arccotg}\frac{\sqrt{x_D^2 + x_{D-1}^2} + x_{D-1}}{x_D}.
\end{aligned} \tag{15.15}$$

The single surface area of n-sphere can be calculated by:

$$S_{Single}^n = r^n d\phi \prod_{m=1}^{D-2} (\sin \Theta_m)^m d\Theta_m, \tag{15.16}$$

where $D = (n+1)$. Then the whole filled surface, following the flow Ω of attractor consist of N discrete points is:

$$S_\Omega = \sum_{i_1}^{N} \cdots \sum_{i_{D-2}}^{N} |r^n i_{D-2} \frac{2\pi}{N} \prod_{m=1}^{D-2} (\sin \Theta_m)^m \prod_{k=1}^{D-2} i_k \frac{\pi}{N}|. \tag{15.17}$$

The absolute value is used in equation (15.17). to meet the conditions of sum by changing the sign of negative angles.

15.3 Experimental Results

The proposed new algorithm is designed to recognize chaotic and non-chaotic solution. Hyper-chaotic behavior can be also indicated since the volume element defined by neighborhood trajectories in the state space expands in two or more directions. To be more specific this quantifier responds to the orbit density in state space, higher value results into number closer to unity.

Roughly speaking the state space attractor fills the Cartesian space and is extracted by the algorithm on the surface of sphere. If the solutions tend to be periodical, diverging or is represented by point, etc... , the result (or covered surface on the sphere) tends to be minimal, sometimes it can be considered as almost zero.

To identify the solution certain threshold can be set. The transient needs to be considered when analyzing the time series. Long transient can cause significant errors in setting the scale for the spherical transformations.

Tab. 15.1: Table of parameters and results for under test taken systems.

Eq.	**Equation parameters**	S_Ω	**Lyapunov exp.** λ_i
A	$a_x = 10, a_y = 0, a_z = 0,\ b_{x,y,z} = 10$	0.022	0.0238, -0.428, -9.595
	$a_x = 0.1, a_y = 0.1, a_z = 0.1,\ b_{x,y,z} = 10$	0.959	3.572, 0.005, -3.870
	$a_x = 2, a_y = 1, a_z = 1,\ b_{x,y,z} = 10$	0.225	1.186, -0.009, -5.177
	$a_x = 2, a_y = 2, a_z = 1,\ b_{x,y,z} = 10$	0.123	0.479, -0.005, -5.474
	$a_x = 2, a_y = 2, a_z = 1,\ b_{x,y,z} = 1$	0.003	-1.247, -1.256, -2.497
B	$a = 2, b = 2$	0.138	0.086, 0.007, -2.096
	$a = 3, b = 2$	0.061	0.005, -0.061, -1.944
C	$a = 1.1, b = 0.2$	0.135	0.101, 0.023, -1.113
	$a = 1.1, b = 0$	0	-0.004, -0.007, -0.992
	$a = 3.2, b = 0.1$	0.297	0.020, 0.015, -1.034
D	$p = 16, r = 45.92, b = 4$	0.143	1.444, -0.017, -22.335
	$p = 2, r = 45.92, b = 1$	0.103	0.534, -0.007, -4.526
	$p = 2, r = 80, b = 1$	0.056	0.048, -0.6730, -3.372
E	$a = 1.3, b = 4$	0.276	0.553, 0.052, -4.507
	$a = 1.3, b = 2$	0.054	0.016, -0.049, -3.866

Systems, more in [61] and [66], were taken under test. The systems are denoted by letters. System proposed in equation (15.1) is denoted in Table15.1. as A. In this system the method of Fourier transform was used to obtain LE.

The next tested system B is defined by:

$$\begin{aligned} \dot{x} &= az \\ \dot{y} &= -by + z \\ \dot{z} &= -x + y + y^2. \end{aligned} \tag{15.18}$$

The next system denoted as C is defined as:

$$\begin{aligned} \dot{x} &= y + az \\ \dot{y} &= bx^2 - y \\ \dot{z} &= 1 - x. \end{aligned} \tag{15.19}$$

More informations about systems (15.18) and (15.19) can the reader find in [65].

The next tested dynamical system D is the Lorenz's [104] famous system defined by:

$$\begin{aligned} \dot{x} &= p(y - x) \\ \dot{y} &= -xz + rx - y \\ \dot{z} &= xy - bz. \end{aligned} \tag{15.20}$$

And the last Halvorsen's system denoted as E, 3-D system of chaotic flows that are symmetric with respect to cyclic interchanges of x, y, and z:

$$\begin{aligned} \dot{x} &= -ax - by - bz - y^2 \\ \dot{y} &= -ay - bz - bx - z^2 \\ \dot{z} &= -az - bx - by - x^2. \end{aligned} \tag{15.21}$$

15.4 Conclusion

Results explained in this chapter show that the proposed quantifier is suitable for dynamical systems with large state space attractors. The principle itself is very simple and can be easily implemented.

The significant speed-up of the computation is obvious because of reduction of one degree of freedom. The advantage of this method is also, that it can be used for a time-series recognition. Some well known systems of dynamical equations were

tested. The result were compared with the LE.

The preliminary results showed, that the method can be used for chaotic motion recognition.

16 MULTI GRID CHAOTIC ATTRACTORS WITH DISCRETE JUMPS

In this chapter the discrete step functions are used in order to generate $m \times n$ scroll chaotic hypercube attractors. The design and realization of multi-scroll attractors depends on synthesizing the nonlinearity with an electrical circuit.

The essence of the novel approach is in designing the transfer function with analog to digital converters connected directly without any microcomputer, instead of using standard comparator or hysteresis methods. Therefore there is no special need for synthesizing the nonlinearity towards $m \times n$ scroll chaotic attractors. The approach is verified with PSpice 16.0 circuit simulator and experimentally measured.

16.1 Definition of the Problem

Over past three decades, generating multi-scroll chaotic attractors became an aim of many researchers [69, 122, 70, 120, 105]. Many techniques involving different approaches (usually using comparators or hysteresis) have been published [106, 107]. Chaos control and generation has a dramatic increase of interest since many real world applications and observations in engineering or other fields have been presented.

For example in fields such as biomedical engineering, digital data encryption, power systems protection, re-configurable hardware, and so on. But yet there is no simple rule for quantifying chaos origin. Generating chaotic attractors may help to understand better dynamics of real world systems.

In the chapter we would like to study third order nonlinear system, where such behavior is very rare [60]. We are presenting a generalized method for generating 2D $m \times n$ grid scroll, where a special case of solution is set of 1D grid scrolls [108, 72].

The chosen 2D $m \times n$ scroll attractor can be in fact considered as particular case of Chua's attractor [61]. Of course similar approach can be utilized for 3D grid scrolls by adding another nonlinear functional block. Our solution involves only analog to digital converters (AD) and digital to analog converters (DA) for implementation of the non-linear function. It comes to this, that there is no need for any

micro-controller.

The model describing chaotic 2D $m \times n$ scroll generation is described by three first-order differential equations:

$$\dot{x} = \mathbf{A}x + \mathbf{B}\varphi(C\ x) \tag{16.1}$$

Matrices $\mathbf{A}, \mathbf{B}, \mathbf{C}$ and function $\varphi(.)$ are defined as:

$$\begin{aligned} \mathbf{A} &= \begin{pmatrix} 0 & 1 & 0 \\ 0 & 0 & 1 \\ -a & -b & -c \end{pmatrix}, \ \mathbf{B} = \begin{pmatrix} 0 & -1 & 0 \\ 0 & 0 & -1 \\ a & b & c \end{pmatrix} \\ \mathbf{C} &= \begin{pmatrix} 1 & 0 & 0 \\ 0 & 1 & 0 \\ 0 & 0 & 1 \end{pmatrix}, \ \varphi = \begin{pmatrix} f(x) \\ f(y) \\ 0 \end{pmatrix} \end{aligned} \tag{16.2}$$

For numerical integration the fourth-order numerical Runge-Kutta method with variable step is used. Where $\dot{x}$ represents first order derivative. Function $f(.)$ denotes a nonlinear step function. Parameters a, b and c are constants.

For synthesis of the nonlinear step function, connecting the ADC directly with the DAC generate step transfer function. The step can be defined as:

$$\Delta = \frac{\text{Dynamical range (V)}}{\text{Number of bits}}. \tag{16.3}$$

Then output value with steps is:

$$out(x) = \begin{cases} l\ \Delta + \frac{\Delta}{2}, & \text{if } x > 0 \\ l\ \Delta - \frac{\Delta}{2}, & \text{if } x < 0 \end{cases} \tag{16.4}$$

$$l = \frac{x}{\Delta}\ \wedge\ l \in \mathbb{N} \tag{16.5}$$

and $\mathbb{N}$ stands for set of natural numbers. Then model representing ADC connected directly to DAC, the step function with saturation can be written as:

$$f(x) = \begin{cases} out(x), & \text{if } |x| < \Psi \\ -\Psi + \frac{\Delta}{2}, & \text{if } x \leq -\Psi \\ \Psi - \frac{\Delta}{2}, & \text{if } x \neq \Psi, \end{cases} \tag{16.6}$$

where function Ψ is defined as:

$$\Psi = \frac{\text{Dynamical range (V)}}{2}. \tag{16.7}$$

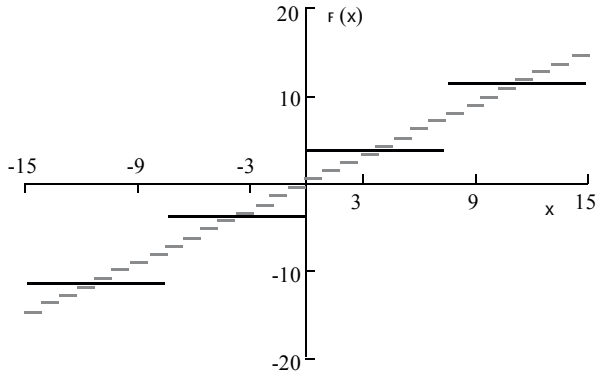

Fig. 16.1: The model of step function $f(x)$ for 2bit (black) and for 5bit(gray)

Fig. 16.2: The numerically integrated system (16.1), the Monge's projections V(x) *vs* V(y).

A system (16.1) with function (16.6 - visualized in Fig.16.1) and with constants set to $a = b = c = 0.8$ can bee seen in Fig.16.2 and Fig.16.3. Where the both functions (16.6) consists of 4 levels, ie is equal to utilizing 2 bit AD/DA converters.

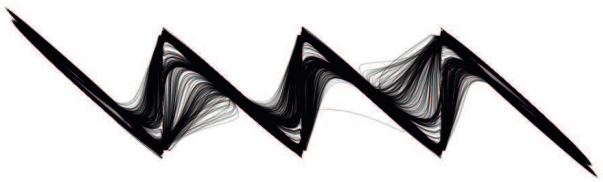

Fig. 16.3: The numerically integrated system (16.1), the Monge's projections V(y) *vs* V(z).

16.2 Circuit Implementation

Synthesis of the electronic circuits is the easiest way how to accurately model the nonlinear dynamical systems. There exist several ways how to practically realize chaotic oscillators. To synthesize circuit from differential equations system (16.1), integrator synthesis has been chosen. After thinking about how to reduce the complexity of the nonlinear network a very simple circuitry has been revealed. Only few basic building blocks are necessary: inverting integrators, summing amplifier, AD and DA converters and voltage sources. Electronic circuit system consists of three integrator circuits (using operational amplifier AD713), which integrate (16.1). Values of passive parts are estimated directly from the equations.

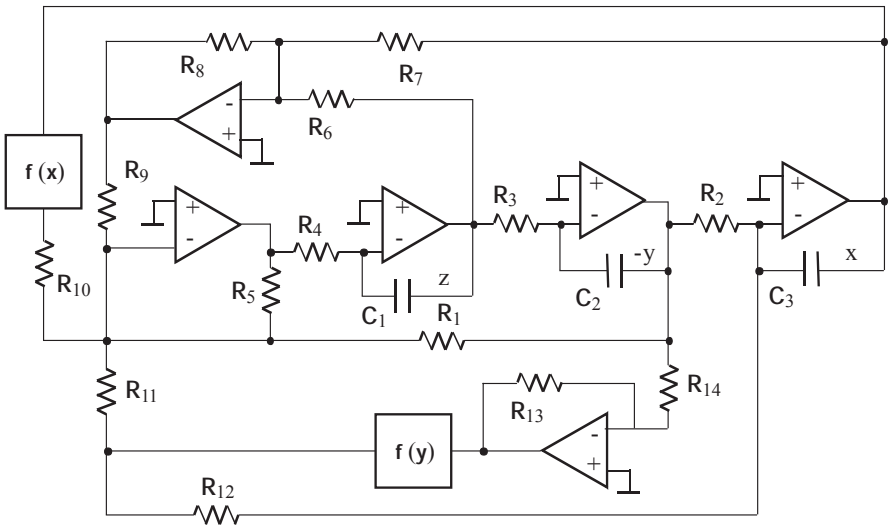

Fig. 16.4: The block schematics of realization of (16.1).

The synthesized schematics is in Fig.16.4. In order to ensure Nyquist-Shannon sampling criterion for the converters, frequency re-normalization is an easy and

straightforward process covering identical change of all integration constants simultaneously.

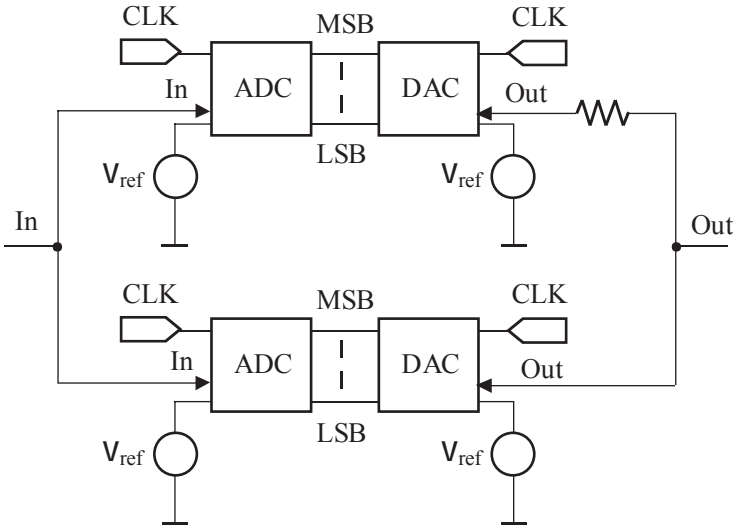

Fig. 16.5: The block schematics of realization of function $f(x)$ using data converters.

To create step transfer functions $f(x)$ and $f(y)$, the data converters are used. The schematics in Fig.16.5 shows the data converters connected directly to produce step transfer function.

In order to process positive and negative voltages, the circuit is divided in the two branches. Voltage sources are used as references for the converters. The circuitry realization was evaluated using OrCAD PSpice. The overall simulation time is set to $100ms$.

The simulated output of Monge's projections is in the in Figs.16.6- 16.8. The values of passive resistors are $R_1 = R_6 = R_7 = 125k\Omega, R_5 = R_8 = R_9 = R_{13} = R_{14} = 100k\Omega, R_2 = R_3 = R_4 = 1k\Omega, R_{10} = R_{11} = 118k\Omega, R_{12} = 1k\Omega, R_{Out} = 1\Omega$ and values of the capacitors are $C_1 = C_2 = C_3 = 100nF$.

Towards to produce various number (less) of levels for the step function, one possibility is to use only certain number of bits between converters. Another possibility is to invoke Boolean logical functions between converters (can be implemented eg in FPGA).

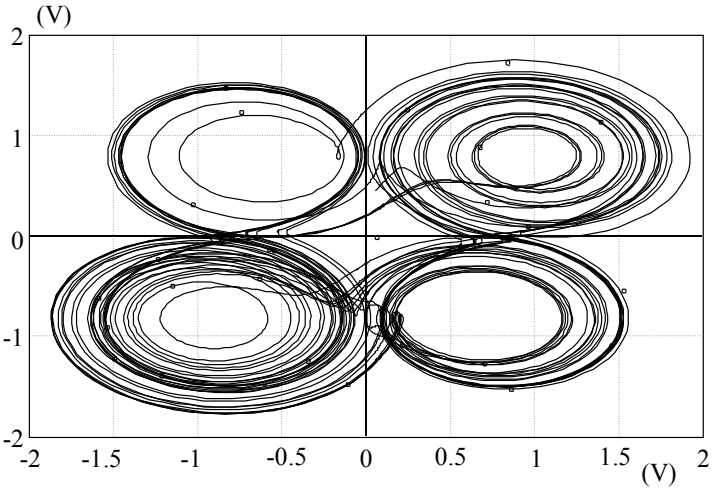

Fig. 16.6: The simulations from PSpice program, V(x) *vs* V(y) projections.

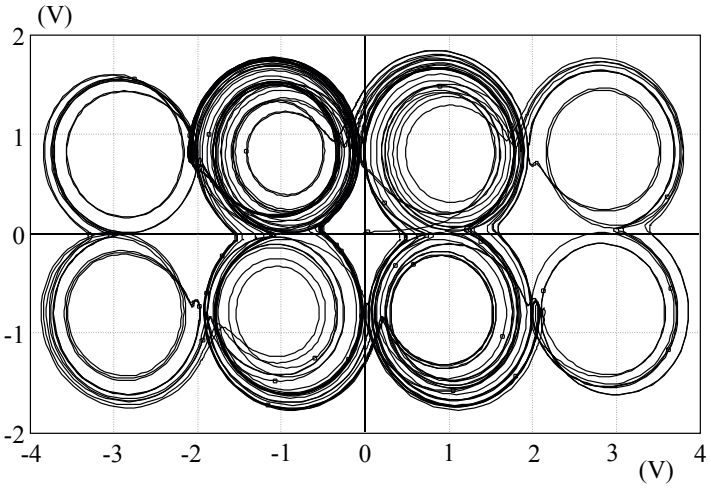

Fig. 16.7: The simulations from PSpice program, V(x) *vs* V(y) projections.

16.3 Experimental Results

It should be pointed out that hardware implementation of 2-D $m \times n$ scroll chaotic attractors is technically very difficult [106, 109], despite there is no theoretical limitation in the mathematical model for generating the large numbers of the multidimensional scrolls. The above circuit design method provides a theoretical principle for hardware implementation of such chaotic attractors with multi-directional orientations and a satisfactory number of scrolls. The measurements presented in Figs 16.9- 16.14 have been done using HP 54645D oscilloscope.

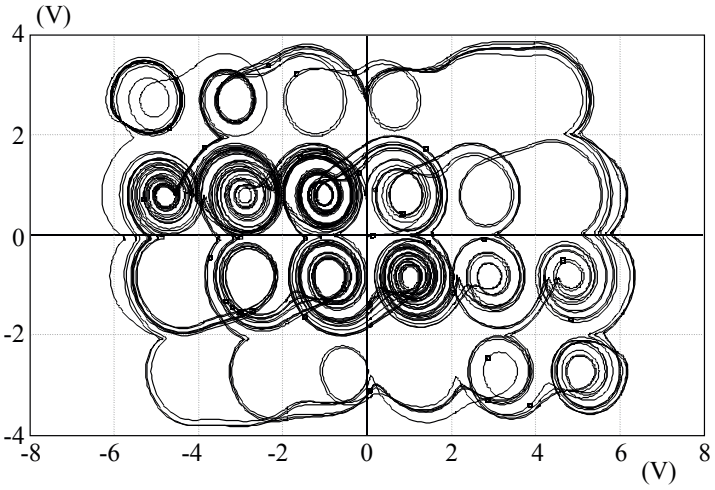

Fig. 16.8: The simulations from PSpice program, V(x) *vs* V(y) projections.

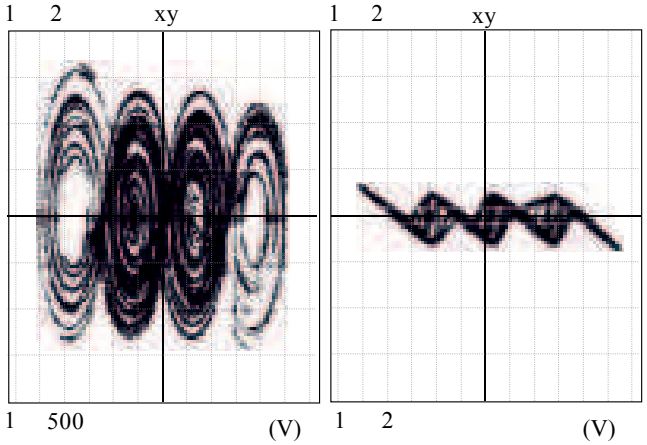

Fig. 16.9: Special setup where step function $f(y)$ vanishes: projections V(x) vs V(-y) (left), V(-y) vs V(z) (right).

16.4 3D Grid Chaotic Scrolls

By simple modification of the matrix $\mathbf{B}$ and the matrix function $\varphi(.)$ as follows:

$$\mathbf{B} = \begin{pmatrix} 0 & -1 & 0 \\ 0 & 0 & -1 \\ d & b & c \end{pmatrix}, \ \varphi = \begin{pmatrix} f(x) \\ f(y) \\ f(z), \end{pmatrix} \tag{16.8}$$

one can obtain 3D (k, l, m) grid scrolls by setting $a = b = c = 0.8$ and $d = 0.77$. The constants k, l, m stand for the number of levels of the nonlinearity (16.6). The simulated 3D scrolls can be found in the Fig.16.15.

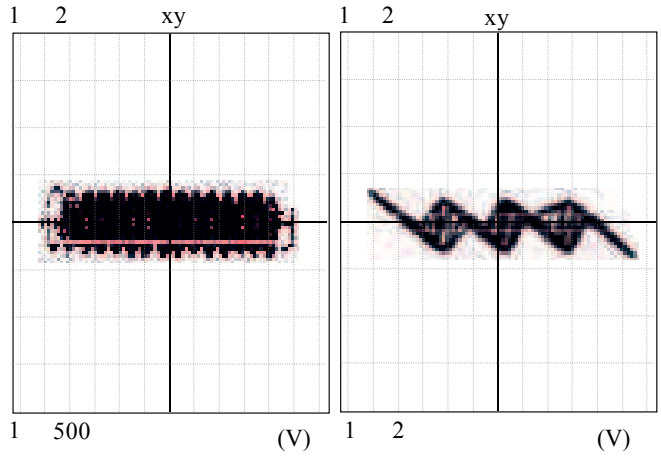

Fig. 16.10: 1D 16 scroll, step function $f(y)$ vanishes: projections V(x) vs V(-y) (left), V(-y) vs V(z) (right).

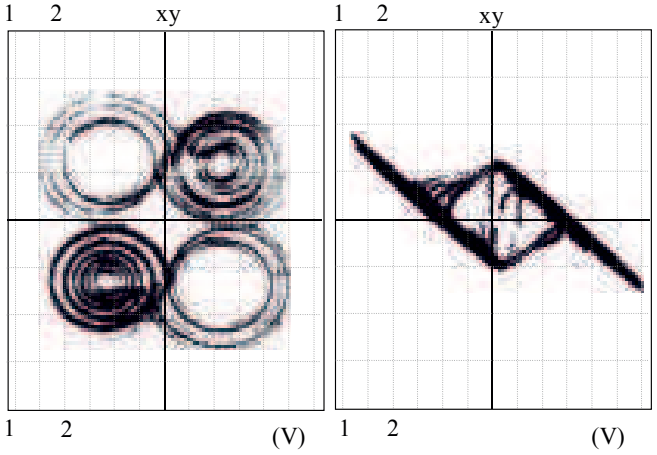

Fig. 16.11: Measured system, 2×2 scroll: projections V(x) vs V(-y) (left), V(-y) vs V(z) (right).

16.5 Conclusion

Generating chaotic behavior in third-order autonomous systems is quite delicate process. The whole system is extremely sensitive as for the initial conditions as for the realization. It is known that avoiding fractional integrators the third order of autonomous dynamical systems is the minimum order to produce chaos. To obtain chaotic behavior, the whole system has to be perfectly balanced.

With the growing order of the system, the presence of chaotic behavior is more probable. In this chapter the well known 2-D $m \times n$ scroll system was chosen and was

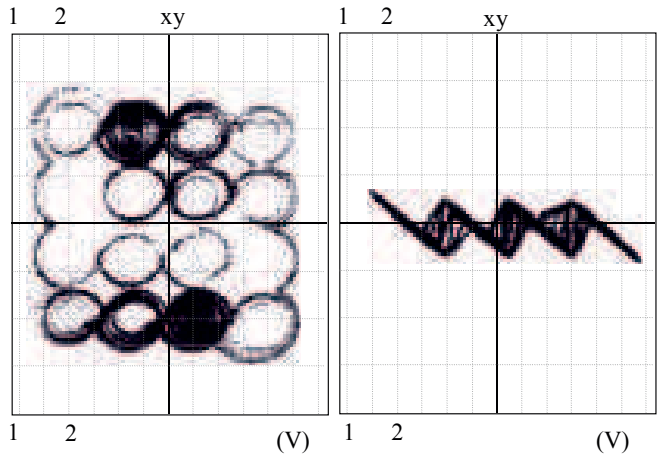

Fig. 16.12: Measured system, 4×4 scroll: projections V(x) vs V(-y) (left), V(-y) vs V(z) (right).

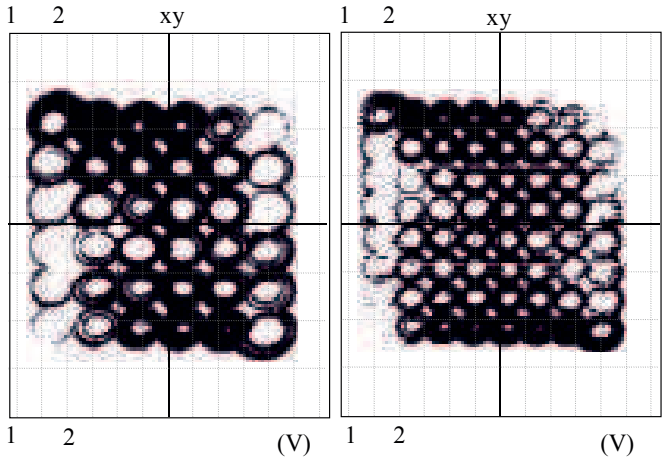

Fig. 16.13: Measured system, 6×6 scroll: projections V(x) vs V(-y) (left), 8×8 scroll, projections V(x) vs V(-y) (right).

realized utilizing novel approach using the data converters as non-linear functions. First the models were derived to simulate the data converters connected directly (ADC-DAC).

Then the connection was reduced to produce less scrolls. To verify the chaotic behavior of proposed conception, the circuit simulator PSpice was used. Then the circuit was build and measured. The measured results are rather matching the theoretical expectations.

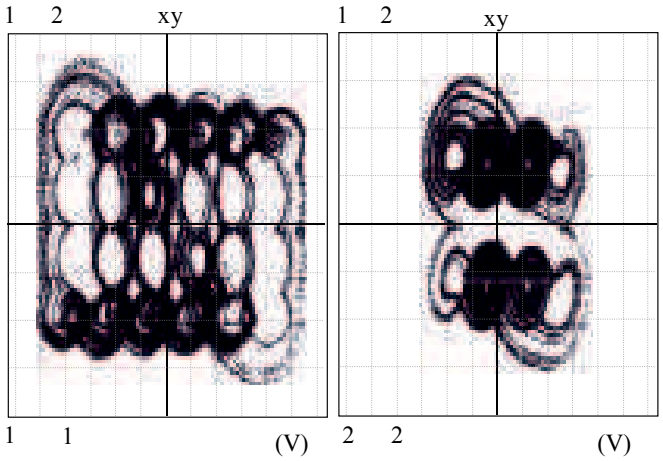

Fig. 16.14: Measured system - perturbation of parameters, 6×4 scroll (left) and 4×2 scroll (right): projections V(x) vs V(-y).

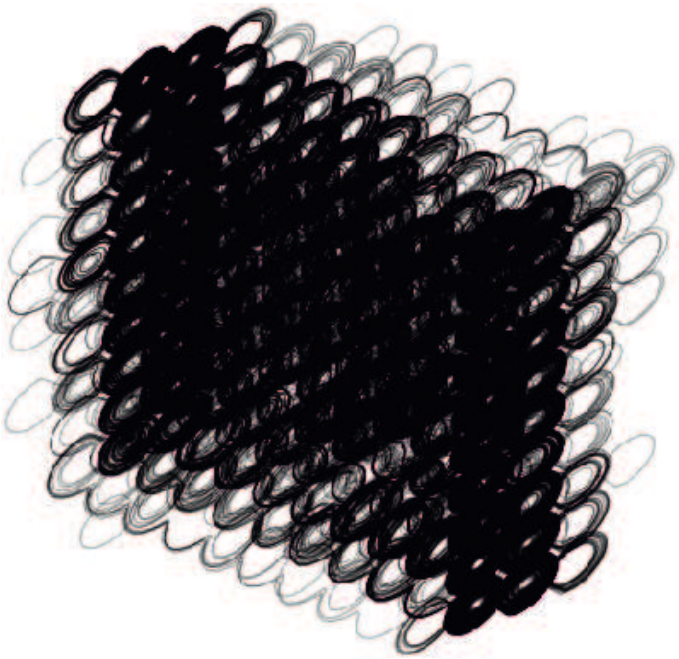

Fig. 16.15: Numerically simulated 3D (10,10,10) grid scrolls.

17 ON THE PARALLEL APPROACHES

In this chapter we would like to present several methods optimized for parallel computations. Basically the needs for parallel computing are increasing with multi-core processor architectures.

First we present section where a parallel calculation of Lyapunov exponents have been reviled. Then we present parallelization of a stochastic optimization method known as particle swarm optimization which is been used for finding the chaotic solutions of a generic set of ODEs.

17.1 Advanced Parallel Processing of Lyapunov Exponents

This section presents parametric non-linear system analysis, especially quantifying and detecting chaotic behavior. Almost every article dealing with chaotic non-linear behavior is using Lyapunov exponents for system analysis. Calculating exponents is well known process [73]. It is very important when analyzing stability of dynamical systems.

17.1.1 Parallel Lyapunov Exponents

It is well known fact due aging system (harmonic oscillator) can became erratic. In order to evaluate selected parameters and system stability, it is good to examine all permutations of parameters on a bounded set.

Special classical chaotic system so-called Lorenz system [104] was chosen for illustrating and verification the algorithms. It is notable that such system behave chaotically for certain parameter values and initial conditions.

In particular, the Lorenz attractor is a set of chaotic solutions of the Lorenz system:

$$\begin{aligned} \dot{\mathbf{x}} &= \sigma(y - x) \\ \dot{\mathbf{y}} &= x(\rho - z) - y \\ \dot{\mathbf{z}} &= xy - \beta z. \end{aligned} \tag{17.1}$$

Where σ, ρ and β are real numbers. The usual parameters, for which the system is chaotic are $\sigma = 10$, $\rho = \frac{8}{3}$, $\beta = 28$. The Lyapunov exponents Fig.10.2 for such configuration are $\lambda_1 = 0.703$, $\lambda_2 = 0$ and $\lambda_3 = -13.120$.

When resolving systems of ODEs, especially when calculating it's Lyapunov exponents, one algorithm with multiple data approach was used. A parallel algorithm using decomposition and distribution of constants and parallel toolbox from Matlab can be used. Proposed algorithm has been tested on a chaotic circuit and has also been computed with different numbers of CPU cores compared with standard non distributed method. This technique has proved to be very effective on new multicore central processing units.

It is been calculated for which real numbers (meaning σ and ρ) the system behave chaotically. Setting $\sigma, \rho > 0$, initial conditions are located at $\mathbf{Ic}_0(1, 0, 0)^T$.

The results of the largest Lyapunov exponent are presented in Fig. 17.1. The matrix of evaluated parameters (σ, ρ) consists of 10000 elements.

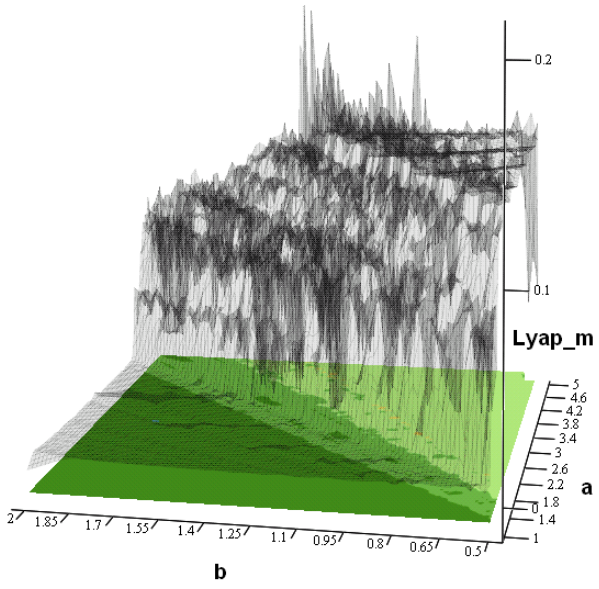

Fig. 17.1: The largest Lyapunov exponent for data set, where $a = \sigma$ and $b = \rho$.

The parallel method is a good improvement to contemporary approach. In Table 17.1. we can see the demonstrable speed up of the process. Utilizing the parallel computing one can use the full potential af computing units. Comparing the speed, it was used data set of size 10 by 10 matrix.

No. of CPUs	1 CPU	2 CPUs	4 CPUs	8 CPUs
Elapsed time[s]	353.6	180.3	116.2	88.4

Tab. 17.1: Comparing consumed time of computing for set of size 10 by 10

The proposed method is suitable for Beowulf clusters. As we have demonstrated in the Fig. 17.1 and the Table 17.1, the time consumption is great. One can also use stochastic optimization methods presented in [110, 111] for finding the chaotic solutions.

17.2 Parallel Particle Swarm Optimization on The Chaotic Solution of Dynamical Systems

A parallel approach for finding chaotic solutions of general third-order autonomous dynamical systems with piecewise-linear vector field utilizing particle swarm optimization (PPSO) was proposed. PPSO is a metaheuristic method that can search very large spaces of candidate solutions using modern multi-core processors performance.

To discover such sensitive systems in respect to chaotic behavior, special attention was devoted to the fitness function. Some of found systems are presented and analyzed in the section. A significant speedup using multi-core operations was proved.

17.2.1 Introduction

In recent years the research in optimization field was focused on description of behavior of several animals such as bees, birds, ants, etc. It is well known that swarm of bees is able to locate the best most fertile source of flowers on certain field. To achieve and design algorithm describing bees finding such collective behavior organized in almost orchestral manner that is known as swarm intelligence, first mathematical models need to be set. Gerardo Beni and Jing Wang introduced the term swarm intelligence in a 1989 article [112].

Swarm intelligence techniques are population based stochastic methods used in combinatorial optimization problems in which the collective behavior of relatively simple individuals arises from their local interactions with their environment to

produce functional global patterns. Swarm intelligence represents a meta-heuristic approach to solve a variety of problems.

Numerical optimization has been widely used in engineering to solve a variety of NP-complete problems in areas such as structural optimization, training neural networks or simple finding kernels coefficient for nonlinear equations. Typical NP-complete tasks include for example well known traveling salesman problem (finding the Hamiltonian circle). Optimization of such problems often imposes large computational demands, resulting in long solution times even on modern high-end processors.

17.2.2 Serial Particle Swarm Algorithm

In 1995, Dr. Kennedy and Dr. Eberhart developed method known as Particle swarm Optimization (PSO) [1], a population based stochastic optimization strategy, inspired by the social behavior of swarms. The method can also represent even social behavior of humans. Although PSO method is similar to the genetic algorithm (GA) in terms of initializing the population with random solutions and in terms of searching for the global optimum in successive generations.

The key difference is that PSO does not undergo crossover and mutation, while the particles move through the state space following the current optimum particles. Consider the swarm of p particles. Each particle representing the solution point by its position in the D dimensional state space.

The underlying concept is that for every instant moment, the velocity of each particle also known as the potential solution, changes between potential solution known as f^i_{best}. The particle associated with the best solution, the best value of fitness function, seems to be the leader and each particle keeps track of its coordinates in the problem state space.

The fitness value is stored and is referred as f^i_{best}. When a particle takes all the population as its topological neighbors, the best value is a global best and is called f^g_{best}. The whole algorithm is described by Fig. 17.2.

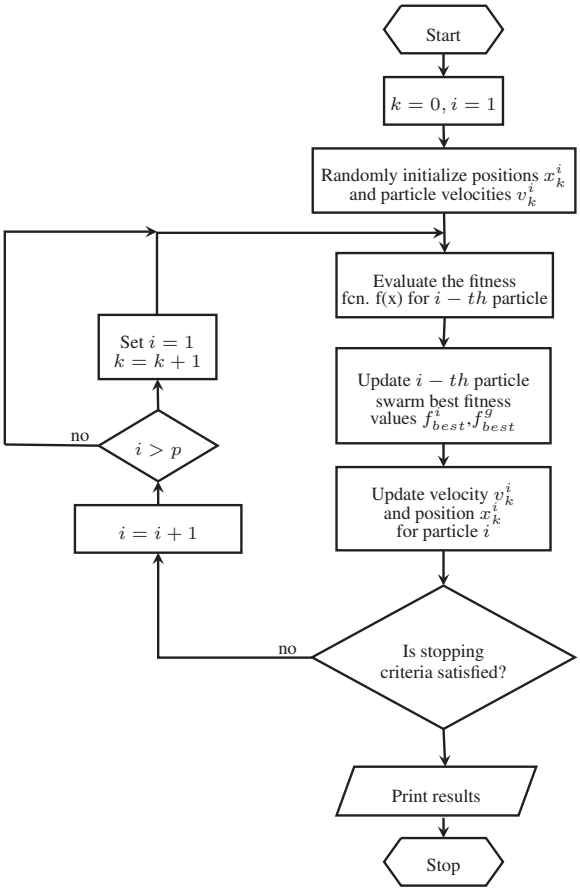

Fig. 17.2: The flowchart of asynchronous (serial) particle swarm algorithm [1].

17.2.3 Parallel Particle Swarm Algorithm

The approach itself is almost the same, but few features were changed. Parallel processing allows to evaluate more fitness functions or to solve more complex tasks (or with higher accuracy) in the same time span as the asynchronous version described in previous section. Fitness functions are evaluated for different particles in parallel. Because of different complexity of each solution, the results need to be synchronized. The whole algorithm is described by Fig. 17.3.

17.2.4 Speedup and Efficiency

In parallel computing, speedup refers to how much a parallel algorithm is faster than a corresponding sequential algorithm defined as:

$$S_p = \frac{T_1}{T_p}, \tag{17.2}$$

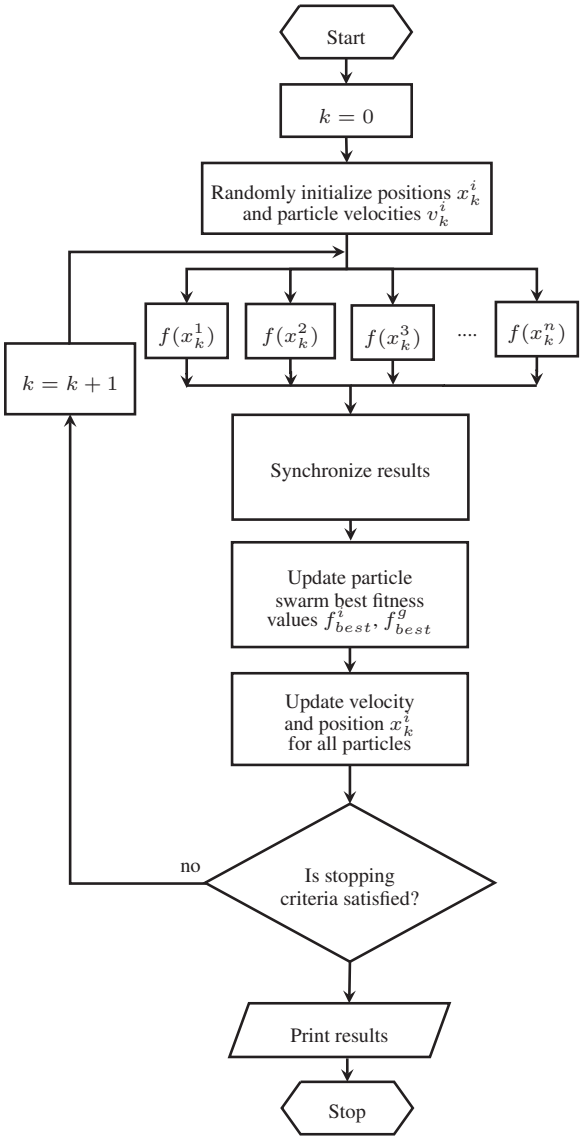

Fig. 17.3: The flowchart of parallel particle swarm algorithm.

where p is the number of processors, T_1 is the execution time of serial algorithm, T_p is the execution time of parallel algorithm.

It is obvious, that ideal speedup is (linear speedup) when it is equal to number of processors. Sometimes a speedup of more than p when using p processors is observed in parallel computing, which is called super linear speedup. One possible reason for a super linear speedup is the cache effect resulting from the different memory hierarchies of modern computers.

Efficiency performance scale defined as:

$$E_p = \frac{S_p}{p} = \frac{T_1}{p \cdot T_p}. \tag{17.3}$$

Considering serial algorithm, its efficiency is equal to 1, but the value usually lies in the set $E_p \in < 0; 1 >$.

Some tasks are difficult to parallelize, or even not possible. Theoretical value for the efficiency can be defined as:

$$E_p = \frac{1}{\ln p}. \tag{17.4}$$

17.2.5 Numerical Simulations

For evaluating the algorithm general system of differential equations of third order and absolute nonlinear function was chosen [69, 122, 70]. The system can be expressed by the following set of the dimensionless differential equations as:

$$\begin{aligned} \dot{x} &= a_1 x + a_2 y + a_3 z + |a_4 x| + a_5 \\ \dot{y} &= a_6 x + a_7 y + a_8 z + |a_9 y| + a_{10} \\ \dot{z} &= a_{11} x + a_{12} y + a_{13} z + |a_{14} z| + a_{15}, \end{aligned} \tag{17.5}$$

where $a_1, \cdots, a_{15}$ are constants to be found by algorithm. The x, y, z are the state variables.

We can observe, that the non-linear function is made of absolute values over state variables.

The vector field is divided by non-linear function into the several planes. To find chaotic solution effectively, Lyapunov exponents (LE) [61] can be used as quantifier.

They are calculated from general differential equations using the JM. To get derivatives the absolute value was substituted supposing $(x \wedge y \wedge z) \in \mathbb{R}^3$ we can write:

$$\begin{aligned} \frac{d}{dx}|x| &= \lim_{h \longrightarrow 0} \frac{|x+h| - |x|}{h} \\ &\approx \lim_{h \longrightarrow 0} \frac{\sqrt{(x+h)^2} - \sqrt{(x)^2}}{h} \\ &= \frac{x}{\sqrt{(x)^2}} \approx \frac{x}{|x|} \end{aligned} \tag{17.6}$$

Then the JM for dynamical system (17.5) is defined as:

$$\mathbf{J} = \begin{pmatrix} a_1 + \frac{\sqrt{(a_4 \cdot x)^2}}{x} & a_2 & a_3 \\ a_6 & a_7 + \frac{\sqrt{(a_9 \cdot y)^2}}{y} & a_8 \\ a_{11} & a_{12} & a_{13} + \frac{\sqrt{(a_{14} \cdot z)^2}}{z} \end{pmatrix}, \tag{17.7}$$

and satisfying constrain conditions:

$$(x, y, z) \in \mathbb{R}^3 \neq 0. \tag{17.8}$$

Several problems can appear in the process of calculation [120, 113, 114]. First of all, the regions of chaos are very small and often surrounded by an unbounded solution[141, 115]. It is because chaotic systems are perfectly balanced systems. While using the concept of exponential divergence the routine for the calculation of LE spectrum can fail providing two positive numbers [122, 121]. To improve the general convergence, first step is to check if integrated system meets the chosen boundary conditions. It allows us to reduce computation time and also omits diverge results.

Another problem can arise from JM itself. The matrix J is undefined for $(x \vee y \vee z) = 0$ (the system is defined there). Thus we have to be careful of choosing the initial conditions. They were chosen to be $\mathbf{I}_c = (0.1, 0.1, 0.1)^T$. Setting the integration time long enough avoids analysis of transient. Fortunately such setup would lead to correct result (avoiding equilibrium points and meeting previous conditions). It is because of folding and stretching the state space on to the state space attractor.

Due to using such powerful optimizing method it is no longer matter of finding only chaotic solutions. Measure called Kaplan-Yorke dimension can be utilized to obtain the "most" chaotic solution. Such dimension for chaotic solution of equations (17.5) is real number $D_{KY} \in < 2, 3 >$. The calculation of Kaplan-Yorke dimension is defined by using Lyapunov exponents in section (10.1.3):

17.2.6 Results

Simulations were done on personal computer with parameters: CPU Intel Core i5 ($4 \times 2.5GHz$), 4GB RAM, Matlab R2010b. The algorithm is also designed to be used on Beowulf clusters. The algorithm was able to find 15 constants that exhibit chaotic solution.

The integrated system using Runge-Kutta method with variable step size. Two different possible solutions are in the Fig. 17.4. and in the Fig. 17.5. First one is denoted as P_1, equations (17.9):

$$\begin{aligned} \dot{x} &= 0.7x - 1.7y + 0.8z + |\pm 1.4x| + 0.5 \\ \dot{y} &= 2.42x + 0.571y + 0.8z + |\pm 1.2208y| + 0.3583 \\ \dot{z} &= 1.6322x + 0.595y - 0.641z + |\pm 0.67z| + 1.2375, \end{aligned} \tag{17.9}$$

the second is denoted as P_2, equations (17.10):

$$\begin{aligned} \dot{x} &= 0.7482x - 1.6934y + 0.81z + |\pm 1.242x| + 0.7927 \\ \dot{y} &= 2.3854x + 0.5713y + 0.7908z + |\pm 1.2208y| + 0.3583 \\ \dot{z} &= 1.6322x + 0.595y - 0.641z + |\pm 0.6702z| + 1.2375, \end{aligned} \tag{17.10}$$

The solutions presented in equations (17.9) and (17.10) seems to be very complex. Thus several conditions restricting the set (precision in fact) of parameters were applied to satisfy produce solutions. Such solution is presented in equations (17.11), the state attractor is in Fig. 17.6. The final equations can be expressed as:

$$\begin{aligned} \dot{x} &= x - 2y + 0.5z + |\pm 0.5x| + 1 \\ \dot{y} &= 3x + y - 0.5z + |\pm 0.2y| + 1 \\ \dot{z} &= 2x + y - 0.5z + |\pm 0.5z| + 1. \end{aligned} \tag{17.11}$$

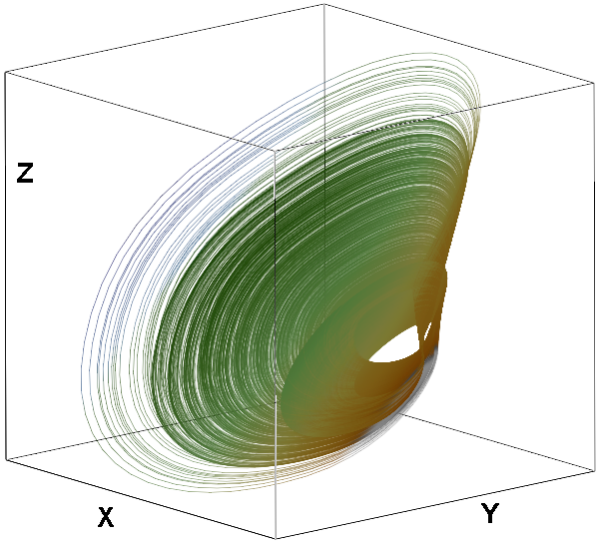

Fig. 17.4: Possible chaotic solution, equations (17.9), attractor for parameters of P_1.

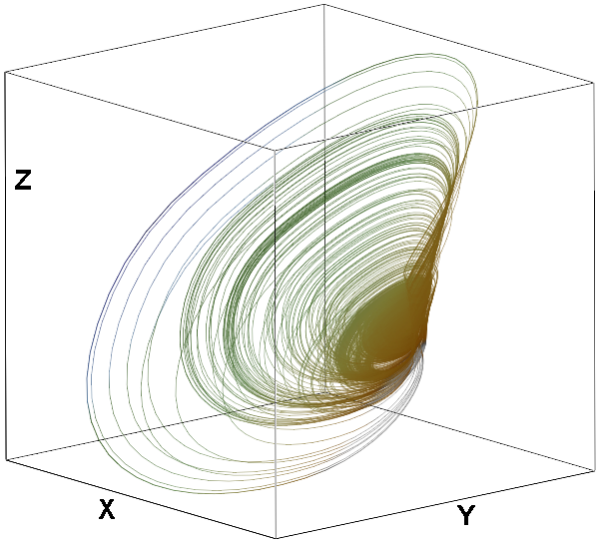

Fig. 17.5: Possible chaotic solution, equations (17.10), attractor for parameters of P_2.

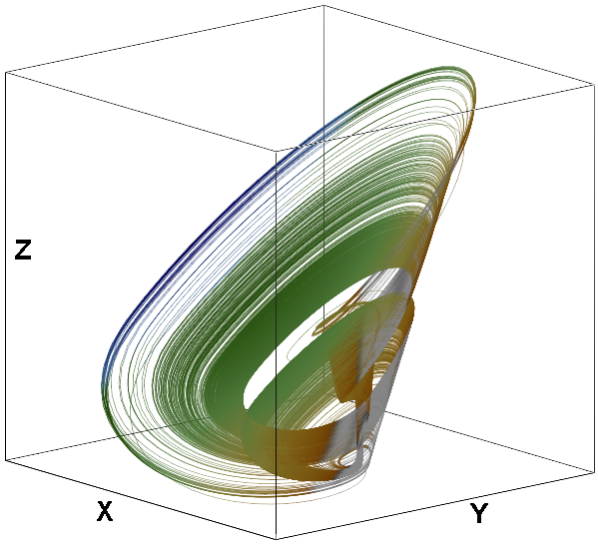

Fig. 17.6: Possible chaotic solution, equations (17.11), attractor for parameters of P_3.

17.3 Conclusion

In the first section of this chapter, the novel method for parallel computing of Lyapunov exponents for large data sets has been presented. The method was tested on various systems and proved to be efficient in terms of speeding up the computations. In the [130] the calculations have been verified by practical implementation into the circuit.

Tab. 17.2: Table of parameters and results for under test taken systems (for 10 particles and 10 iterations).

No. of CPUs	**Elap. time [s]** (Matlab)	**Speedup** S_P	**Efficiency** E_P
1	626.7448	1.00	1.00
2	374.5314	1.67	0.83
3	291.8926	2.15	0.72
4	229.6355	2.72	0.68

The optimization method using parallel particle swarms for finding the chaotic solutions is proposed. The algorithm itself showed significant speedup (Tab. 17.2) of this particular problem. Despite better throughput (efficiency) of the algorithm, there are still several problems to overcome. Finding better quantification for identification of chaos would be topic for further research.

Although nonlinear dynamics especially the chaos theory is the research interest for many decades there are still some unanswered questions. Few of them are listed in the papers [70, 141, 136]. The whole algorithm is dealing with the unanswered question how natural chaotic behavior is for complex systems and for simple systems.

18 CONCLUSIONS AND PERSPECTIVES OF PART II

The purpose of this chapter is to summarize the work dedicated to methods for analyzing the nonlinear dynamical systems.

In this chapter the concept of mathematical model analysis was briefly discussed. First one of the oldest method called Poincare sections for quantification of the motion is presented. This method is not very accurate, but can be used also for time series approach. One of the main issues is the setup of intersection planes.

The next section presents bifurcation analysis. The method is often used in order to investigate the stability of the systems.

The last section presents quantifier so-called Lyapunov exponents. The LE are one of the most widely used for investigation of the mathematical systems. As will be presented later, there exist cases, where the quantifier is limited.
In the first section reconstruction of attractor dynamics is introduced. It is very useful tool, because in real-valued measurements the availability of state variables is highly limited. One of the main issues that hast to be overcome is the estimation of parameters for reconstruction.

In the next section the estimation of embedded dimension is presented.

The next section presents one of the methods for estimation of τ that is used for reconstruction of dynamics of attractor.

The last section presents example of time series analysis, on the well known Lorenz attractor, applying the previously presented tools.

It is known that avoiding fractional integrators the third order of autonomous dynamical systems is the minimum order to produce chaos. Generating chaotic behavior in less than third order autonomous systems is quite delicate process. The whole system is extremely sensitive as for the initial conditions as for the realization. To obtain chaotic behavior, the whole system has to be perfectly balanced. With the growing order of the system, the presence of chaotic behavior is more probable.

Probably the first physical system to be recognized as demonstrating the frac-

tional properties is the semi infinite lossy (RC) transmission lines [85]. Another example of using fractional order circuits can be found in [86, 87], where the author utilize the fractional-order two-port circuit element in different filtering applications.

Several ideas from the area of numerical analysis of the dynamical systems with low dissipation have been suggested and verified. These procedures allow solving the serious problems where standard existing procedures can not be used.

Moreover, the authors believe that GP oscillator models the three-dimensional Brownian-like motion [92] of the single microscopic particle without interactions.

The vector field discontinuity and flow jumping resembles the particle-like behavior known from the quantum theory [93]. There is no doubt that there are a lot of real physical systems with the similar mathematical description.
The main purpose of this chapter is to extend current state-of-the-art in the field of complicated vector field approximations. Discovered method can be marked as general and applicable to dynamical systems with almost any type and number of the nonlinear functions.

This can be handy especially in the case theoretical study of the underlying dynamics. It is well known that dynamical motion in each region of the vector field can be described analytically.

Proposed algorithm for approximation can be extended for higher-order mathematical models as well as for higher-dimensional nonlinear functions.

There have been also other definitions of the metric dimensions that can be used for motion quantification. For example the capacity (box-counting) dimension has enormous computational time demands which increases drastically for large state space attractors. For example it proves to be worthless if labyrinth chaos [118] is a reference behavior.
It is demonstrated by means of the several examples that it is effective to use mixed analog-digital synthesis even in the case of the chaotic dynamics. There exist some dynamical systems (for example with cyclically symmetrical vector field) with multiple complex nonlinear functions making its truly analog circuitry implementation almost impossible. The presented approach can be utilized to solve such problem. In fact, the whole circuitry can be fully implemented in the language of a digital signal processing.
The results, explained in this chapter, show that the proposed quantifier is suitable for dynamical systems with large attractors. The principle itself is very simple and

can be easily implemented.

The significant speed-up of the computation is obvious because of reduction of one degree of freedom. The advantage of this method is also, it can be used for a time-series recognition. Some well known systems of dynamical equations were tested. The result were compared with the LE.

The preliminary results showed, that the method can be used for chaotic motion recognition.
. Generating chaotic behavior in third-order autonomous systems is quite delicate process. The whole system is extremely sensitive as for the initial conditions as for the realization. It is known that avoiding fractional integrators the third order of autonomous dynamical systems is the minimum order to produce chaos. To obtain chaotic behavior, the whole system has to be perfectly balanced.

With the growing order of the system, the presence of chaotic behavior is more probable. In this chapter the well known 2-D $m \times n$ scroll system was chosen and was realized utilizing novel approach using the data converters as non-linear functions. First the models were derived to simulate the data converters connected directly (ADC-DAC).

Then the connection was reduced to produce less scrolls. To verify the chaotic behavior of proposed conception, the circuit simulator PSpice was used. Then the circuit was build and measured. The measured results are rather matching the theoretical expectations.

In the first section of this chapter, the novel method for parallel computing of Lyapunov exponents for large data sets has been presented. The method was tested on various systems and proved to be efficient in terms of speeding up the computations. In the [130] the calculations have been verified by practical implementation into the circuit.

The optimization method using parallel particle swarms for finding the chaotic solutions is proposed. The algorithm itself showed significant speedup (Tab. 17.2) of this particular problem. Despite better throughput (efficiency) of the algorithm, there are still several problems to overcome. Finding better quantification for identification of chaos would be topic for further research.

Although nonlinear dynamics especially the chaos theory is the research interest

for many decades there are still some unanswered questions. Few of them are listed in the papers [70, 141, 136]. The whole algorithm is dealing with the unanswered question how natural chaotic behavior is for complex systems and for simple systems.

BIBLIOGRAPHY

[1] J. Kennedy and R. Eberhart, "Particle swarm optimization," in *Neural Networks, 1995. Proceedings., IEEE International Conference on*, vol. 4, pp. 1942–1948 vol.4, 1995.

[2] M. M. Rana, "Performance comparison of lms and rls channel estimation algorithms for 4g mimo ofdm systems," in *Computer and Information Technology (ICCIT), 2011 14th International Conference on*, pp. 635–639, 2011.

[3] E. Ngoya, C. Quindroit, and J. M. Nebus, "On the continuous-time model for nonlinear-memory modeling of rf power amplifiers," *Microwave Theory and Techniques, IEEE Transactions on*, vol. 57, no. 12, pp. 3278–3292, 2009.

[4] J. Ibanez-Diaz, C. Pantaleon, I. Santamaria, T. Fernandez, and D. Martinez, "Nonlinearity estimation in power amplifiers based on subsampled temporal data," *Instrumentation and Measurement, IEEE Transactions on*, vol. 50, no. 4, pp. 882–887, 2001.

[5] J. P. Martins, P. M. Cabral, N. B. Carvalho, and J. C. Pedro, "A metric for the quantification of memory effects in power amplifiers," *Microwave Theory and Techniques, IEEE Transactions on*, vol. 54, no. 12, pp. 4432–4439, 2006.

[6] O. Hammi, M. Younes, and F. M. Ghannouchi, "Metrics and methods for benchmarking of rf transmitter behavioral models with application to the development of a hybrid memory polynomial model," *Broadcasting, IEEE Transactions on*, vol. 56, no. 3, pp. 350–357, 2010.

[7] H. Seidel, "A microwave feedforward experiment," *Bell Systems Technical Journal*, vol. Vol. 50, pp. 2879–2918, 1971.

[8] Y. Jaehyok, Y. Youngoo, P. Myungkyu, K. Wonwoo, and B. Kim, "Analog predistortion linearizer for high-power rf amplifiers," *Microwave Theory and Techniques, IEEE Transactions on*, vol. 48, no. 12, pp. 2709–2713, 2000.

[9] Y. Nagata, "Linear amplification technique for digital mobile communications," in *Vehicular Technology Conference, 1989, IEEE 39th*, pp. 159–164 vol.1, 1989.

[10] J. K. Cavers, "Amplifier linearization using a digital predistorter with fast adaptation and low memory requirements," *Vehicular Technology, IEEE Transactions on*, vol. 39, no. 4, pp. 374–382, 1990.

[11] J. K. Cavers, "A linearizing predistorter with fast adaptation," in *Vehicular Technology Conference, 1990 IEEE 40th*, pp. 41–47, 1990.

[12] L. Ding and G. T. Zhou, "Effects of even-order nonlinear terms on power amplifier modeling and predistortion linearization," *Vehicular Technology, IEEE Transactions on*, vol. 53, no. 1, pp. 156–162, 2004.

[13] O. Shimbo, "Effects of intermodulation, am-pm conversion, and additive noise in multicarrier twt systems," *Proceedings of the IEEE*, vol. 59, no. 2, pp. 230–238, 1971.

[14] A. Saleh, "Intermodulation analysis of fdma satellite systems employing compensated and uncompensated twt's," *Communications, IEEE Transactions on*, vol. 30, no. 5, pp. 1233–1242, 1982.

[15] A. A. M. Saleh, "Frequency-independent and frequency-dependent nonlinear models of twt amplifiers," *Communications, IEEE Transactions on*, vol. 29, no. 11, pp. 1715–1720, 1981.

[16] J. R. Cadenas, M. Valdez, B. Palafox, C. Gontrand, and J. C. N. Perez, "Performance evaluation of a memory-polynomial model for microwave power amplifiers," *Programacion Matematica y Software*, vol. 4, pp. 13–23, 2012.

[17] M. Honkanen and S. G. Haggman, "New aspects on nonlinear power amplifier modeling in radio communication system simulations," in *Personal, Indoor and Mobile Radio Communications, 1997. Waves of the Year 2000. PIMRC '97., The 8th IEEE International Symposium on*, vol. 3, pp. 844–848 vol.3, 1997.

[18] C. Dudak and N. D. Kahyaoglu, "A descriptive study on am-am and am-pm conversion phenomena through evm-snr relation," in *Power Amplifiers for Wireless and Radio Applications (PAWR), 2012 IEEE Topical Conference on*, pp. 69–72, 2012.

[19] A. Ghorbani and M. Sheikhan, "The effect of solid state power amplifiers (sspas) nonlinearities on mpsk and m-qam signal transmission," in *Digital Processing of Signals in Communications, 1991., Sixth International Conference on*, pp. 193–197, 1991.

[20] G. P. White, A. G. Burr, and T. Javornik, "Modelling of nonlinear distortion in broadband fixed wireless access systems," *Electronics Letters*, vol. 39, no. 8, pp. 686–687, 2003.

[21] M. Schoukens, R. Pintelon, and Y. Rolain, "Parametric identification of parallel hammerstein systems," *Instrumentation and Measurement, IEEE Transactions on*, vol. 60, no. 12, pp. 3931–3938, 2011.

[22] D. Silveira, M. Gadringer, H. Arthaber, and G. Magerl, "Rf-power amplifier characteristics determination using parallel cascade wiener models and pseudo-inverse techniques," in *Microwave Conference Proceedings, 2005. APMC 2005. Asia-Pacific Conference Proceedings*, vol. 1, pp. 4 pp.–, 2005.

[23] V. A. Bohara, M. A. Hussein, and O. Venard, "Parameter identification algorithm for multi-stage digital predistorter," in *Proceedings of the 43rd European Microwave Conference*, 2013.

[24] M. E. Gadringer, D. Silveira, and G. Magerl, "Efficient power amplifier identification using modified parallel cascade hammerstein models," in *Radio and Wireless Symposium, 2007 IEEE*, pp. 305–308, 2007.

[25] N. Calinoiu, S. Bachir, and C. Duvanaud, "A power amplifier envelope distortion model using direct calculation of polynomial parameters and delay taps," in *Microwave Integrated Circuits Conference (EuMIC), 2011 European*, pp. 292–295, 2011.

[26] E. G. Lima, T. R. Cunha, H. M. Teixeira, M. Pirola, and J. C. Pedro, "Baseband derived volterra series for power amplifier modeling," in *Microwave Symposium Digest, 2009. MTT '09. IEEE MTT-S International*, 2009.

[27] M. Schetzen, *The Volterra and Wiener Theories of Nonlinear Systems*. Wiley, 1980.

[28] J. Kim and K. Konstantinou, "Digital predistortion of wideband signals based on power amplifier model with memory," *Electronics Letters*, vol. 37, no. 23, pp. 1417–1418, 2001.

[29] L. Ding, G. T. Zhou, D. R. Morgan, M. Zhengxiang, J. S. Kenney, K. Jaehyeong, and C. R. Giardina, "A robust digital baseband predistorter constructed using memory polynomials," *Communications, IEEE Transactions on*, vol. 52, no. 1, pp. 159–165, 2004.

[30] R. Marsalek, P. Jardin, and G. Baudoin, "From post-distortion to predistortion for power amplifiers linearization," *Communications Letters, IEEE*, vol. 7, no. 7, pp. 308–310, 2003.

[31] R. Dallinger, H. Ruotsalainen, R. Wichman, and M. Rupp, "Adaptive predistortion techniques based on orthogonal polynomials," in *Signals, Systems and Computers (ASILOMAR), 2010 Conference Record of the Forty Fourth Asilomar Conference on*, pp. 1945–1950, 2010.

[32] R. Raich, H. Qian, and G. T. Zhou, "Orthogonal polynomials for power amplifier modeling and predistorter design," *Vehicular Technology, IEEE Transactions on*, vol. 53, no. 5, pp. 1468–1479, 2004.

[33] Z. Anding, J. C. Pedro, and T. J. Brazil, "Dynamic deviation reduction-based volterra behavioral modeling of rf power amplifiers," *Microwave Theory and Techniques, IEEE Transactions on*, vol. 54, no. 12, pp. 4323–4332, 2006.

[34] G. Lei and A. Zhu, "Simplified dynamic deviation reduction-based volterra model for doherty power amplifiers," in *Integrated Nonlinear Microwave and Millimetre-Wave Circuits (INMMIC), 2011 Workshop on*, pp. 1–4, 2011.

[35] Z. Anding, P. Draxler, J. Yan, T. Brazil, D. Kimball, and P. Asbeck, "Open-loop digital predistorter for rf power amplifiers using dynamic deviation reduction-based volterra series," *Microwave Theory and Techniques, IEEE Transactions on*, vol. 56, no. 7, pp. 1524–1534, 2008.

[36] D. R. Morgan, M. Zhengxiang, K. Jaehyeong, M. Zierdt, and J. Pastalan, "A generalized memory polynomial model for digital predistortion of rf power amplifiers," *Signal Processing, IEEE Transactions on*, vol. 54, no. 10, pp. 3852–3860, 2006.

[37] N. Benvenuto, F. Piazza, and A. Uncini, "A neural network approach to data predistortion with memory in digital radio systems," in *Communications, 1993. ICC '93 Geneva. Technical Program, Conference Record, IEEE International Conference on*, vol. 1, pp. 232–236 vol.1, 1993.

[38] M. Doufana, P. Chan-Wang, and M. Bahoura, "A neural network based online adaptive predistorter for power amplifier," in *Wireless and Microwave Technology Conference (WAMICON), 2010 IEEE 11th Annual*, pp. 1–4, 2010.

[39] M. Isaksson, D. Wisell, and D. Ronnow, "Wide-band dynamic modeling of power amplifiers using radial-basis function neural networks," *Microwave Theory and Techniques, IEEE Transactions on*, vol. 53, no. 11, pp. 3422–3428, 2005.

[40] M. Rawat, K. Rawat, and F. Ghannouchi, "Adaptive digital predistortion of wireless power amplifiers/transmitters using dynamic real-valued focused

time-delay line neural networks," *Microwave Theory and Techniques, IEEE Transactions on*, vol. 58, no. 1, pp. 95–104, 2010.

[41] M. Rawat and F. M. Ghannouchi, "Distributed spatiotemporal neural network for nonlinear dynamic transmitter modeling and adaptive digital predistortion," *Instrumentation and Measurement, IEEE Transactions on*, vol. 61, no. 3, pp. 595–608, 2012.

[42] G. Cybenko, "Approximation by superpositions of a sigmoidal function," *Mathematics of Control, Signals, and Systems (MCSS)*, vol. 2, pp. 303–314, 1989.

[43] N. Naskas and Y. Papananos, "Neural-network-based adaptive baseband predistortion method for rf power amplifiers," *Circuits and Systems II: Express Briefs, IEEE Transactions on*, vol. 51, no. 11, pp. 619–623, 2004.

[44] F. Mkadem and S. Boumaiza, "Physically inspired neural network model for rf power amplifier behavioral modeling and digital predistortion," *Microwave Theory and Techniques, IEEE Transactions on*, vol. 59, no. 4, pp. 913–923, 2011.

[45] L. Taijun, S. Boumaiza, and F. M. Ghannouchi, "Dynamic behavioral modeling of 3g power amplifiers using real-valued time-delay neural networks," *Microwave Theory and Techniques, IEEE Transactions on*, vol. 52, no. 3, pp. 1025–1033, 2004.

[46] D. Luongvinh and K. Youngwoo, "A fully recurrent neural network-based model for predicting spectral regrowth of 3g handset power amplifiers with memory effects," *Microwave and Wireless Components Letters, IEEE*, vol. 16, no. 11, pp. 621–623, 2006.

[47] R. E. Kalman, "A new approach to linear filtering and prediction problems," *Journal of Basic Engineering*, vol. 82, p. 35âĂŞ45, 1960.

[48] M. Djamai, S. Bachir, and C. Duvanaud, "Kalman filtering algorithm for on-line memory polynomial predistortion," in *Microwave Conference, 2008. EuMC 2008. 38th European*, pp. 575–578, 2008.

[49] A. V. Malipatil and H. Yih-Fang, "Amplifier predistortion using unscented kalman filtering," in *Signal Processing Advances in Wireless Communications, 2005 IEEE 6th Workshop on*, pp. 221–225, 2005.

[50] S. Bachir, C. Duvanaud, and D. Djamai, "On-line memory polynomial predistortion based on the adapted kalman filtering algorithm," in *Circuits and Systems and TAISA Conference, 2008. NEWCAS-TAISA 2008. 2008 Joint 6th International IEEE Northeast Workshop on*, pp. 65–68, 2008.

[51] A. Malipatil and H. Yih-Fang, "Amplifier predistortion using unscented kalman filtering," in *Signal Processing Advances in Wireless Communications, 2005 IEEE 6th Workshop on*, pp. 221–225, 2005.

[52] S. Bachir, N. Calinou, and C. Duvanaud, "Linearization of rf power amplifiers using adaptive kalman filtering algorithm," *Journal of Circuits, Systems and Computers*, vol. 20, no. 06, pp. 1001–1018, 2011.

[53] P. Jardin and G. Baudoin, "Filter lookup table method for power amplifier linearization," *Vehicular Technology, IEEE Transactions on*, vol. 56, no. 3, pp. 1076–1087, 2007.

[54] W. A. Chang and R. S. Ramakrishna, "Elitism-based compact genetic algorithms," *Evolutionary Computation, IEEE Transactions on*, vol. 7, no. 4, pp. 367–385, 2003.

[55] S. D. Waele and P. M. T. Broersen, "Order selection for vector autoregressive models," *Signal Processing, IEEE Transactions on*, vol. 51, no. 2, pp. 427–433, 2003.

[56] J. Lienig, "A parallel genetic algorithm for performance-driven vlsi routing," *Evolutionary Computation, IEEE Transactions on*, vol. 1, no. 1, pp. 29–39, 1997.

[57] H. Hao, Q. Hua, X. Hui, and W. Xiaotao, "Fractional delay compensation in digital predistortion system," in *Acoustics, Speech and Signal Processing (ICASSP), 2012 IEEE International Conference on*, pp. 3569–3572, 2012.

[58] T. I. Laakso, V. Valimaki, M. Karjalainen, and U. K. Laine, "Splitting the unit delay in fir/all pass filters design," *Signal Processing Magazine, IEEE*, vol. 13, no. 1, pp. 30–60, 1996.

[59] G. Maalouli and D. R. Stephens, "Joint fractional resampler with delay equalization for high synchronization accuracy with a reduced number of samples per symbol," in *Acoustics, Speech, and Signal Processing, 2004. Proceedings. (ICASSP '04). IEEE International Conference on*, vol. 5, pp. V–349–52 vol.5, 2004.

[60] E. Zeraoulia and J. C. Sprott, "Some open problems in chaos theory and dynamics," *International Journal of Open Problems in Computer Science and Mathematics*, vol. 4, pp. 1–10, 2011.

[61] M. Small, *Applied Nonlinear Time Series Analysis: Applications in Physics, Physiology and Finance*. World Scientific series in nonlinear science, Series A, World Scientific, 2005.

[62] D. A. Arroyo-Almanza, A. N. Pisarchik, and F. R. Ruiz-Oliveras, "Route to chaos in a ring of three unidirectionally-coupled semiconductor lasers," *Photonics Technology Letters, IEEE*, vol. 24, no. 7, pp. 605–607, 2012.

[63] H. G. E. Hentschel and I. Procaccia, "The infinite number of generalized dimensions of fractals and strange attractors," *Physica D Nonlinear Phenomena*, vol. 8, pp. 435–444, Sept. 1983.

[64] J. C. Sprott, *Chaos and Time-Series Analysis*. Oxford University Press, 2003.

[65] J. C. Sprott, "Some simple chaotic flows," *Phys. Rev. E*, vol. 50, pp. R647–R650, 1994.

[66] G. P. Williams, *Chaos Theory Tamed*. London: Taylor and Francis, 1997.

[67] H. Kantz and T. Schreiber, *Nonlinear Time Series Analysis*. Cambridge nonlinear science series, Cambridge University Press, 2004.

[68] J. C. Sprott and K. E. Chlouverakis, "Labyrinth chaos," *I. J. Bifurcation and Chaos*, vol. 17, no. 6, pp. 2097–2108, 2007.

[69] J. Petrzela and J. Prokopec, "Some practical experiments with simple driven dynamical systems," in *Radioelektronika, 2009. RADIOELEKTRONIKA '09. 19th International Conference*, pp. 247–250, 2009.

[70] J. C. Sprott, *Elegant Chaos: Algebraically Simple Chaotic Flows*. World Scientific, 2010.

[71] K. Grygiel and P. Szlachetka, "Lyapunov exponents analysis of autonomous and nonautonomous set of ordinary differential equations," *Acta Physica Polonica B*, vol. 26, pp. 1321 – 1331, 1995.

[72] V. Spany, P. Galajda, M. Guzan, L. Pivka, and M. Olejar, "Chua's singularities: Great miracle in circuit theory.," *I. J. Bifurcation and Chaos*, vol. 20, no. 10, pp. 2993–3006, 2010.

[73] A. Wolf, J. B. Swift, H. L. Swinney, and J. A. Vastano, "Determining Lyapunov exponents from a time series," *Physica D*, vol. 16, p. 285, 1985.

[74] N. K. Bari, *A treatise on trigonometric series*. No. v. 1 in A Treatise on Trigonometric Series, Pergamon Press, 1964.

[75] P. Morters, Y. Peres, O. Schramm, and W. Werner, *Brownian Motion*. Cambridge Series in Statistical and Probabilistic Mathematics, Cambridge University Press, 2010.

[76] H. Ocampo, S. Paycha, and A. Vargas, *Geometric and Topological Methods for Quantum Field Theory*. Lecture Notes in Physics, Springer, 2005.

[77] P. Grassberger and I. Procaccia, "Characterization of strange attractors," *Physical Review Letters*, vol. 50, pp. 346–349, 1983.

[78] L. Min, W. Zhizhong, and F. Zhengjin, "A method of embedding dimension estimation based on symplectic geometry," *Physics Letters A*, vol. 303, pp. 179–189, 2002.

[79] E. N. Lorenz, "Deterministis nonperiodic flow," *Journal of Atmospheric Sciences*, vol. 1, pp. 130–141, 1963.

[80] F. Takens, "Detecting strange attractors in turbulence dynamical systems and turbulence," *Dynamical Systems and Turbulence*, vol. 898, pp. 366–381, 1981.

[81] I. Podlubny, *Fractional Differential Equations*. Academic Press, 1 ed., Nov. 1998.

[82] I. Podlubny, "Fractional-order systems and pid-controllers," *IEEE Transactions on Automatic Control*, vol. 44, no. 1, pp. 208–214, 1999.

[83] I. Petras, "The fractional - order controllers: Methods for their synthesis and application," *ArXiv Mathematics e-prints*, Apr. 2000.

[84] I. Podlubny, I. Petras, B. M. Vinagre, P. O'Leary, and L. Dorcak, "Analogue realizations of fractional-order controllers," *Nonlinear Dynamics*, vol. 29, no. 1-4, pp. 281–296, 2002.

[85] J. Valsa, P. Dvorak, and M. Friedl, "Network model of the cpe," *Radioengineering*, vol. 20, pp. 619–626, 2011.

[86] J. Petrzela, "Analog continuous-time filtering extended to fractional-order network elements," in *Telecommunications and Signal Processing (TSP), 2013 36th International Conference on*, pp. 417–421, 2013.

[87] J. Petrzela, "Fundamental analog cells for fractional-order two-port synthesis," in *Radioelektronika (RADIOELEKTRONIKA), 2013 23rd International Conference*, pp. 182–187, 2013.

[88] M. Itoh, "Synthesis of topologically conjugate chaotic nonlinear circuits," *International Journal of Bifurcation and Chaos*, vol. 07, no. 06, pp. 1195–1223, 1997.

[89] M. Itoh, "Synthesis of electronic circuits for simulating nonlinear dynamics," *International Journal of Bifurcation and Chaos*, vol. 11, no. 03, pp. 605–653, 2001.

[90] M. Stork, J. Hrusak, and D. Mayer, "Synthesis of electronic circuits for nonlinear dynamic system simulation and realization," in *Radioelektronika (RADIOELEKTRONIKA), 2012 22nd International Conference*, pp. 1–5, 2012.

[91] M. Stork, "Synthesis of nonlinear electronic system simulation and construction," in *ELEKTRO, 2012*, pp. 469–474, 2012.

[92] P. Morters and Y. Peres, *Brownian motion*. Cambridge University Press, 2008.

[93] H. Ocampo, S. Paycha, and A. Reyes, *Geometric methods for quantum theory*. World Scientific, 2008.

[94] L. Chua and A. C. Deng, "Canonical piecewise-linear modeling," *Circuits and Systems, IEEE Transactions on*, vol. 33, no. 5, pp. 511–525, 1986.

[95] V. Pospisil and Z. Kolka, "The piecewise-linear approximation using genetic algorithm," in *Proceedings of international confe-rence Electronic Devices and Systems*, 2005.

[96] D. M. W. Leenaerts and W. M. V. Bokhoven, *Piecewise Linear Modeling and Analysis*. Norwell, MA, USA: Kluwer Academic Publishers, 1998.

[97] J. Petrzela, "Optimal piecewise-linear approximation of the quadratic chaotic dynamics," *Radioengineering*, vol. 1, pp. 20–28, 2012.

[98] J. Slezak, R. Sotner, and J. Petrzela, "On the derivation of piecewise-linear chaotic oscillators using simulated annealing method and hspice," *Przeglad Electrotechniczny*, vol. 1, pp. 261–265, 2011.

[99] L. O. Chua, M. Komuro, and T. T. Matsumoto, "The double scroll family," *Circuits and Systems, IEEE Transactions on*, vol. 33, no. 11, pp. 1072–1118, 1986.

[100] O. E. Rossler, "An equation for continuous chaos," *Physics letters A*, vol. 5, pp. 397–398, 1976.

[101] J. Petrzela, *Modeling of the strange behavior in the selected nonlinear dynamical systems, part I: oscillators*. VUTIUM Press, 2008.

[102] J. Petrzela and V. Pospisil, "Nonlinear resistor with polyno-mial av characteristic and its application in chaotic oscillator," *Radioengineering*, vol. 13, pp. 20–25, 2004.

[103] J. Petrzela, *Modeling of the Strange Behavior in the Selected. Nonlinear Dynamical Systems, part II: Analysis*. VUTIUM Press, 2010.

[104] J. Froyland and H. Knut, "Lyapunov-exponent spectra for the lorenz model," *Phys. Rev. A*, vol. 29, pp. 2928–2931, May 1984.

[105] W. M. Ahmad, "Generation and control of multi-scroll chaotic attractors in fractional order systems," *Chaos, Solution & Fractals*, vol. 25, pp. 727–735, 2005.

[106] J. Lu and G. Chen, "Generating multiscroll chaotic attractors: Theories, methods and applications," *International Journal of Bifurcation and Chaos*, vol. 16, pp. 775–858, 2004.

[107] S. Ozoguz, A. S. Elwakil, and K. N. Salama, "n-scroll chaos generator using nonlinear transconductor," *Electronics Letters*, vol. 38, no. 14, pp. 685–686, 2002.

[108] R. Trejo-Guerra, E. Tlelo-Cuautle, C. Sanchzlopez, M. Munoz-Pachecoj, and C. Cruz-Hernandez, "Realization of multiscroll chaotic attractors by using current-feedback operational amplifers," *Revista Mexicana de Fisica*, vol. 56, pp. 268–274, 2010.

[109] J. Lu, F. Han, X. Yu, and G. Chen, "Generating 3-d multi-scroll chaotic attractors: A hysteresis series switching method," *Automatica*, vol. 2004, p. 1677âĂŞ1687, 2004.

[110] V. Genovese, L. Odetti, R. Magni, and P. Dario, "Self organizing behavior and swarm intelligence in a cellular robotic system," in *Intelligent Control, 1992., Proceedings of the 1992 IEEE International Symposium on*, pp. 243–248, 1992.

[111] J. Kennedy and R. Eberhart, "Particle swarm optimization," in *Neural Networks, 1995. Proceedings., IEEE International Conference on*, vol. 4, pp. 1942–1948 vol.4, 1995.

[112] G. Beni and J. Wang, "Swarm intelligence in cellular robotic systems," in *Proceed. NATO AdvancedWorkshop on Robots and Biological Systems*, 1989.

[113] G. Bhatnagar and Q. M. J. Wu, "Chaos-based security solution for fingerprint data during communication and transmission," *Instrumentation and Measurement, IEEE Transactions on*, vol. 61, no. 4, pp. 876–887, 2012.

[114] D. A. Arroyo-Almanza, A. N. Pisarchik, and F. R. Ruiz-Oliveras, "Route to chaos in a ring of three unidirectionally-coupled semiconductor lasers," *Photonics Technology Letters, IEEE*, vol. 24, no. 7, pp. 605–607, 2012.

[115] M. Guzan, "Boundary surface and stable manifold in sequential circuits," in *Radioelektronika (RADIOELEKTRONIKA), 2011 21st International Conference*, pp. 1–4, 2011.

LIST OF INTERNATIONAL JOURNAL PAPERS

[116] T. Gotthans and G. Baudoin. On multiple solutions in adaptive indirect digital predistortion. *IEEE Transactions on Vehicular Technology*, 2013. In Submission.

[117] T. Gotthans and Z. Hrubos. Multi grid chaotic attractors with discrete jumps. *Journal of Electrical Engineering*, 63:118–122, 2013.

[118] T. Gotthans and J. Petrzela. Experimental study of the sampled labyrinth chaos. *Radioengineering*, 20:420–427, 2011.

[119] T. Gotthans and J. Petrzela. Analysis and implementation of dynamical system with periodical discrete jumps. *Przeglad Elektrotechniczny*, 4:161–167, 2012.

[120] J. Petrzela and T. Gotthans. Chaotic oscillators with single polynomial nonlinearity and digital sampled dynamics. *Przeglad Elektrotechniczny*, 3:161–163, 2011.

[121] J. Petrzela, T. Gotthans, and M. Guzan. Dynamical tangles in third-order oscillator with single jump function. *International Journal of Bifurcation and Chaos*, pages 1–12, 2014. In Submission.

[122] J. Petrzela, T. Gotthans, and Z. Hrubos. Modeling deterministic chaos using electronic circuits. *Radioengineering*, 20:438–444, 2011.

[123] Z. Raida, Z. Kolka, R. Marsalek, J. Petrzela, A. Prokes, J. Sebesta, T. Gotthans, Z. Hrubos, Z. Kincl, L. Klozar, A. Povalac, R. Sotner, and P. Kadlec. Communication subsystems for emerging wireless technologies. *Radioengineering*, 21:1–14, 2012.

[124] J. Slezak, T. Gotthans, and J. Drinovsky. Evolutionary synthesis of fractional capacitor using simulated annealing method. *Radioengineering*, 4:1252–1259, 2012.

LIST OF INTERNATIONAL CONFERENCES

[125] T. Gotthans. On fractional autonomous algebraicly simple low order chaotic flow. In *International Conference on Circuits, Systems, Control, Signals*, 2012.

[126] T. Gotthans and G. Baudoin. Overview on the modeling and digital linearization of power amplifiers. In *International Conference on Circuits, Systems, Control, Signals*, 2012.

[127] T. Gotthans, G. Baudoin, and A. Mbaye. Comparison of modeling techniques for power amplifiers. In *Radioelektronika (RADIOELEKTRONIKA), 2013 23rd International Conference*, pages 232–235, 2013.

[128] T. Gotthans, G. Baudoin, and A. Mbaye. Influence of delay mismatch on digital predistortion for power amplifiers. In *20th International Conference Mixed design of integrated circuits and systems MIXDES*, 2013.

[129] T. Gotthans and J. Petrzela. Novel quantification for chaotic dynamical systems with large state attractors. In *Proceedings of the 13th IASME/WSEAS international conference on Mathematical Methods and Computational Techniques in Electrical Engineering conference on Applied Computing*, ACC'11/MMACTEE'11, pages 99–103, Stevens Point, Wisconsin, USA, 2011. World Scientific and Engineering Academy and Society (WSEAS).

[130] T. Gotthans, J. Petrzela, and Z. Hrubos. Advanced parallel processing of lyapunov exponents verified by practical circuit. In *Radioelektronika (RADIOELEKTRONIKA), 2011 21st International Conference*, pages 1–4, 2011.

[131] T. Gotthans, J. Petrzela, and Z. Hrubos. Analogue circuitry realization of neuron network. In *4th Chaotic Modeling and Simulation International Conference*, 2011.

[132] T. Gotthans, J. Petrzela, and Z. Hrubos. Analysis of hindmarsh-rose neuron model and novel circuitry realisation. In *Mixed Design of Integrated Circuits and Systems (MIXDES), 2011 Proceedings of the 18th International Conference*, pages 576–580, 2011.

[133] T. Gotthans, J. Petrzela, Z. Hrubos, and G. Baudoin. Parallel particle swarm optimization on chaotic solutions of dynamical systems. In *Radioelektronika (RADIOELEKTRONIKA), 2012 22nd International Conference*, pages 1–4, 2012.

[134] Z. Hrubos and T. Gotthans. Analysis and synthesis of the chaotic circuits based on ota elements. In *18th Iinternational Conference on Applied Electronics*, 2012.

[135] Z. Hrubos, T. Gotthans, and J. Petrzela. Circuit realization of the inertia neuron. In *Radioelektronika (RADIOELEKTRONIKA), 2011 21st International Conference*, pages 1–4, 2011.

[136] Z. Hrubos, T. Gotthans, and J. Petrzela. Novel circuit implementation of the nose-hoover thermostated dynamic system. In *Telecommunications and Signal Processing (TSP), 2011 34th International Conference on*, pages 307–311, 2011.

[137] Z. Hrubos, T. Gotthans, and J. Petrzela. Two equivalent circuit realizations of the ueda's oscillator. In *Mixed Design of Integrated Circuits and Systems (MIXDES), 2011 Proceedings of the 18th International Conference*, pages 694–698, 2011.

[138] Z. Hrubos, T. Gotthans, and J. Petrzela. Electronic experiments with dynamical model of thermostat system. In *Elektrorevue*, 2012.

[139] Z. Hrubos, T. Gotthans, and R. Sotner. Influence of gain changes for tuning purposes on observance of oscillation condition in simple oscillator. In *10th international conference Vsacky Cab*, 2012.

[140] A. Mbaye, G. Baudoin, M. Villegas, and T. Gotthans. Effect and adaptive correction of impedance mismatch between antenna and power amplifier on digital predistortion. In *New Circuits and Systems Conference (NEWCAS), 2013 IEEE 11th International*, pages 1–4, 2013.

[141] J. Petrzela and T. Gotthans. Selected general problems in chaos theory and nonlinear dynamics. In *Proceedings of the 13th IASME/WSEAS international conference on Mathematical Methods and Computational Techniques in Electrical Engineering conference on Applied Computing*, ACC'11/MMACTEE'11, pages 206–211, Stevens Point, Wisconsin, USA, 2011. World Scientific and Engineering Academy and Society (WSEAS).

[142] J. Petrzela, T. Gotthans, and Z. Hrubos. Analog implementation of gotthans-petrzela oscillator with virtual equilibria. In *Radioelektronika (RADIOELEKTRONIKA), 2011 21st International Conference*, pages 1–4, 2011.

[143] J. Petrzela, T. Gotthans, and Z. Hrubos. General review of the passive networks with fractional- order dynamics. In *International Conference on Circuits, Systems, Control, Signals*, 2012.

[144] J. Petrzela, Z. Hrubos, and T. Gotthans. Behavior identification in the real electronic circuits. In *Mixed Design of Integrated Circuits and Systems*

(MIXDES), 2011 Proceedings of the 18th International Conference, pages 438–441, 2011.

[145] J. Petrzela, Z. Hrubos, and T. Gotthans. Canonization of dynamical system representation using trivial linear transformations. In *Radioelektronika (RADIOELEKTRONIKA), 2012 22nd International Conference*, pages 1–4, 2012.

[146] R. Sotner, J. Jerabek, T. Gotthans, R. Prokop, T. Dostal, and K. Vrba. Controlled gain current and differential voltage amplifier and study of its application in simple adjustable oscillator. In *Telecommunications and Signal Processing (TSP), 2013 36th International Conference on*, pages 407–411, 2013.

LIST OF NATIONAL JOURNAL PAPERS

[147] T. Gotthans. Analyza dimenzi nelinearnich dynamickych systemu. In *Pokrocile metody, struktury a komponenty elektronicke bezdratove komunikace*, 2010.

[148] T. Gotthans. Obecny kvantifikator stavovych atraktoru s velkou prostorovou dynamikou. In *Pokrocile metody, struktury a komponenty elektronicke bezdratove komunikace*, 2011.

LIST OF NATIONAL CONFERENCES

[149] T. Gotthans. Estimating dimension of state space attractors. In *Proceedings of the 14th Conference STUDENT EEICT 2008*, 2008.

[150] T. Gotthans, G. Baudoin, and A. Mbaye. Influence d'un decalage temporel sur les performances de la predistorsion numerique d'amplificateur de puissance. In *18emes Journees Nationales Microondes*, 2013.

[151] A. Mbaye, G. Baudoin, and T. Gotthans. Etude de l'influence de la desadaptation d'impedance a l'antenne sur la linearisation d'amplificateurs de puissance par pre-distorsion numerique. In *18emes Journees Nationales Microondes*, 2013.

Resumé en français
Méthodes avancées pour l'analyse des systèmes dynamiques non-linéaires

Introduction

L'augmentation des performances des futurs systèmes dynamiques nécessite la prise en compte des phénomènes physiques non linéaires. Cette thèse apporte un éclairage et des contributions sur deux sujets complémentaires liés aux phénomènes dynamiques non linéaires. Le mémoire de thèse est divisé en deux parties.

La première partie porte sur les non-linéarités des amplificateurs de puissance dans le cadre d'applications destinées aux télécommunications ou à la diffusion audio-visuelle. Plusieurs méthodes de modélisation et de linéarisation des amplificateurs de puissance ont été conçues et discutées. Un banc de test a été développé afin d'évaluer les méthodes sur des amplificateurs réels. La robustesse de ces techniques à un mauvais alignement temporel des signaux a été évaluée. Par ailleurs, nous avons effectué une étude théorique sur l'existence et la prise en compte de solutions multiples dans l'approche adaptative par apprentissage indirect.

La deuxième partie traite des systèmes dynamiques non linéaires qui présentent des solutions chaotiques. Ces systèmes sont bien connus, mais les techniques d'identification de ces solutions manquent de fiabilité ou nécessitent une puissance de calcul importante. Dans cette thèse, plusieurs méthodes utilisant également le calcul parallèle sont présentées. Les systèmes à commande différentielle fractionnaire sont briévement discutés. Il est aussi montré, qu'il existe des systèmes liés à des fonctions de transfert non linéaires avec quantification pour lesquels les méthodes d'analyse classiques échouent.

Le travail de thèse s'est effectué dans le cadre du projet AMBRUN (projet FUI, partenariat : Thalès, TeamCast, Supélec et ESIEE Paris). Le projet AMBRUN vise à améliorer les performances des émetteurs de puissance pour l'amplification de signaux multiplexés via des corrections adaptatives pour des applications duales de communications tactiques et de radiodiffusion numérique en bande VHF. Une des originalités du projets réside dans la grande largeur de bande des signaux à transmettre (plus de 40 MHz), les fortes puissances émises (de l'ordre de la centaine de Watts) et la non-stationnarité des signaux multiplexés dans le cas des communications tactiques.

Chapitre 1

Modélisation et linéarisation des systèmes non-linéaires

1.1 Généralités sur les amplificateurs de puissance

Un amplificateur de puissance idéal ne devrait pas déformer le signal à transmettre. Le signal de sortie V_{out} devrait être proportionnel au signal d'entrée V_{in} avec un gain G :

$$V_{out} = G\, V_{in}. \tag{1.1}$$

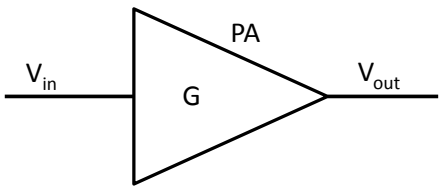

FIGURE 1.1 – Représentation shématique d'un amplificateur de puissance.

Le schéma d'amplification idéale est présenté Fig.1.1.

Pour les amplificateurs réels, la puissance d'alimentation est limitée et la puissance du signal de sortie ne pourra pas dépasser cette valeur. Pour de petits niveaux de puissance d'entrée, on peut souvent considérer l'amplificateur comme quasi-idéal. Mais, lorsque le niveau de puissance augmente, l'amplificateur commence à saturer. En conséquence de la saturation, le gain de l'amplificateur n'est pas constant. Il a généralement tendance à diminuer avec l'augmentation de la puissance d'entrée. Ce phénomène de compression de gain est dû au fait que le signal de sortie (tension, courant, puissance) sature en raison de la limitation de la tension ou du courant d'alimentation.

Les amplificateurs réels (non-idéaux) présentent des effets non désirés principalement des phénomènes non-linéaires et des effets mémoire (à long terme ou à court terme).

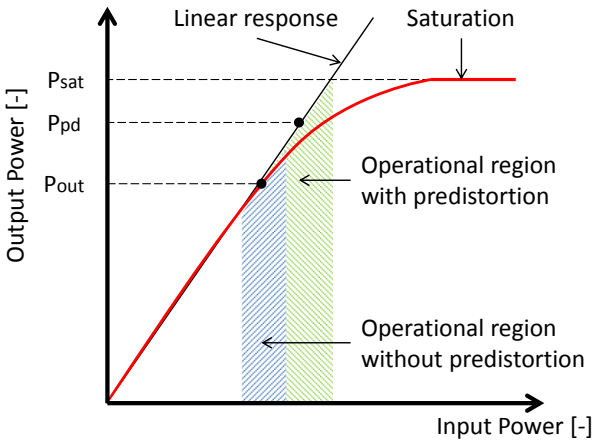

FIGURE 1.2 – Exemple de caractéristique AM/AM d'amplificateur de puissance.

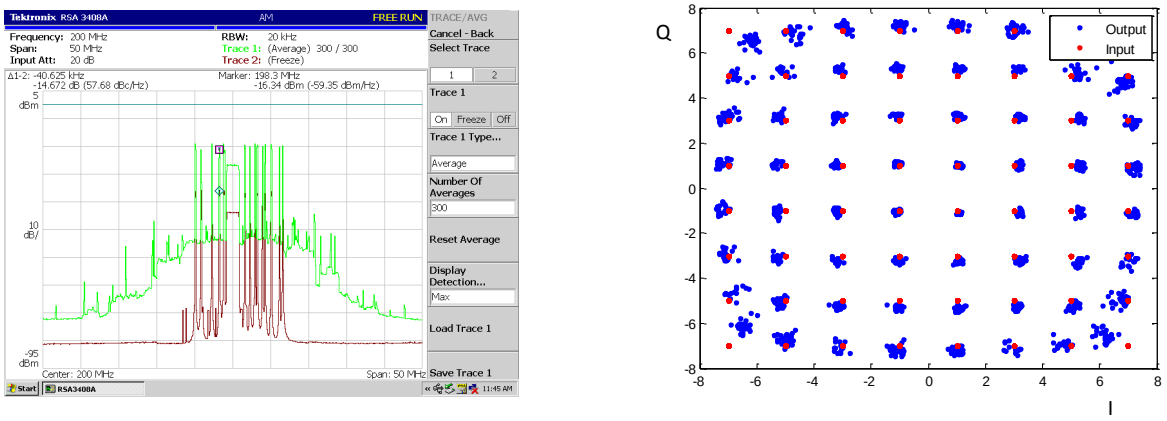

FIGURE 1.3 – Conséquences des non-linéarités et effets mémoire. À gauche : remontées spectrales. À droite : déformation de la constellation d'une modulation QAM.

1.2 Linéarisation et modélisation des amplificateurs de puissance

De nombreuses méthodes ont été proposées pour la linéarisation des amplificateurs de puissance. La prédistorsion numérique adaptative en bande de base est une des plus performantes. Elle consiste à faire précéder l'amplificateur d'un bloc de traitement non-linéaire (on dira prédistorteur par la suite) qui cherche à pré-corriger les distorsions de l'amplificateur. Dans cette thèse nous nous sommes focalisés sur cette approche.

L'opérateur de prédistorsion de même que le modèle de l'amplificateur s'appuie souvent sur des modèles dérivés des séries de Volterra.

Le calcul du prédistorteur peut appliquer soit une approche d'apprentissage direct qui minimise l'erreur quadratique moyenne entre la sortie de l'amplicateur divisée par le gain de référence et l'entrée du prédistorteur soit une approche d'apprentissage indirect qui consiste à calculer un postdistorteur. Dans cette approche indirecte, on minimise l'erreur quadratique moyenne entre l'entrée de l'amplificateur et le signal obtenu en appliquant un postdistorteur à la sortie de l'amplicateur divisée par le gain de référence.

Il existe de nombreux modèles pour la modélisation des amplificateurs de puissance (ou pour les prédistorteurs) allant des plus simples qui modélisent seulement les distorsions d'amplitude en négligeant les effets mémoires aux plus généraux comme les séries de Volterra et les modèles dérivés des séries de Volterra.

On peut distinguer trois catégories de modèles : les modèles statiques (sans effets mémoire), les modèles semi-statiques (où les effets mémoire se limitent à des distorsions de phase dépendant seulement de l'amplitude des signaux) et les modèles dynamiques (avec prise en compte des effets mémoire).

Dans cette thèse, nous nous sommes centrés sur les modèles dynamiques dérivés des séries de Volterra et s'exprimant linéairement en fonction de leurs coefficients. L'intérêt de ces modèles est leur généralité et la dépendance linéaire par rapport à leurs coefficients ce qui conduit à des problèmes d'optimisation convexe pour un critère d'optimisation quadratique dans le cas de la modélisation d'un apmlificateur de puissance ou de l'identification d'un prédistorteur avec une approche d'apprentissage indirect. Le problème se ramène alors à la résolution d'un système d'équations linéaires. Nous nous sommes plus particulièrement intéressés aux modèles de types polynômes à mémoire (PMS), polynômes à memoire généralisés (GMP) et DDR (dynamic deviation reduction).

Pour identifier les coefficients des modèles on peut utiliser des techniques d'identification par blocs ou des méthodes adaptatives travaillant échantillon par échantillon telles que les approches RLS ou LMS. Une des contributions de cette thèse est d'avoir proposé une technique intermédiaire entre RLS et LMS appelée moindres carrés franctionnaires ou FLMS (Fractional Least Mean Square).

1.3 Algorithme FLMS Fractional Least Mean Square Algorithm

Pour résoudre le système d'équations linéaires correspondant à l'optimisation du critère des moindres carrés pour la modélisation des amplificateurs ou le calcul des prédistorteurs, nous proposons une technique de moindres carrés franctionnaires appelée FMLS réalisant un compromis entre RLS et LMS en termes de complexité et de performance. Les méthodes fractionnaires comme leur nom l'indique, utilisent des dérivées non-entières qui généralisent la notion de dérivation à des nombres non-entiers qui peuvent être réels ou complexes.

La fonction de coût $\mathbf{J}$ construite sur l'erreur e est donnée par :

$$J(n) = E[e(n)e^*(n)] \tag{1.2}$$

Et le calcul du vecteur $\mathbf{b}$ pour le FLMS est défini comme :

$$\mathbf{b}(n+1) = \mathbf{b}(n) - \mu_1 \frac{\partial J(n)}{\partial \mathbf{b}(n)} - \mu_2 \frac{\partial^v J(n)}{\partial^v \mathbf{b}(n)}. \tag{1.3}$$

En utilisant l'opérateur différentiel de Riemann-Liouville d'ordre v nous obtenons :

$$\frac{\partial^v J(n)}{\partial^v \mathbf{b}(n)} = \mu_2 e \mathbf{\Phi}^H(n) \frac{\mathbf{b}^{(1-v)}(n)}{\Gamma(2-v)}. \tag{1.4}$$

On en déduit que la solution itérative pour le vecteur $\mathbf{b}$ s'écrit :

$$\mathbf{b}(n+1) = \mathbf{b}(n) + \mu_1 e\ \mathbf{\Phi}^H(n) + \mu_2 e\ \mathbf{\Phi}^H(n) \frac{\mathbf{b}^{(1-v)}}{\Gamma(2-v)}, \tag{1.5}$$

où Γ est la fonction Gamma, v représente l'ordre fractionnaire du système et μ_1 et μ_2 sont les constantes d'adaptation.

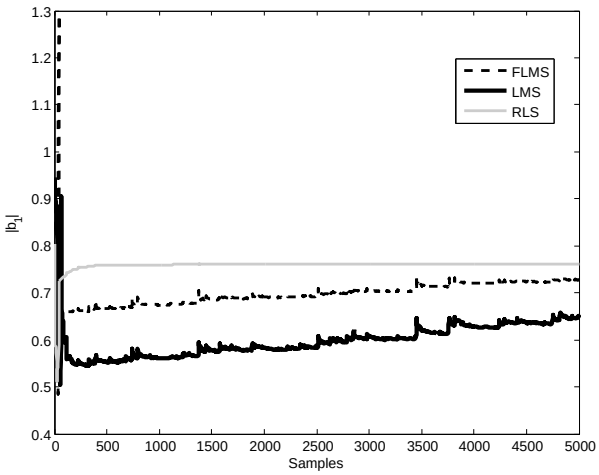

FIGURE 1.4 – Comparaison de la convergence du coeffcient $|b_1|$ pour les algorithmes LMS, FLMS et RLS. Amplificateur Smart PA de Thalès avec des signaux d'entrée OFDM large bande.

1.4 Amplificateurs et signaux utilisés pour les tests, comparaison des modèles

Pour le test et la comparaison des différents modèles et approches, plusieurs amplificateurs de puissance ont été utilisés :

- **Amplificateurs de diffusion radio-vidéo (données fournies par Teamcast) :**
  - Amplifcateur A1 (75 W_{rms}, 100 W_{rms}, 460 - 860 MHz)
  - Amplificateur A2 (120 W_{rms}, 460 - 860 MHz)
  - Amplificateur B (200 W_{rms}, 620 - 700 MHz)
- **Amplificateur (appelé SmartPA) pour les communications tactiques, fourni par thalès et mesuré à l'ESIEE :**
  - amplificateur SmartPa de Thalès (10 W_{rms}, 30 - 512 MHz, reconfigurable en polarisation)

Les signaux de test suivants ont été utilisés :

- **Avec les amplificateus de diffusion audio-vidéo de TeamCast :**
  - signal de type OFDM (DVB or DAB)
- **Avec le Smart PA de Thales :**
  - 64 QAM
  - GMSK
  - OFDM
  - Multiplex 1 (Burst : somme de 3 signaux GMSKs avec évasion de fréquence)
  - Multiplex 2 (Burst : somme de signaux GMSKs avec évasion de fréquence et d'un signal 64QAM)
  - Multiplex 3 (Burst : somme de signaux GMSKs avec évasion de fréquence et d'un signal OFDM)

Plusieurs tests ont été réalisés pour estimer les ordres des différents modèles pour la modélisation des amplificateurs et la prédistorsion de façon à obtenir un compromis entre la complexité et les performances. La Fig.1.5 illustre cette étude en présentant les résultats de la recherche exhaustive pour les ordres des modèles dans le cas des modèles OPMS (orthogonal memory polynomial et DDR dynamic deviation reduction d'ordre 1 et 2 : DDR1 et DDR2).

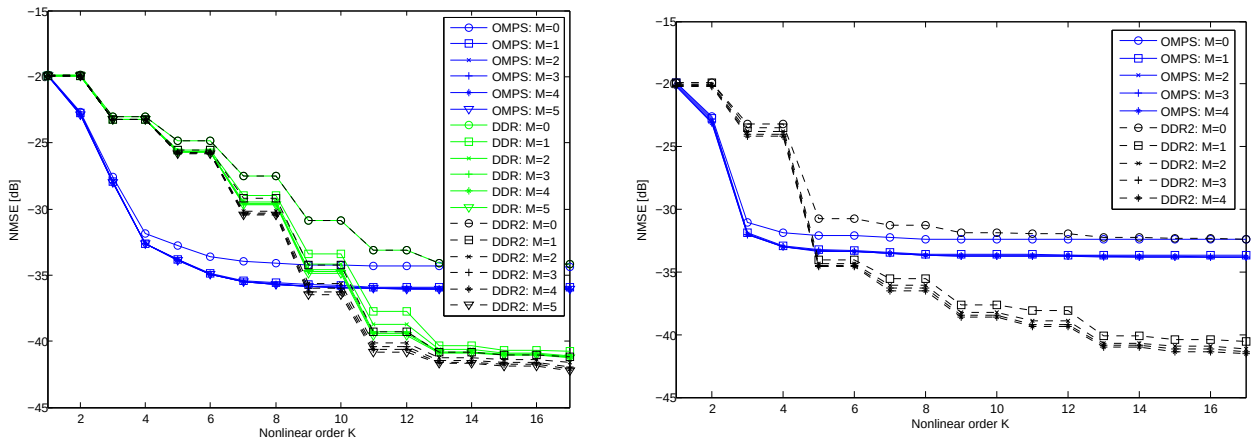

FIGURE 1.5 – À gauche : recherche exhaustive des ordres des modèles optimaux pour la modélisation de l'amplificateur B. À droite recherche exhaustive des ordres des modèles optimaux pour la prédistorsion de l'amplificateur B. (Modèles OMPS et DDR2).

1.5 Détermination des ordres optimaux des modèles pour la modélisation et la prédistorsion des amplificateurs de puissance - Détermination de la structuures des modèles

La détermination des différents ordres des modèles qui déterminent la structure de séries (ordres de non-linéarité, profondeur mémoire etc) est une tâche difficile quand le modèle comporte de nombreux ordres à déterminer. Par exemple, les modèles polynomiaux à mémoire ne comportent que 2 paramètres pour fixer leur structure : l'ordre de non-linéarité K et la profondeur mémoire M. Si on fixe $1 \leq K \leq 17$ et $1 \leq M \leq 5$, le test exhaustif de toutes les configurations possibles représente 85 évaluations (soit 85 résolutions de systèmes d'équations linéaires). Mais pour le modèle GMP (polynômes à mémoire généralisés) il faut déterminer 8 paramètres pour fixer la structure du modèle et si on impose que ces paramètres soient compris entre 1 et 10, la détermination de la structure optimale demande 10^8 évaluations. La détermination de la structure optimale des modèles GMP est donc très coûteuse en calculs.

Aussi avons-nous proposé un algorithme d'optimisation génétique en nombres entiers pour la détermination de la structure optimale des modèles. La fonction de coût (fitness) est un compromis entre la performance (NMSE erreur quadratique normalisée) et la complexité du modèle (nombre de coefficients).

Pour évaluer l'algorithme proposé, nous avons utilisé la configuration de test suivante : amplificateur de Broadcast $120W_{rms}$, signal OFDM, nombre de générations : 100, taille de la population : 20 individus, condition d'arrêt : 40 générations, modèle polynôme à mémoire (PMS) avec les conditions limites suivantes : $K = 13$ et $M = 8$, modèle GMP avec les conditions limites : $K_a = 7$, $K_b = 3$, $K_c = 3$, $L_a = 3$, $L_b = 3$, $L_c = 3$, $M_b = 5$, $M_c = 5$.

Nous avons obtenu les structures suivantes. Pour le modèle PMS : $K = 8$ et $M = 2$, $NMSE = -37.25dB$, 24 coefficients. Pour le modèle GMP : $K_a = 7, L_a = 2, K_b = 2, L_b = 0, M_b = 2, K_c = 2, L_c = 0, M_c = 0$ et $NMSE = -37.56dB$, 14 coefficients.

L'algorithme proposé est capable de réduire le temps de calcul nécessaire à la détermination

de la structure par un facteur au moins égal à 20.

1.6 Proposition d'une approche par réseau de neurones à mémoire

Nous avons proposé un nouveau modèle s'appuyant sur un réseau de neurones à mémoire pour la prédistorsion. Les réseaux de neurones classiques ne sont pas conçus pour des signaux complexes comme ceux utilisés dans les modèles en bande de base, aussi des solutions ont-elles été proposées dans lesquelles on sépare les signaux complexes en partie réelle et partie imaginaire qui sont traitées par des réseaux séparés.

Nous avons proposé une approche originale qui s'appuie sur une structure de perceptron multicouches dans laquelle le signal à l'entrée du réseau est retardé mais aussi avancé de façon à mieux modéliser les effets mémoire.La Fig.1.6 illustre cette approche.

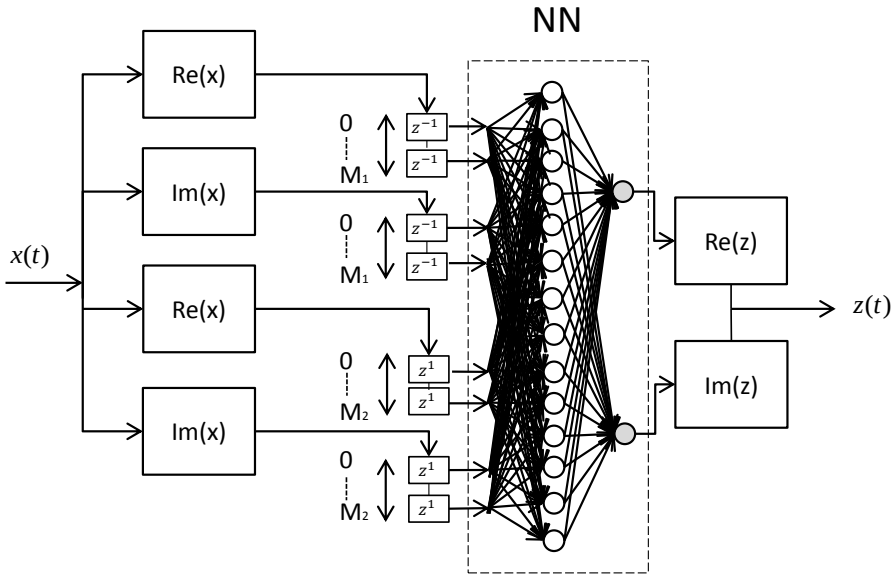

FIGURE 1.6 – Principe du réseau de neurones à mémoire proposé avec : $2(M_1+1)+2(M_2+1)$ entrées. Avec $(M_1 = M_2 = 6)$, 14 neurones dans la couche cachée et 2 neurones en sortie.

Les résultats obtenus avec ce réseau de neurones pour la linéarisation de l'amplificateur A1 (75W) sont donnés Table 1.1.

TABLE 1.1 – Table de résultats pour la prédistorsion de l'amplificateur A1 (75W) avec le réseau de neurones à mémoire.

Ordre mémoire	**Nombre de couches cachées**	**NMSE [dB]**
1	1	-27.29
2	1	-29.00
3	1	-31.09
5	1	-31.71
10	1	-32.20
10,-10	1	-37.61

1.7 Influence d'un décalage temporel ente la voie directe et la voie de retour sur les performances de la prédistorsion

Nous avons évalué la sensibilité de la prédistorsion à un décalage temporel entre la voie directe (celle comprenant le prédistorteur et l'amplificateur) et la voie de retour (celle permettant de mesurer la sortie de l'amplificateur et d'adapter ensuite le prédistorteur). La configuration du système linéarisé par prédistorsion avec un décalage temporel entre les 2 voies est présenté Fig.1.7.

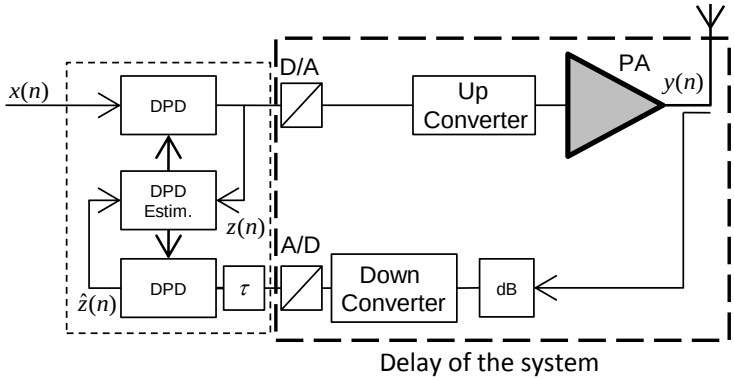

FIGURE 1.7 – Predistortion numérique avec un décalage teporel entre les 2 voies.

On a observé que pour un décalage temporel égal à un nombre entier d'échantillons, les modèles PMS et GMP sont capables de compenser assez bien ce décalage tant que celui-ci est de durée inférieure à la profondeur mémore du modèle et qu'il s'agit d'un retard. Ces modèles ne sont pas capables de corriger une avance. La Fig.1.8 représente les résultats obtenus pour des décalages entiers.

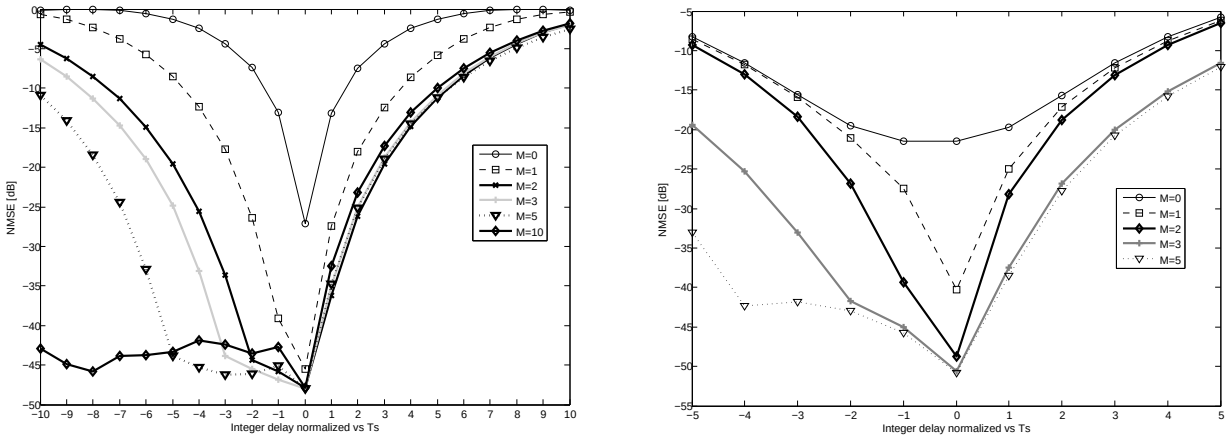

FIGURE 1.8 – À gauche : influence d'un décalage temporel égal à un nombre entier d'échantillons, cas du modèle PMS. À droite : mêmes résultats pour le modèle GMP.

Nous avons aussi testé la sensibilité du système de prédistorsion à un décalage temporel égal à une fraction d'intervalle d'échantillonnage (décaage fractionnaire). Comme précédemment, ces décalages sont compensés si la profondeur mémoire du prédistorteur est suffisante.

De façon à pouvoir compenser les avances, nous avons proposé une modification du modèle polynôme à mémoire et nous avons appelé le nouveau modèle PMM (modified polynomial model). Il est défini par :

$$\begin{aligned} y(t) &= \sum_{k=0}^{K_a-1}\sum_{l=0}^{L_a-1} a_{k,l}x(t-l)|x(t-l)|^k \\ &+ \sum_{k=0}^{K_b-1}\sum_{l=0}^{L_b-1} b_{k,l}x(t+l)|x(t+l)|^k, \end{aligned} \tag{1.6}$$

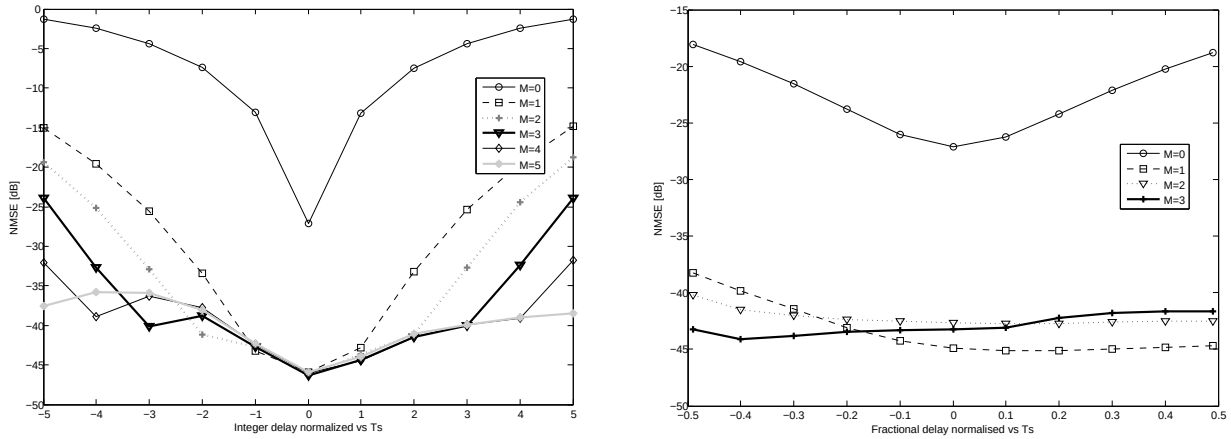

FIGURE 1.9 – À gauche : effet d'un décalage entier cas du modèle PMM. À droite : effet d'un décalage temporel fractionnaire, cas du modèle PMM.

On peut observer sur la Fig.1.9 que le modèle proposé est capable de compenser les avances comme les retards entiers ou fractionnaires quand l'ordre mémoire du prédistorteur est suffisant.

1.8 Contribution à l'étude des solutions multiples dans les systèmes de prédistorion avec apprentissage indirect

Nous avons mis en évidence l'existence de solutions multiples pour le prédistorteur dans l'architecture avec apprentissage indirect. Comme on peut voir Fig.1.10, fixer les coefficients du prédistorteur à 0 conduit à une ereur minimale sur les signaux mais correspond à un résultat sans intérêt pratique.

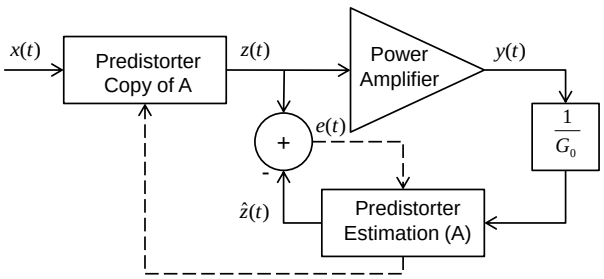

FIGURE 1.10 – Architecture de prédistorsion adaptative avec apprentissage indirect.

Aussi avons-nous proposé un nouveau critère construit sur la minimisation d'une erreur de gain plutôt qu'une erreur de signal. Ce critère permet naturellement d'éliminer la solution nulle

et régularise le comportement de la convergence.

1.9 Conclusion sur la 1ère partie

Nous avons présenté et comparé plusieurs méthodes pour la modélisation et la linéarisation des amplificateurs de puissance. Nous avons conçu et mis en place un banc de mesure large bande pour le test des amplificateurs et effectué plusieurs campagne de mesure.

Plusieurs amplificateurs ont été mesurés, modélisés et linéarisés avec les différentes approches. Les modèles ont été comparéses en termes de complexité et de performance.

Une architecture originale de réseau de neurones capable de traiter des signaux complexes a été proposée.

Un des chapitre est consacré à l'étude de la sensibilité de la prédistorsion à un décalage temporel entre les signaux de la voie directe et ceux de la voie de retour.

Un autre chapitre décrit l'existence de solutions multiples pour la prédistorsion dans le cas de l'approche adaptative à apprentissage indirect.

Nous avons aussi travaillé sur la détermination de la structure des modèles et proposé un algoruthme d'optimisation génétique en nombres entiers.

Chapitre 2

Méthodes avancées pour les systèmes non-linéaires

La deuxième partie de cette thèse est centrée sur l'analyse des systèmes dynamiques non-linéaires dans lesquels un comportement chaotique peut apparaître. Le but est d'essayer de répondre à la question suivante : à quel point le comportement chaotique est-il naturel dans la nature ?

2.1 Analyse des modèles mathématiques

Un des chapitres présente une synthèse des méthodes qui sont utilisées pour l'analyse des systèmes dynamiques non-linéaires. Généralement, ces systèmes sont décrits par des équations différentielles non-linéaires.

Un exemple de telles équations est donné par le système de Lorenz :

$$\begin{aligned} \dot{x} &= 10(y-x) \\ \dot{y} &= 28\ x - x\ z - y \\ \dot{z} &= x\ y - \frac{8}{3}\ z. \end{aligned} \tag{2.1}$$

qui est décrit par 3 équations différentielles d'ordre 1.

La connaissance du système permet d'utiliser des outils comme :

- les sections de Poincare.
- L'analyse des bifurcations (Fig. 2.1).
- Les exposants de Lyapunov.
- La dimension de Kaplan-Yorke.

2.2 Analyse des séries temporelles

Malheureusement, pour des mesures réelles, nous ne disposons pas toujours de toutes les variables. Mais il existe des techniques comme la reconstruction d'espaces d'états (state space dynamic reconstruction) définie par :

$$\mathbf{X} = \begin{pmatrix} X_0 & \cdots & X_{(m-1)\tau} \\ \vdots & \ddots & \vdots \\ X_n & \cdots & X_{n+(m-1)\tau} \end{pmatrix}, \tag{2.2}$$

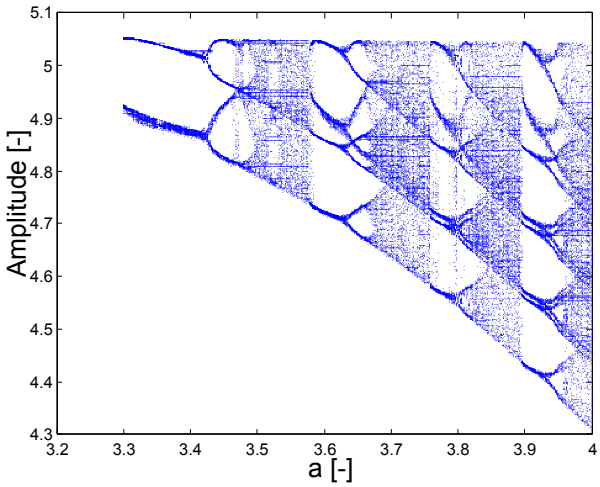

FIGURE 2.1 – Analyse des bifurcations de système dynamique

où nous avons besoin d'estimer la dimension m (nombre de variables) et le décalage τ (Fig.2.2). Nous pouvons ensuite utiliser des technique telles que celle des exposnats de Lyapunov ou la technique "box-counting".

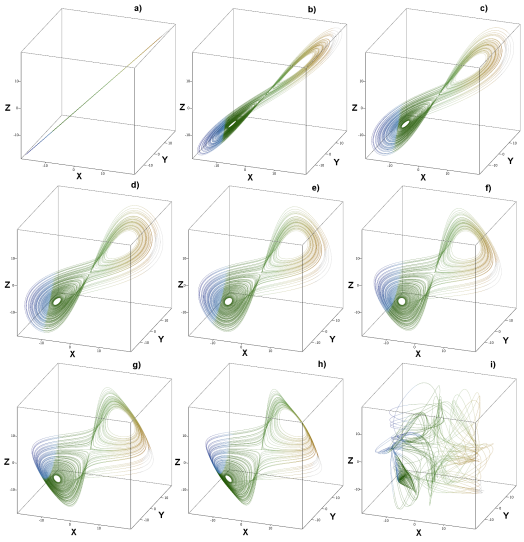

FIGURE 2.2 – Différents décalages τ $a)$ $\tau = 0$, $b)$ $\tau = 2$, $c)$ $\tau = 4$, $d)$ $\tau = 6$, $e)$ $\tau = 8$, $f)$ $\tau = 10$, $g)$ $\tau 12$, $h)$ $\tau = 14$, $i)$ $\tau = 98$.

2.3 Sur les flux chaotiques fractionnaires autonomes d'ordre peu élevé et algébriquement simples

La calcul fractionnaire est décrit succinctement dans la thèse. Il s'agit du calcul dans lequel les ordres de dérivations et d'intégration peuvent être des nombres réels non entiers ou des complexes. De façon à montrer les propriétés du calcul fractionnaire, nous avons choisi un flux chaotique défini par 3 équations d'ordre 1 :

$$\begin{aligned} \dot{x} &= -y \\ \dot{y} &= x + z \end{aligned}$$

$$\dot{z} = xz + 3y^2. \tag{2.3}$$

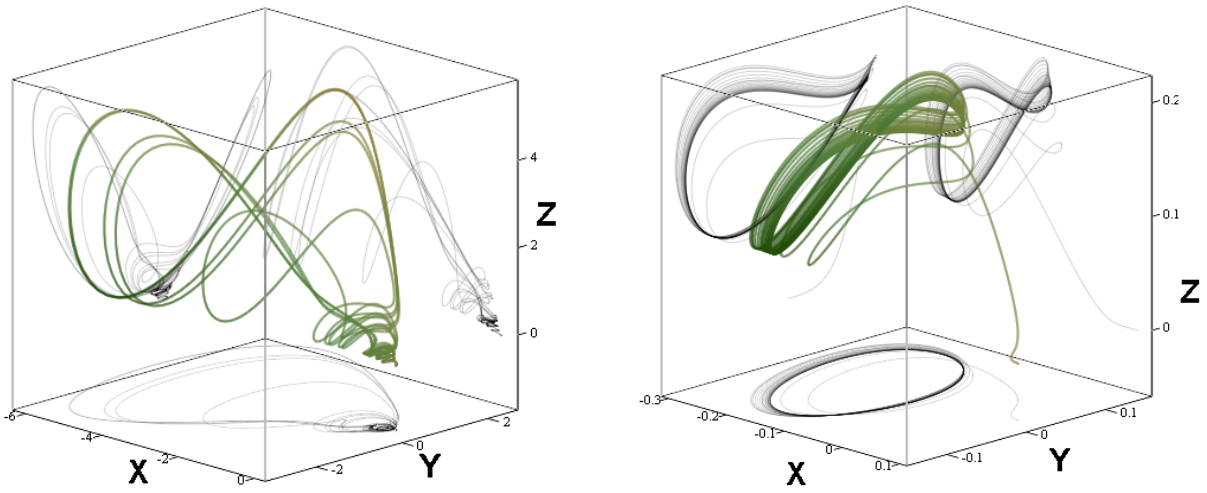

FIGURE 2.3 – À gauche : système simulé numériquement avec $\alpha_1 = 1, \alpha_2 = 1, \alpha_3 = 1$. À droite : Système avec intégrateurs $\alpha_1 = 0.86, \alpha_2 = 1$ and $\alpha_3 = 0.6$.

On peut observer Fig.2.3 que le comportement chaotique peut apparaitre même dans des systèmes dynamiques autonomes d'ordre inférieur à 3. Les intégrateurs sont fixés à : $\alpha_1 = 0.86, \alpha_2 = 1$ et $\alpha_3 = 0.6$. Dans ce cas particulier, l'ordre est de 2.43. Dans la figure, on peut voir la modification du comportement dynamique du système, avec préservation du comportement chaotique.

2.4 Généralisation de l'approximation linéaire par morceau des dynamiques chaotiques

Dans cette section nous présentons une conception automatisée de l'approximation linéaire par morceau de champs de vecteurs non-linéaires. L'approximation linéaire par morceau est importante, car elle permet de resoudre les systèmes à l'aide d'outils linéaires.

Pour l'estimation des coefficients nous utilisons une technique d'optimisation par essaim de particules avec comme fonction d'objectif une combinaison des exposants de Lyapunov, de la densité spectrale de puisance et du nombre de points fixes.

Dans la Fig.2.4 on peut observer les approximations obtenues pour les fonctions cubiques et quadratiques pour le modèle mathématiqu de neurone.

Plusieurs exemples de fonctions non-linéaires complexes et de leur approximation linéaire par morceaux sont présentées dans la thèse.

2.5 Systèmes dynamiques avec sauts discrets périodiques

Nous présentons les systèmes dynamiques avec sauts discrets périodiques, appelés aussi systèmes de Gotthans-Petrzela (modèles GP), présentant des solutions chaotiques.

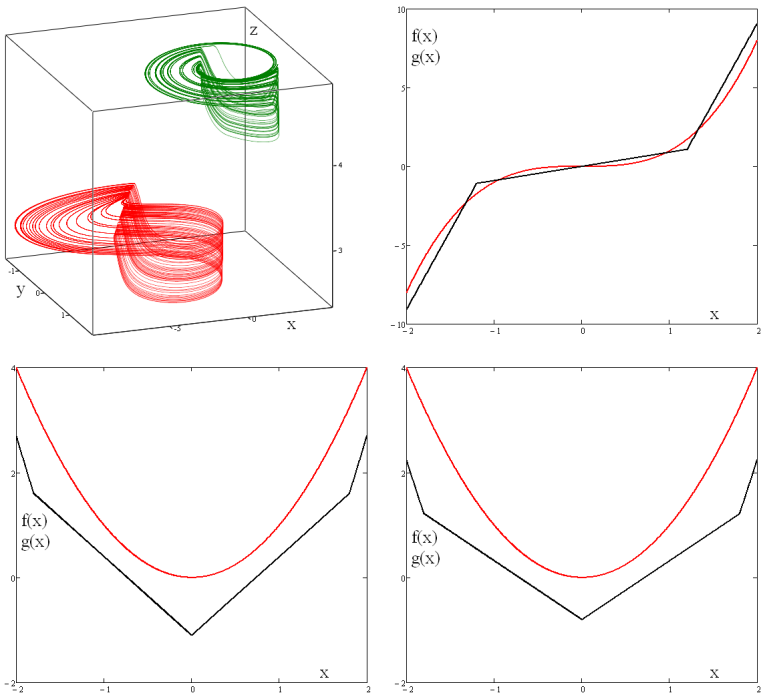

FIGURE 2.4 – Approximation du modèle mathématique d'un neurone , attracteurs et fonctions non-linéaires.

$$\begin{aligned} \dot{x} &= -a_x\ x \pm sign[\sin(b_y y)] \\ \dot{y} &= -a_y\ y \pm sign[\sin(b_z z)] \\ \dot{z} &= -a_z\ z \pm sign[\sin(b_x x)]. \end{aligned} \tag{2.4}$$

On montre que le calcul des exposants de Lyapunov n'est pas possible à cause des valeurs extrêmes présentes dans la matrice de Jacobi. On présente une approximation de ces systèmes, obtenue par série de Fourier permettant d'éviter les gradients extrêmes des trajectoires proches.

À cause de la grande densité d'attracteurs, on ne peut pas appliquer la méthode de dimension box-counting. Aussi avons-nous présenté un quantificateur sphérique qui permet de réduire la complexité.

2.6 Attracteurs multi-grille avec sauts discrets

De façon à prouver l'existence de systèmes dynamiques chaotiques avec des champs de vecteurs discrets, nous avons choisi l'attracteur multi grille et nous l'avons réalisé par un circuit électronique. La fonction non-linéaire, pour garder la quantification, est réalisée par une cascade de 2 convertisseurs analogique-numérique et numérique-analogique.

La Fig.2.6 présente les projections de Monge observées à l'oscilloscope.

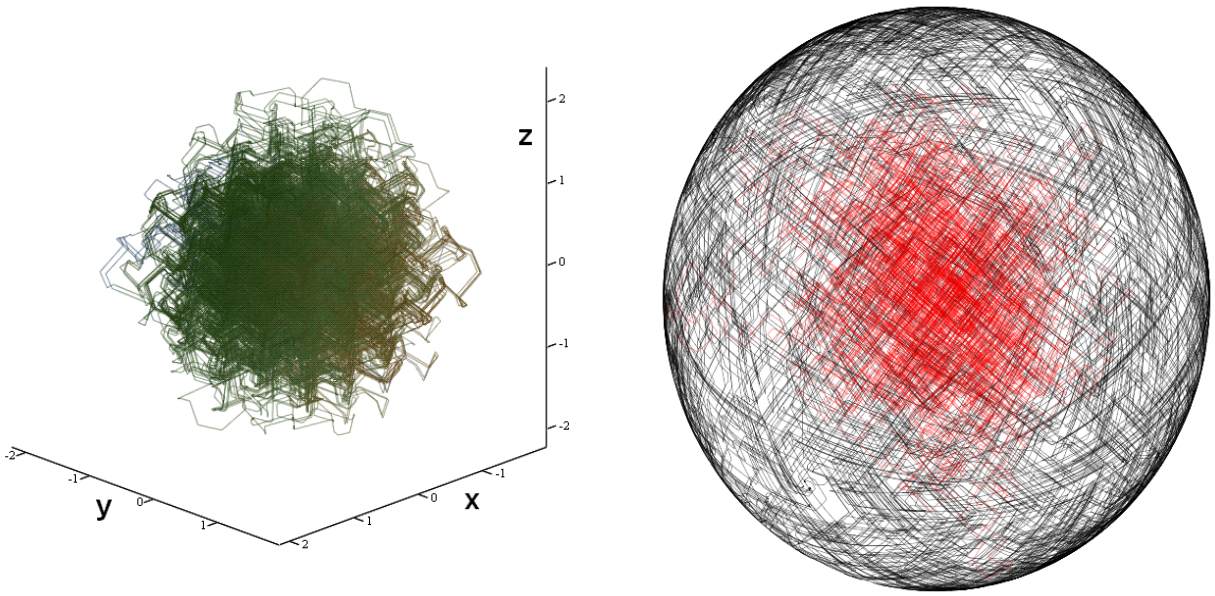

FIGURE 2.5 – Quantification du mouvement dynamique, attracteur analysé (rouge) et sa projection sur la sphère (noir), système GP avec des paramètres uniformes $a_x =_{ay}= a_z = 0.1$ and $b_x = b_y = b_z = 10$.

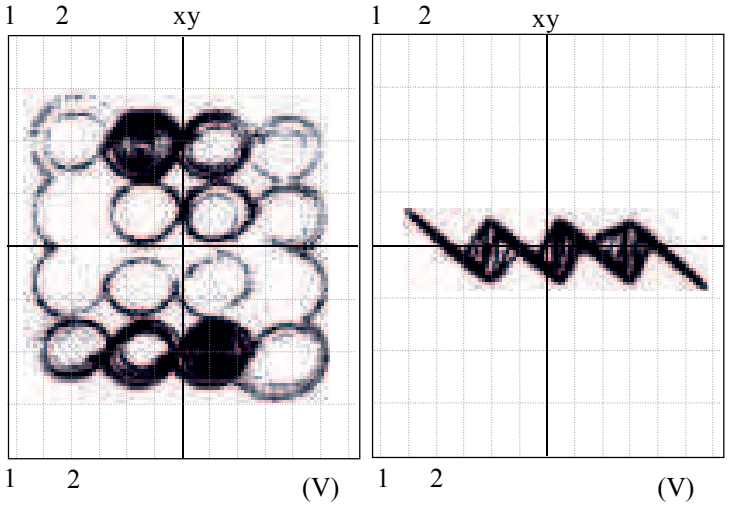

FIGURE 2.6 – Système measuré, scroll 4×4 : projections V(x) vs V(-y)(left), V(-y) vs V(z) (right).

2.7 Approches parallèles

Les ordinateus récents sont réalisés avec des processuers multi-coeurs. Il est donc utile d'adapter les algorithmes pour tirer partie du parallélisme de ces architectures.

Dans cette thèse, nous avons présenté des méthodes pour paralléliser le calcul des exposants de Lyapunov. Nous avons démontré l'efficacité de ces méthodes sur un vrai système dynamique. Le calcul implémenté sur 8 processeurs en parallèle est 4 fois plus rapide que le calcul sur un seul processeur.

La partie suivante présente un algorithme parallèle d'optimisation par essaim de particules et démontre son efficacité pour un système dynamique non-linéaire général avec 15 paramètres

inconnus :

$$\begin{aligned} \dot{x} &= a_1 x + a_2 y + a_3 z + |a_4 x| + a_5 \\ \dot{y} &= a_6 x + a_7 y + a_8 z + |a_9 y| + a_{10} \\ \dot{z} &= a_{11} x + a_{12} y + a_{13} z + |a_{14} z| + a_{15}, \end{aligned} \tag{2.5}$$

On montre que l'algorihme implémenté sur 4 processeurs en parallèle est capable de trouver les solutions chaotiques deux fois et demi plus rapidement que l'algorithme stanard.

Une solution possible est :

$$\begin{aligned} \dot{x} &= 0.7482x - 1.6934y + 0.81z + |\pm 1.242x| + 0.7927 \\ \dot{y} &= 2.3854x + 0.5713y + 0.7908z + |\pm 1.2208y| + 0.3583 \\ \dot{z} &= 1.6322x + 0.595y - 0.641z + |\pm 0.6702z| + 1.2375, \end{aligned} \tag{2.6}$$

correspondant à la Fig.2.7.

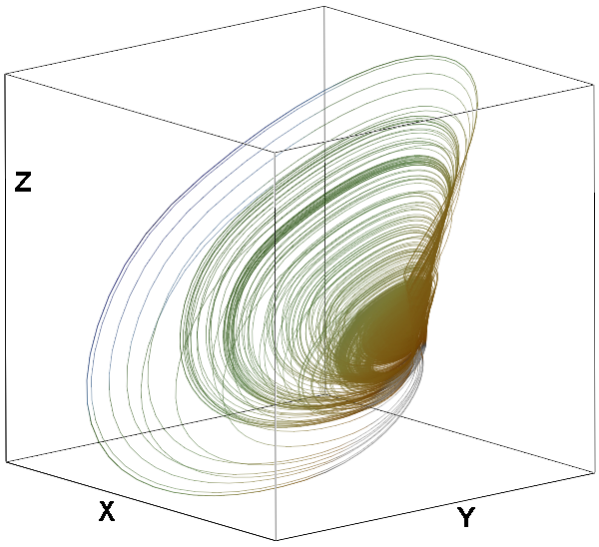

FIGURE 2.7 – Solution chaotique possible.

2.8 Conclusion sur la deuxième partie

Dans la deuxième partie, nous avons d'abord présenté plusieurs méthodes d'analyse des systèmes dynamiques non-linéaires.

Puis nous avons présenté les séries d'ordre fractionnaires et nous avons apporté la preuve de l'existence de comportements chaotiques pour des systèmes dynamiques autonomes non-linéaires d'ordre inférieur à 2.5.

Nous avons proposé une méthode automatique d'approximation de champs de vecteurs non-linéaires. La méthode utilise un algorithme d'optimisation par essaim de particules. Plusieurs exemples d'approximations ainsi obtenues sont présentés.

Nous avons ensuite présenté un type de système avec des champs de vecteurs discrets périodiques et nous avons montré qu'on ne peut pas utiliser dans ce cas les méthodes d'analyse standard. Aussi avons-nous proposé une approche de quantification sphérique de manière à réduire la complexité de calcul.

Le théorème sur les champs de vecteurs discrétisésa été validé par la réalisation d'un circuit électronique.

Le dernier chapitre expose la parallélisation du calul des exposants de Lyapunov et la parallélisation de l'algorithme d'optimisation par essaim de particules. L'efficacité des ces parallélisations est illustrée sur des systèmes particuliers.

Resumé

Méthodes avancées pour l'analyse des systèmes dynamiques non-linéaires

L'augmentation des performances des futurs systèmes dynamiques nécessite la prise en compte des phénomènes physiques non linéaires. Cette thèse apporte un éclairage et des contributions sur deux sujets complémentaires liés aux phénomènes dynamiques non linéaires. Le mémoire de thèse est divisé en deux parties.

La première partie porte sur les non-linéarités des amplificateurs de puissance dans le cadre d'applications destinées aux télécommunications ou à la diffusion audio-visuelle. Plusieurs méthodes de modélisation et de linéarisation des amplificateurs de puissance ont été conçues et discutées. Un banc de test a été développé afin d'évaluer les méthodes sur des amplificateurs réels. La robustesse de ces techniques à un mauvais alignement temporel des signaux ainsi que leur capacité à faire face à des artefacts spectraux ont été évaluées. Par ailleurs, nous avons effectué une étude théorique sur l'existence et la prise en compte de solutions multiples dans l'approche adaptative par apprentissage indirect.

La deuxième partie traite des systèmes dynamiques non linéaires qui présentent des solutions chaotiques. Ces systèmes sont bien connus, mais les techniques d'identification de ces solutions manquent de fiabilité ou nécessitent une puissance de calcul importante. Dans cette thèse, plusieurs méthodes utilisant également le calcul parallèle sont présentées. Les systèmes à commande différentielle fractionnaire sont brièvement discutés. Il est aussi montré, qu'il existe des systèmes liés à des fonctions de transfert non linéaires avec quantification pour lesquels les méthodes d'analyse classiques échouent.

Mots-clés: Systèmes non-linéaires, pré-distorsion, amplificateur de puissance, chaos, exposant de Lyapunov, Systèmes dynamiques.

Abstract

Advanced methods for analyzing nonlinear dynamical systems

In order to achieve better performance of modern communication devices, that have to be operated on its physical limits, the nonlinear phenomena need to be taken into the account. This thesis brings insight into two different subjects related with nonlinear dynamical phenomena. The thesis itself is divided into two parts.

The first part is focused on the domain of nonlinear power amplifiers from the system point of view. Several methods for modelization and linearization of power amplifiers have been designed and discussed. A test-bench has been assembled in order to evaluate the proposed methods on real power amplifiers. Then the robustness to time misalignment in the system and the ability to deal with spectral artifacts in the system of presented methods have been evaluated. Also a theoretical study has been conducted on the existence and management of multiple solutions in the frame of adaptive indirect learning approach.

The second part deals with nonlinear dynamical systems that are exhibiting chaotic solutions. Such systems are well known, but techniques for identifying reliable such solutions are either missing or are computational intense. In this thesis several methods using also parallel computing are presented. Systems with fractional differential order are briefly discussed. It is as well shown, that there exists systems related with quantified nonlinear transfer functions for which the standard analyzing methods fails.

Keywords: Non-linear systems, pre-distortion, power amplifier, chaos, Lyapunov exponents, dynamical systems.